BEILSTEIN JOURNAL OF NANOTECHNOLOGY

Advanced atomic force microscopy techniques IV

Edited by Thilo Glatzel

Imprint

Beilstein Journal of Nanotechnology
www.bjnano.org
ISSN 2190-4286
Email: journals-support@beilstein-institut.de

The *Beilstein Journal of Nanotechnology* is published by the Beilstein-Institut zur Förderung der Chemischen Wissenschaften.

Beilstein-Institut zur Förderung der Chemischen Wissenschaften
Trakehner Straße 7–9
60487 Frankfurt am Main
Germany
www.beilstein-institut.de

BEILSTEIN JOURNAL OF NANOTECHNOLOGY

Distribution of Pd clusters on ultrathin, epitaxial TiO_x films on $Pt_3Ti(111)$

Christian Breinlich[1], Maria Buchholz[1,2], Marco Moors[*1,3], Tobias Pertram[1], Conrad Becker[1,4] and Klaus Wandelt[1,5]

Full Research Paper

Open Access

Address:
[1]Institute of Physical and Theoretical Chemistry, University of Bonn, Wegelerstraße 12, D-53115 Bonn, Germany, [2]Institute of Functional Interfaces, Karlsruhe Institute of Technology, D-76021 Karlsruhe, Germany, [3]Peter Grünberg Institute, Forschungszentrum Jülich, Wilhelm-Johnen-Straße, D-52425 Jülich, Germany, [4]Aix Marseille Université, CNRS, CINaM UMR 7325, 13288 Marseille, France and [5]Institute of Experimental Physics, University of Wroclaw, Pl. Maksa Borna, 50-204 Wroclaw, Poland

Email:
Marco Moors* - m.moors@fz-juelich.de

* Corresponding author

Keywords:
cluster growth; palladium; platinum–titanium alloy; scanning tunnelling microscopy (STM); template; titanium oxide

Beilstein J. Nanotechnol. **2015,** *6,* 2007–2014.
doi:10.3762/bjnano.6.204

Received: 01 June 2015
Accepted: 22 September 2015
Published: 09 October 2015

This article is part of the Thematic Series "Advanced atomic force microscopy techniques IV".

Guest Editor: T. Glatzel

Abstract

Scanning tunnelling microscopy (STM) was used to investigate the nucleation and growth of palladium clusters on two different, ultrathin, epitaxial, titania films grown on a $Pt_3Ti(111)$ surface. The first oxide phase, z'-TiO_x, is anisotropic and consists of parallel stripes separated by trenches. Defects (i.e., oxygen vacancies) in this structure are confined to these trenches and act as nucleation sites. Therefore, the Pd clusters are mostly arranged in unidirectional rows along the trenches, creating a template effect. The second phase, w'-TiO_x, exhibits a hexagonal, long range, $(7 \times 7)R21.8°$, Moiré-type superstructure with fewer and shallower defects, making the template effect less discernible.

Introduction

Catalysts often consist of metal nanoparticles dispersed on an oxide support structure. Small metal particles on an insulating substrate exhibit different electronic properties than the corresponding bulk metal phase. Moreover, in many cases, the oxide surface not only acts as a support structure but also takes part in the reaction cycle, for example, in oxygen spillover to the metal particles [1,2]. Thus, the investigation of the properties of supported metal clusters and the influence of the metal-oxide interfaces are of great interest. In particular, titanium oxides are often correlated with the so-called strong metal support interaction (SMSI) effect, which describes the influence of a transition metal oxide support on noble metal clusters yielding novel catalytic properties [1-7]. In order to understand this effect, well-defined model systems are needed. “Well-defined”

refers to both the clusters and the supporting substrate, as exemplified in [8-10] for example. In the ideal case, the clusters should be monodisperse or have at least a known size distribution. Ideal oxide surfaces can be favourably implemented in the form of thin epitaxial films. Such films grown on a single crystalline, metal support have several advantages: (a) standard surface science techniques can be applied due to the high conductivity of these films compared to the respective bulk oxides, (b) the films can be prepared with a very high degree of structural preciseness, and (c) the influence of bulk effects such as subsurface oxygen vacancies is excluded.

In this sense we concentrate here on the preparation of uniform Pd clusters on two different, ultrathin, epitaxial TiO_x films grown on a chemically ordered, $Pt_3Ti(111)$, single crystal surface. One of the TiO_x films has a rectangular structure and the other a hexagonal structure. In a recent publication we described the detailed protocol on how to grow these TiO_x films by direct oxidation of the $Pt_3Ti(111)$ surface at elevated temperatures [6]. Granozzi et al., who found very similar phases by "reactive evaporation" of titanium onto a Pt(111) surface in oxygen [7], introduced the notation z'-TiO_x (zigzag-like) for the rectangular and w'-TiO_x (wagon-wheel-like) for the hexagonal oxide phase, according to their appearance in STM images. Due to the similarity of our films to those described for Pt(111), we decided to simply adopt the same nomenclature throughout this paper. The rectangular z'-TiO_x phase obtained on the $Pt_3Ti(111)$ surface exhibits characteristic stripes of densely packed, Ti–O rows of bilayer thickness. These are separated 1.44 nm apart from each other with parallel trenches in between. The w'-TiO_x phase consists of a hexagonal, oxygen-terminated, Ti–O bilayer, which shows similarities to the Moiré superstructure of ultrathin aluminium oxide films grown on the chemically ordered, $Ni_3Al(111)$ surface [11-14]. The advantages of growing an oxide film from a component of an ordered alloy surface with a higher enthalpy of oxide formation are the somewhat better structural quality of the resulting films and their improved reproducibility compared to films grown by "reactive evaporation" [7].

Both the z'-TiO_x phase on Pt(111) and the Moiré superstructure of the alumina film on $Ni_3Al(111)$ have already been proven to be excellent templates for the ordered growth of metal clusters. Granozzi et al. found ordered rows of Fe and Au clusters along the trenches of the z'-TiO_x phase [15,16], while other studies (also of our own group) demonstrated the growth of ordered arrays of, for example, Pd-, Au-, and Fe- [11-14] or Co-clusters on $Al_2O_3/Ni_3Al(111)$ [10]. In the present paper we investigate the template effect of two different structures of the same type of oxide on the cluster growth of the same metal, namely Pd on z'-TiO_x and w'-TiO_x.

Experimental setup

The scanning tunnelling microscopy (STM) experiments were conducted on our custom-built LT-STM, which for the experiments presented in this paper, was run at room temperature. The sample was prepared in an adjacent preparation chamber, which was equipped with a sputter gun, low energy electron diffraction (LEED) optics and an Auger electron spectroscopy (AES) analyser. The STM tips were electrochemically etched from a 0.5 mm tungsten wire and cleaned under ultra-high vacuum (UHV) conditions using voltage pulses of 10 ms duration between −10 and +10 V. The STM data were analysed with the WSxM freeware program [17].

The (111)-oriented Pt_3Ti crystal was purchased from MaTeck (Jülich, Germany) and cleaned using several cycles of argon sputtering at 900 K for 10 min with subsequent annealing at 1100 K for another 10 min in order to restore the surface structure. The crystallographic and chemical order of the surface was verified by a sharp (2 × 2) superstructure visible in LEED experiments and the absence of any carbon or oxygen contamination in AES experiments.

Palladium was evaporated from a simple Knudsen cell with a slow deposition rate of approximately $2 \cdot 10^{-3}$ MLs^{-1}. The amount deposited was controlled by the deposition time and monitored by the evolution of the 330 eV Pd AES signal in relation to the 505 eV oxygen signal, as well as by the number density and size of the metal clusters seen in the STM images. The surface was kept at room temperature during evaporation and no post-deposition annealing was carried out.

Results and Discussion

The rectangular z'-TiO_x (zig-zag-like) phase

Exposing the clean $Pt_3Ti(111)$ surface to rather small amounts of oxygen gas (less than 200 L dosed in the 10^{-8} mbar range) at temperatures between 800 and 1100 K results in the formation of the z'-TiO_x phase [6]. This atomically thin, titanium oxide phase is characterized by a typical striped pattern in the STM images. Former LEED measurements have shown a commensurate rectangular unit cell with a $(6 \times 3\sqrt{3})$ superstructure with respect to the (1 × 1) spots of the alloy surface and a unit cell size of (16.6 ± 0.2) × (14.4 ± 0.2) Å, while high resolution electron energy loss spectroscopy (HREELS) and X-ray photoelectron spectroscopy (XPS) measurements indicated the existence of an oxygen-terminated Ti–O bilayer [6,7]. Depending on the applied oxygen dose, the z'-TiO_x phase covers different fractions of the crystal surface, ranging from small separated islands up to a nearly complete film covering the whole surface. Figure 1a,b shows STM images of such an ultrathin oxide film, which was prepared by dosing 45 L of oxygen while holding the sample temperature at 1000 K. This amount of oxygen was

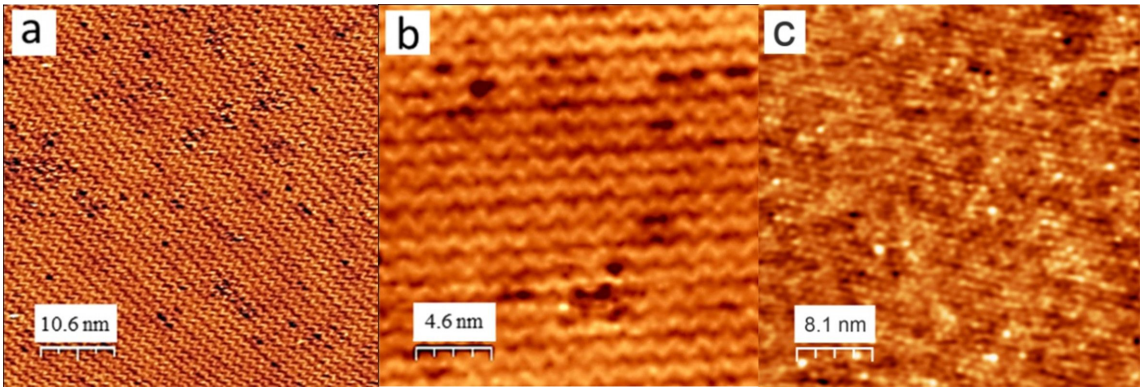

Figure 1: STM image of the z'-TiO_x phase: (a) 53.3 × 53.3 nm^2, bias voltage U_B = 0.91 V, I_T = 50 pA, (b) 22.8 × 22.8 nm^2, U_B = 0.99 V, I_T = 40 pA, and (c) STM image of the w'-TiO_x phase (57.1 × 57.1 nm^2, U_B = −1.08 V, I_T = 55 pA). The images in (a) and (c) have been adapted with permission from [6], copyright 2014 American Chemical Society.

sufficient to cover more than 80% of the alloy surface with z'-TiO_x. The stripes, which are approximately 1.4 nm apart from each other and separated by darker trenches, show the characteristic zigzag motif after which this structure was named. Inside the bright stripes the density of titanium atoms is higher than in the trenches, which is a result of the lattice mismatch between the titanium oxide film and the metallic substrate.

As suggested by theoretical calculations, the stripes consist of titanium atoms of different coordination [18]. Using a negative tip potential, four-fold oxygen-coordinated Ti atoms appear with the highest contrast in the STM images. They are surrounded by less bright, three-fold oxygen-coordinated Ti atoms. This mixture of Ti atoms of different electronic density is responsible for the characteristic striped pattern of the z'-TiO_x phase [18]. The STM images in Figure 1a,b also show several defects with the appearance of small black holes and a rough depth of 40 pm, which are all located within the trenches. At these point defects, titanium and oxygen atoms are probably missing and, thus, the bare metallic substrate is exposed [7]. Growth experiments with Au and Fe have already shown that both the trenches and, in particular, these defect sites within the trenches are preferred nucleation sites for cluster growth [15,16].

Pd cluster growth on the z'-TiO_x phase

Figure 2a shows an STM image of a z'-TiO_x surface onto which Pd was deposited at room temperature for 90 s (≈0.1 ± 0.05 ML). The stripes and trenches of the z'-TiO_x structure are visible in Figure 2a running from the upper left to the lower right of the image. In the close-up Figure 2b, the direction and separation of the trenches are accentuated by parallel lines. The individual Pd clusters are nearly all located within the trenches between the stripes. Only a few larger elongated clusters are visible. The tilted orientation of their long axis with respect to the trench orientation may be suggestive of two coalesced clusters at adjacent defects in two neighbouring stripes. They are not equally spaced within the trenches and appear more or less randomly distributed along the trenches. Most of the clusters are imaged larger than the width of the trenches, but their centres are always within the trenches. The distribution of the cluster diameters and cluster heights as taken from Figure 2a are displayed in Figure 2c,d and show a mean diameter of 3.5 ± 1.6 nm and a height of 1.5–2 Å. It should be noted, however, that the measured particle diameter is actually the result of a convolution between the true particle size and the STM tip shape [14]. The actual particle diameter is smaller, but the distribution obtained for different coverages and the two different substrates still allow for comparison. Regarding the measured heights of 1.5–2 Å, it must be considered that this may not be the true geometric height due to electronic effects. However, it is safe to assume that the Pd particles are only one layer thick. These results are in good agreement with the published results of Au clusters grown on the corresponding z'-TiO_x phase on Pt(111) [15].

The observed arrangement of the clusters is a consequence of the diffusion behaviour of the deposited metal atoms on this structurally anisotropic oxide surface. On the one hand the palladium–oxygen interaction is not very strong, permitting metal atom mobility at room temperature [19]. On the other hand, the trenches (1D depressions) guide the Pd atom diffusion preferentially along the grooves. Such anisotropic diffusion behaviour has been observed in the inverse system, namely the oxidation of Pd(110) leading to the growth of pronounced, elongated, oxide islands [20]. Thus, in the initial phase of the cluster growth, two competing processes take place: The defects, which are distributed randomly within (and only

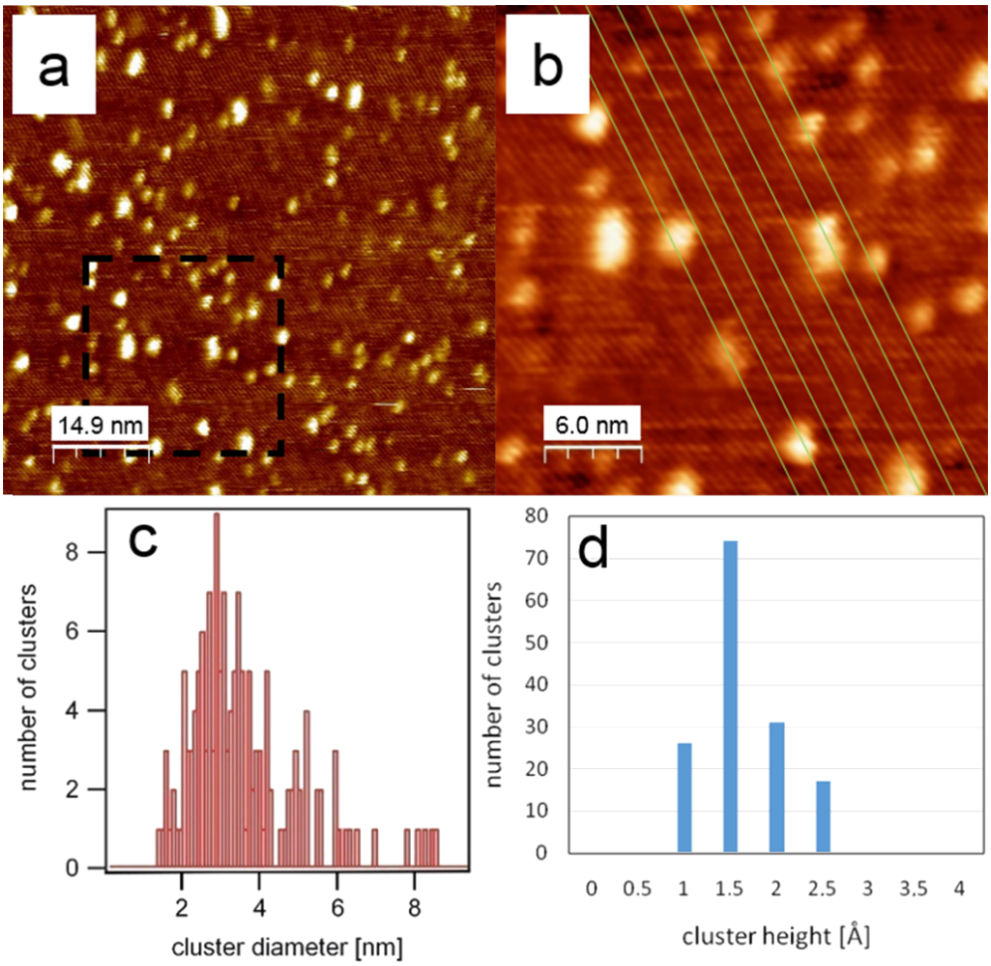

Figure 2: (a) STM image of Pd clusters grown at room temperature on a z'-TiO_x covered surface with a Pd coverage of 0.1 ± 0.05 ML after 90 s of Pd deposition (76.1 × 76.1 nm^2, U_B = 0.8 V, I_T = 56 pA), (b) detailed view for the marked section from image (a), (c) corresponding size distribution and (d) height distribution of Pd clusters. The green lines in (b) mark the trenches of the z'-TiO_x substrate.

within) the trenches, will trap some Pd atoms and thereby act as heterogeneous nucleation sites. In principle, homogeneous nucleation may also occur at other places within the trenches when two or three diffusing Pd atoms meet and form an immobile nucleus. However, in the case of low coverage as studied here, heterogeneous nucleation dominates. Counting the number of visible defects in typical images of the z'-TiO_x phase such as in Figure 1a leads to a typical defect density of approximately $3.9 \cdot 10^4$ defects per μm^2. Comparing this value with a typical cluster density of $3.7 \cdot 10^4$ clusters per μm^2 (calculated by counting the Pd clusters in Figure 2a) supports our observation that the cluster formation on the surface is directly related to the defects along the trenches of the z'-TiO_x phase.

The result is an anisotropic template effect of the z'-TiO_x phase: The clusters are arranged in lines along the trenches, but not equally spaced within the trenches or across the stripes in neighbouring trenches.

The hexagonal w'-TiO_x (wagon-wheel-like) phase

The w'-TiO_x phase is the second stable titanium oxide phase that can be grown on the $Pt_3Ti(111)$ surface with oxygen doses higher than 200 L within a temperature window of 800–1100 K [6]. HREELS and XPS studies also indicated a Ti–O bilayer structure with oxygen termination as a basic structure element for this phase [6,7]. LEED measurements revealed a hexagonal, higher-order commensurate (7 × 7)R21.8° superstructure with unit cell lattice vectors of 19.4 ± 0.2 Å. In contrast to the z'-TiO_x phase, however, it always covers the entire surface. This can be seen as the crucial factor for the symmetry change. At complete surface coverage, it is energetically more favourable for the oxide film to adopt the hexagonal symmetry of the substrate. This is normally not very common for titanium oxides and makes the w'-TiO_x phase a very interesting object of investigation. For the experiments presented here, the oxide film was prepared by exposing the sample to a temperature of

1000 K with 400 L of oxygen at a pressure of $1 \cdot 10^{-7}$ mbar. The STM image in Figure 1c shows a hexagonal arrangement of bright protrusions with nearly the same lattice parameters as measured by LEED [6]. This structure can be interpreted as a Moiré pattern that arises from the coincidence of the lattices of the metal support and the oxide overlayer. A Moiré pattern with a (7 × 7)R21.8° superstructure can be created by superimposing a hexagonal oxide layer with a unit cell size of 3.18 Å on the metal substrate with a unit cell size of 2.76 Å, rotated by 3.5° [7]. Those positions where the oxygen atoms are situated on top or on bridge sites of the metal substrate lattice are imaged brighter in the STM when using a negative tip potential. The number density of defects that exhibit an apparent depth of 18 pm is significantly lower than on the z'-TiO_x surface, as visualized later in Figure 5b,d.

Pd cluster growth on the w'-TiO_x phase

Figure 3 shows two STM images obtained at comparatively low (≈0.15 ML, Figure 3a) and high (≈0.75 ML, Figure 3b) Pd coverages on the w'-TiO_x surface obtained after 90 s and 420 s of deposition, respectively.

The clusters are imaged as bright spots with an almost circular shape on the oxide surface (see Figure 4a,b). For the lower coverage (Figure 3a and Figure 4a), the clusters appear to be distributed randomly on the surface and have an apparent height between 1.5 and 3 Å, as indicated by the height distribution in Figure 4c. This height corresponds to a single layer of Pd. The imaged mean diameter of a cluster is 1.9 ± 0.7 nm, as shown in the histogram in Figure 3c. At the higher coverage (Figure 3b and Figure 4b), the apparent height of the clusters increased to about 6–8 Å. This value suggests that the clusters are now 1 to 4 Pd layers thick and thus indicates that 3D growth has started. The imaged mean diameter increased to 5.5 nm with a broader size distribution of ±2.9 nm (Figure 3d).

From the energetic point of view, a precondition for 3D growth (i.e., nonwetting), is that the adhesion energy of the Pd metal on the oxide is smaller than twice the surface free energy of the vacuum–metal interface of the liquid metal [19]. In the case of late transition metals on oxides, this criterion is usually met, and thus 3D growth is observed in most cases [14]. From a kinetic point of view, the growth process can be divided into two

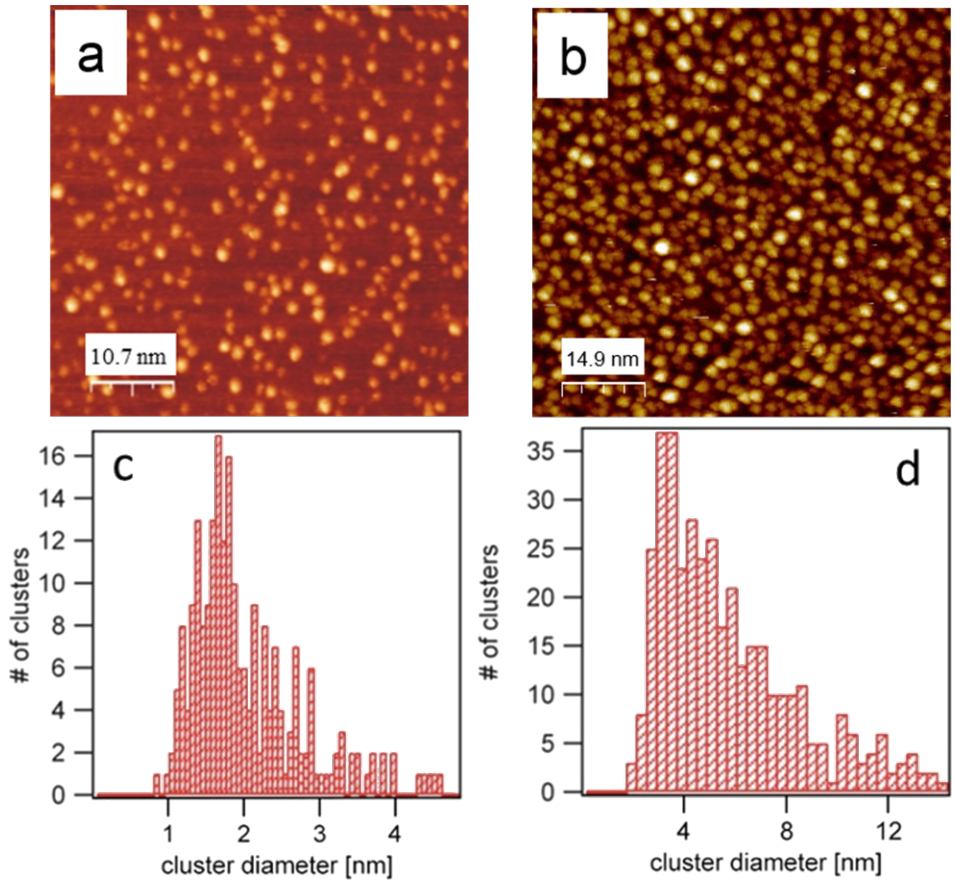

Figure 3: Pd clusters grown at RT on the w'-TiO_x phase: (a) low Pd coverage of 0.15 ± 0.02 ML after 90 s of Pd deposition (53.3 × 53.3 nm^2, U_B = 0.9 V, I_T = 53 pA), (b) high Pd coverage of 0.73 ± 0.05 ML after 420 s of Pd deposition (76.1 × 76.1 nm^2, U_B = 2.13 V, I_T = 57 pA, (c) size distribution of the cluster from (a), and (d) size distribution of the clusters from (b).

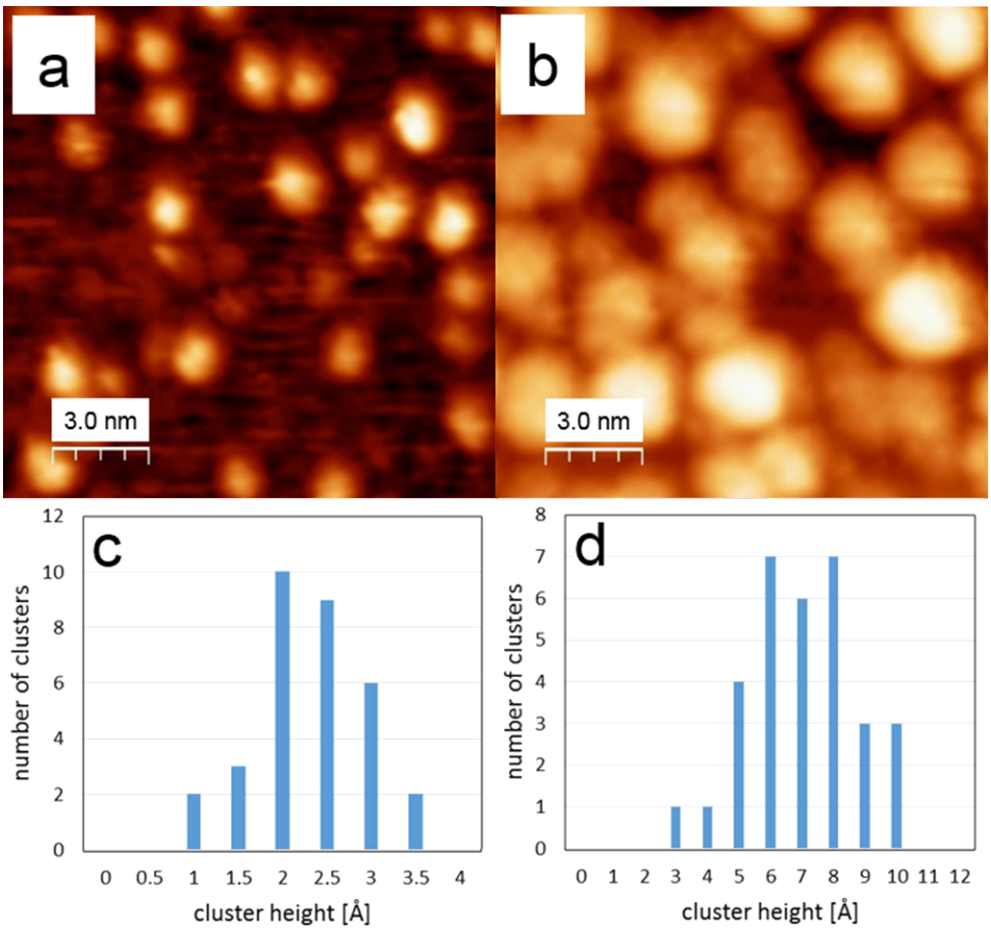

Figure 4: Enlarged STM images of Pd clusters on the w'-TiO_x phase: (a) with the low coverage, indicating a height of one layer (2–3 Å), (b) with the high coverage, indicating a height of up to four layers (9–10 Å), (c) and (d) show the cluster height distributions from (a) and (b), respectively.

regimes: In the case of homogeneous nucleation, deposited metal atoms diffuse across a low corrugation surface and randomly combine to form stable nuclei at random positions on the surface until a saturation density is reached; then these nuclei grow in size during the further deposition process. Heterogeneous nucleation occurs on a surface of higher corrugation on which the diffusing atoms are trapped at the sites of highest adsorption energy, which thereby become preferred nucleation and growth sites. Obviously, defect sites are such traps. As shown in Figure 5a, defects in the z'-TiO_x phase (depth ≈40 pm) are largely found within the trenches as an inherent property of this phase. As a consequence, the z'-TiO_x phase exerts a "template effect": The trenches are the defect locations, which in turn are the preferred nucleation sites for the Pd clusters. In turn, as shown in Figure 5b, the w'-TiO_x phase contains much fewer and shallower (depth ≈18 pm) defects of no particular distribution. Therefore, under the given experimental conditions, it does not exert a noticeable "template effect".

This result is quite in contrast to Pd cluster growth on Al_2O_3/Ni_3Al(111) surfaces, where actually two different hexagonal superstructures with lattice constants of 2.4 nm and 4.1 nm act as templates for the growth of ordered metal cluster arrays [14]. A hexagonal arrangement of more equally sized clusters on the w'-TiO_x Moiré structure, which is even more ideal than described in this work, is certainly achievable. This could be accomplished by varying the impact rate of Pd atoms and their mobility on the surface (i.e., the deposition rate and the substrate temperature), as was the case for Pd cluster growth on the Al_2O_3/Ni_3Al(111) surface.

Summary

Pd clusters were grown on two different, ultrathin, TiO_x films, the so-called rectangular z'-TiO_x and the hexagonal w'-TiO_x phase. The first one consists of stripes separated by trenches and acts as a unidirectional template. This is due to the defect sites, which act as heterogeneous nucleation sites for the Pd clusters. These are an inherent property of the z'-TiO_x phase and

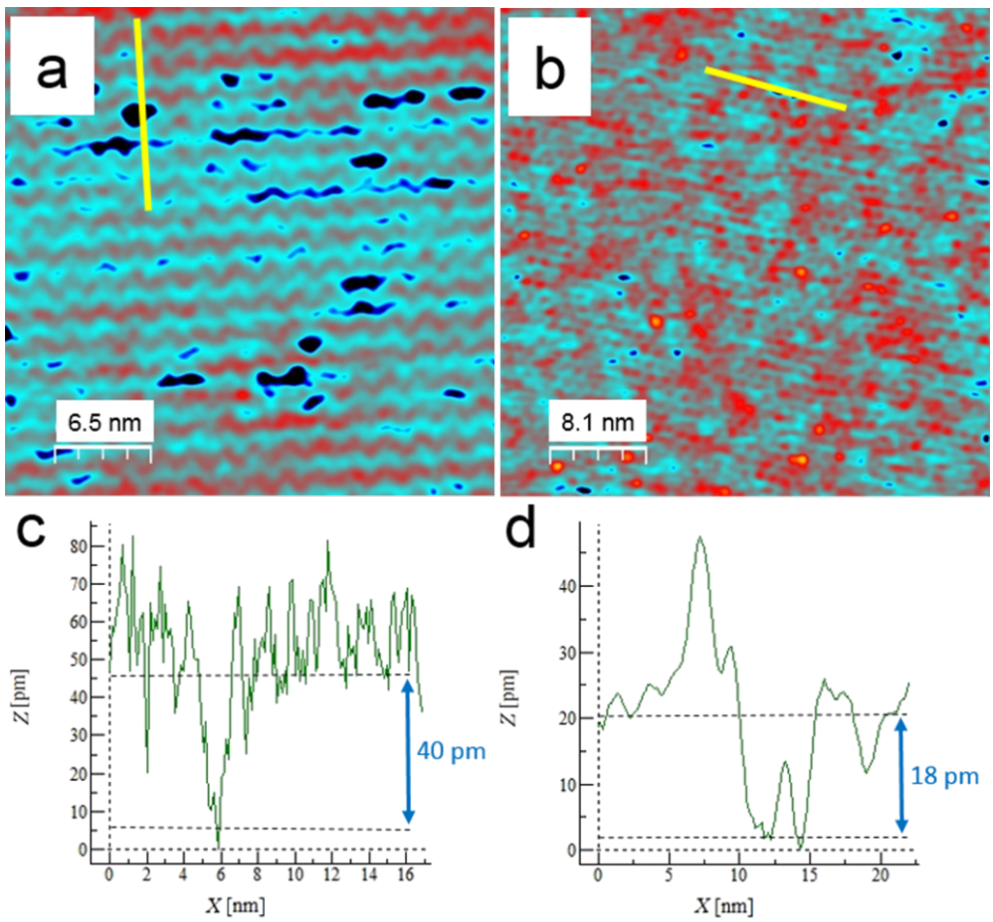

Figure 5: STM images of the oxide films: (a) z'-TiO_x phase (32.6 × 32.6 nm^2, bias voltage U_B = 0.97 V, I_T = 50 pA, (b) w'-TiO_x phase (57.1 × 57.1 nm^2, U_B = −1.08 V, I_T = 55 pA), (c) and (d) corresponding line profiles along the markings in image (a) and (b), respectively. Image (b) has been adapted with permission from [6], copyright 2014 American Chemical Society.

are aligned within the trenches of this structure. Along the trenches, no long-range order of the defects, and hence of the clusters, is discernible.

The w'-TiO_x phase possesses a long-range (7 × 7)R21.8° superstructure, which is formed as a Moiré pattern from the superposition of the hexagonal lattices of the substrate and the oxide film. Since this structure exhibits much fewer (and shallower) defects, no "template effects" could be observed for this surface and this type of metallic cluster under the given experimental conditions.

The next reasonable steps would be (a) to attempt to achieve a hexagonal cluster distribution on the w'-TiO_x phase by varying the metal deposition rate and/or the substrate temperature as was the case for metal clusters on $Al_2O_3/Ni_3Al(111)$, and (b) the investigation of the electronic as well as the adsorption and reactivity properties of the Pd clusters. In this regard, the influence of the two different titania films on these properties of clusters of the same metal is of particular interest [21].

References

1. Dulub, O.; Hebenstreit, W.; Diebold, U. *Phys. Rev. Lett.* **2000,** *84,* 3646. doi:10.1103/PhysRevLett.84.3646
2. Bowker, M.; Stone, P.; Morrall, P.; Smith, R.; Bennett, R.; Perkins, N.; Kvon, R.; Pang, C.; Fourre, E.; Hall, M. *J. Catal.* **2005,** *234,* 172. doi:10.1016/j.jcat.2005.05.024
3. Tauster, S. J.; Fung, S. C.; Garten, R. L. *J. Am. Chem. Soc.* **1978,** *100,* 170. doi:10.1021/ja00469a029
4. Resaco, D. E.; Haller, G. L. *J. Catal.* **1983,** *82,* 279. doi:10.1016/0021-9517(83)90194-X
5. Santos, J.; Phillips, J.; Dumesic, J. A. *J. Catal.* **1983,** *81,* 147. doi:10.1016/0021-9517(83)90154-9
6. Breinlich, C.; Buchholz, M.; Moors, M.; Le Moal, S.; Becker, C.; Wandelt, K. *J. Phys. Chem. C* **2014,** *118,* 6186. doi:10.1021/jp4105213
7. Sedona, F.; Rizzi, G. A.; Agnoli, S.; Labrès i Xamena, F. X.; Papageorgiou, A.; Ostermann, D.; Sambi, M.; Finetti, P.; Schierbaum, K.; Granozzi, G. *J. Phys. Chem. B* **2005,** *109,* 24411. doi:10.1021/jp0543173
8. N'Diaye, A. T.; Gerber, T.; Busse, C.; Mysliveček, J.; Coraux, J.; Michely, T. *New J. Phys.* **2009,** *11,* 103045. doi:10.1088/1367-2630/11/10/103045

9. Venkataramani, K.; Helveg, S.; Hunnemann, B.; Reichling, M.; Besenbacher, F.; Lauritsen, J. V. *Nanotechnology* **2010,** *21,* 265602. doi:10.1088/0957-4484/21/26/265602
10. Chaudhury, A.; Gragnaniello, L.; Ma, T.; Surnev, S.; Netzer, F. P. *J. Phys. Chem. C* **2013,** *117,* 18112. doi:10.1021/jp4056329
11. Degen, S.; Becker, C.; Wandelt, K. *Faraday Discuss.* **2004,** *125,* 343. doi:10.1039/b303244b
12. Becker, C.; von Bergmann, K.; Rosenhahn, A.; Schneider, J.; Wandelt, K. *Surf. Sci.* **2001,** *486,* L443. doi:10.1016/S0039-6028(01)01052-4
13. Lehnert, A.; Krupski, A.; Degen, S.; Franke, K.; Decker, R.; Rusponi, S.; Kralj, M.; Becker, C.; Brune, H.; Wandelt, K. *Surf. Sci.* **2006,** *600,* 1804. doi:10.1016/j.susc.2006.02.013
14. Becker, C.; Wandelt, K. *Scanning Tunneling Microscopy in Surface Science;* Wiley-VCH: Weinheim, Germany, 2010.
15. Sedona, F.; Agnoli, S.; Fanetti, M.; Kholmanov, I.; Cavaliere, E.; Gavioli, L.; Granozzi, G. *J. Phys. Chem. C* **2007,** *111,* 8024. doi:10.1021/jp0687652
16. Cavaliere, E.; Kholmanov, I.; Gavioli, L.; Sedona, F.; Agnoli, S.; Granozzi, G.; Barcaro, G.; Fortunelli, A. *Phys. Chem. Chem. Phys.* **2009,** *11,* 11305. doi:10.1039/b915641k
17. Horcas, I.; Fernández, R.; Gómez-Rodríguez, J. M.; Colchero, J.; Gómez-Herrero, J.; Baro, A. M. *Rev. Sci. Instrum.* **2007,** *78,* 013705. doi:10.1063/1.2432410
18. Sedona, F.; Granozzi, G.; Barcaro, G.; Fortunelli, A. *Phys. Rev. B* **2008,** *77,* 115417. doi:10.1103/PhysRevB.77.115417
19. Campbell, C. T. *Surf. Sci. Rep.* **1997,** *27,* 1. doi:10.1016/S0167-5729(96)00011-8
20. Kralj, M.; Pertram, T.; Seriani, N.; Mittendorfer, F.; Krupski, A.; Becker, C.; Wandelt, K. *Surf. Sci.* **2008,** *602,* 3706. doi:10.1016/j.susc.2008.10.008
21. The authors were no longer in the position to do these experiments because of the retirement of the group leader (K.W.) and the closure of the laboratories.

License and Terms

BEILSTEIN JOURNAL OF NANOTECHNOLOGY

Kelvin probe force microscopy for local characterisation of active nanoelectronic devices

Tino Wagner*[1], Hannes Beyer[1], Patrick Reissner[1], Philipp Mensch[2], Heike Riel[2], Bernd Gotsmann[2] and Andreas Stemmer*[1]

Full Research Paper

Open Access

Address:
[1]Nanotechnology Group, ETH Zürich, Säumerstrasse 4, 8803 Rüschlikon, Switzerland and [2]IBM Research — Zurich, Säumerstrasse 4, 8803 Rüschlikon, Switzerland

Email:
Tino Wagner* - tiwagner@ethz.ch; Andreas Stemmer* - astemmer@ethz.ch

* Corresponding author

Keywords:
capacitive crosstalk; frequency modulation; Kalman filter; Kelvin probe force microscopy; sidebands

Beilstein J. Nanotechnol. **2015,** *6,* 2193–2206.
doi:10.3762/bjnano.6.225

Received: 10 August 2015
Accepted: 30 October 2015
Published: 23 November 2015

This article is part of the Thematic Series "Advanced atomic force microscopy techniques IV".

Guest Editor: T. Glatzel

Abstract

Frequency modulated Kelvin probe force microscopy (FM-KFM) is the method of choice for high resolution measurements of local surface potentials, yet on coarse topographic structures most researchers revert to amplitude modulated lift-mode techniques for better stability. This approach inevitably translates into lower lateral resolution and pronounced capacitive averaging of the locally measured contact potential difference. Furthermore, local changes in the strength of the electrostatic interaction between tip and surface easily lead to topography crosstalk seen in the surface potential. To take full advantage of the superior resolution of FM-KFM while maintaining robust topography feedback and minimal crosstalk, we introduce a novel FM-KFM controller based on a Kalman filter and direct demodulation of sidebands. We discuss the origin of sidebands in FM-KFM irrespective of the cantilever quality factor and how direct sideband demodulation enables robust amplitude modulated topography feedback. Finally, we demonstrate our single-scan FM-KFM technique on an active nanoelectronic device consisting of a 70 nm diameter InAs nanowire contacted by a pair of 120 nm thick electrodes.

Introduction

Device performance of current nanoelectronic devices, and even more so of potential future generations including nanowires or molecular junctions, critically depends on transport properties varying on a length scale of a few nanometres only in the active channel or at electrode interfaces. Methods for local electronic characterisation, providing accurate measurements with nanometre spatial resolution, are in very high demand, but have been lagging behind the technological requirements.

Kelvin probe force microscopy (KFM) is an established technique that allows for the mapping of local electrostatic potentials with an atomic force microscope (AFM) [1-3]. In contrast

to electrostatic force microscopy (EFM), which measures merely the effect of electrostatic forces on the oscillation of the tip, a feedback loop nullifies the electric field by adjusting a bias voltage between tip and sample. Hence, Kelvin probe force microscopy is able to quantify the local contact potential difference (CPD), U_{lcpd}, which contains contributions, e.g., from the difference in work function between the AFM tip and structures on the sample, dopants and trapped charges in the device, or voltages applied to electrodes.

For electronic devices on the nanoscale, KFM measurements provide a unique tool to shed light upon a variety of otherwise inaccessible properties. For example, with a constant current passing through a two-terminal device, the potential drop at the contacts directly relates to the contact resistance. To extract contact resistance through traditional four-point measurements becomes increasingly difficult for scaled devices, in which the contact length is comparable to the device length. Recently, KFM has been used to extract the surface state density and Schottky depletion region in semiconductor nanowires [4,5] or to determine the mean free path in carbon nanotubes [6]. KFM also allows one to determine intrinsic doping of two-dimensional crystals such as graphene [7,8], where surface potential and electronic properties depend on the number of layers.

KFM has found widespread use in both vacuum and ambient environments. Most commercial instruments for operation in air include a scan mode based on amplitude modulation KFM (AM-KFM). In this mode, the feedback loop nullifies the cantilever oscillation that is excited by a modulated electrostatic force. Hence, the KFM image is a map of voltages required to compensate the electrostatic force at every point of the scanned field. However, since cantilever and AFM tip are extended objects, this voltage does not necessarily correspond to the local contact potential difference, U_{lcpd}, but represents a weighted average over the potentials present on the entire sample surface [9]. For AM-KFM, the weights are determined by the capacitance gradient, C', between the probe and the sample. Due to the long range electrostatic force, even parts far from the surface, such as the cantilever beam, can account for a significant fraction of the signal, limiting the spatial resolution and accuracy of the measurement. Within nanoscale devices, for example, electrode potentials may completely overshadow the channel [10].

Known approaches to increase spatial resolution and accuracy of surface potential measurements include deconvolution techniques [11,12] or the use of slightly blunt tips supported by a cantilever of minimal surface area [9]. However, deconvolution techniques require a detailed model of the AFM tip to be accurate and usually neglect the sample topography [12], whereas blunt tips inevitably reduce topography resolution on three-dimensional structures.

KFM measurements are further complicated by a strong dependence of the detected signal on the tip–sample distance. In the often employed lift-mode schemes, each line is scanned twice: first to acquire topography, and subsequently to retrace the scanned line at a small distance, Δz, above the surface to perform KFM measurements. This enables tuning the ac modulation frequency for KFM to resonance to enhance the signal, and, at the same time, to reduce the contribution of van der Waals forces to the total force measured and compensated. The scan at elevated height, however, reduces lateral resolution and accuracy of the KFM data as we will detail below. To minimise such lateral averaging, single-scan methods are preferred, performing topography and KFM measurements simultaneously. An additional benefit of single-scan AFM and KFM is the inherent suppression of electrostatically induced topography artefacts present in non-compensated topography scans [13,14]. In AM-KFM, single-scan methods can be implemented taking advantage of multiple eigenmodes of the cantilever, using one mode for topography and another for KFM. Nevertheless, the averaging effect of the cantilever beam remains (see below in Figure 1).

An alternative approach typically applied in vacuum is based on frequency modulation [15]. To this end, the frequency of the cantilever is usually tracked by a phase-locked loop (PLL). Its output signal, the frequency shift Δf, exhibits a frequency component at the electrostatic modulation frequency, which is nullified by the Kelvin feedback loop. Frequency modulated KFM (FM-KFM) [16,17] thus provides a map of potentials required to minimise the electrostatic force gradient, proportional to Δf for small mechanical amplitudes, at every point during the scan. As a consequence, the contributions from different parts of the sample and the probe to the measured signal are weighted by the second-order capacitance gradient, C'', which effectively eliminates the averaging contribution of the cantilever beam as we explain in the following.

Figure 1 shows a model calculation using typical cantilever and interaction parameters, summarising how much tip apex, cone, and beam of an AFM cantilever probe contribute to the measured KFM signal in AM and FM operation. Shown are the percentages of the contributions and corresponding weighting factors C' and C'' for AM and FM, respectively. To this end, we applied an analytic model of the electrostatic tip–sample interaction force [18] to the approximate geometry of a typically used cantilever (Olympus AC160), and we calculated C' and C'' as a function of tip–sample separation for different oscillation amplitudes (see Supporting Information File 1 for details).

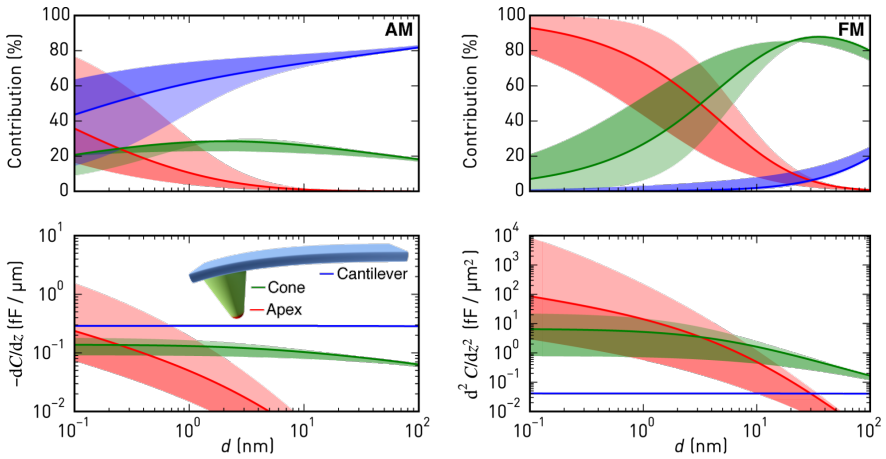

Figure 1: Contributions of apex, cone, and cantilever to the first (AM, left) and second (FM, right) order capacitance gradient as a function of distance for a mechanical oscillation amplitude of 5 nm (solid line) and an Olympus AC160 cantilever (r_{tip} = 5 nm, H_{tip} = 14 µm, θ = 17.5°, and A_{lever} = 160 µm × 40 µm). The light (dark) shaded regions indicate the range up to A = 0.1 nm (50 nm).

While tip apex and cone clearly dominate the FM-KFM signal, opening the avenue to high resolution quantitative imaging, the cantilever beam at a distance of 14 µm dominates the AM-KFM signal even close to the sample, which is the main reason for the notoriously low lateral resolution and poor potential accuracy in this mode. When comparing AM and FM modes, one should note that in lift-mode AM-KFM the cantilever is not oscillating anymore when the electrostatic forces are nullified, whereas the mechanical oscillation remains in multifrequency AM-KFM and FM-KFM. Hence, for lift-mode the case $A \rightarrow 0$ should be considered, whereas in single-scan modes the oscillation applied for tracking topography remains. For best sensitivity and minimal spatial averaging, AM and FM modes need to be operated very close to the surface.

While the FM-KFM approach is clearly superior in terms of signal composition, several issues complicate its use in practice. First, it is often performed together with frequency modulated topography feedback that employs a PLL to determine Δf. The non-monotonous tip–sample interaction, by which Δf can change its slope between net-attractive and net-repulsive forces, can complicate stable operation of the topography feedback and may ultimately render PLL and amplitude controller unstable. On samples with coarse topography and steep features, maintaining stable FM topography feedback demands careful selection of operating parameters and slow scanning speeds. Furthermore, the choice of suitable bandwidths for topography and KFM feedback is more involved in traditional FM-AFM/FM-KFM implementations. For example, when Δf is used as an input to the lock-in amplifier detecting the electrostatic modulation, the PLL bandwidth must be wide enough to include the modulation frequency. Yet, it should be kept as small as possible for stable PLL operation and maximum noise rejection [19]. Finally, the pronounced distance dependence of C'' for apex and cone, as depicted in Figure 1, makes operation close to the surface more challenging, since small errors of the topography feedback produce marked changes of the effective Kelvin feedback gain. Similarly, when the tip encounters steep edges in topography, C'' may increase due to a larger effective tip–sample capacitor area, further complicating stable feedback operation. The distance dependence is less pronounced at larger distances employed in lift-mode FM-KFM [10], but in addition to reduced lateral resolution, large modulation voltages are required due to weaker signals [20], which may induce band bending. Furthermore, when scanning across insulating parts of devices, such as gate oxides, not only the local dielectric constant changes, but because of their thickness also a limit is put on the minimum approachable distance in Figure 1. As a result, deliberately slow feedback settings to ensure stable operation are common practice.

In this paper, we describe a practical approach to FM-KFM providing solutions to these issues. We remove the interdependence of topography and KFM feedbacks by focusing on the information contained in the sidebands produced by the electrostatic modulation [20]. Employing a commercially available lock-in amplifier, we detect these sidebands directly. Thus, with frequency modulated distance feedback, the PLL bandwidth can be restricted to the topography only. We further demonstrate the advantage of combining FM-KFM with amplitude modulated AFM (AM-AFM) for tracking topography of highly structured surfaces with small amplitudes and net-attractive interaction in air. Since the oscillation amplitude decreases monotonically with distance, no special precautions are required to ensure feedback stability. Finally, we introduce an improved Kelvin feedback loop based on stochastic optimal control that continu-

ously adjusts its sensitivity to local changes in C'', thereby reducing the risk of feedback instabilities and topography crosstalk on difficult heterogeneous samples.

Theory

The origin of sidebands

The cantilever motion and the origin of sidebands are understood from a damped harmonic oscillator driven by an external drive, $a(t)$, and perturbed by the tip–sample interaction force $F_{\mathrm{ts}}(z,\dot{z},t)$,

$$\ddot{z}+\frac{\omega_0}{Q}\dot{z}+\omega_0^2 z=\omega_0^2 a(t)+\frac{\omega_0^2}{k}F_{\mathrm{ts}}(z,\dot{z},t), \tag{1}$$

where $z(t)$ is the cantilever deflection, ω_0 the eigenfrequency, k the spring constant, and Q the quality factor of the cantilever. For an oscillation with amplitude A and drive frequency $\omega_\mathrm{d} \approx \omega_0$, the interaction force can be approximated to

$$F_{\mathrm{ts}} \approx \langle F_{\mathrm{ts}}\rangle\big|_{z=z_0}+\langle \partial F_{\mathrm{ts}}/\partial z\rangle\big|_{z=z_0}(z-z_0),$$

where z_0 is the mean tip position, and $\langle F_{\mathrm{ts}}\rangle$ and $\langle \partial F_{\mathrm{ts}}/\partial z\rangle$ are the effective force and force gradient, respectively. Explicit expressions for the effective force and force gradient, averaged over the oscillation period, $T \approx 2\pi/\omega_\mathrm{d}$, are [21]

$$\begin{aligned}\langle F_{\mathrm{ts}}\rangle(z_0)&=\frac{1}{T}\int_0^T \mathrm{d}t F_{\mathrm{ts}}\left(z_0+A\sin(\omega_\mathrm{d}t)\right)\\&=\frac{1}{\pi}\int_{-A}^{A}\mathrm{d}q\,\frac{F_{\mathrm{ts}}(z_0+q)}{\sqrt{A^2-q^2}}\end{aligned} \tag{2}$$

and

$$k_{\mathrm{ts}}(z_0)=\frac{2}{\pi A^2}\int_{-A}^{A}\mathrm{d}q\,\frac{\partial F_{\mathrm{ts}}}{\partial z}(z_0+q)\sqrt{A^2-q^2}. \tag{3}$$

The effective force and force gradient, as introduced here, allow one to describe the motion of the tip in the non-linear force field close to the sample with the model of a perturbed harmonic oscillator, provided the oscillation remains approximately harmonic with constant amplitude [22].

With a small perturbation, $k_{\mathrm{ts}} << k$, the resonant frequency of the cantilever changes from ω_0 to $\omega_0 + \Delta\omega$ with $\Delta\omega/\omega_0 = -k_{\mathrm{ts}}/2k$ [15]. Accordingly, a modulation of the force gradient, e.g., by an oscillating electric field, will cause a frequency modulation of the resonance. A modulation at a single frequency ω_m will produce sidebands at integer multiples of the modulation frequency, that is, cantilever oscillations at $\omega_0 \pm \omega_\mathrm{m}$, $\omega_0 \pm 2\omega_\mathrm{m}$ and so on.

For the derivation of the sideband signals and their respective amplitudes, we assume a modulation of the force gradient at the frequency ω_m: $k_{\mathrm{ts}}(z_0,t)=\hat{k}_{\mathrm{ts}}(z_0)\cos(\omega_\mathrm{m}t+\varphi_\mathrm{k})$. Note that the effective force gradient as calculated above, Equation 3, is valid for $\omega_\mathrm{m} << \omega_\mathrm{d}$.

Then, by Fourier transformation of the equation of motion, Equation 1, we arrive at

$$\begin{aligned}G^{-1}(\omega)\tilde{z}(\omega)=\tilde{a}(\omega)+\frac{\hat{k}_{\mathrm{ts}}(z_0)}{2k}\Big[&e^{i\varphi_\mathrm{k}}\tilde{z}(\omega-\omega_\mathrm{m})\\&+e^{-i\varphi_\mathrm{k}}\tilde{z}(\omega+\omega_\mathrm{m})\Big]\end{aligned} \tag{4}$$

with

$$G(\omega)=\frac{\omega_0^2}{\omega_0^2-\omega^2+i\dfrac{\omega_0\omega}{Q}}, \tag{5}$$

where $\tilde{z}(\omega)=\int_{-\infty}^{\infty}\mathrm{d}t\,z(t)\exp(-i\omega t)/\sqrt{2\pi}$ and $\tilde{a}(\omega)$ are the Fourier transformed deflection and drive, respectively, and $G(\omega)$ is the complex transfer function of the damped harmonic oscillator.

Equation 4 and Equation 5 present an iterative scheme to determine the spectral components of the cantilever oscillation, where in each step $\tilde{z}(\omega)$ on the left hand side of Equation 4 is refined by the expressions on the right hand side. Starting from an oscillator at rest, $\tilde{z}_0(\omega)=G(\omega)\tilde{a}(\omega)$ is the carrier oscillation due to the external drive, as in the unperturbed system. Spectral components at $\omega \pm \omega_\mathrm{m}$ emerge in the next iteration step,

$$\tilde{z}_1(\omega\pm\omega_\mathrm{m})=\frac{\hat{k}_{\mathrm{ts}}}{2k}e^{\pm i\varphi_\mathrm{k}}G(\omega\pm\omega_\mathrm{m})\tilde{z}_0(\omega). \tag{6}$$

This is the fundamental pair of sidebands of the force modulated damped harmonic oscillator. With $\hat{k}_{\mathrm{ts}} << k$, the higher order sidebands arising in the subsequent iterations are usually negligible.

Equation 6 also describes the sideband amplitude transfer function when the expression is evaluated close to the sideband frequencies. With the substitution $\omega - \omega_d \rightarrow \omega$, we find

$$\frac{\tilde{z}_{\pm}(\omega)}{\tilde{z}_c(\omega)} = \frac{\tilde{z}_1(\omega_d \pm \omega_m + \omega)}{\tilde{z}_0(\omega_d + \omega)} = \frac{\hat{k}_{ts}}{2k} e^{\pm i\varphi_k} G(\omega_d \pm \omega_m + \omega) \quad (7)$$

with the approximation

$$\frac{\tilde{z}_{\pm}(\omega)}{\tilde{z}_c(\omega)} \approx -\frac{\hat{k}_{ts}}{2k}\frac{\omega_0}{2}\frac{ie^{\pm i\varphi_k}}{i(\omega \pm \omega_m) + \omega_c} = \frac{\Delta\hat{\omega}}{2\omega_m}\frac{ie^{\pm i\varphi_k}}{i(\omega/\omega_m \pm 1) + \omega_c/\omega_m}, \quad (8)$$

where, in the latter approximation, we consider only the dominant term for a drive close to the eigenfrequency, i.e., $\omega_d \approx \omega_0$ and $\omega << \omega_0$, and $\omega_c = \omega_0/2Q$ is the cantilever bandwidth.

For modulation frequencies well beyond the cantilever bandwidth, $G(\omega_0 \pm \omega_m) \approx -i\omega_0/2\omega_m$, and the amplitude of each sideband is $|\tilde{z}_{\pm}| \approx A\Delta\hat{\omega}/2\omega_m$, where A is the carrier amplitude. The latter expression also follows immediately from a narrow-band frequency modulation of a carrier oscillation at ω_d. With a carrier amplitude A and the peak frequency deviation $\Delta\hat{\omega}$, a frequency modulation at ω_m produces two sidebands with amplitudes $\beta A/2$, where $\beta \equiv \Delta\hat{\omega}/\omega_m$ is the modulation index [23]. Under ultra-high vacuum conditions, large Q factors typically cause negligible cantilever bandwidths, making this approximation valid, e.g., for finding the noise power spectral density of the frequency shift signal in FM-AFM [24]. When the narrow-band conditions are not met ($\beta >> 1$), the iterative scheme for the sideband amplitudes in Equation 4 and Equation 5 still approaches the Bessel functions describing the sideband amplitudes in a general frequency modulation for $\omega_m >> \omega_c$ (see Supporting Information File 1).

The Fourier approach presented above also accurately models the behaviour of the sideband amplitude and phase for modulation frequencies approaching the cantilever bandwidth ω_c. In Figure 2a, we show the expected and experimentally measured sideband amplitudes and phases. The excellent agreement with the above model proves the validity of our derivation. Each sideband is phase-shifted by $\pm\varphi_k + \arg G(\omega_d \pm \omega_m)$.

For narrow-band frequency modulation, we can define a complex modulation index $\tilde{\beta}$ by the sideband and carrier amplitudes as $\tilde{\beta} \equiv z_+/z_c - \overline{z_-/z_c}$. With Equation 8, the dc response ($\omega \rightarrow 0$) of $\tilde{\beta}$ thus is

$$\tilde{\beta} = \beta\frac{ie^{i\varphi_k}}{i + \omega_c/\omega_m}. \quad (9)$$

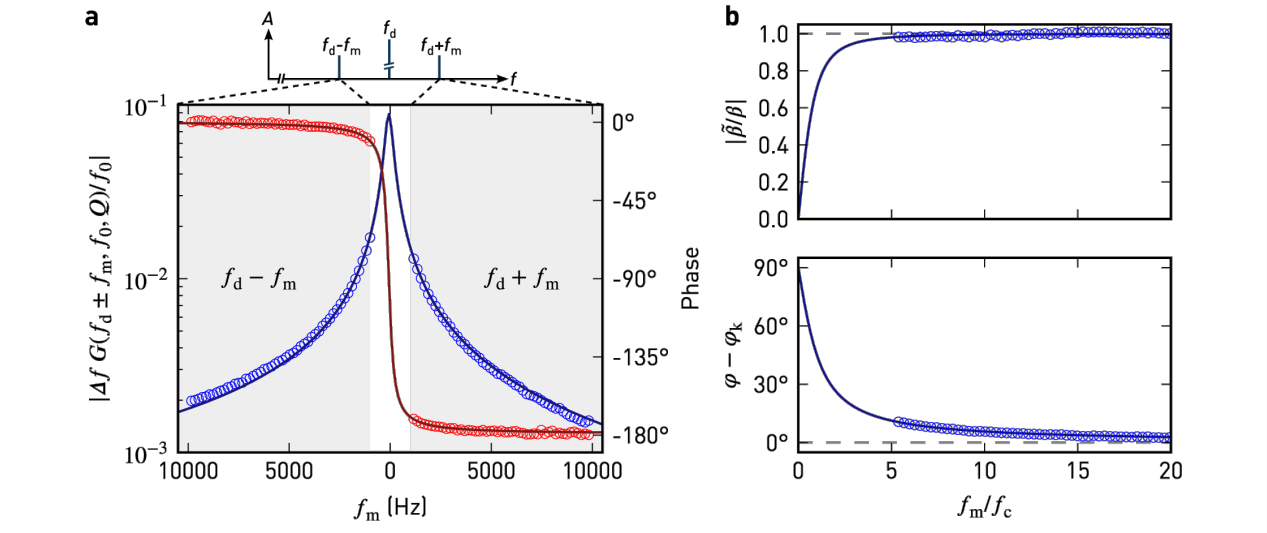

Figure 2: a) Sideband amplitude (blue) and phase (red) relative to the carrier oscillation measured during a sweep of the modulation frequency (markers), and a fit of the harmonic oscillator (solid lines). At a constant height of approx. 25 nm above the sample, the tip was driven mechanically at $f_d = \omega_d/2\pi = 70657$ Hz and electrically at f_m. Parameters to the least-squares fit are $\Delta\hat{f} = 33$ Hz, $f_0 = 70586$ Hz, and $Q = 190$. b) Amplitude and phase of the complex modulation index for a narrow-band frequency modulation, $\tilde{\beta} \equiv z_+/z_c - \overline{z_-/z_c}$. The solid lines are a plot of the approximation in Equation 9. The dashed lines indicate the expected behaviour for $f_m >> f_c$, neglecting the influence of the damped harmonic oscillator.

Figure 2b shows the amplitude and phase of $\tilde{\beta}$ for pure narrow-band FM and the harmonic oscillator as a function of ω_m/ω_c. The amplitude and phase only agree with the result for pure narrow-band frequency modulation when the cantilever bandwidth is negligible compared to the modulation frequency. For low modulation frequencies $|\tilde{\beta}|$ approaches $\Delta\hat{\omega}/\omega_c = 2Q\Delta\hat{\omega}/\omega_0$ instead (Equation 9).

To further demonstrate the validity of the sideband transfer function, we show in Figure 3 the response to a step in $\hat{k}_{ts}$ from both the approximation in Equation 8 and from a numerical simulation of the perturbed harmonic oscillator, Equation 1, including lock-in amplifiers at $\omega_d \pm \omega_m$. Each change in the force gradient modulation also excites a transient oscillation at the resonant frequency of the cantilever, which appears in the sideband signal and decays exponentially with $1/\omega_c$. Therefore, the filter settings of the lock-in amplifier should be set accordingly to provide sufficient rejection near ω_m.

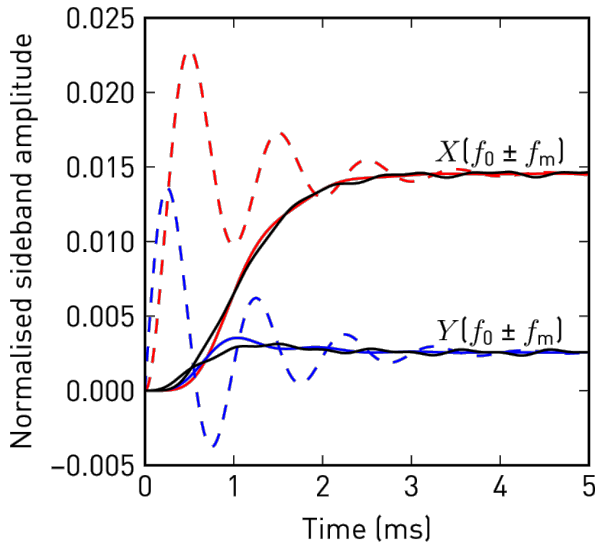

Figure 3: In-phase (red) and quadrature (blue) sideband amplitudes, normalised to the carrier oscillation amplitude A, in response to a step in the force gradient modulation amplitude. The step responses following from Equation 8 (dashed), show oscillations at f_m, exponentially decaying with $1/\omega_c$, which are removed by the low-pass filter of the lock-in amplifier (solid, f_{cut} = 250 Hz, 24 dB/oct). The solid black lines show the demodulated sideband amplitudes from a direct numerical simulation of the perturbed harmonic oscillator. (Numerical parameters: f_0 = 70500 Hz, Q = 200, A = 10 nm, f_m = 1000 Hz, φ_k = 0, $\Delta\hat{f}$ = 30 Hz).

We conclude that sidebands evolve as soon as k_{ts} gets modulated and it is not important whether the resonant frequency is actually tracked or not. The main benefit of tracking the resonant frequency (e.g., with a phase-locked loop) is merely to keep the carrier phase constant, which would otherwise affect the sideband phases.

Electrostatic force and force gradient

The electrostatic force between the AFM tip and sample is

$$\langle F_{el}\rangle = \frac{1}{2}\langle \partial C/\partial z\rangle \left(U_{ts} - U_{lcpd}\right)^2,$$

where $\langle \partial C/\partial z\rangle$ is the effective capacitance gradient, U_{ts} is the tip–sample voltage, and U_{lcpd} is the local contact potential difference.

For Kelvin probe force microscopy, U_{ts} is modulated around a dc voltage: $U_{ts} = U_{dc} + U_{ac}\cos(\omega_m t)$. Therefore, the electrostatic force and likewise its gradient, k_{ts}^{el}, are modulated at ω_m and $2\omega_m$,

$$k_{ts}^{el} = \left\langle \partial F_{ts}^{el}/\partial z\right\rangle = k_{ts}^{el,dc} + \hat{k}_{ts}^{el,\omega}\cos\left(\omega_m t\right) + \hat{k}_{ts}^{el,2\omega}\cos\left(2\omega_m t\right),$$

where

$$k_{ts}^{el,dc} = \frac{1}{2}\left\langle\frac{\partial^2 C}{\partial z^2}\right\rangle\left[\frac{U_{ac}^2}{2} + \left(U_{dc} - U_{lcpd}\right)^2\right], \tag{10}$$

$$\hat{k}_{ts}^{el,\omega} = \left\langle\frac{\partial^2 C}{\partial z^2}\right\rangle U_{ac}\left(U_{dc} - U_{lcpd}\right), \tag{11}$$

and

$$\hat{k}_{ts}^{el,2\omega} = \frac{1}{4}\left\langle\frac{\partial^2 C}{\partial z^2}\right\rangle U_{ac}^2. \tag{12}$$

These modulations of the force gradient cause sidebands of the cantilever deflection at $\omega_d \pm \omega_m$ and $\omega_d \pm 2\omega_m$, which can be detected directly with lock-in amplifiers at the respective frequencies. The lock-in amplifiers return, relative to the reference oscillator, amplitude and phase of each sideband as well as their cartesian projection: the in-phase component X and the quadrature component Y. In the narrow-band approximation for $\omega_m >> \omega_c$, the in-phase components of the modulation at ω_m and the amplitudes at $2\omega_m$ are

$$\begin{aligned} X\left(\omega_d \pm \omega_m\right) &= \pm\frac{A_0}{2\omega_m}\frac{\omega_0}{2k}\hat{k}_{ts}^{el,\omega} \\ &= \pm\frac{A_0}{2\omega_m}\frac{\omega_0}{2k}\left\langle\frac{\partial^2 C}{\partial z^2}\right\rangle U_{ac}\left(U_{dc} - U_{lcpd}\right), \end{aligned} \tag{13}$$

and

$$A(\omega_d \pm 2\omega_m) = \frac{A_0}{4\omega_m}\frac{\omega_0}{2k}\hat{k}_{ts}^{el,2\omega} = \frac{A_0}{4\omega_m}\frac{\omega_0}{8k}\left\langle\frac{\partial^2 C}{\partial z^2}\right\rangle U_{ac}^2. \quad (14)$$

The reference phase offsets of the lock-in amplifier for the first set of sidebands at $\pm\omega_m$ are chosen to maximise their respective in-phase components, taking into account the 180° phase shift of the lower sideband. Then, $X_\omega = X(\omega_d + \omega_m) - X(\omega_d - \omega_m) = \mathrm{Re}\,\tilde{\beta}_\omega A$ is the total in-phase component, which depends linearly on the applied dc bias. Furthermore, when U_{dc} matches U_{lcpd}, X_ω is nullified and the $\pm\omega_m$ sidebands disappear.

The total amplitude of the second set of sidebands, $A_{2\omega} = A(\omega_d + 2\omega_m) + A(\omega_d - 2\omega_m) = |\tilde{\beta}_{2\omega}|A$, only depends on the ac modulation amplitude and the second order capacitance gradient, $C'' = \langle\partial^2 C/\partial z^2\rangle$. This signal thus provides a handle for imaging variations in the tip–surface capacitance, surface dielectric properties [25], or lateral dopant profiling [26].

In Figure 4, we show experimental data of modulation indices $\tilde{\beta}_\omega$ and $\tilde{\beta}_{2\omega}$, calculated from the ω_m and $2\omega_m$ sidebands, respectively, as a function of U_{dc} for different electrostatic modulation amplitudes, U_{ac}. During this experiment, the tip was positioned above a nickel electrode with amplitude modulated topography feedback enabled in net-attractive mode.

As expected from Equation 13, the ω_m sideband amplitudes (Figure 4a) vanish when $U_{dc} = U_{lcpd}$. While they change linearly with U_{dc} close to this point, there are non-linear deviations at larger voltage offsets, which are caused by changes in C''. This is also evident from the $2\omega_m$ sideband amplitudes (Figure 4b), showing the decrease of C'' with increasing voltage offsets. Since these sweeps are acquired with topography feedback enabled, the observed variations in C'' are most likely due to changes in the tip–surface separation: The AM topography feedback is sensitive to the static force gradient, which contains electrostatic interactions, Equation 10, that increase as the dc bias does not match the surface potential; consequently, the topography feedback retracts the tip, reducing C''.

In Figure 4c, we plot the ratio of the ω_m and $2\omega_m$ sideband amplitudes, normalised to U_{ac}. As apparent from Equation 13 and Equation 14, this process cancels out the non-linearities and collapses the sweeps at different U_{ac} to a single curve.

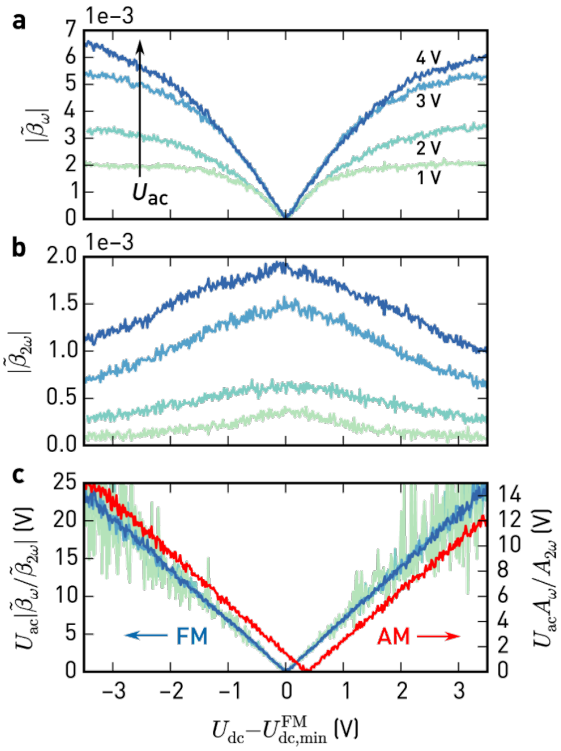

Figure 4: Modulation indices of the sidebands at ω_m (a) and $2\omega_m$ (b) against $U_{dc} - U_{dc,min}^{FM}$ for different modulation amplitudes U_{ac}. Topography feedback in amplitude modulation (net-attractive interaction) was enabled during these measurements. $U_{dc,min}^{FM}$, given by the minimum of $|\tilde{\beta}_\omega|$, is the contact potential difference found by FM detection. c) Signals in (a) normalised using U_{ac} and $|\tilde{\beta}_{2\omega}| \propto C''$ (light green to blue, FM). Normalised electrostatic force (red, AM), simultaneously detected with lock-in amplifiers at ω_m and $2\omega_m$. (Scan parameters: A_{free} = 11.2 nm, A_{set} = 10.4 nm, Q = 500, k = 35 N/m, f_0 = 302.5 kHz, f_m = 4 kHz).

Additionally, we show the similarly normalised amplitudes due to the electrostatic force at ω_m and $2\omega_m$ in the deflection signal, which we acquired simultaneously with the sidebands at $\omega_d \pm \omega_m$. They show the same v-shaped relationship, with their minimum being slightly shifted with respect to the FM case. This shift is due to the different weights of contributions in the AM signal (cf. Figure 1). Setting the dc bias to the minimum obtained by AM-KFM does not guarantee to compensate the electrostatic force gradient and can cause height errors in topography. At the minimum determined from the sidebands, $|\tilde{\beta}| \propto C''$ in Figure 4b reaches its maximum value, corresponding to the closest approach.

There are two major methods to find the local contact potential difference at every point during the scan. *Open-loop* KFM exploits the fact that the $2\omega_m$ amplitudes do depend on C'' but not on $U_{dc} - U_{lcpd}$. As demonstrated in Figure 4, the ratio of the ω_m and $2\omega_m$ sidebands is independent of changes in C'' and only depends on the chosen modulation amplitude and dc bias,

$$\frac{X\left(\omega_{\mathrm{d}}\pm\omega_{\mathrm{m}}\right)}{A\left(\omega_{\mathrm{d}}\pm2\omega_{\mathrm{m}}\right)}=\pm\frac{8}{U_{\mathrm{ac}}}\left(U_{\mathrm{dc}}-U_{\mathrm{lcpd}}\right)=\pm K'\left(U_{\mathrm{dc}}-U_{\mathrm{lcpd}}\right), \quad (15)$$

hence U_{lcpd} can easily be determined. Note, however, that the above definition of the prefactor K' is only valid for modulation frequencies well beyond the cantilever bandwidth. In the general case, $K' = (4/U_{\mathrm{ac}})\ G(\omega_{\mathrm{d}} \pm \omega_{\mathrm{m}})/G(\omega_{\mathrm{d}} \pm 2\omega_{\mathrm{m}})$, that is, it also depends on the resonant frequency and the quality factor, which may change while scanning. Furthermore, there may be differences in the sideband phase shift when Q or ω_0 are not constant (cf. Figure 2). Together, such inaccuracies in the model easily translate into uncertainties of U_{lcpd} in an open-loop method. A PLL can reduce these effects, but then its transfer function needs to be considered as well [27], and the bandwidth must be larger than $2\omega_{\mathrm{m}}$.

In *closed-loop* KFM, the local contact potential difference is found by nullifying the in-phase components of the ω_{m} sidebands (Equation 13) with a feedback loop adjusting the applied dc voltage [1-3,16]. Thus, the $2\omega_{\mathrm{m}}$ sidebands are not necessary to determine the CPD, and the effect of model deviations and non-linearities is cancelled by the feedback. Furthermore, the nulling process also minimises the dc electrostatic force and force gradient (Equation 10), reducing electrostatically induced height errors [14,28,29].

However, a few critical issues remain with simple Kelvin feedback loops. For example, when the sidebands are not completely nullified by the feedback, leaving a small error δ, it follows from Equation 13 that $U_{\mathrm{dc}} - U_{\mathrm{lcpd}} \propto \delta/C''$ [30]. C'' depends strongly on the electrostatic interactions between tip and surface and may change significantly on structured surfaces even for a well-tuned topography controller. During a scan, imperfect Kelvin feedback therefore leads to errors in the measured CPD, constituting a source of topography-induced crosstalk.

If additional apparent forces (or force gradients) are detected at the frequencies used for KFM, the Kelvin feedback does not compensate the CPD, but rather nullifies the in-phase component affected by offsets [31]. Such crosstalk is due to parasitic capacitive coupling and observed mainly in AM-KFM, where the electrostatic modulation is at high frequencies [32]. When coupling to the shaker piezo [33], cantilever resonances can amplify this effect.

Another source of crosstalk can appear when ω_{m} is set too low and the Kelvin lock-ins capture the modulation of k_{ts} induced by topography. This can happen on highly structured surfaces when the bandwidth of the topography feedback is insufficient for the scan speed. By monitoring the deflection power spectral density near the driving frequency, an upper frequency bound of the remaining k_{ts} modulations can be determined. In order to avoid crosstalk, ω_{m} should be chosen above this bound, considering both the bandwidth and filter steepness of the Kelvin lock-ins.

As already mentioned above, the tuning of the Kelvin feedback loop itself can be a challenge because its sensitivity depends on C''. This becomes even more acute for small tip–sample distances and single-scan techniques on structured surfaces, where the tip–surface interaction is not limited to the apex.

In order to address the topography crosstalk due to C'', Lee et al. [34] suggested to use a feedback signal normalised to the $2\omega_{\mathrm{m}}$ sideband, thus rendering the CPD tracking error independent of C'' (cf. Equation 15). However, as shown in Figure 4c, the normalisation procedure may introduce additional noise when dividing by small signals, e.g., for low U_{ac}.

In the following section we introduce a novel Kelvin feedback scheme that resolves these subtleties.

Results and Discussion

Optimal CPD estimation and Kelvin control

Most instruments provide a generic PID controller for Kelvin control, which compares the signal (X_ω) to a setpoint (0), yielding the error signal e. The sum of e, $\int \mathrm{d}t e$, and $\mathrm{d}e/\mathrm{d}t$, scaled by respective proportional (P), integral (I), and derivative (D) gains, is fed back into the system. In case of KFM, the resulting dc voltage compensates the electrostatic interactions. This standard PID feedback loop is illustrated in Figure 5a. Knowing the system dynamics, a multitude of tuning rules can be applied [35]. In practice, however, the feedback gains are often tuned by trial and error, and the derivative part is omitted altogether [36]. In many cases, only the integral part is necessary for good tracking and to eliminate steady-state errors. Integral-only controllers are therefore prevalent for topography or Kelvin feedback.

Controllers basing their actions on an error signal only are unaware of the systems they control. Thus, they need to be retuned as soon as the system bandwidths or gains change considerably, either due to different operator settings or, more importantly during KFM scans, due to local variations of electronic properties and topography of the sample. To maintain best feedback settings at every location during a scan, we introduce a novel controller for FM-KFM based on stochastic optimal control [37]. Optimal control and model-based controllers have been successfully used before in AFM, e.g., for active damping of cantilevers [38] or fast scanning [39].

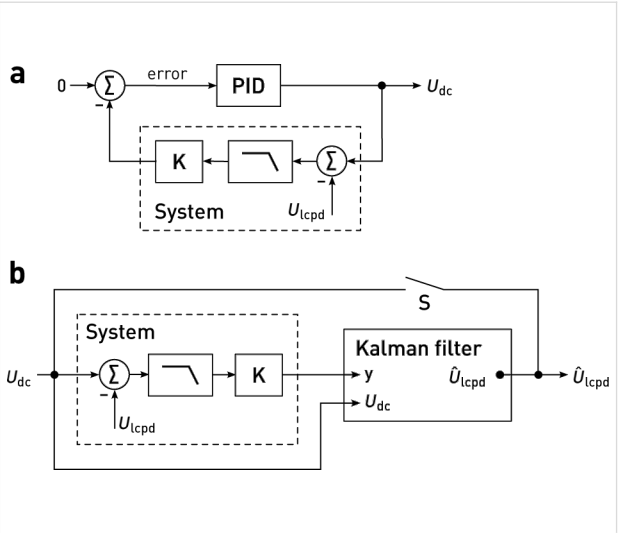

Figure 5: Block diagram of a Kelvin controller based on a) a proportional–integral–differential (PID) controller, and b) the Kalman filter. In the PID controller, the system output is compared to a setpoint to yield the error signal. The output signal, i.e., the sum of amplified errors and their respective integral or derivative, is fed back into the system. When the system output is nullified (setpoint 0), the controller output U_{dc} equals the surface potential U_{lcpd}. In contrast, knowing an approximate model of the system, the Kalman filter estimates $\hat{U}_{lcpd}$ solely based on the system output and the applied dc bias, U_{dc}. With the switch *S* closed, the estimated surface potential $\hat{U}_{lcpd}$ is applied as the dc bias, corresponding to a feedback configuration.

According to the separation principle [37], the optimal controller that minimises the expected error can be constructed by finding an optimal 'observer' and an optimal 'regulator'. As an observer, we use a Kalman filter [40], which continuously blends the sideband measurements at $\pm\omega_m$ into an estimate of the contact potential difference, $\hat{U}_{lcpd}$, based on a simplified model of the FM-KFM detection system. The Kalman filter is the stochastically optimal observer that minimises the state error covariance [37], taking into account both measurement noise and the uncertainties in the knowledge of its state. Adapted for KFM control, the Kalman filter minimises the estimation error variance of the surface potential, $\left\langle \left(U_{lcpd} - \hat{U}_{lcpd}\right)^2 \right\rangle$. Since the aim of the regulator in KFM is to minimise electrostatic interactions, the optimal regulator is found by matching the dc bias to $\hat{U}_{lcpd}$, thereby closing the feedback loop (Figure 5b).

Our Kalman filter design based on a model of the KFM detection system includes the sideband dynamics, Equation 8, the electrostatic force gradients acting on the cantilever, Equation 11 and Equation 12, and the transfer function of the demodulating lock-in amplifier. Since the lock-in bandwidths must be kept well below ω_m to avoid carrier and topography crosstalk, the sideband transfer functions reduce to an effective gain and phase, Equation 9. The lock-in transfer function can either be measured or is known from its filter properties. We focus on a particularly simple case, the *n*-th order critically damped lowpass filter, which is formed by *n* consecutive first order stages with a time constant τ. With these considerations, the transfer function for the in-phase lock-in components is $G(s = i\omega) = K(1 + \tau s)^{-n}$, where, following Equation 13, we find the static gain $K \propto C''U_{ac}$ and the system output $G(s)(U_{dc} - U_{lcpd})$.

Based on the transfer function, we find a state-space model of the system, in which we incorporate U_{lcpd} as a *hidden* state, and U_{dc} is the control signal. We further model the uncertainties of state transitions ($\dot{U}_{lcpd}$) and our measurements as uncorrelated, zero-mean white noise with power spectral densities *V* and *W*, respectively. Hence, U_{lcpd} follows a Wiener process or Brownian motion [37]. For a derivation of the continuous-time Kalman(-Bucy) filter [41], see Supporting Information File 1. In discrete time, the Kalman filter is similarly found from a discrete-time state-space model [40]. In this formulation the state estimate and covariances are refined recursively as new measurements are incorporated:

At the time *t*, an a priori state and covariance estimate is found using the state and covariances at the time $t - \Delta t$, based on the system model. Then, the Kalman gain *L* is computed from the covariance matrices of the a priori estimated state and the system model. *L* controls the innovations process, in which the measurements at the time *t* are incorporated to the a posteriori estimate of state and covariances [42].

This recursive predictor–corrector structure allows for updates of the system parameters, such as the static gain *K*, at each instant of the state update. With Equation 15, the 2ω sideband amplitudes can thus be exploited to continuously update $K = K'A_{2\omega}$. Consequently, the observer model will follow changes in the Kelvin signal strength due to variations of C''. This strategy avoids normalisation by potentially noisy C'' signals [34], yet changes in C'' do not affect closed-loop performance. We demonstrate this in Figure 6, where we compare step responses of the closed-loop Kalman observer and PI controller. As soon as the gain *K* drops, the noise level increases with a PI controller, whereas the Kalman estimate remains clean.

To further elucidate the performance of the controller, we plot in Figure 7 its −3 dB closed-loop bandwidth, normalised to the −3 dB filter bandwidth, as a function of the normalised noise power spectral densities $\tilde{V}$ and $\tilde{W}$ of state transitions and observations, respectively. As the noise at the output, $\tilde{W}$, increases for a fixed $\tilde{V}$, the bandwidth is reduced (Figure 7a). The ratio $\tilde{V}/\tilde{W} \propto (\tau K)^2 \approx K^2/\mathrm{BW}^2$ resembles a signal-to-noise ratio (SNR), which increases for large *K* and small filter bandwidths BW. The closed-loop bandwidth is a function of this SNR.

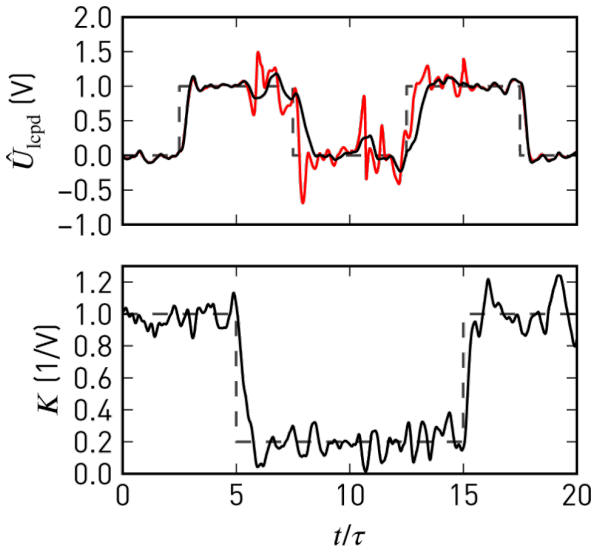

Figure 6: Closed-loop response of the Kelvin observer (black) and a proportional-integral controller (red) to steps in U_{lcpd} and K. Both controllers incorporate the separately measured static gain, K, and are tuned for similar step responses at high K. Noise in K and at the inputs is artificial white noise lowpass-filtered with $\tau f_{\mathrm{cut}} = 1$ and the filter order $n = 4$, corresponding to the simulated system.

Therefore, in addition to avoiding divisions by small signals, the Kalman filter improves noise performance by bandwidth adjustments. For normalised closed-loop bandwidths ≤ 1, the bandwidth is adjusted following $\sqrt{\tilde{V}/\tilde{W}}$ (Figure 7b). Larger bandwidths are not desired, since they would counteract the lock-in lowpass action.

Our setup is shown in Figure 8. We implemented the Kalman-filtering Kelvin controller as a real-time program on the digital signal processor (DSP) of a digital lock-in amplifier and PLL (HF2, Zurich Instruments), which demodulates the sidebands at $\omega_d \pm \omega_m$ and $\omega_d \pm 2\omega_m$ as well as the carrier signal at ω_d. Since our implementation of the Kalman filter is integrated into the lock-in, all signals are available without additional digital/analog/digital conversions. Additional offsets that might affect the feedback accuracy are avoided. We have implemented the Kalman filter as a reusable component in C++ using the Eigen template library for linear algebra [43], allowing us to perform offline tests with the same code that is compiled for the DSP. In its current state, our custom FM-KFM controller can work at sampling rates of up to 7200 Sa/s.

Since the sideband signals are detected individually, we do not depend on the Δf signal as in a typical FM-KFM setup. Therefore, the Kelvin feedback remains the same for AM and FM topography feedback schemes. For example, on samples with coarse topography one may use AM topography feedback to avoid instabilities typically experienced with FM operation. In vacuum, this may require additional application of active Q control [44,45] to lower the Q-factor of the cantilever.

Performance on a nanowire device

To demonstrate the performance of our Kalman-KFM controller, we examine an active nanowire device as depicted in Figure 8 and Figure 9. Such devices exhibit some of the most typical and relevant issues hindering reliable KFM measurements in the past: a combination of large topography with a

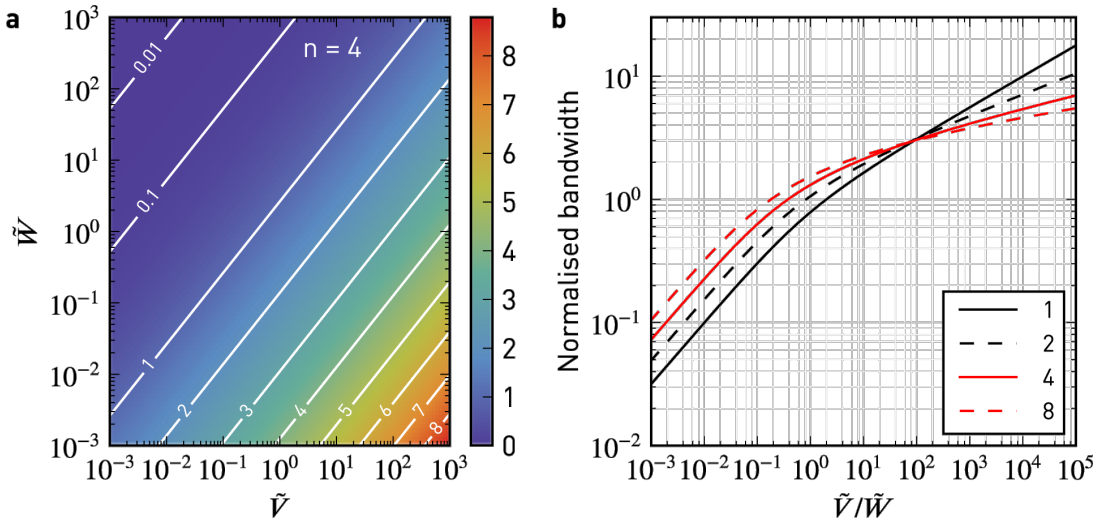

Figure 7: Normalised closed-loop bandwidth (−3 dB) of the steady-state Kelvin observer as a function of the normalised power spectral densities $\tilde{V} = \tau V$ and $\tilde{W} = W/\tau K^2$ for different orders of the low-pass filter, n. a) Two-dimensional map for $n = 4$. As the observation noise density, $\tilde{W}$, increases for a fixed transition noise density, $\tilde{V}$, the closed-loop bandwidth is reduced. b) Closed-loop bandwidth normalised to the bandwidth of the corresponding n-th order low-pass filter.

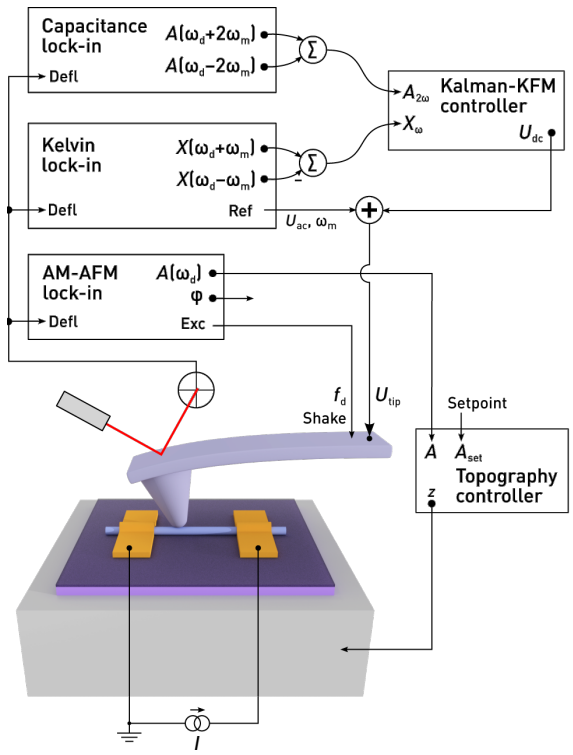

Figure 8: Schematic of the modified KFM setup. For topography feedback, the cantilever is excited at a constant frequency ω_d close to resonance. Lock-in amplifiers at $\omega_d \pm \omega_m$ and $\omega_d \pm 2\omega_m$ detect sidebands of the cantilever oscillation which contain information about the surface potential and tip–sample capacitance. Both contributions are used by the Kalman-KFM controller for the CPD estimate.

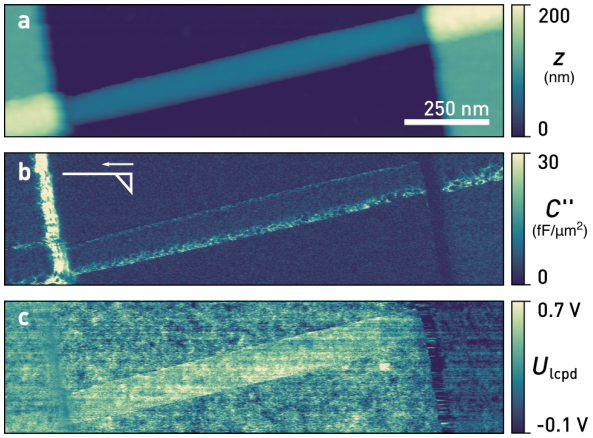

Figure 9: a) Topography, b) tip–sample capacitance gradient, C'', and c) local contact potential difference, U_{lcpd}, of an InAs nanowire at a bias current of 1.4 μA. U_{lcpd}, determined by the Kelvin observer, exhibits no crosstalk. The inset in b) indicates the tip shape and fast scan direction. (Scan parameters: A_{free} = 8.6 nm, A_{set} = 7.2 nm, Q = 390, k = 26 N/m, f_0 = 304.2 kHz, f_m = 4 kHz, U_{ac} = 1 V, f_{cut} = 100 Hz, n = 4, v_{tip} = 800 nm/s).

multitude of different materials including oxides prone to charging. In Figure 9, we show a scan of a 70 nm diameter indium arsenide (InAs) nanowire with nickel (Ni) contacts (height ≈ 120 nm), obtained at a bias current of 1.4 μA under ambient conditions using a commercial AFM (Cypher, Asylum Research). The steep edges at the electrodes necessitated AM topography feedback. Oftentimes the contact resistances between nanowire and metal contacts are uneven and large, obscuring the electrostatics of devices. Traditional four-point measurements are limited at sub-micron length scales because the contact length can become comparable to the channel dimensions. For such samples, KFM appears to be an ideal tool to characterise the electrostatics in order to optimise device performance, for example as field effect transistors.

Figure 9b displays the simultaneously acquired C'', calculated from the $2\omega_m$ sideband amplitudes, Equation 14. To ensure highest lateral potential resolution, we used highly doped silicon AFM tips (Olympus AC160TS-R3) without a metal coating. These tips are sharp and not symmetrical at the apex (schematically depicted in the inset), explaining the increased C'' on the edge of the left electrode.

Figure 9c shows $\hat{U}_{lcpd}$ as estimated by the Kalman-KFM controller. Since its gain is continuously updated using the $2\omega_m$ sidebands, crosstalk due to changes of C'' is absent from the scan. Near the left electrode edge the measured U_{lcpd} displays less spatial variation because also the sides of the tip are in close proximity to the electrode edge, increasing their contribution to the tip–sample capacitance and widening the KFM point spread function. Even though the Kalman-KFM controller remains stable and works unaffected by the increased C'', reaching up to seven times the mean value of the scan, the geometry of both tip and sample fundamentally limit the attainable resolution. The disturbances remaining on the edge of the right contact are due to imperfect topography feedback and accidental switches from net-attractive to net-repulsive tip–sample interactions. Most importantly, edge effects are absent at the boundaries of the nanowire. Long-range potential averaging due to the cantilever beam is absent due to the gradient-sensitive FM detection.

For an extraction of contact resistances, the voltage profile due to current flow needs to be separated from additional offsets in U_{lcpd}, such as spatial variations in work function. These are easily obtained from a scan at zero bias. Knowing the potential drop at the contacts, the bias current, and assuming uniform material or transport properties, for the nanowire device in Figure 9 we hereby obtain a contact resistance of 40 kΩ at the left electrode, 150 kΩ at the right electrode, and a channel resistance of 50 kΩ.

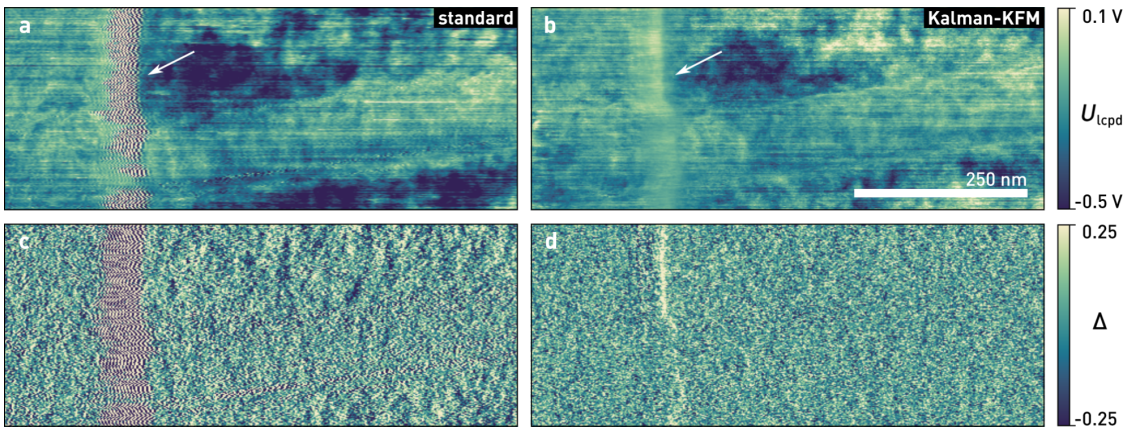

Figure 10: a), b) Kelvin and c), d) error signal of an InAs nanowire similar to the device shown in Figure 9, measured with a standard integral controller, a) & c), and the Kelvin observer, b) & d). Feedback oscillations, as indicated by the arrow, are absent in the Kalman control scheme, while the standard deviation of the error signal also decreases from 0.19 to 0.13. (Scan parameters: A_{free} = 11.2 nm, A_{set} = 9.6 nm, Q = 500, k = 35 N/m, f_0 = 304.5 kHz, f_m = 4 kHz, U_{ac} = 2 V, f_{cut} = 50 Hz, n = 4, v_{tip} = 250 nm/s; all images show raw data).

In Figure 10, we compare the performance of our Kalman-KFM controller with a standard integral controller. Both controllers are tuned for optimised closed-loop performance on the nanowire. The integral controller exhibits ringing artefacts at electrode edge, indicated by an arrow in Figure 10a, since the gain margin of the controller is exceeded due to the increased C''. Such feedback oscillations should be avoided particularly in single-scan techniques, because they may perturb the topography controller. Next to the nanowire, where C'' is slightly reduced because of the gate oxide, the bandwidth of the feedback loop drops due to a lower gain.

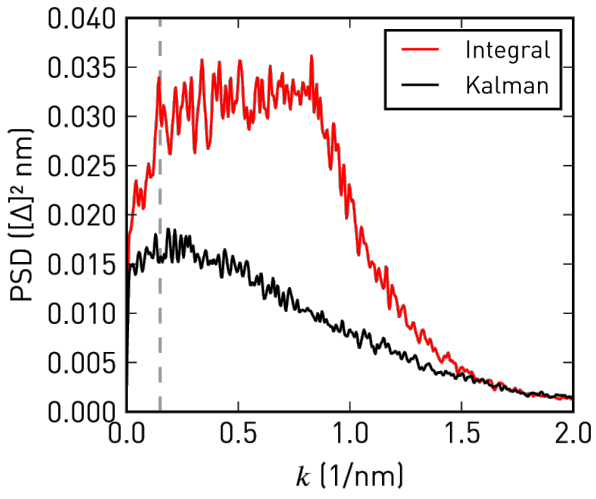

Figure 11: One-dimensional power spectral densities of the error signals in Figure 10c,d. Integral feedback works well at low spatial frequencies, k, but is unable to follow higher-frequency modulations. Kalman-KFM control consistently shows a lower error signal at all frequencies. In both cases the roll-off at high k is due to the Kelvin lock-in bandwidths.

As shown in Figure 10b, with the Kalman-KFM controller the feedback performance and image quality remain consistent during the scan. The error signal (X_ω) is almost feature-less and its standard deviation reduces by about 30% on average (excluding edge effects). Better tracking is also apparent from the power spectral densities of the error signals, depicted in Figure 11. For given lock-in filter bandwidths, the Kalman-KFM controller can nullify the $\pm\omega_m$ sidebands faster and better than the integral controller, without adding to the noise level or introducing feedback artefacts.

Conclusion

We have demonstrated a novel feedback controller for high resolution, frequency modulated Kelvin probe force microscopy. Based on Kalman filtering and stochastic optimal control, our feedback employs a model-driven estimation process, which allows one to integrate sensitivity information from the $2\omega_m$ sidebands. In comparison to normalisation approaches [34], this strategy does not increase the noise level.

We have tested performance on an InAs nanowire device with rough surface and abrupt height variations, which pose severe challenges to both traditional single-scan and lift-mode FM-KFM setups. Since direct sideband demodulation allowed us to perform FM-KFM irrespective of the topography feedback, we could perform these scans with amplitude modulation in air. Similarly, Magonov and Alexander [46] demonstrated a setup in which the modulated force gradients are detected from the phase output of the carrier oscillation lock-in, requiring ω_m to be within its bandwidth. With direct sideband detection, the detour via a phase modulation is avoided, and ω_m can be chosen independently of the lock-in bandwidth to achieve best separation from topography.

We have provided a detailed quantitative description of the evolution of sidebands in dynamic AFM modes. Precise knowledge of their frequency dependence in low and high Q environments is not only neccessary for accurate open-loop KFM techniques, but also offers a direct approach to noise performance and optimisation of frequency modulated KFM [19]. For example, ω_m should ideally be chosen below the thermal noise limited bandwidth of the cantilever [24], but the modulation induced by rough surfaces as well as the desired scan bandwidth establish lower limits. Furthermore, the sideband transfer function explains the higher resolution obtained by heterodyne amplitude-modulated KFM [47]. In this technique, the cantilever is driven mechanically at ω_0 and electrically at $\omega_m = \omega_1 - \omega_0$, where ω_0 and ω_1 are the lowest two eigenfrequencies of the cantilever. Accordingly, the sideband at $\omega_0 + \omega_m$ coincides with the second eigenmode of the cantilever, resulting in an amplified signal proportional to the electrostatic force gradient instead of the electrostatic force.

Although we have found our feedback loop superior to existing controllers, we see several aspects for improvement in the future. For example, the dynamics of U_{lcpd} are currently modelled as white noise. Since successive lines in AFM scans only change slightly, information from the previous line could be incorporated, similar to a feed-forward controller [29]. Other state estimators could also be integrated, including H-∞ filters for minimising the worst-case error [42].

Finally, we would like to point out that using our Kalman-KFM controller is not complicated. Since it automatically incorporates the lock-in filter settings and the system sensitivity, the only parameters left to tune are the noise power spectral density of the U_{lcpd} transitions and sideband observations. Because the latter is easily determined from a power spectrum near the sidebands, the controller performance can be tuned in practice using the transition noise only. Independent of the chosen parameters, the feedback loop will be stable thanks to the Kalman filter structure.

Supporting Information

Supporting Information File 1

Detailed derivations of the effective forces and the state-space KFM controller.
[http://www.beilstein-journals.org/bjnano/content/supplementary/2190-4286-6-225-S1.pdf]

Acknowledgements

The authors thank Daniel Wright (Zurich Instruments) for his assistance with the real-time programming interface, and Romain Stomp (Zurich Instruments) for many stimulating discussions as well as joint first experiments on the frequency dependence of the sidebands. InAs nanowire fabrication was facilitated by Siegfried Karg and Ute Drechsler (IBM). We gratefully acknowledge financial support from the Swiss National Science Foundation (Project No. 134777).

References

1. Weaver, J. M. R.; Abraham, D. W. *J. Vac. Sci. Technol., B* **1991,** *9,* 1559–1561. doi:10.1116/1.585423
2. Nonnenmacher, M.; O'Boyle, M. P.; Wickramasinghe, H. K. *Appl. Phys. Lett.* **1991,** *58,* 2921. doi:10.1063/1.105227
3. Jacobs, H. O.; Knapp, H. F.; Stemmer, A. *Rev. Sci. Instrum.* **1999,** *70,* 1756–1760. doi:10.1063/1.1149664
4. Halpern, E.; Cohen, G.; Gross, S.; Henning, A.; Matok, M.; Kretinin, A. V.; Shtrikman, H.; Rosenwaks, Y. *Phys. Status Solidi A* **2014,** *211,* 473–482. doi:10.1002/pssa.201300302
5. Koren, E.; Berkovitch, N.; Azriel, O.; Boag, A.; Rosenwaks, Y.; Hemesath, E. R.; Lauhon, L. J. *Appl. Phys. Lett.* **2011,** *99,* 3511. doi:10.1063/1.3665182
6. Fuller, E. J.; Pan, D.; Corso, B. L.; Gul, O. T.; Collins, P. G. *Phys. Rev. B* **2014,** *89,* 245450. doi:10.1103/PhysRevB.89.245450
7. Ziegler, D.; Gava, P.; Guttinger, J.; Molitor, F.; Wirtz, L.; Lazzeri, M.; Saitta, A. M.; Stemmer, A.; Mauri, F.; Stampfer, C. *Phys. Rev. B* **2011,** *83,* 235434. doi:10.1103/PhysRevB.83.235434
8. Wagner, T.; Köhler, D.; Milde, P.; Eng, L. M. *Appl. Phys. Lett.* **2013,** *103,* 023102. doi:10.1063/1.4813076
9. Jacobs, H. O.; Leuchtmann, P.; Homan, O. J.; Stemmer, A. *J. Appl. Phys.* **1998,** *84,* 1168. doi:10.1063/1.368181
10. Ziegler, D.; Stemmer, A. *Nanotechnology* **2011,** *22,* 075501. doi:10.1088/0957-4484/22/7/075501
11. Strassburg, E.; Boag, A.; Rosenwaks, Y. *Rev. Sci. Instrum.* **2005,** *76,* 083705. doi:10.1063/1.1988089
12. Cohen, G.; Halpern, E.; Nanayakkara, S. U.; Luther, J. M.; Held, C.; Bennewitz, R.; Boag, A.; Rosenwaks, Y. *Nanotechnology* **2013,** *24,* 295702. doi:10.1088/0957-4484/24/29/295702
13. Sadewasser, S.; Lux-Steiner, M. C. *Phys. Rev. Lett.* **2003,** *91,* 266101. doi:10.1103/PhysRevLett.91.266101
14. Ziegler, D.; Rychen, J.; Naujoks, N.; Stemmer, A. *Nanotechnology* **2007,** *18,* 225505. doi:10.1088/0957-4484/18/22/225505
15. Albrecht, T. R.; Grütter, P.; Horne, D.; Rugar, D. *J. Appl. Phys.* **1991,** *69,* 668. doi:10.1063/1.347347
16. Kitamura, S.; Iwatsuki, M. *Appl. Phys. Lett.* **1998,** *72,* 3154–3156. doi:10.1063/1.121577
17. Kitamura, S.; Suzuki, K.; Iwatsuki, M. *Appl. Surf. Sci.* **1999,** *140,* 265–270. doi:10.1016/S0169-4332(98)00538-8
18. Hudlet, S.; Saint Jean, M.; Guthmann, C.; Berger, J. *Eur. Phys. J. B* **1998,** *2,* 5. doi:10.1007/s100510050219
19. Diesinger, H.; Deresmes, D.; Mélin, T. *Beilstein J. Nanotechnol.* **2014,** *5,* 1–18. doi:10.3762/bjnano.5.1
20. Zerweck, U.; Loppacher, C.; Otto, T.; Grafström, S.; Eng, L. M. *Phys. Rev. B* **2005,** *71,* 125424. doi:10.1103/PhysRevB.71.125424
21. Giessibl, F. J. *Appl. Phys. Lett.* **2001,** *78,* 123. doi:10.1063/1.1335546
22. Giessibl, F. J. *Phys. Rev. B* **1997,** *56,* 16010. doi:10.1103/PhysRevB.56.16010
23. Carlson, A. B.; Crilly, P. B. *Communication Systems,* 5th ed.; McGraw Hill: New York, NY, U.S.A., 2009.

24. Lübbe, J.; Temmen, M.; Rode, S.; Rahe, P.; Kühnle, A.; Reichling, M. *Beilstein J. Nanotechnol.* **2013,** *4,* 32–44. doi:10.3762/bjnano.4.4
25. Martin, Y.; Abraham, D. W.; Wickramasinghe, H. K. *Appl. Phys. Lett.* **1988,** *52,* 1103. doi:10.1063/1.99224
26. Abraham, D. W.; Williams, C.; Slinkman, J.; Wickramasinghe, H. K. *J. Vac. Sci. Technol., B* **1991,** *9,* 703–706. doi:10.1116/1.585536
27. Kou, L.; Ma, Z.; Li, Y. J.; Naitoh, Y.; Komiyama, M.; Sugawara, Y. *Nanotechnology* **2015,** *26,* 195701. doi:10.1088/0957-4484/26/19/195701
28. Sadewasser, S.; Carl, P.; Glatzel, T.; Lux-Steiner, M. C. *Nanotechnology* **2004,** *15,* S14–S18. doi:10.1088/0957-4484/15/2/004
29. Ziegler, D.; Naujoks, N.; Stemmer, A. *Rev. Sci. Instrum.* **2008,** *79,* 063704. doi:10.1063/1.2947740
30. Efimov, A.; Cohen, S. R. *J. Vac. Sci. Technol., A* **2000,** *18,* 1051. doi:10.1116/1.582472
31. Barbet, S.; Popoff, M.; Diesinger, H.; Deresmes, D.; Théron, D.; Mélin, T. *J. Appl. Phys.* **2014,** *115,* 144313. doi:10.1063/1.4870710
32. Sadewasser, S.; Glatzel, T., Eds. *Kelvin Probe Force Microscopy;* Springer: Berlin, Germany, 2012.
33. Polak, L.; de Man, S.; Wijngaarden, R. J. *Rev. Sci. Instrum.* **2014,** *85,* 046111. doi:10.1063/1.4873331
34. Lee, M.; Lee, W.; Prinz, F. B. *Nanotechnology* **2006,** *17,* 3728–3733. doi:10.1088/0957-4484/17/15/019
35. Ziegler, J. G.; Nichols, N. B. *Trans. ASME* **1942,** *64,* 759–765.
36. Bechhoefer, J. *Rev. Mod. Phys.* **2005,** *77,* 783–836. doi:10.1103/RevModPhys.77.783
37. Friedland, B. *Control System Design: An Introduction to State-Space Methods;* Dover Publications, Inc.: Mineola, NY, U.S.A., 2005.
38. Degen, C. L.; Meier, U.; Lin, Q.; Hunkeler, A.; Meier, B. H. *Rev. Sci. Instrum.* **2006,** *77,* 043707. doi:10.1063/1.2183221
39. Schitter, G.; Menold, P.; Knapp, H. F.; Allgöwer, F.; Stemmer, A. *Rev. Sci. Instrum.* **2001,** *72,* 3320–3327. doi:10.1063/1.1387253
40. Kalman, R. E. *J. Basic Eng.* **1960,** *82,* 35–45. doi:10.1115/1.3662552
41. Kalman, R. E.; Bucy, R. S. *J. Basic Eng.* **1961,** *83,* 95–108. doi:10.1115/1.3658902
42. Simon, D. *Optimal State Estimation;* Wiley-Interscience: New York, NY, U.S.A., 2006.
43. Eigen v3. http://eigen.tuxfamily.org (accessed Aug 9, 2015).
44. Sulchek, T.; Hsieh, R.; Adams, J. D.; Yaralioglu, G. G.; Minne, S. C.; Quate, C. F.; Cleveland, J. P.; Atalar, A.; Adderton, D. M. *Appl. Phys. Lett.* **2000,** *76,* 1473–1475. doi:10.1063/1.126071
45. Hölscher, H.; Schwarz, U. D. *Int. J. Non-Linear Mech.* **2007,** *42,* 608–625. doi:10.1016/j.ijnonlinmec.2007.01.018
46. Magonov, S.; Alexander, J. *Beilstein J. Nanotechnol.* **2011,** *2,* 15–27. doi:10.3762/bjnano.2.2
47. Sugawara, Y.; Kou, L.; Ma, Z.; Kamijo, T.; Naitoh, Y.; Jun Li, Y. *Appl. Phys. Lett.* **2012,** *100,* 223104. doi:10.1063/1.4723697

BEILSTEIN JOURNAL OF NANOTECHNOLOGY

High-bandwidth multimode self-sensing in bimodal atomic force microscopy

Michael G. Ruppert*[1] and S. O. Reza Moheimani[2]

Full Research Paper

Open Access

Address:
[1]School of Electrical Engineering and Computer Science, The University of Newcastle, Callaghan, NSW, 2308, Australia and [2]Department of Mechanical Engineering, The University of Texas at Dallas, Richardson, TX, 75080, U.S.A.

Email:
Michael G. Ruppert* - Michael.Ruppert@uon.edu.au

* Corresponding author

Keywords:
atomic force microscopy; charge sensing; feedthrough cancellation; multimode sensor; piezoelectric cantilever; self-sensing

Beilstein J. Nanotechnol. **2016,** *7,* 284–295.
doi:10.3762/bjnano.7.26

Received: 19 October 2015
Accepted: 06 February 2016
Published: 24 February 2016

This article is part of the Thematic Series "Advanced atomic force microscopy techniques IV".

Guest Editor: T. Glatzel

Abstract

Using standard microelectromechanical system (MEMS) processes to coat a microcantilever with a piezoelectric layer results in a versatile transducer with inherent self-sensing capabilities. For applications in multifrequency atomic force microscopy (MF-AFM), we illustrate that a single piezoelectric layer can be simultaneously used for multimode excitation and detection of the cantilever deflection. This is achieved by a charge sensor with a bandwidth of 10 MHz and dual feedthrough cancellation to recover the resonant modes that are heavily buried in feedthrough originating from the piezoelectric capacitance. The setup enables the omission of the commonly used piezoelectric stack actuator and optical beam deflection sensor, alleviating limitations due to distorted frequency responses and instrumentation cost, respectively. The proposed method benefits from a more than two orders of magnitude increase in deflection to strain sensitivity on the fifth eigenmode leading to a remarkable signal-to-noise ratio. Experimental results using bimodal AFM imaging on a two component polymer sample validate that the self-sensing scheme can therefore be used to provide both the feedback signal, for topography imaging on the fundamental mode, and phase imaging on the higher eigenmode.

Introduction

Emerging methods in multifrequency atomic force microscopy (MF-AFM) rely on the detection and excitation of higher order eigenmodes of a microcantilever [1-3] and as such, present a number of practical challenges to cantilever instrumentation. Both high-bandwidth cantilever actuation and deflection sensing are necessary, ideally without distorting the frequency response of the cantilever and involving a minimum amount of external equipment. For example, the commonly used piezoelectric actuator at the base of the cantilever leads to a highly distorted frequency response with numerous resonances which renders the identification and subsequent analysis of higher eigenmodes exceedingly difficult.

To circumvent this problem, integrated actuation such as magnetic [4], photothermal [5], resistive thermal [6], ultrasonic [7] or through a piezoelectric layer [8] have been employed. Among the sensing techniques to detect the cantilever oscillations, the optical beam deflection (OBD) method [9] remains the most widely used approach mostly due to its low noise characteristics. However, its limitations such as frequent laser alignment, imaging artifacts due to optical interferences [10] and limited bandwidth requiring custom-built read-out electronics [11,12] have led to the development of numerous integrated sensing approaches. These include capacitive [13], piezoresistive [14], piezoelectric [15] and magnetoresistive [16] sensing.

A common drawback of self-sensing approaches applied to microelectromechanical systems (MEMS) is the fact that drive and sense electrodes share a common node (the MEMS electrical network) resulting in a potentially large feedthrough path from actuation to sensing [17]. If not properly accounted for, this feedthrough can almost entirely conceal the signal originating from the motion of the structure and is especially dominant if the same transduction principle is used for both actuation and sensing. Recently, the authors proposed two reciprocal self-sensing schemes for tapping-mode atomic force microscopy (TM-AFM) utilizing charge sensing and charge actuation respectively [18,19], using a single piezoelectric layer. The proposed techniques enable the elimination of the piezoelectric base actuator and the OBD sensor from the cantilever instrumentation setup, avoiding tedious laser alignment and distorted frequency responses. In this contribution, we demonstrate that the self-sensing method can be extended to MF-AFM techniques such as bimodal imaging by measuring the charge simultaneously at multiple higher eigenmodes. However, the individual resonances are heavily buried in feedthrough originating from the piezoelectric capacitance which yields a dynamic range of less than 1 dB at the resonant modes. In order to recover these modes for subsequent application in MF-AFM, two parallel analog feedforward compensators are employed to cancel the feedthrough at each eigenmode leading to a substantial increase in dynamic range. We demonstrate that on the higher eigenmode, a two order of magnitude increase of sensitivity is achieved due to the large deflection to strain sensitivity. The applicability of the multimodal self-sensing principle is verified by bimodal AFM experiments to obtain qualitative phase contrast on the higher eigenmode when imaging a soft polymer blend.

Modeling

Piezoelectric constitutive laws

By sputtering a piezoelectric layer to the surface of a cantilever, a transducer with inherent self-sensing capabilities is obtained. The electromechanical equations describing the independent variables applied stress σ [N/m^2] and applied electrical field E [V/m] and the dependent variables resulting strain ε [m/m] and resulting electrical displacement D [C/m^2] within a piezoelectric material are governed by the IEEE standard on piezoelectricity [20]. They are usually written in compact matrix notation such that redundant and symmetrical terms are accounted for. By convention of the axis defined in Figure 1, an electric field or a deflection in the (3)-direction causes normal stress in the (1)-direction [21]. Then, the constitutive equations reduce to two scalar equations

$$\varepsilon_1 = \frac{1}{Y_{31}^E}\sigma_1 + d_{31}E_3, \tag{1}$$

$$D_3 = d_{31}\sigma_1 + \xi_{33}^{\sigma}E_3 \tag{2}$$

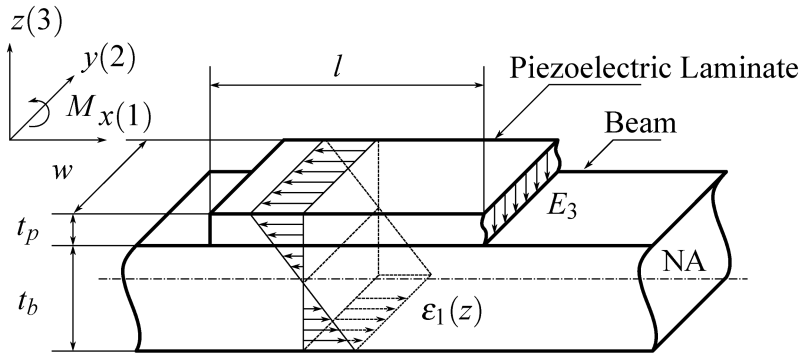

Figure 1: Simplified cross-section schematic of a beam with bonded piezoelectric layer. An electric field E_3 applied to the piezoelectric layer causes a cantilever deflection in the z-direction. Conversely, a deflection in the z-direction causes stress in the x-direction $\varepsilon_1(x)$, which leads to a charge accumulation on the piezoelectric layer.

with Young's modulus Y [N/m^2], piezoelectric d [m/V] and dielectric ξ [F/m] material constants. The superscripts E and σ indicate that these constants are measured during constant electrical field (electrodes short-circuited) and constant stress (electrodes open-circuited), respectively. Here, Equation 1 states that the total strain is the sum of the mechanical strain due to mechanical stress (passive) and the strain caused by applying an electrical field (active) and therefore describes the transducer if used as an actuator, i.e., the converse piezoelectric effect. On the other hand, Equation 2 states that the total electrical displacement is the sum of induced electrical displacement due to mechanical stress (sensing) and applied electrical field (feedthrough) and therefore describes the transducer if used as a sensor, i.e., the direct piezoelectric effect.

In the following we assume an Euler–Bernoulli beam with homogeneous isotropic linear elastic material with constant cross section and perfect bonding of the piezoelectric layer which is thin and lightweight compared to the beam. The assumption implies a linearly varying strain distribution throughout the beam and enables analytical actuator and sensor equations to be derived [22].

Piezoelectric actuator

For a piezoelectric layer with thickness t_p, applying a voltage V across the electrodes along the polarization direction, generates the electrical field

$$E_3 = \frac{V}{t_p} \tag{3}$$

and results in the free strain

$$\varepsilon_p = \frac{d_{31}V}{t_p}. \tag{4}$$

Further, the asymmetrical strain distribution along the (1)-axis in the actuator as shown in Figure 1 can be stated as [23]

$$\varepsilon_1(z) = \alpha z + \varepsilon_0. \tag{5}$$

By equating Equation 1 and Equation 5 and using Hooke's law, the stress distribution in the actuator is found to be

$$\sigma_1(z) = Y_{31}(\alpha z + \varepsilon_0 - \varepsilon_p). \tag{6}$$

By applying the moment equilibrium around the center of the beam and the force equilibrium along the (1)-axis of the beam, α and ε_0 can be determined. By further integrating Equation 6 across the beam, the distributed moment as a function of the applied voltage is found to be [23,24]

$$M(V) = Y_b I_b \alpha(V). \tag{7}$$

where I_b and Y_b are the moment of inertia and Young's modulus of the beam and $\alpha(V)$ contains geometrical constants of the beam and the piezoelectric layer and is linear in the applied voltage. Thus, a voltage applied to the electrodes results in a bending moment causing the cantilever to deflect.

Piezoelectric sensor

With the foregoing assumptions, the stress in the (1)-direction is given by Hooke's law

$$\sigma_1(z) = Y_{31}\varepsilon_1(z) = -\frac{Y_{31}z}{R} \tag{8}$$

where R is the bending radius which can be related to the second derivative along the x-axis of the displacement $z''(x,t) = 1/R$ to yield

$$\sigma_1(z) = -zY_{31}z''(x,t). \tag{9}$$

Here, stress is defined to be positive under elongation (tensile stress) and negative under compression (compressive stress). Assuming zero applied electrical field E, the electrical displacement D due to bending stress is given by Equation 2. Hence, the charge collected on the electrodes located at $z = t_b/2 + t_p$ can be determined by integrating the electrical displacement over the electrode area

$$Q = \int_A D_3 dA = \int_A d_{31}\sigma_1 dA = \kappa \int_x z''(x,t)\,dx \tag{10}$$

where $\kappa = -d_{31}(t_b/2 + t_p)wY_{31}$.

System model

The transverse deflection of a uniform cantilever (YI = const) are governed by the Euler–Bernoulli beam equation, which for the free vibration case are described by the partial differential equation (PDE) [25]

$$YI\frac{\partial^4 z(x,t)}{\partial x^4}+\rho A\frac{\partial^2 z(x,t)}{\partial t^2}=0 \tag{11}$$

where Y,I,ρ,A are Young's modulus, area moment of inertia, mass density and cross section of the beam respectively. A common approach to solve Equation 11 is the modal analysis approach. Here, it is assumed that the solution can be represented by separable space and time functions representing the mode shape $Z_k(x)$ and modal coordinates $q_k(t)$

$$z(x,t)=\sum_{k=1}^{\infty} Z_k(x)q_k(t) \tag{12}$$

with

$$\frac{\partial^2 q_k(t)}{\partial t^2}+\omega_k^2 q_k(t)=0 \tag{13}$$

$$\frac{\partial^4 Z_k(x)}{\partial x^4}-\beta_k^4 Z_k(x)=0. \tag{14}$$

For the case of a homogenous isotropic linear elastic beam with constant cross section, the displacement and strain modeshapes for varying standard boundary conditions can be derived analytically from Equation 14 [25]. Discontinuous beam models have been proposed to take into account varying cross-sections but system identification based on parameter optimization must be employed to reduce modeling errors [26]. In order to arrive at a system-based model and to use frequency domain system identification, a damping term is added to Equation 13 and taking the Laplace transform yields a sum of second order modes to describe the frequency response of the first n flexural modes of the beam relating the actuator voltage $V(s)$ to cantilever deflection $D(s)$ [24]

$$G_{dv}(s)=\frac{D(s)}{V(s)}=\sum_{i=1}^{n}\frac{\alpha_i\omega_i^2}{s^2+\frac{\omega_i}{Q_i}s+\omega_i^2},\ \alpha_i\in\mathbb{R}. \tag{15}$$

where each second order mode is associated with a specific vibrational mode shape and is characterized in terms of the quality factor Q_i, natural frequency ω_i and gain α_i. Similarly, when a piezoelectric transducer is subjected to mechanical strain it becomes electrically polarized, producing a charge on the surface of the material, described by Equation 10. This direct piezoelectric effect can be modeled as a strain dependent voltage source V_p in series with a capacitor C_p as shown in Figure 2c.

While the capacitor sufficiently represents the dielectric properties of the piezoelectric material, this simplified model does not take into account dielectric losses or heat dissipation which can be modeled by adding a resistor in parallel to V_p and C_p. The model is a simplified version of the Butterworth–van Dyke model as proposed by the IEEE Standard on piezoelectricity [20]. The piezoelectric voltage V_p can be modeled as the linear combination of the direct excitation voltage $V(s)$ and a voltage due to the tip–sample force acting as a disturbance $W(s)$

$$V_p(s)=G_{vv}(s)V(s)+G_{vw}(s)W(s) \tag{16}$$

with

$$G_{vv}(s)=\sum_{i=1}^{n}\frac{\beta_i\omega_i^2}{s^2+\frac{\omega_i}{Q_i}s+\omega_i^2},\ \beta_i>0 \tag{17}$$

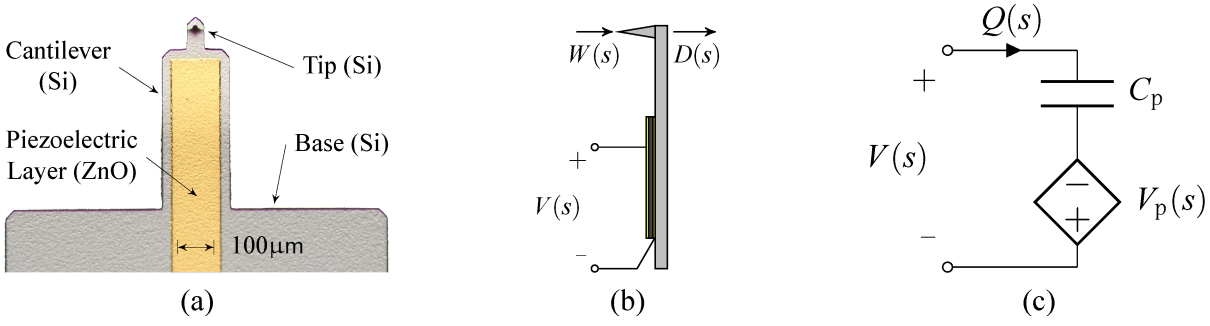

Figure 2: (a) Annotated photo, (b) schematic and (c) electrical circuit model of the piezoelectric cantilever.

$$G_{vw}(s)=\sum_{i=1}^{n}\frac{\gamma_i\omega_i^2}{s^2+\frac{\omega_i}{Q_i}s+\omega_i^2},\ \gamma_i>0. \tag{18}$$

Applying Kirchhoff's law to Figure 2c, one obtains

$$V(s)=\frac{1}{C_\mathrm{p}}Q(s)-V_\mathrm{p}(s). \tag{19}$$

Substituting Equation 16 into Equation 19 yields

$$Q(s)=\left[C_\mathrm{p}+C_\mathrm{p}G_{vv}(s)\right]V(s)+C_\mathrm{p}G_{vw}(s)W(s), \tag{20}$$

which is illustrated in the block diagram in Figure 3.

We note that the charge in the piezoelectric layer depends on the excitation voltage and the disturbance input but most importantly is dominated by a feedthrough term $C_\mathrm{p}V(s)$. Consequently, the disturbance will remain unnoticed in the charge output if the feedthrough is large. Furthermore, while $G_{vw}(s)$ can be estimated [27,28], it cannot be measured directly. Thus we focus on the system

$$G_{qv}(s)=\frac{Q(s)}{V(s)}=C_\mathrm{p}+C_\mathrm{p}\sum_{i=1}^{n}G_{vv,i}(s) \tag{21}$$

to demonstrate the effect of the feedthrough. Observing that each mode of Equation 15 and Equation 17 only differ by a constant factor, Equation 21 can be rewritten as

$$G_{qv}(s)=C_\mathrm{p}+C_\mathrm{p}\sum_{i=1}^{n}\delta_i G_{dv,i}(s). \tag{22}$$

From Equation 22 we conclude that by exciting the cantilever with a voltage and measuring the charge, a deflection estimate of the cantilever can be obtained if the feedthrough term $C_\mathrm{p}V(s)$ can be canceled.

Results and Discussion

Implementation

The proposed self-sensing scheme was realized using surface-mount high-bandwidth analog components on a printed circuit board (PCB) according to the block diagram shown in Figure 4; a photo of the corresponding implemented circuit is shown in Figure 5. Here, the block $H_{qv}(s)$ models the dynamics of the charge amplifier [18] and the blocks $K_1(s) = C_\mathrm{p}H_{qv}(s)$ and $K_2(s) = C_\mathrm{p}H_{qv}(s)$ are feedforward compensators, each contain-

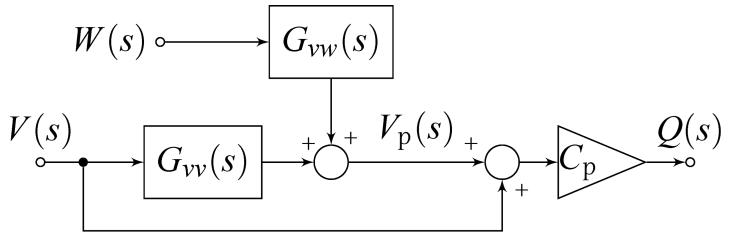

Figure 3: Block diagram representing the transfer function from voltage actuation and tip disturbance to charge in the piezoelectric material.

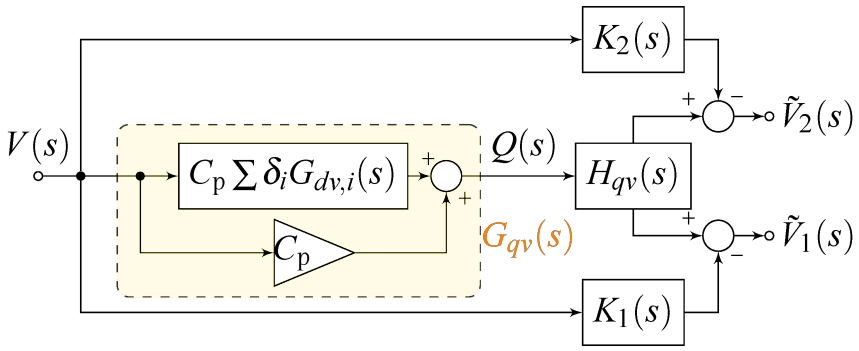

Figure 4: Block diagram of the self-sensing scheme with dual feedforward compensator to cancel the capacitive feedthrough at two resonances.

ing a model of the charge amplifier stage, to compensate the feedthrough at each resonance. As the charge amplifier can be approximated by a first order high-pass filter in the bandwidth of interest [19], the feedforward compensators will have the same dynamics and can be implemented with simple op-amp circuits. After compensation, the outputs $\tilde{V}_1$ and $\tilde{V}_2$ are proportional to the displacement at the respective mode.

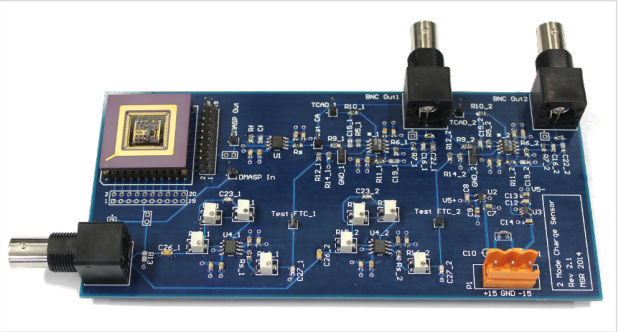

Figure 5: Photo of the implemented PCB circuit for bimodal charge sensing.

System identification

The AFM cantilever used in this work is a piezoelectric self-actuated silicon microcantilever described in section Modeling. Compared to a standard base excited cantilever whose frequency response is shown in Figure 6a, the piezoelectric cantilever has closely spaced eigenmodes due to the stepped geometry [29] and its frequency response is not distorted by additional actuator dynamics owing to the integrated actuation. The clean nature of the frequency response data, obtained by performing a sinusoidal sweep (Zürich Instruments HF2LI lock-in amplifier), allows for the use of frequency domain subspace identification [30] to obtain a 12-order state space model for the first six eigenmodes of the cantilever. The model along with the measured data is shown in Figure 6b where only the flexural modes have been included in the model (the torsional modes, noticeable between *M*3 and *M*4 as well as in the vicinity of *M*5, have been neglected). From the model, the fixed structure form (Equation 15) for $n = 6$ is calculated with parameters shown in Table 1.

The experimentally obtained voltage to charge frequency response is shown in Figure 6c. We note that the first and fifth modes, while almost entirely buried in feedthrough, show nearly equal gains at the resonance peaks compared to the voltage to deflection frequency response shown in Figure 6b. This is due to the large deflection to strain sensitivity on the higher mode which can be exploited by using a charge sensor.

In order to experimentally verify the model Equation 22, a parameter optimization procedure is employed to fit the model Equation 22 to the experimentally obtained voltage to charge frequency response shown in Figure 6c. The optimization method aims to minimize the difference in magnitude and phase of the measured transfer function and Equation 22. The resulting parameters are also shown in Table 1. We note that the optimization procedure did not converge for the second, third and fourth mode due to the excessive amount of feedthrough. The differences in the estimated feedthrough of each mode is due to numerical rounding occurring when scaling the optimization parameters back to real world quantities (pF) and due to slight variations in the passive components of the analog implementation. Additionally, knowing that the capacitance is an inherent property of the piezoelectric layer, an impedance analyzer such as the Keysight E4990A was used to measure C_p and the obtained value of 20.27 pF adequately matches the estimation.

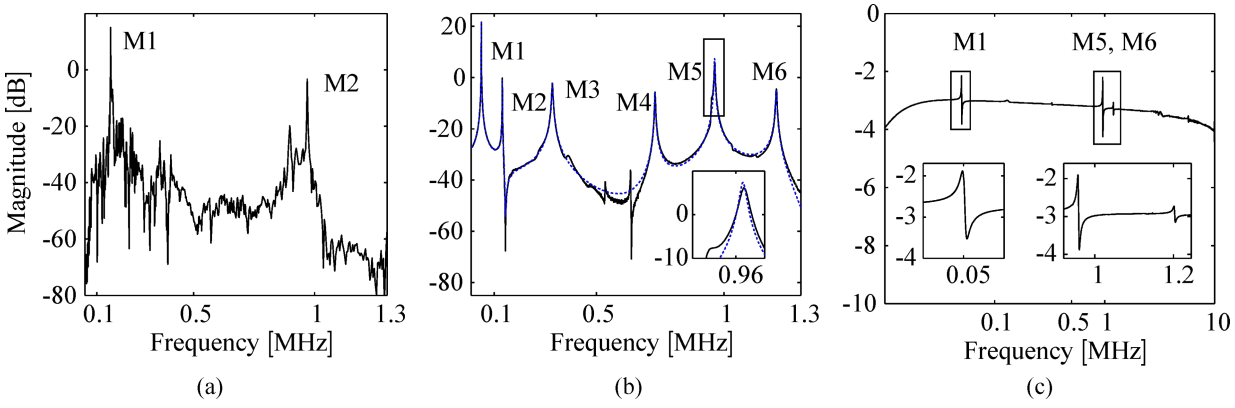

Figure 6: (a) Frequency response measured with the OBD sensor (−) of an NT-MDT NSG01 base-excited cantilever highlighting the first two flexural modes. (b) Frequency response measured with the OBD sensor (−) and identified 12th-order model (−−) of the piezoelectric cantilever highlighting the first six flexural modes. The inset shows a zoomed view of the fifth flexural mode. (c) Frequency response measured with the charge amplifier (−) highlighting the first and fifth flexural modes. The insets show a zoomed view of the first, fifth and sixth modes embedded in capacitive feedthrough.

Table 1: Parameters of the fixed structure model.

M	shape	f_i [kHz]	Q_i	α_i	C_p [pF]	δ_i
1		50.1	230	0.054	20.48	0.015
2		132.4	240	−0.004	—	—
3	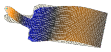	327.9	86	−0.008	—	—
4	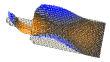	729.3	264	−0.0005	—	—
5	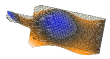	962.5	322	0.004	19.82	0.17
6	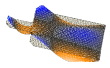	1203.9	335	−0.002	19.71	−0.08

Feedthrough cancellation

The first and the fifth modes are clearly visible in the frequency response shown in Figure 6c albeit excessively buried in capacitive feedthrough. In order to use the charge sensor for dynamic mode AFM, the eigenmodes need to be recovered from the capacitive feedthrough. Here, an analog feedforward compensation method was employed based on the block diagram shown in Figure 4. It can be seen in Figure 7a how this compensation method leads to an increase in dynamic range around the first resonance from 0.7 dB to 25 dB. Similarly, it can be seen in Figure 7b how the dynamic range around the fifth resonance frequency is increased from 0.9 to 26 dB. Due to slight component mismatches which leads to a phase mismatch, the feedthrough is not compensated entirely which can be seen in the phase response. However, the de-embedded eigenmodes have enough dynamic range to be suitable for bimodal AM-AFM imaging as will be discussed in section Bimodal AFM application.

Sensor sensitivity

The optical lever method measures the bending angle of the cantilever at the measurement position rather than the displacement [9,31]. As such, the voltage output from the OBD sensor has to be calibrated individually for each eigenmode in order to obtain a deflection measurement from the sensor output [32,33], which is usually done by performing an approach and retract curve on a stiff sample. Assuming that the z-axis actuator has been calibrated beforehand, the vibrational inverse optical lever sensitivity (invOLS) can be found by calculating the slope of the linear region of the amplitude versus distance curve [32]. While this approach is common practice for the fundamental mode, it is not feasible for higher eigenmodes, due to their in-

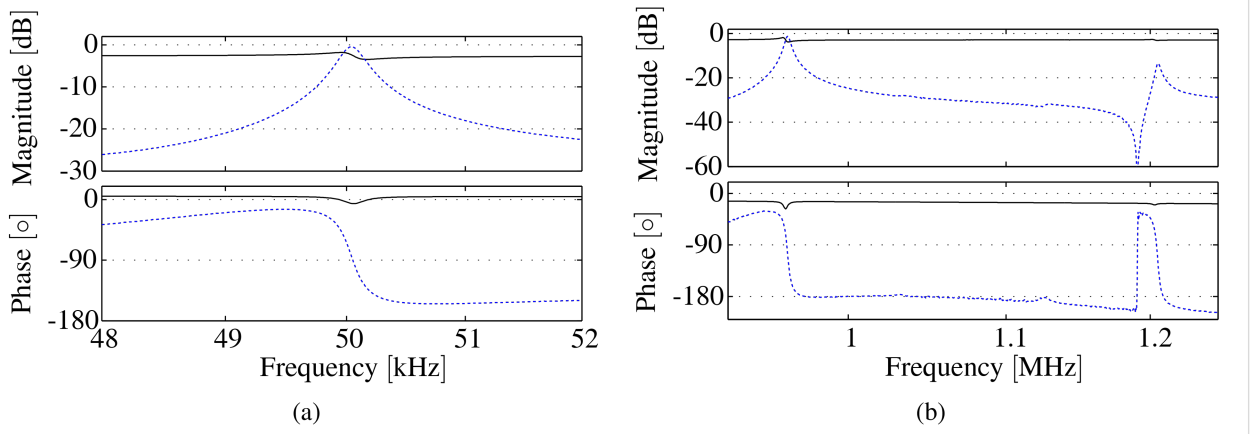

Figure 7: (a) Frequency response of the first flexural mode measured with the charge sensor before (−) and after feedthrough cancellation (−−). The dynamic range has been increased from 0.7 to 25 dB. (b) Frequency response of the fifth and sixth flexural modes measured with the charge sensor before (−) and after feedthrough cancellation (−−). The dynamic range has been increased from 0.9 to 26 dB.

creased dynamic stiffnesses and associated small free-air amplitudes. As such, the sensor sensitivities are calibrated by comparing the sensor outputs for a given drive voltage and comparing it to the displacement measurements obtained from a laser-doppler vibrometer (LDV) (Polytec MSA-100-3D). For the cantilever used in this work and the NT-MDT NTegra AFM system, the inverse optical lever sensitivity for the first mode was found to be

$$\text{invOLS}_1 = 647\ \text{nm/V} \tag{23}$$

and

$$\text{invOLS}_5 = 43\ \text{nm/V} \tag{24}$$

for the fifth mode. Notice, that the sensitivity on the higher eigenmode is an order of magnitude better than on the fundamental mode due to measurement of slope. Similarly, the inverse charge amplifier sensitivity (invCAS) for the first mode was determined to be

$$\text{invCAS}_1 = 8999\ \text{nm/V}. \tag{25}$$

Notice, that this value is significantly higher than the one obtained with the OBD sensor but it can be lowered if subsequent gain stages are employed at the expense of introducing additional sensor noise. However, on the fifth mode we obtain an invCAS of

$$\text{invCAS}_5 = 48\ \text{nm/V}, \tag{26}$$

which is more than two orders of magnitude better than on the fundamental mode. This highlights the increased deflection to strain sensitivity on the higher mode which was already noticed from Figure 6c. On the fifth mode, the strain sensor produces the same output for a much smaller deflection, yielding a much larger sensitivity.

Noise analysis

The noise performance of cantilever deflection sensors used in dynamic AFM is commonly evaluated with the deflection noise density acquired from thermally induced vibrations. However, this method is only suitable for the fundamental mode as higher eigenmode deflections due to Brownian motion decrease rapidly [34]. For the cantilever used in this work, the thermally induced vibration amplitude corresponding to the first mode is below the sensitivity of the charge sensor associated with that mode. As the use of the charge sensor in amplitude modulation AFM always requires demodulation, we state the total integrated noise from the voltage noise density (ND) plot and standard deviation (RMS noise) of the amplitude obtained from a lock-in amplifier (LIA) (HF2LI Zürich Instruments) and compare the measurements with the OBD sensor. The cantilever is actively driven at each mode, resulting in a deflection of 253 nm on the first mode and 1.62 nm on the fifth mode. A 4th-order low-pass filter with cut-off frequency of f_c = 1 kHz is used in the LIA. The ND estimates are shown in Figure 8a which are obtained from the time-domain demodulated amplitude signals sampled at 28.8 kHz using Welch's segment averaging estimator with 8 sections windowed with the Hamming window. The results are summarized in Table 2.

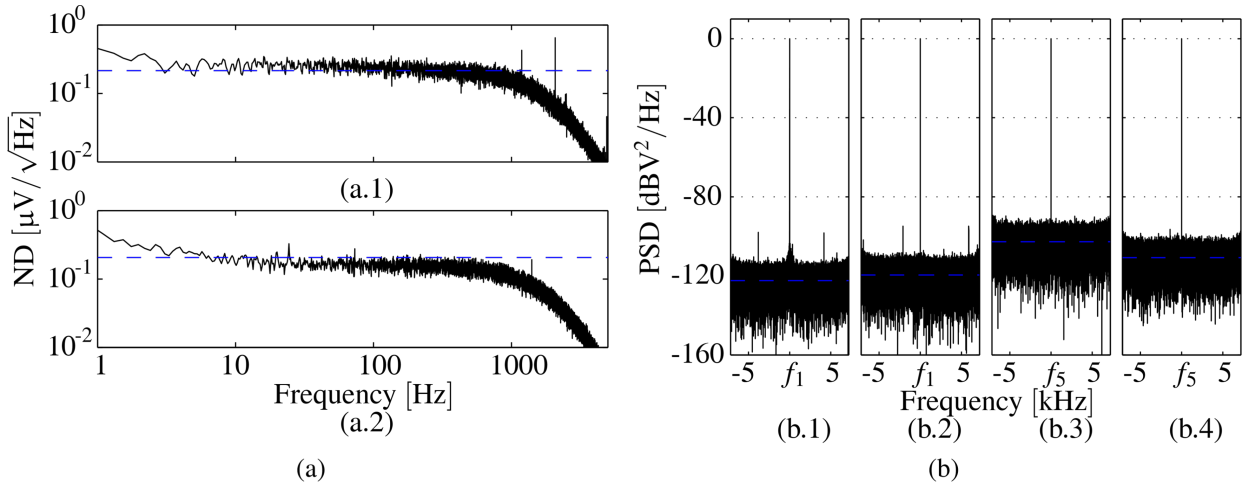

Figure 8: (a) Voltage noise density estimate of demodulated amplitude obtained from LIA with low-pass filter cut-off frequency of f_c = 1 kHz measured with charge sensor (−) and total integrated noise (−−) of (a.1) first mode and (a.2) fifth mode. (b) Zoom FFT of the deflection estimate on the fundamental mode from (b.1) OBD sensor and (b.2) charge sensor with a span of 14.4 kHz around the resonance. Zoom FFT of the deflection estimate on the fifth mode from (b.3) OBD sensor and (b.4) charge sensor with a span of 14.4 kHz around the resonance.

Table 2: Noise performance of OBD and charge sensor.

	OBD M1	CA M1	OBD M5	CA M5
ND [μV/√Hz]	0.90	0.22	0.70	0.21
ND [fm/√Hz]	585	1940	30.2	9.91
RMS [μV]	30.3	7.20	23.5	6.91
RMS [pm]	19.6	64.8	1.01	0.33

It can be noticed, that the charge sensor shows a lower voltage noise density, but it is inferior to the OBD sensor on the fundamental mode due to the low deflection to strain sensitivity. However, on the fifth mode the large increase in sensitivity results in a deflection noise density of only 9.91 fm/√Hz and RMS noise of 0.33 pm from DC to the equivalent noise bandwidth of the LIA low-pass filter. The values on the fundamental mode are higher than the ones reported for optimized OBD sensor systems using thermal deflection noise density [11]. This is due to the lower sensitivity of the sensor at that mode and the fact that the cantilever is actively driven at resonance. However, the authors believe that the procedure is closer to the actual dynamic AFM application (using lock-in demodulation of actively driven cantilevers) and therefore the values reported are a realistic representation of values obtained during AFM imaging. To qualify the resolution of the overall AFM system, a noise image with the actively driven cantilever in contact with the sample surface should be acquired [35] which takes into account all contributing noise processes.

Additionally, the signal-to-noise-ratio (SNR) is determined from narrowband demodulation (ZoomFFT, HF2LI Zürich Instruments) at a frequency span of 14.4 kHz around the resonance frequency of interest. The results for driving the fundamental mode at an amplitude of 253 nm are presented in Figure 8b.1 and Figure 8b.2, yielding a SNR of the OBD sensor of 122.4 dB and of the charge sensor of 120.0 dB. The results for driving the fifth mode at an amplitude of 1.62 nm are presented in Figure 8b.3 and Figure 8b.4 yielding a SNR of the OBD sensor of 102.8 dB and of the charge sensor of 110.9 dB. The SNR has been calculated from the difference between the fitted noise floor and the peak at the signal of interest. Maximum signal levels have been shifted to 0 dB and the horizontal blue line indicates the fitted noise floor.

Bimodal AFM application

Experimental setup

The experimental setup consists of an unaltered NT-MDT NTegra Prima AFM fitted with a custom cantilever holder to mount the piezoelectric cantilever used in this work. The signal access module (SAM) of the AFM provides the relevant inputs and outputs to change the feedback signal from the OBD sensor measurement to charge measurement. Approach and retract curves as well as all AFM imaging data were recorded using two synchronized Zürich Instrument HF2LI lock-in amplifiers for which custom imaging scripts were written. Therefore, it is possible to obtain AFM images relating to either sensor while z-axis feedback is performed on one specific sensor.

The samples under investigation are a TGZ1 silicon calibration grating available from NT-MDT with periodic rectangular features of heights $h = 21.6 \pm 1.5$ nm and a blend of polystyrene (PS) and polyolefin elastomer (ethylene-octene copolymer) (LDPE) available from Bruker (PS-LDPE-12M). The PS regions of the sample have elastic modulus numbers around 2 GPa, while the LDPE regions have elastic modulus numbers around 0.1 GPa making it a widely used standard to image material contrast. The scan speed was set to 20 μm/s at an area of 10 μm × 10 μm.

Approach curves

Approach and retract curves have been performed on the (stiff) TGZ1 calibration grating where the fundamental and the fifth modes are actively driven and the amplitude of the fundamental mode obtained from the OBD sensor is used for z-feedback. As can be seen from Figure 9a,b,e,f, the fundamental and higher eigenmode amplitudes measured with either OBD sensor or charge sensor show a similar trend for small drive voltages (free-air amplitudes) which resembles approach and retract curves in one of the two stable branches of the cantilever [36]. However, when the drive voltage of the fundamental mode is increased, the approach curve is characterized by the well known transition between the low and high amplitude branch as can be seen in Figure 9c and Figure 9g. It is worth noting that for this case, the fifth mode amplitudes obtained from the OBD sensor and from the charge sensor form a hysteresis loop and more significantly show inverse behavior for small separations (compare Figure 9d and Figure 9h). As such, the deflection of the fifth mode increases and the strain decreases when the cantilever oscillation state jumps from one amplitude branch into the other.

Imaging TGZ1 calibration grating

The TGZ1 calibration grating was imaged alternating between the OBD sensor and the charge sensor as the topography feedback signal in order to verify the suitability of imaging with charge. It can be seen from Figure 10 that due to the excellent SNR of the charge sensor the topography obtained from either of the two methods yields identical quality. Moreover, it can be noted that for stiff samples like the TGZ1, the overall conservative interactions result in no difference between the amplitude of the actual feedback signal and the auxiliary signal (compare Figure 10b with Figure 10c and Figure 10e with Figure 10f).

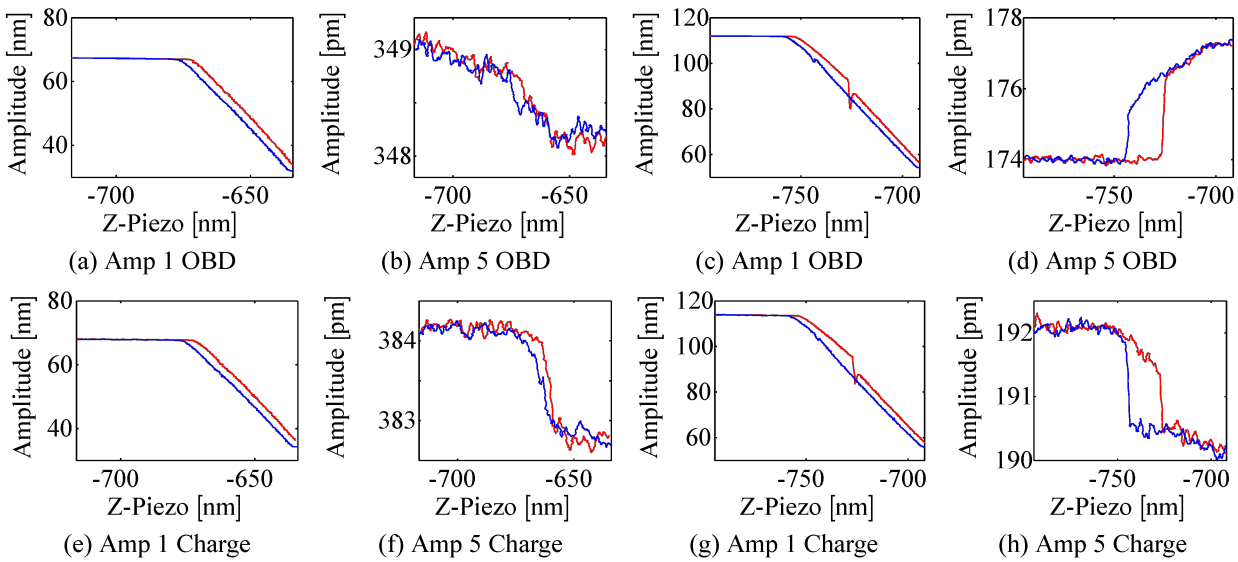

Figure 9: Approach (red, −) and retract (blue, −) curves obtained on a TGZ1 calibration grating with OBD sensor used for feedback: (a)–(d) fundamental and fifth mode amplitude measured with the OBD sensor and (e)–(h) fundamental and fifth mode amplitude measured with the charge sensor.

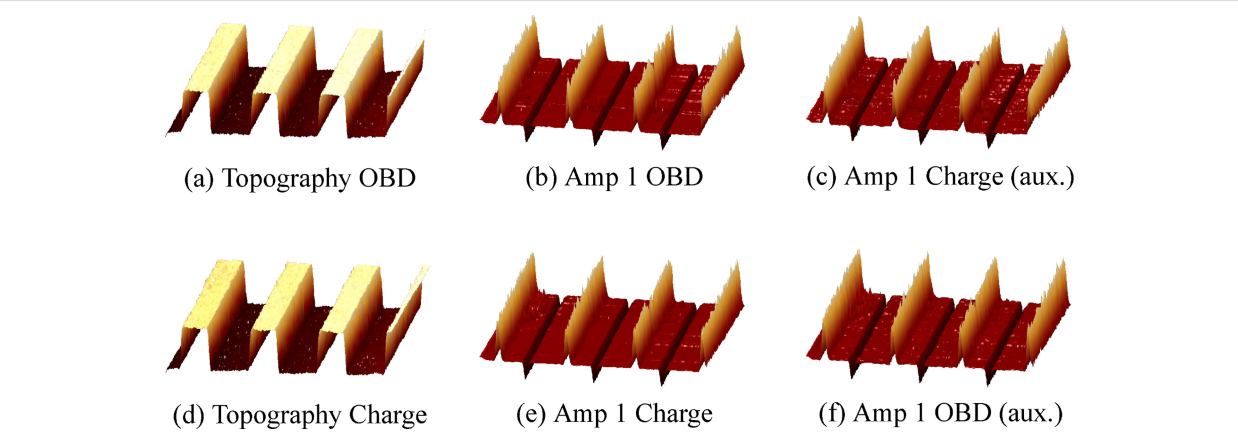

Figure 10: AFM Experiment on a TGZ1 calibration grating showing the 3D images of topography and fundamental mode amplitudes for (a)–(c) using the OBD sensor for feedback and (d)–(f) the charge sensor for feedback. Note, the respective auxiliary signal plotted in the third column shows no difference to the feedback signal plotted in the second column.

For both experiments, the interaction was mostly attractive as can be seen from the fundamental mode phase image (not shown) and only shows repulsive interaction at the rising edges of the features.

Bimodal AFM on PS/LPDE

A two component polymer as described in section Experimental setup was imaged using bimodal AFM, i.e., by actively driving the first and fifth eigenmodes of the piezoelectric cantilever. While the *z*-axis feedback controller maintains a constant amplitude at the fundamental frequency by commanding the *z*-actuator, the higher mode is left uncontrolled and can respond freely to sample features. As such, the higher eigenmode phase contrast is often used to distinguish between material properties [37]. The experimental results are presented in Figure 11; a plane level algorithm has been applied to the topography images. The first row represents a bimodal experiment with the OBD sensor and the second row shows bimodal imaging of the same area with the charge sensor. For clarity, the phase of the first and fifth modes for each sensor have been shifted such that $\phi_{1,L/Q}(f_1)=\phi_{2,L/Q}(f_2)=90°$ and as such $\phi_{1/2,L/Q}>90°$ indicates a net attractive imaging regime and $\phi_{1/2,L/Q}<90°$ indicates a net repulsive imaging regime. We note that the first mode interaction using either sensor is attractive on the LPDE islands and repulsive on the surrounding PS matrix. In contrast, the fifth mode interaction is consistently attractive across both

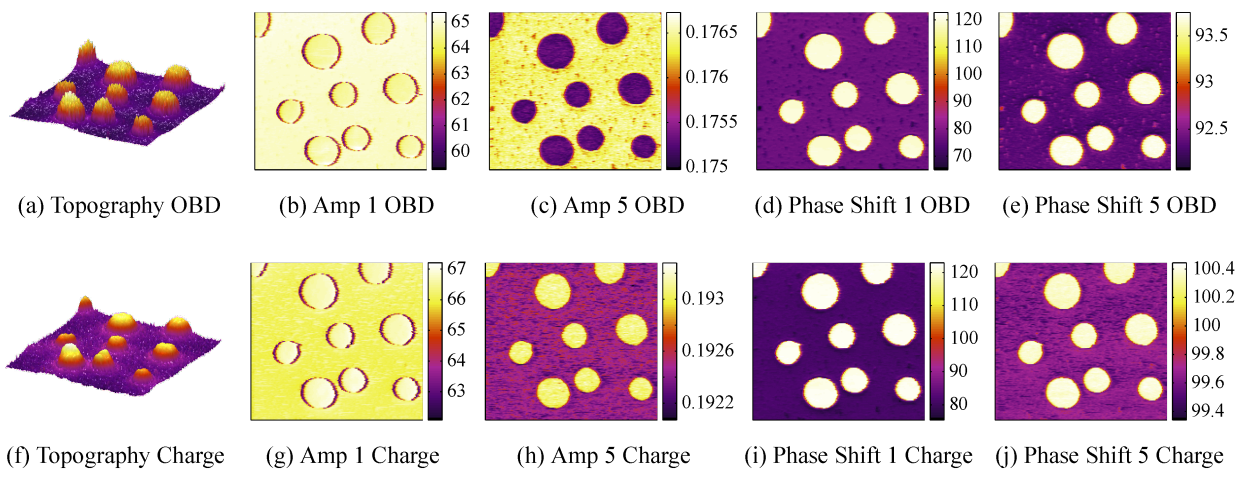

Figure 11: Bimodal experiment with the first and fifth eigenmode of the piezoelectric cantilever on a PS/LPDE sample showing amplitude in [nm] and phase in [°] using (a)–(e) the OBD sensor and (f)–(j) the charge sensor. Note the contrast reversal of the amplitude of the fifth mode between the OBD and charge sensor.

features with either sensor. A clear contrast between the two polymer regions can be observed in the fifth mode phase image for either sensor. Comparing the amplitude image on the fifth mode, the contrast reversal discussed in section Approach curves is clearly visible.

Conclusion

Experimental results using monomodal and bimodal atomic force microscopy with the first and fifth eigenmode of a piezoelectric cantilever on a variety of samples validate that the self-sensing scheme proposed in this work achieves remarkable signal-to-noise ratios and can therefore be used to provide both the feedback signal for topography imaging on the fundamental mode and phase imaging on the higher eigenmode. The charge sensor as well as the feedthrough compensation are implemented in analog using high-bandwidth surface mount components. In this approach, due to small circuit mismatches, the feedthrough has to be canceled for each mode separately to achieve the best dynamic range which is necessary for tapping-mode AFM. The inherent self-sensing capability of a single piezoelectric layer enables the omission of the commonly used optical lever method, promoting the potential downsizing of an AFM. In future work, the authors aim to extend this work to the point where quantitative material properties can be extracted using a multimode charge sensor. Furthermore, we aim to implement an automatic feedthrough compensation scheme using disturbance observer concepts which would eliminate the need for individual analog compensation circuits. Lastly, we note that not all eigenmodes are equally observable with the present cantilever geometry and location of the piezoelectric layer. In order to observe a specific higher eigenmode, a modal optimization routine should be employed which places individual piezoelectric transducers at locations where that mode shows a uniform and maximum strain distribution. Therefore, future work will aim at exploring optimal cantilever geometry and piezoelectric layer layout to maximize the deflection to strain sensitivity at each mode.

Acknowledgements

This research was performed in the Laboratory for Dynamics and Control of Nanosystems (LDCN) at The University of Newcastle, Callaghan, NSW, Australia. The authors would like to acknowledge the support from the University of Newcastle, the Australian Research Council (ARC) and the CSIRO, Clayton, VIC, Australia.

References

1. García, R.; Herruzo, E. T. *Nat. Nanotechnol.* **2012,** *7,* 217–226. doi:10.1038/nnano.2012.38
2. Herruzo, E. T.; Perrino, A. P.; Garcia, R. *Nat. Commun.* **2014,** *5,* 3126. doi:10.1038/ncomms4126
3. Forchheimer, D.; Forchheimer, R.; Haviland, D. B. *Nat. Commun.* **2015,** *6,* 6270. doi:10.1038/ncomms7270
4. Han, W.; Lindsay, S. M.; Jing, T. *Appl. Phys. Lett.* **1996,** *69,* 4111–4113. doi:10.1063/1.117835
5. Umeda, N.; Ishizaki, S.; Uwai, H. *J. Vac. Sci. Technol., B* **1991,** *9,* 1318–1322. doi:10.1116/1.585187
6. Fantner, G. E.; Burns, D. J.; Belcher, A. M.; Rangelow, I. W.; Youcef-Toumi, K. *J. Dyn. Syst., Meas., Control* **2009,** *131,* 061104. doi:10.1115/1.4000378
7. Yamanaka, K.; Nakano, S. *Jpn. J. Appl. Phys., Part 1* **1996,** *35,* 3787–3792. doi:10.1143/JJAP.35.3787

8. Indermühle, P.-F.; Schürmann, G.; Racine, G.-A.; de Rooij, N. F. *Sens. Actuators, A* **1997,** *60,* 186–190. doi:10.1016/S0924-4247(96)01440-9
9. Meyer, G.; Amer, N. M. *Appl. Phys. Lett.* **1988,** *53,* 1045–1047. doi:10.1063/1.100061
10. Kassies, R.; van der Werf, K. O.; Bennink, M. L.; Otto, C. *Rev. Sci. Instrum.* **2004,** *75,* 689–693. doi:10.1063/1.1646767
11. Enning, R.; Ziegler, D.; Nievergelt, A.; Friedlos, R.; Venkataramani, K.; Stemmer, A. *Rev. Sci. Instrum.* **2011,** *82,* 043705. doi:10.1063/1.3575322
12. Nievergelt, A. P.; Adams, J. D.; Odermatt, P. D.; Fantner, G. E. *Beilstein J. Nanotechnol.* **2014,** *5,* 2459–2467. doi:10.3762/bjnano.5.255
13. Göddenhenrich, T.; Lemke, H.; Hartmann, U.; Heiden, C. *J. Vac. Sci. Technol., A* **1990,** *8,* 383–387. doi:10.1116/1.576401
14. Tortonese, M.; Barrett, R. C.; Quate, C. F. *Appl. Phys. Lett.* **1993,** *62,* 834–836. doi:10.1063/1.108593
15. Itoh, T.; Suga, T. *Nanotechnology* **1993,** *4,* 218. doi:10.1088/0957-4484/4/4/007
16. Sahoo, D. R.; Sebastian, A.; Häberle, W.; Pozidis, H.; Eleftheriou, E. *Nanotechnology* **2011,** *22,* 145501. doi:10.1088/0957-4484/22/14/145501
17. Lee, J. E.-Y.; Seshia, A. A. *Sens. Actuators, A* **2009,** *156,* 36–42. doi:10.1016/j.sna.2009.02.005
18. Ruppert, M. G.; Moheimani, S. O. R. *Rev. Sci. Instrum.* **2013,** *84,* 125006. doi:10.1063/1.4841855
19. Ruppert, M. G.; Moheimani, S. O. R. Novel Reciprocal Self-Sensing Techniques for Tapping-Mode Atomic Force Microscopy. In *Proc. 19th IFAC World Congress,* IFAC, Cape Town, South Africa; 2014; pp 7474–7479.
20. Meitzler, A. H.; Tiersten, H. F.; Warner, A. W.; Berlincourt, D.; Coquin, G. A. *ANSI/IEEE Std 176-1987;* 1988. doi:10.1109/IEEESTD.1988.79638
21. Dosch, J. J.; Inman, D. J.; Garcia, E. *J. Intell. Mater. Syst. Struct.* **1992,** *3,* 166–185. doi:10.1177/1045389X9200300109
22. Crawley, E. F.; De Luis, J. *AIAA J.* **1987,** *25,* 1373–1385. doi:10.2514/3.9792
23. Fuller, C. C.; Elliott, S.; Nelson, P. A. *Active control of vibration;* Academic Press, 1996.
24. Moheimani, S. O. R.; Fleming, A. J. *Piezoelectric Transducers for Vibration Control and Damping;* Springer-Verlag London Limited, 2006.
25. de Silva, C. W. *Vibration - Fundamentals and Practice;* CRC Press, 2000.
26. Salehi-Khojin, A.; Bashash, S.; Jalili, N. *J. Micromech. Microeng.* **2008,** *18,* 085008. doi:10.1088/0960-1317/18/8/085008
27. Shamsudhin, N.; Rothuizen, H.; Nelson, B. J.; Sebastian, A. Multi-frequency atomic force microscopy: A system-theoretic approach. In *Proc. 19th IFAC World Congress,* IFAC, Cape Town, South Africa; 2014.
28. Karvinen, K. S.; Ruppert, M. G.; Mahata, K.; Moheimani, S. O. R. *IEEE Trans. Nanotechnol.* **2014,** *13,* 1257–1265. doi:10.1109/TNANO.2014.2360878
29. Sadewasser, S.; Villanueva, G.; Plaza, J. A. *Rev. Sci. Instrum.* **2006,** *77,* 073703. doi:10.1063/1.2219738
30. McKelvey, T. Subspace methods for frequency domain data. In *Proc. of the American Control Conference,* IEEE; 2004; pp 673–678.
31. Alexander, S.; Hellemans, L.; Marti, O.; Schneir, J.; Elings, V.; Hansma, P. K.; Longmire, M.; Gurley, J. *J. Appl. Phys.* **1989,** *65,* 164–167. doi:10.1063/1.342563
32. Proksch, R.; Schäffer, T. E.; Cleveland, J. P.; Callahan, R. C.; Viani, M. B. *Nanotechnology* **2004,** *15,* 1344. doi:10.1088/0957-4484/15/9/039
33. Kiracofe, D.; Raman, A. *J. Appl. Phys.* **2010,** *107,* 033506. doi:10.1063/1.3284206
34. Butt, H.-J.; Jaschke, M. *Nanotechnology* **1995,** *6,* 1. doi:10.1088/0957-4484/6/1/001
35. Dukic, M.; Adams, J. D.; Fantner, G. E. *Sci. Rep.* **2015,** *5,* 16393. doi:10.1038/srep16393
36. García, R.; Pérez, R. *Surf. Sci. Rep.* **2002,** *47,* 197–301. doi:10.1016/S0167-5729(02)00077-8
37. Martínez, N. F.; Patil, S.; Lozano, J. R.; García, R. *Appl. Phys. Lett.* **2006,** *89,* 153115. doi:10.1063/1.2360894

License and Terms

BEILSTEIN JOURNAL OF NANOTECHNOLOGY

Contact-free experimental determination of the static flexural spring constant of cantilever sensors using a microfluidic force tool

John D. Parkin and Georg Hähner*

Full Research Paper

Open Access

Address:
EaStCHEM School of Chemistry, University of St. Andrews, North Haugh, St. Andrews, KY16 9ST, UK

Email:
Georg Hähner* - gh23@st-andrews.ac.uk

* Corresponding author

Keywords:
AFM; cantilever sensors; microfluidic force tool; spring constant

Beilstein J. Nanotechnol. **2016,** *7,* 492–500.
doi:10.3762/bjnano.7.43

Received: 18 November 2015
Accepted: 12 March 2016
Published: 30 March 2016

This article is part of the Thematic Series "Advanced atomic force microscopy techniques IV".

Guest Editor: T. Glatzel

Abstract

Micro- and nanocantilevers are employed in atomic force microscopy (AFM) and in micro- and nanoelectromechanical systems (MEMS and NEMS) as sensing elements. They enable nanomechanical measurements, are essential for the characterization of nanomaterials, and form an integral part of many nanoscale devices. Despite the fact that numerous methods described in the literature can be applied to determine the static flexural spring constant of micro- and nanocantilever sensors, experimental techniques that do not require contact between the sensor and a surface at some point during the calibration process are still the exception rather than the rule. We describe a noncontact method using a microfluidic force tool that produces accurate forces and demonstrate that this, in combination with a thermal noise spectrum, can provide the static flexural spring constant for cantilever sensors of different geometric shapes over a wide range of spring constant values (≈0.8–160 N/m).

Introduction

Micro- and nanocantilevers are routinely employed as probes down to the nanometer scale. In atomic force microscopy (AFM), microcantilever sensors are used, for example, to image the topography of surfaces and to map mechanical properties with nanometer resolution [1-3]. In addition, so-called force curves can reveal information about the interaction between the AFM tip and the surface, thus providing information about local interactions [4]. Cantilever structures also form an integral part of micro- and nanoelectromechanical systems (MEMS and NEMS) [5-7] and can be employed as freestanding sensors [8-13].

In many applications where a cantilever-type sensor is involved, the calibration of the sensor stiffness (spring constant, k) is a prerequisite for obtaining quantitative data. Several methods describing how the static flexural spring constant can be calibrated have been reported in the literature, in particular in relation to AFM [14,15]. However, many of the experimental ap-

proaches have drawbacks or limitations and cannot easily be extended to an array of cantilevers. One of the major drawbacks of many of the available experimental techniques is the requisite contact between the probe and surface during the calibration process, which can damage the AFM tip. Therefore, methods that do not involve any contact are highly desirable.

For softer cantilevers (k < 5 N/m) and simple geometries, such as rectangular-shaped beams, several calibration methods have been demonstrated to work well [16-18]. However, for stiff cantilevers (k > 20 N/m) and "unusual" geometric shapes, the determination of the spring constant is still a challenge [14,19]. The most direct method for the determination of the static spring constant comprises the application of a well-defined force to the sensor and measuring the resulting deflection. One way to do this is by pressing the cantilever against a balance [20,21] or a precalibrated cantilever [22,23]. However, the disadvantage is that the tip is in mechanical contact with a hard surface and can therefore be damaged [24,25]. Furthermore, these methods are appropriate for cantilevers with a spring constant typically greater than ≈1 N/m [20] and less than ≈10 N/m [26]. The application of forces other than mechanical force, such as magnetic or electrostatic force, requires modification of the cantilever, for example, with a magnetic coating. This can pose a problem in itself because of the small dimensions of the cantilever structure. In addition, the coating can cause stress, resulting in a static deflection of the sensor beam. It is therefore desirable to have a universal force tool that can exert well-defined forces on all types of cantilever sensors independent from their physical and chemical properties. A microfluidic flow tool has been previously employed in connection with cantilever spring constant determination [27-30], and it was shown that forces due to the flow from a microfluidic channel can be exploited to determine the dynamic flexural spring constants [29] as well as the torsional and lateral spring constants [30]. In the following, we describe a method to determine the static flexural spring constant for cantilevers of any geometric shape. The approach can be applied to very soft as well as very stiff cantilevers. We demonstrate that a microfluidic flow can provide accurate forces and allows the static spring constant of cantilever sensors to be determined with high precision and without any contact between the sensor and a surface. We show the applicability of the method for spring constants in the range of 0.8 N/m to ≈160 N/m.

Method

Determination of the static flexural spring constant

The static flexural spring constant depends on the force distribution, $\tilde{F}$, applied to the cantilever sensor as well as the position, x, along the beam where the resulting deflection, $\tilde{d}$, is measured [31,32]. The corresponding general expression for the static spring constant, $k_{\tilde{F},s}$, is:

$$k_{\tilde{F},s} = \frac{\tilde{F}_{\text{total}}}{\tilde{d}_L}, \tag{1}$$

where $\tilde{F}_{\text{total}} = \int_0^L \tilde{F}(x)dx$ is the total force exerted by the force distribution, $\tilde{F}(x)$, over the cantilever length, L, and $\tilde{d}_L$ is the resulting static deflection of the cantilever measured at position L.

In AFM, a point load $\check{F}$ applied at the position of the probe tip results in a deflection $\check{d}_L$ of the cantilever that is typically measured at or close to the free end of the beam. The static spring constant resulting from this point load, $\check{k}_s$, is therefore given by

$$\check{k}_s = \frac{\check{F}}{\check{d}_L}. \tag{2}$$

The spring constant for any force distribution, $k_{\tilde{F},s}$, can be converted to an equivalent spring constant for a point load, $\check{k}_s$, applied at the position of the probe tip by a generalization of the procedure described in [31]. In general, there is no analytical expression for the conversion factor $\beta(\check{k}_s = \beta \cdot k_{\tilde{F},s})$, but it can be determined numerically. Experimentally measuring the spring constant $k_{\tilde{F},s}$ therefore allows $\check{k}_s$ to be determined if the conversion factor β is known.

The static spring constant for a point load, $\check{k}_s$, can be obtained from the dynamic spring constant of the first flexural mode $\check{k}_{d,1}$ if the dynamic-to-static spring constant conversion factor γ is known [32,33]: $\check{k}_s = \gamma^{-1} \cdot \check{k}_{d,1}$. The dynamic spring constant is related to the mean-squared displacement, $\langle z^2 \rangle$, of the fundamental flexural mode of the cantilever: $\check{k}_{d,1} = k_B T / \langle z^2 \rangle$ [16], where k_B is the Boltzmann constant, and T is the absolute temperature. The mean-squared displacement $\langle z^2 \rangle$ is obtained from the area under the thermal resonance curve. Combining these equations gives

$$\check{k}_s = \gamma^{-1} \frac{k_B T}{\langle z_V^2 \rangle \sigma_1^2}, \tag{3}$$

where z_V is the photodiode signal in native units of the instrument (volts) and σ_1 is the optical lever sensitivity for thermal oscillations [34,35]. Knowledge of σ_1 is required for calibration of the spring constant via the thermal noise method [16]. It can be experimentally obtained, for example, from a force curve.

Similarly, the measured spring constant for a force distribution $\tilde{F}$ is

$$k_{\tilde{F},s} = \frac{\tilde{F}_{\text{total}}}{d_{\text{V}}\sigma_2}, \tag{4}$$

where d_{V} is the deflection in the native units of the instrument (volts) and σ_2 is the optical lever sensitivity for bending under the force distribution $\tilde{F}(x)$. Note that even without knowledge of σ_1 and σ_2, the dynamic-to-static sensitivity ratio $\alpha = \sigma_1/\sigma_2$ can still be theoretically obtained. This conversion is similar to the dynamic-to-static optical lever sensitivity conversion required in the thermal noise method [33].

From the photodiode signal, the deflection for a total force and the peak area under a thermal noise curve are obtained in units of volts and volts squared, respectively. The spring constant $\check{k}_s$ can then be determined without knowledge of the individual optical lever sensitivities σ_1 and σ_2 by combining Equation 3 and Equation 4 and rearranging them as

$$\check{k}_s = \frac{\langle z_{\text{V}}^2 \rangle}{k_{\text{B}}T} \frac{\tilde{F}_{\text{total}}^2}{d_{\text{V}}^2} \alpha^2\beta^2\gamma. \tag{5}$$

Experimental

Setup and measurements

Experiments were performed with a commercial Bruker Dimension FastScan AFM system (Bruker, Santa Barbara, CA, USA). In our setup, a custom-built, smooth parallel plate microchannel of height ≈100 μm and length 4.5 mm was used [27,29,30]. An accurate value of the channel height was obtained by contacting the free end of a cantilever on the bottom surface of the channel with the channel aligned parallel to the cantilever length and measuring the distance to the top of the channel by lifting the cantilever with the AFM microstepper motor until it contacted the top surface of the channel. This gave a value of 106 μm.

For the measurements, the channel was fixed on the sample stage of the AFM and positioned such that fluid flow from its exit interacted with the cantilever as illustrated in Figure 1. The channel was aligned such that the free end of the cantilever was level with the edge of the channel and 100 μm above the channel exit. This alignment was chosen because of the ease of reproducibility.

Nitrogen gas was used as the working fluid. Pressure differences were applied to the microchannel to drive the flow, establishing stable Poiseuille velocity profiles [27]. The maximum pressure applied to the channel depended on the cantilever studied. The highest pressure used was ≈3.5 kPa, resulting in a nitrogen velocity value of about ≈62 m/s in the channel mid-line [28], corresponding to a laminar, incompressible flow [36].

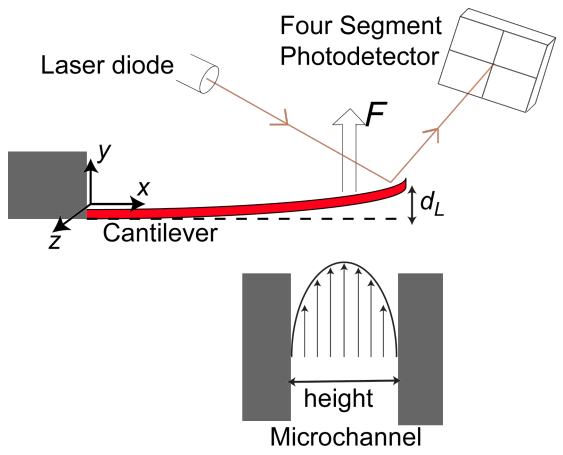

Figure 1: Schematic side view of the microchannel with Poiseuille profile of the fluid and a cantilever that bends due to forces exerted by the fluid.

The forces applied to the cantilever by the fluid flow cause a static flexural bending [30]. The bending of the cantilever as a function of fluid velocity was recorded by reading out the photodiode signal of the AFM with a self-coded LabVIEW routine via a signal access module (SAM-V, Bruker, CA, USA) and an external interface (USB-6251, National Instruments). The power spectral density of the thermal noise was obtained with the Bruker software. The peak area, resonant frequency and *Q*-factor of the thermal noise spectra were determined with a self-coded MATLAB routine by fitting Lorentzian curves to the resonance peaks of the first flexural modes. Force curves, to calibrate the deflection sensitivity (σ_1) for the thermal noise method, were recorded on clean sapphire substrates.

Cantilevers studied

To test our approach, a range of commercially available cantilevers were studied (see Figure 2). RA2 and RC2 are tipless cantilevers (Mikromasch, Tallinn, Estonia) while OTESPA, Tap150, NCHV, Tap525, and Fastscan-C all have tips attached (Bruker, Santa Barbara, USA). Some cantilevers had metal coatings to increase the reflectivity of the laser: Tap150, Tap525 and OTESPA were aluminum-coated and Fastscan-C was gold-coated. RA2, RC2 and NCHV had no metal coating.

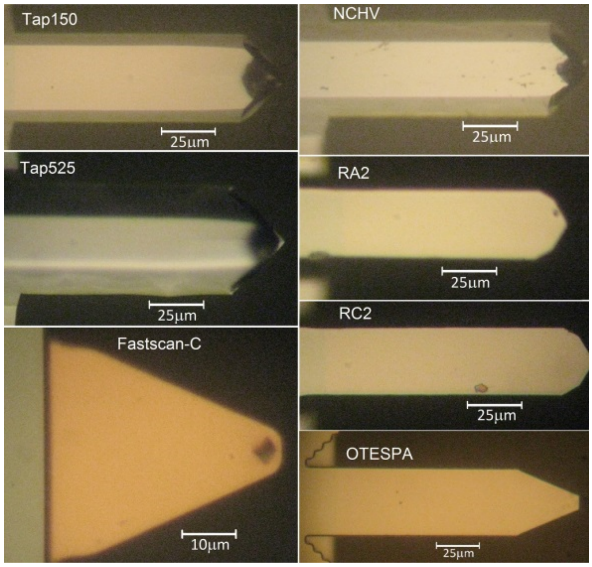

Figure 2: Optical images of the AFM cantilevers studied showing their plan view geometries (view from the tip side). Details of the cantilever dimensions are given in the Results section.

Results

Cantilever dimensions, resonant frequency and *Q*-factor

Table 1 summarizes the geometrical dimensions, resonant frequency and *Q*-factor of the cantilevers studied. Here, "Nominal" refers to the information provided by the manufacturers. The actual plan view dimensions of all microcantilevers were determined with an Olympus optical microscope. Some of the cantilevers had a trapezoidal cross-section (see Figure 2), in which case both the width at the top and the bottom were determined.

Determination of the force distribution and the conversion factors α, β, and γ

To provide information about the interaction between the fluid flow escaping from the microchannel and the cantilevers, we performed finite element method simulations with COMSOL Multiphysics [37]. The mesh independence of the results was confirmed by mesh refinement. The forces applied to the cantilever by the fluid flow were extracted from the simulations. Figure 3 displays the force per unit length for different fluid speeds at the center of the microchannel applied to a cantilever using the example of NCHV (see Table 1).

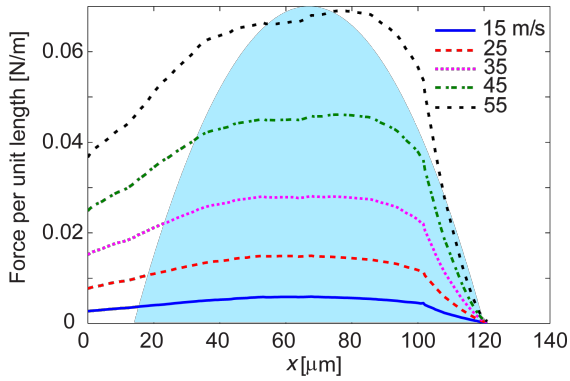

Figure 3: Force per unit length as a function of the fluid speed experienced by cantilever NCHV. The fixed end of the cantilever is at $x = 0$. The shaded area is a sketch of the fluid speed profile escaping the channel and also indicates the boundaries of the microchannel exit along the *x*-axis.

The total force $\tilde{F}_{\text{total}}$ experienced by the cantilever sensor was obtained by integrating the force distribution over the cantilever length. The conversion factor α was determined with a self-

Table 1: Nominal and experimentally determined geometric dimensions (width, *w*, thickness, *t*, full length, *L*, and length of picketed end, *l*, all given in µm), fundamental frequency, *f* (kHz), and *Q*-factor of the cantilevers studied.

	RA2	RC2	OTESPA	Tap150	NCHV	Tap525	Fastscan-C
w_{nominal}	35	35	40	30	40	40	40 (footprint)
$w_{\text{exp,top}}$	31.0	31.0	42.5	40.0	42.0	52.0	42.0 (fixed end) 6.0 (free end)
$w_{\text{exp,bottom}}$	31.0	31.0	41.0	30.0	25.5	24.0	42.0 (fixed end) 6.0 (free end)
t_{nominal}	2	2	3.7	1.85	4	6.25	0.3
L_{nominal}	110	130	160	125	125	125	40
L_{exp}	110.0	124.5	149.0	124.0	121.0	123.0	44.5
l_{exp}	15.0	15.0	40.0	15.0	19.0	26.0	–
$f_{1,\text{nominal}}$	210	150	300	150	320	525	300
$f_{1,\text{exp}}$	231.658	162.283	297.540	173.952	324.167	512.316	210.916
Q-factor	268	222	470	262	439	773	102

coded MATLAB routine. This conversion factor is similar in nature to a factor that is also required for calibration with the thermal noise method [33].

For the conversion factor β, the static deflection of the cantilever beam as a function of the force profile for different fluid speeds and for the force profiles obtained from the simulations was determined with a self-coded MATLAB routine following the procedures described in [31,32]. In addition, the bent shape was also determined for a point load applied at the free end of the cantilever.

The conversion factors α and β depend on the force distribution. They are therefore dependent on the fluid speed if the force distribution changes with speed. Figure 4 displays α and β for some of the cantilevers studied and for fluid speeds above 15 m/s. The conversion factors are fairly constant for all cantilevers and for the alignment chosen in our experiment. The behavior of the conversion factors for the cantilevers not shown (RA2, RC2, Tap150) was very similar to that shown for NCHV and Tap525.

In Table 2, the mean values of α and β together with their standard deviations for the speed range above 15 m/s are reported. The standard deviation of α is well below 1% over this range for all cantilevers, while it is typically less than 1% for β with the exception of FastScan-C (2.1%) and OTESPA (2.3%), which are the most picketed cantilevers studied. The conversion factor γ, also given in Table 2, is identical to the one required in the thermal noise calibration method. We determined γ for the different geometries of the cantilevers with self-coded MATLAB routines. For many cantilever geometries, this can also be found in the literature (see for example [33]). The geometric data reported in Table 1 was used for the calculations of all conversion factors.

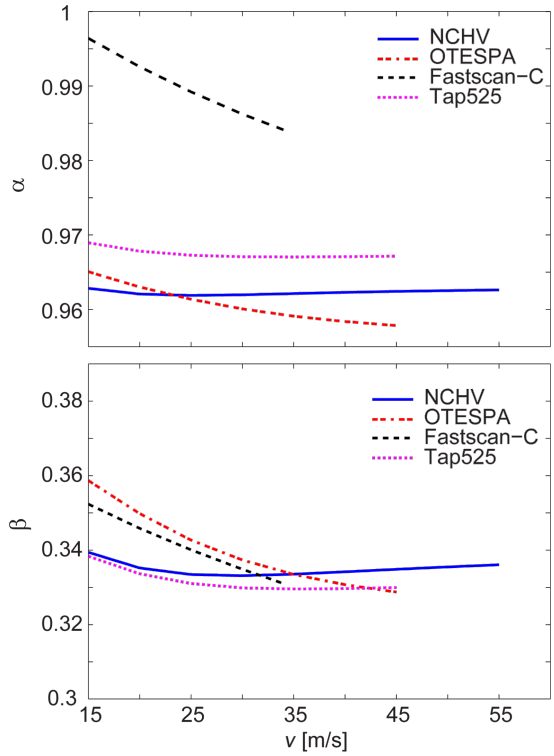

Figure 4: Fluid-flow-dependent conversion factors α and β for some of the cantilevers studied. The conversion factors of cantilevers RA2, RC2 and Tap150 (not shown) showed a behavior very similar to that of NCHV and Tap525.

Deflection under fluid flow and determination of the static flexural spring constant

Figure 5 shows a typical deflection curve for cantilever NCHV as a function of the fluid flow speed. The pressure applied to the channel, and hence the fluid flow speed, was first increased and then decreased in the experiment. A slight hysteresis can be observed in the deflection curve for fluid speeds below ≈15 m/s, corresponding to pressure values of <0.8 kPa.

Table 2: Conversion factors with their standard deviations (Δ), and nominal (manufacturer quoted) and experimentally determined spring constant values. No individual error estimates are stated for the thermal noise measurements but are typically found to be in the range of 10–20% [14,34].

	RA2	RC2	OTESPA	Tap150	NCHV	Tap525	Fastscan-C
χ	1.1290	1.1236	1.1916	1.1237	1.1378	1.1620	1.1801
α	0.9773	0.9762	0.9606	0.9630	0.9623	0.9674	0.9355
Δα	0.0002	0.0002	0.0021	0.0004	0.0003	0.0005	0.0074
β	0.3541	0.3811	0.3385	0.3481	0.3342	0.3310	0.3423
Δβ	0.0012	0.0013	0.0078	0.0024	0.0011	0.0019	0.0072
γ	1.0490	1.0470	1.0740	1.0470	1.0530	1.0630	1.0900
k_{nom}	7.5	4.5	26	5	42	200	0.8
(k_{min}; k_{max})	(3.5;12.5)	(2.5; 8.5)	(8.4; 57)	(2.5; 10)	(20; 80)	(100; 400)	(0.4; 1.2)
$\check{k}_{s,thermal}$	7.7	5.26	26.5	10.3	36.7	123.8	0.63
$\check{k}_s$	8.5 ± 0.3	4.35 ± 0.09	33.1 ± 2.4	8.3 ± 0.3	42.4 ± 2.1	154.2 ± 2.4	0.88 ± 0.07

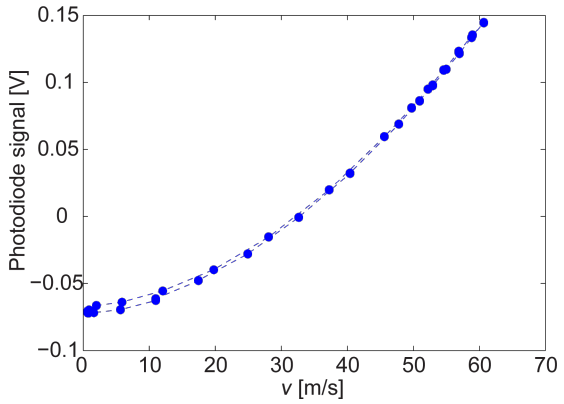

Figure 5: Cantilever deflection of NCHV under fluid flow from the microchannel measured at the free end of the cantilever.

To properly normalize the curve to zero deflection, the photodiode signal value at very low speeds was subtracted. Subsequently, Equation 3 was used to determine $\check{k}_s$. The result is shown in Figure 6. The highest deflection of NCHV was ≈52 nm in our experiments and therefore well within the linear response range of the cantilever [38].

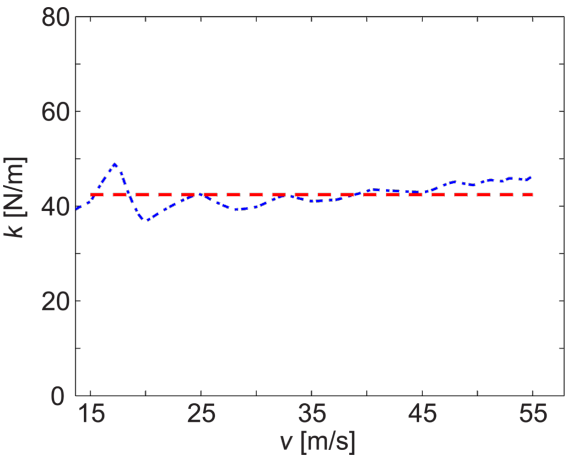

Figure 6: Experimentally determined $\check{k}_s$ value for cantilever NCHV. The dashed line indicates the mean $\check{k}_s$ value for fluid speeds of 15–55 m/s.

This procedure was applied to all cantilevers studied. Table 2 summarizes the resulting spring constant values $\check{k}_s$ for fluid speeds above ≈15 m/s, together with their standard deviations.

For comparison, the spring constant values obtained by the thermal noise method (as described in [33]) are also provided, calculated according to

$$\check{k}_{s,\text{thermal}} = \frac{1}{\gamma\chi^2}\frac{k_\text{B}T}{\langle z^2\rangle}. \tag{6}$$

The dynamic-to-static optical lever sensitivity ratio, χ, was obtained with a self-coded MATLAB routine and was calculated for cantilevers with the geometrical dimensions reported in Table 1.

Discussion

Force profiles and cantilever deflection

The force profiles and the corresponding force per unit length exerted on the cantilevers by the fluid flow depend on the geometry of the beam and its alignment, (i.e., the position of the cantilever relative to the channel exit). In the case of a constant force distribution, the force profile would largely mirror variations in the cantilever width. As can be seen in Figure 3, the profiles show some deviation from this behavior. The length of some of the cantilevers (such as NCHV) is greater than the channel height and hence the force experienced by the cantilever decreases towards its fixed end. The picket-shaped end of cantilever NCHV, however, is clearly reflected in the force profiles displayed in Figure 3.

It is noteworthy that the position of the maximum force per unit length does not coincide with the center of the channel. This is also due to the chosen alignment in our experiment: the fluid escaping the channel must flow around the cantilever structure and the chip holding the cantilever. The fluid does not flow underneath the chip due to the small (≈100 µm) distance between the bottom of the chip and top edge of the microchannel and moves away from the vertical face of the cantilever chip. This moves the maximum force in the direction of the free end.

The presence of a tip on the cantilever was found to have negligible influence on the force profile and hence the total applied force: simulations of the forces applied to the cantilevers showed no significant difference in the total applied force when simulated with and without a tip. This should not be a surprise as the main fluidic force experienced by the cantilever is due to plan-view-dependent drag as opposed to viscous shear, and the former is not significantly influenced by the presence of the tip.

The reason for the observed hysteresis in the speed-dependent deflection (Figure 5) is not entirely clear. Some cantilevers showed no hysteresis at all while others showed more pronounced hysteresis, in particular Tap525. A change in the alignment of the cantilever relative to the channel had no effect on the observed phenomenon. The hysteresis could be related to changes in the humidity surrounding the cantilever as the fluid flow of dry nitrogen from the microchannel acts to decrease

humidity with increasing fluid speed [8]. The metal coating on some of the cantilevers might also delaminate or let water enter, inducing some stress and causing additional bending, which is removed when nitrogen from the channel decreases the surrounding humidity. Checking the quality factors Q and the resonance frequencies of the resonance peaks for very low flow speeds at the beginning of the measurements and at the end did not reveal significant differences. If there is some stress induced, it is certainly small and not revealed by the Q-factor or the resonance frequency value.

Conversion factors α, β and γ

The conversion factor γ, which relates the dynamic and static spring constants for a point load, is identical to one of the conversion factors required in relation to the thermal noise method. α and β are specific for our experiment and setup. α is a factor in relation to a dynamic-to-static optical lever sensitivity conversion. It is similar to the factor χ required for the thermal noise method [34]. The term "dynamic" in both cases refers to thermal oscillations and the first flexural mode. The term "static" refers to the optical lever sensitivity (in relation to the application of a point load at the free end in case of χ) and is related to the optical sensitivity linked to the force distribution resulting from the microchannel flow in case of α. χ and α are a measure of how much the cantilever bends at the free end compared to its bending in the first flexural mode for a given deflection at the free end. The conversion factor $\chi > 1$ because an applied point load at the free end leads to a higher bending compared to the first flexural mode. In contrast, $\alpha < 1$ because for the chosen cantilever alignment and the resulting force distribution, the bending is lower compared to the bending of the modal shape of the first flexural mode. Note that the α values are close to unity however (Table 2).

It has been reported in the literature that an analytical expression for β can be obtained for some force distributions and cantilever geometries [31]. For a constant force distribution and a rectangular beam $\beta = 3/8 = 0.375$. It can be seen that the values in Table 2 are of similar size because the cantilever shapes are similar to rectangular ones and the resulting force distributions due to the fluid flow show some similarity to a constant force distribution.

α and β depend on the force distribution and change if the force profile changes, for example, with fluid speed or cantilever positioning. However, Figure 4 and Table 2 demonstrate that there is no dramatic change in the values of both conversion factors (<3%) for any of the cantilevers studied and over the fluid speed ranges utilized to determine the spring constants. The highest changes are observed for the OTESPA and Fastscan-C cantilevers. The speed dependence of the conversion factors has been taken into account in the determination of the spring constant values reported in Table 2. Using the average values of α and β reported in Table 2 will give similar values to those reported for all cantilevers and fluid speeds above 15 m/s. Very small deviations would result for OTESPA and Fastscan-C cantilevers, where the values however should still give accurate results for fluid speeds around 25 m/s, corresponding to the speed where the mean values coincide with the calculated values.

Spring constant values

Figure 6 shows a slight increase of the spring constant value $\check{k}_s$ with fluid speed for cantilever NCHV. Ideally the curve should be a flat line. Not all cantilevers showed such an increase, which could be due to a small deviation from the modelled setup because of a slight misalignment of the cantilever or an angle between fluid flow and cantilever in the experiment that is slightly different from the one in the modelling. Another parameter where a small error would lead to this type of behavior is the normalization of the experimentally measured deflection curve to zero deflection. This is another reason, in addition to the observed hysteresis at lower fluid speeds for some of the cantilevers, why only speed values above 15 m/s were considered. The absolute error associated with the zero deflection normalization is the same for all deflections d_V. As a result, the relative error in $\check{k}_s$ will be larger for small deflections, as described by Equation 5. Note, however, that maximum deflection values were in the range of ≈230 nm (Fastscan-C) to ≈17 nm (Tap525) and hence well within the linear response range of the cantilevers and the detector [38]. The size of the deflection itself should therefore not induce an error.

Some of the determined spring constant values show a significant deviation from the nominal values provided by the manufacturer. It is well known that such a discrepancy between the nominal and the actual values can exist [4,39]. All spring constants determined by the fluid flow method are however within the manufacturers quoted range, while for the thermal noise method, only the value for Tap150 falls slightly outside the nominal range.

The biggest deviation between the spring constants determined via thermal noise and the fluid flow method are observed for RC2 and Fastscan-C cantilevers. RC2 is a tipless cantilever and contact between the cantilever and a surface during the force curve required for the thermal noise method is in general not well defined. Therefore, there might be a large error in the experimental optical lever sensitivity, σ_1, and hence in this particular thermal noise spring constant value. The optical lever sensitivity, when determined from force curves, has a potentially significant error even when contact between the cantile-

ver and a surface is established with a tip [19]. In contrast, the method based on the fluidic force does not require this type of measurement.

Most of the spring constant values determined with the fluid flow are higher than those from thermal noise with the exception of RC2 and Tap150. A systematic error such as a misalignment of the cantilever relative to the flow could lead to such a deviation. A misalignment would result in a difference between the force experienced by the cantilever during the experiment in comparison to the force obtained from modelling, although it appears unlikely that such a potential systematic error was then not present for RC2 and Tap150.

An advantage of the presented approach, as compared to most other calibration methods, is that it gives the spring constant value for a range of applied forces and deflections with standard deviation values of typically <5%, while other methods often produce a value based on a single deflection.

The accessible spring constant range is not limited to the range 0.8–155 N/m of the present study. Softer cantilevers require a lower fluid flow speed and stiffer ones a higher speed. In order to have better control over the flow and the resulting forces, the channel height could be reduced for spring constant values <1 N/m and increased for cantilevers with spring constants >100 N/m.

Microfluidic force tool

In the current experiments the specific alignment of the cantilevers relative to the channel exit was chosen for reasons of confidence in positioning and reproducibility. The positioning could however be further optimized for example by aligning the cantilever along the channel width (which was ≈1 mm in our experimental setup) such that the flow and hence force is essentially constant over the full cantilever length. This would potentially simplify the calculation of β. No simulation of the forces will be required if the total force depends on the plan view area and the fluid speed only, in which case forces can be predicted without any modeling. This is currently under investigation. We note that in the current setup, the k values for speeds above 15 m/s are already based on fluid flow profiles that essentially only depend on the speed of the fluid flow, which is evident from the very weak fluid speed dependence of α and β.

In addition to the determination of the static flexural spring constant, the presented setup can also be employed to obtain other useful information: knowledge of the static spring constant and the applied force allows the cantilever deflection to be determined, which in turn can be exploited to extract the torsional and lateral spring constants from the same measurement if the corresponding resonant frequencies are recorded [30]. Furthermore, the setup also allows the linear range of the force constants to be systematically tested for all kinds of cantilever sensors and other micro- and nanomechanical structures.

Conclusion

We have demonstrated that a microfluidic gas flow escaping from a microchannel can be employed to provide accurate forces on the micrometer scale. We showed that a wide range of microcantilevers with very different static spring constants and geometric shapes can be calibrated without the need to bring the sensor into contact with a surface. An array of cantilevers could also easily be calibrated with the force tool described. The setup presents a contactless microfluidic force tool, which is generally applicable on small scales and has the potential to be equally useful in combination with smaller sensors and structures. The method should therefore be equally applicable to nanocantilever sensors and nanostructures.

Supporting Information

Supporting Information File 1

Raw data of thermal noise spectra, cantilever deflection under fluid flow, and sensitivity values σ_1.
[http://www.beilstein-journals.org/bjnano/content/supplementary/2190-4286-7-43-S1.zip]

Acknowledgements

Financial support from the EPSRC (EP/K000411/1 and EP/L017008/1) and the University of St. Andrews under an Impact Acceleration Account (EP/K503940/1) are gratefully acknowledged.

References

1. Stan, G.; Gates, R. S. *Nanotechnology* **2014,** *25,* 245702. doi:10.1088/0957-4484/25/24/245702
2. Schoen, P.; Gosa, M.; Vancso, G. J. *Rev. Roum. Chim.* **2013,** *58,* 577–583.
3. Kosaka, P. M.; González, S.; Domínguez, C. M.; Cebollada, A.; San Paulo, A.; Calleja, M.; Tamayo, J. *Nanoscale* **2013,** *5,* 7425–7432. doi:10.1039/c3nr01186k
4. Butt, H.-J.; Cappella, B.; Kappl, M. *Surf. Sci. Rep.* **2005,** *59,* 1–152. doi:10.1016/j.surfrep.2005.08.003
5. Beeby, S.; Ensell, G.; Kraft, N.; White, N. *MEMS Mechanical Sensors;* Artech House Publishers: London, 2004.
6. Saadon, S.; Sidek, O. *Energy Convers. Manage.* **2011,** *52,* 500–504. doi:10.1016/j.enconman.2010.07.024
7. Boisen, A.; Dohn, S.; Keller, S. S.; Schmid, S.; Tenje, M. *Rep. Prog. Phys.* **2011,** *74,* 036101. doi:10.1088/0034-4885/74/3/036101
8. Parkin, J. D.; Hähner, G. *Rev. Sci. Instrum.* **2011,** *82,* 035108. doi:10.1063/1.3563724

9. McLoughlin, N.; Lee, S. L.; Hähner, G. *Lab Chip* **2007,** *7,* 1057–1061. doi:10.1039/b705787c
10. McLoughlin, N.; Lee, S. L.; Hähner, G. *Appl. Phys. Lett.* **2006,** *89,* 184106. doi:10.1063/1.2374867
11. Li, M.; Tang, H. X.; Roukes, M. L. *Nat. Nanotechnol.* **2007,** *2,* 114–120. doi:10.1038/nnano.2006.208
12. Naik, A. K.; Hanay, M. S.; Hiebert, W. K.; Feng, X. L.; Roukes, M. L. *Nat. Nanotechnol.* **2009,** *4,* 445–450. doi:10.1038/nnano.2009.152
13. Sage, E.; Brenac, A.; Alava, T.; Morel, R.; Dupré, C.; Hanay, M. S.; Roukes, M. L.; Duraffourg, L.; Masselon, C.; Hentz, S. *Nat. Commun.* **2015,** *6,* 6482. doi:10.1038/ncomms7482
14. Palacio, M. L. B.; Bhushan, B. *Crit. Rev. Solid State Mater. Sci.* **2010,** *35,* 73–104. doi:10.1080/10408430903546691
See also correction: Palacio, M. L. B; Bhushan, B. *Crit. Rev. Solid State Mater. Sci.* **2010**, *35*, 261.
15. Munz, M. *J. Phys. D: Appl. Phys.* **2010,** *43,* 063001. doi:10.1088/0022-3727/43/6/063001
16. Hutter, J. L.; Bechhoefer, J. *Rev. Sci. Instrum.* **1993,** *64,* 1868–1873. doi:10.1063/1.1143970
17. Sader, J. E.; Chon, J. W. M.; Mulvaney, P. *Rev. Sci. Instrum.* **1999,** *70,* 3967–3969. doi:10.1063/1.1150021
18. Cook, S. M.; Schäffer, T. E.; Chynoweth, K. M.; Wigton, M.; Simmonds, R. W.; Lang, K. M. *Nanotechnology* **2006,** *17,* 2135–2145. doi:10.1088/0957-4484/17/9/010
19. te Riet, J.; Katan, A. J.; Rankl, C.; Stahl, S. W.; van Buul, A. M.; Phang, I. Y.; Gomez-Casado, A.; Schön, P.; Gerritsen, J. W.; Cambi, A.; Rowan, A. E.; Vancso, G. J.; Jonkheijm, P.; Huskens, J.; Oosterkamp, T. H.; Gaub, H.; Hinterdorfer, P.; Figdor, C. G.; Speller, S. *Ultramicroscopy* **2011,** *111,* 1659–1669. doi:10.1016/j.ultramic.2011.09.012
20. Holbery, J. D.; Eden, V. L.; Sarikaya, M.; Fisher, R. M. *Rev. Sci. Instrum.* **2000,** *71,* 3769–3776. doi:10.1063/1.1289509
21. Kim, M.-S.; Choi, J.-H.; Kim, J.-H.; Park, Y.-K. *Measurement* **2010,** *43,* 520–526. doi:10.1016/j.measurement.2009.12.020
22. Gibson, C. T.; Watson, G. S.; Myhra, S. *Nanotechnology* **1996,** *7,* 259–262. doi:10.1088/0957-4484/7/3/014
23. Cumpson, P. J.; Clifford, C. A.; Hedley, J. *Meas. Sci. Technol.* **2004,** *15,* 1337–1346. doi:10.1088/0957-0233/15/7/016
24. Slattery, A. D.; Blanch, A. J.; Quinton, J. S.; Gibson, C. T. *Ultramicroscopy* **2013,** *131,* 46–55. doi:10.1016/j.ultramic.2013.03.009
25. Slattery, A. D.; Blanch, A. J.; Quinton, J. S.; Gibson, C. T. *Nanotechnology* **2013,** *24,* 015710. doi:10.1088/0957-4484/24/1/015710
26. Ying, Z. C.; Reitsma, M. G.; Gates, R. S. *Rev. Sci. Instrum.* **2007,** *78,* 063708. doi:10.1063/1.2747095
27. Lubarsky, G. V.; Hähner, G. *Rev. Sci. Instrum.* **2007,** *78,* 095102. doi:10.1063/1.2782792
28. Lubarsky, G. V.; Hähner, G. *Nanotechnology* **2008,** *19,* 325707. doi:10.1088/0957-4484/19/32/325707
29. Parkin, J. D.; Hähner, G. *Nanotechnology* **2013,** *24,* 065704. doi:10.1088/0957-4484/24/6/065704
30. Parkin, J. D.; Hähner, G. *Nanotechnology* **2014,** *25,* 225701. doi:10.1088/0957-4484/25/22/225701
31. Hähner, G. *J. Appl. Phys.* **2008,** *104,* 084902. doi:10.1063/1.3000055
32. Hähner, G. *Ultramicroscopy* **2010,** *110,* 801–806. doi:10.1016/j.ultramic.2010.02.008
33. Sader, J. E.; Lu, J. N.; Mulvaney, P. *Rev. Sci. Instrum.* **2014,** *85,* 113702. doi:10.1063/1.4900864
34. Butt, H.-J.; Jaschke, M. *Nanotechnology* **1995,** *6,* 1–7. doi:10.1088/0957-4484/6/1/001
35. Stark, R. W.; Drobek, T.; Heckl, W. M. *Ultramicroscopy* **2001,** *86,* 207–215. doi:10.1016/S0304-3991(00)00077-2
36. Hetsroni, G.; Mosyak, A.; Pogrebnyak, E.; Yarin, L. P. *Int. J. Heat Mass Transfer* **2005,** *48,* 1982–1998. doi:10.1016/j.ijheatmasstransfer.2004.12.019
37. *COMSOL Multiphysics,* Version 5.0; 2014, http://www.comsol.com/release/5.0.
38. Thormann, E.; Pettersson, T.; Claesson, P. M. *Rev. Sci. Instrum.* **2009,** *80,* 093701. doi:10.1063/1.3194048
39. Sader, J. E.; Larson, I.; Mulvaney, P.; White, L. R. *Rev. Sci. Instrum.* **1995,** *66,* 3789–3798. doi:10.1063/1.1145439

License and Terms

BEILSTEIN JOURNAL OF NANOTECHNOLOGY

Nanoscale effects in the characterization of viscoelastic materials with atomic force microscopy: coupling of a quasi-three-dimensional standard linear solid model with in-plane surface interactions

Santiago D. Solares

Full Research Paper

Open Access

Address:
Department of Mechanical and Aerospace Engineering, George Washington University, Washington, DC 20052, United States

Email:
Santiago D. Solares - ssolares@gwu.edu

Keywords:
atomic force microscopy; modeling; polymers; simulation; spectroscopy; standard linear solid; surface elasticity; surface energy; viscoelasticity

Beilstein J. Nanotechnol. **2016,** *7,* 554–571.
doi:10.3762/bjnano.7.49

Received: 30 November 2015
Accepted: 05 April 2016
Published: 15 April 2016

This article is part of the Thematic Series "Advanced atomic force microscopy techniques IV".

Guest Editor: T. Glatzel

Abstract

Significant progress has been accomplished in the development of experimental contact-mode and dynamic-mode atomic force microscopy (AFM) methods designed to measure surface material properties. However, current methods are based on one-dimensional (1D) descriptions of the tip–sample interaction forces, thus neglecting the intricacies involved in the material behavior of complex samples (such as soft viscoelastic materials) as well as the differences in material response between the surface and the bulk. In order to begin to address this gap, a computational study is presented where the sample is simulated using an enhanced version of a recently introduced model that treats the surface as a collection of standard-linear-solid viscoelastic elements. The enhanced model introduces in-plane surface elastic forces that can be approximately related to a two-dimensional (2D) Young's modulus. Relevant cases are discussed for single- and multifrequency intermittent-contact AFM imaging, with focus on the calculated surface indentation profiles and tip–sample interaction force curves, as well as their implications with regards to experimental interpretation. A variety of phenomena are examined in detail, which highlight the need for further development of more physically accurate sample models that are specifically designed for AFM simulation. A multifrequency AFM simulation tool based on the above sample model is provided as supporting information.

Introduction

The accurate characterization of viscoelastic materials with atomic force microscopy (AFM) is of high interest [1-16], but it is also a very difficult task due to the complexity of the material behavior phenomena that govern the AFM observables. In contrast, the description of the bulk behavior of viscoelastic materials can frequently be represented with relatively simple models combining linear springs and dampers [14], which are appropriate for the specimen geometries used at the continuum scale. A common example is a viscoelastic film trapped between two parallel plates that are displaced with respect to one another while the stress in the material is measured [17,18]. Drawing a connection from continuum mechanics to AFM measurements (where the probe geometry is relatively simple, often assumed spherical) may appear to be straightforward at first glance, but a detailed analysis reveals specific complexities that can make quantitative accuracy an elusive goal. For example, in contrast to a typical bulk experiment, the stresses and strains imposed by the AFM probe on the sample are not uniformly distributed throughout the material, but are often localized near the axis of the indentation. Second, at the scale of an AFM measurement, the surface layer mechanical properties (which often differ from the bulk properties, as discussed below) may play a prominent role. Specifically, as the tip compresses the sample, it is easy to imagine how the indentation leads to an increase in the sample surface area, which has an associated energy cost either due to elasticity or surface free energy, or both [19,20]. The overall effect is that as the tip travels into the surface, the surface profile evolves in a way that minimizes the associated energy cost. Third, these surface free energy and elastic energy effects are often neither isotropic nor uniform, as there is generally a variation in the structure and morphology of most viscoelastic surfaces (e.g., polymers) in the horizontal direction (examples are provided below). Furthermore, at the scale of an AFM indentation it may be difficult to properly define the surface energy (even conceptually) since the local material constituents (e.g., polymer chains) can significantly differ from their neighbors and can be, to a varying degree, flexible and mobile. At this scale, the surface is not a smooth continuum but may instead contain molecules oriented in various directions, as well molecules trapped in conformations that do not correspond to a global energy minimum (especially in the compressed volume directly under the AFM tip). Additionally, the behavior of the molecules on the surface may be influenced by chemical or dispersion (van der Waals) forces exerted by the probe, thus leading to a situation in which the sample is influenced by the measurement itself. One could continue extending the list of phenomena that preclude an ideal measurement by considering other issues such as limitations of the measurement method and instrumentation, almost arriving at the conclusion that it is nearly impossible to carry out quantitatively accurate measurements of viscoelasticity with AFM, unless one assumes that the sample follows the simplest continuum behaviors.

For the most part, the development of new AFM imaging and spectroscopy methods has relied on continuum assumptions that enable the construction of well-defined surface models. This is quite reasonable, and in the absence of elaborate surface models that can easily be incorporated into the methods, this has been a very fruitful course of action. For example, within contact-resonance AFM (CR-AFM) methods (including dual-amplitude resonance tracking, DART) [2-6], the surface is treated using a linear Kelvin–Voigt model, which consists of a linear spring in parallel with a linear damper. Linear models are used in this case because the oscillation amplitude of the AFM tip is very small, so the tip–sample interaction force curve at the desired force setpoint can be considered to be a straight line for the range of tip positions explored. Similar approaches have been used in force modulation techniques (FMOD-AFM), where the sample is dynamically probed at frequencies well below the cantilever resonance frequency [21]. Novel spectroscopy methods have also been recently developed for intermittent-contact imaging. For example, it is now possible to extract tip–sample force curves using dual-eigenmode frequency-modulation AFM [10] and intermodulation AFM [11,12]. In these methods, the surface is modeled as a continuum material with a well-defined Young's modulus, which interacts with a spherical AFM probe and is assumed to dissipate energy in proportion to the probe's instantaneous velocity and depth of indentation. Here, an analytical description of the force as a function of tip position and velocity, $F_{\mathrm{ts}} = F_{\mathrm{ts}}(z, \dot{z})$, is postulated, and the experiment is performed with the objective of extracting the model constants. Despite the simplicity of the surface models available, these methods clearly represent very important milestones in the development of AFM spectroscopy and already have a wide range of practical applications. Nevertheless, these rapid AFM developments also call for additional efforts at the other end of the research problem, namely the development and implementation of more physically accurate surface models that are able to describe nanoscale surface complexities such as those discussed in the previous paragraph.

With the above in mind, the objective of this paper is to carry out a qualitative exploratory study of the coupling of viscoelastic behaviors with nanoscale surface effects within a tip–sample model that can be used for the simulation and interpretation of AFM experiments. The work departs from a previously introduced quasi-three-dimensional (Q3D) implementation of the standard linear solid (SLS) model for representing viscoelastic surfaces [13,14,22-24] and considers the enhance-

ment of the model through the incorporation of in-plane elastic effects within the top surface layer. The study highlights measurement interpretation challenges and physical phenomena that have not yet been addressed in depth within AFM. The article is organized as follows: first a thorough presentation of the SLS model is provided, describing its elements, constitutive equations, corresponding complex modulus, and the relationship between its parameters and those one would use in simulating AFM imaging. Next, a detailed discussion of surface effects is offered, followed by a description of the enhanced surface model. A Results and Discussion section follows, which treats specific numerical examples focusing on the tip–sample force curve features, indentation profiles, tip geometry effects and their interaction with one another. The next section consists of a description of the software tool, whose source code and input file are provided as supporting information. The paper closes with the section Conclusion.

The author cautions the reader that although the calculations and discussions presented here can be useful in highlighting future research directions regarding the development of AFM methods and models for viscoelastic materials, all the analyses are based on linear material behaviors that may fall short in the treatment of specific problems. Consider, for example, a tapping-mode experiment, which may involve local stresses and strains that are too large to be treated linearly, or local heating and melting of the sample, which can cause the material properties to vary with time and location within the sample. This paper, therefore, offers only a glimpse into the research gaps that exist in the treatment of sample material properties within AFM simulation.

Viscoelasticity and the standard linear solid

The standard linear solid (SLS) model is shown in Figure 1. It consists of a linear spring in parallel with a Maxwell arm, which in turn consists of a linear spring in series with a linear damper [13,14,25]. The SLS is the simplest viscoelastic model that is capable of reproducing the most fundamental viscoelastic behaviors, namely creep and stress relaxation [13,14,18,25]. There exist simpler models [13], such as the Maxwell model by itself (described above) and the Kelvin–Voigt model, which consists of a linear spring in parallel with a linear damper (this model is used in CR-AFM [3]). However, in the former model, the surface is unable to restore itself to its original state (it remains permanently deformed upon the application of a stress), and the latter model does not exhibit stress relaxation.

The SLS model was previously used in AFM simulations and its general properties and response have been extensively discussed [13,14]. Here the derivation of its constitutive equation [25] and the expressions describing its complex modulus are discussed [17,18], which offer a theoretical connection to experimental bulk measurements.

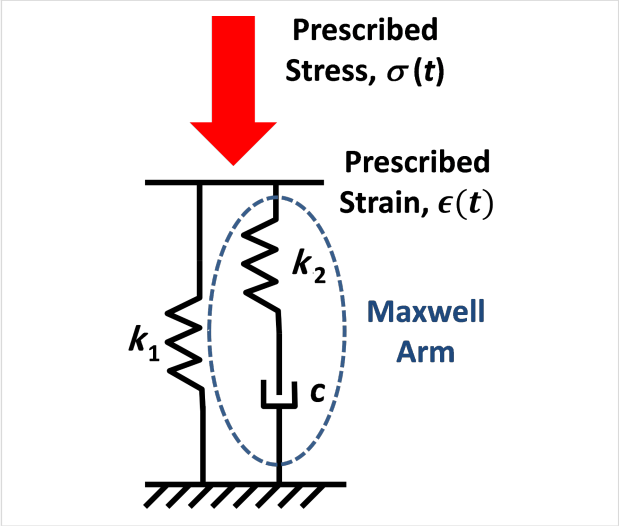

Figure 1: Standard linear solid model. The response of the model generally consists of a time-dependent stress resulting from the application of a prescribed strain trajectory or a time-dependent strain resulting from the application of a prescribed stress trajectory.

SLS constitutive equation

To derive the SLS constitutive equation [25] relating stress and strain, focus is placed on the Maxwell arm, which contains spring k_2 and damper c (see Figure 1). It should be noted that the stress in this Maxwell arm, σ_m, is the same for both of its elements because they are in series:

$$\sigma_m = \sigma_{k_2} = \sigma_c. \tag{1}$$

In contrast, the strain is additive:

$$\varepsilon_m = \varepsilon_{k_2} + \varepsilon_c. \tag{2}$$

The above equation can be differentiated to give

$$\dot{\varepsilon}_m = \dot{\varepsilon}_{k_2} + \dot{\varepsilon}_c. \tag{3}$$

Since the spring k_2 is linear, its stress–strain relationship is given by

$$\sigma_{k_2} = k_2 \varepsilon_{k_2}, \tag{4}$$

which can also be differentiated with respect to time to give

$$\dot{\sigma}_{k_2} = k_2 \dot{\varepsilon}_{k_2}. \tag{5}$$

By definition of the linear damper, we also have

$$\sigma_c = c\dot{\varepsilon}_c. \tag{6}$$

The substitution of Equation 5 and Equation 6 into Equation 3 gives

$$\dot{\varepsilon}_{\mathrm{m}} = \frac{\dot{\sigma}_{k_2}}{k_2} + \frac{\sigma_c}{c}, \tag{7}$$

which, using Equation 1, can be rewritten as

$$\dot{\varepsilon}_{\mathrm{m}} = \frac{\dot{\sigma}_{\mathrm{m}}}{k_2} + \frac{\sigma_{\mathrm{m}}}{c}. \tag{8}$$

Since the Maxwell arm in the SLS model is in parallel with spring k_1, the strain of the Maxwell arm and of the spring k_1 is the same, but the stresses are additive:

$$\varepsilon = \varepsilon_{k_1} = \varepsilon_{\mathrm{m}} \tag{9}$$

$$\sigma = \sigma_{k_1} + \sigma_{\mathrm{m}}. \tag{10}$$

Differentiating Equation 10 gives

$$\dot{\sigma} = \dot{\sigma}_{k_1} + \dot{\sigma}_{\mathrm{m}}. \tag{11}$$

Solving for $\dot{\sigma}_{\mathrm{m}}$ in Equation 8 and substituting it into Equation 11, along with the time derivative of the stress–strain relation for spring k_1 ($\dot{\sigma}_{k_1} = k_1\dot{\varepsilon}_{k_1}$), and making use of Equation 9 to remove the subindices on the strains gives

$$\dot{\sigma} = (k_1 + k_2)\dot{\varepsilon} - \frac{k_2}{c}\sigma_{\mathrm{m}}. \tag{12}$$

Finally, solving for σ_{m} in Equation 10 and introducing it into Equation 12 along with the stress–strain relation for spring k_1 ($\sigma_{k_1} = k_1\varepsilon_{k_1} = k_1\varepsilon$), the constitutive equation for the SLS model is found as:

$$\dot{\sigma} = (k_1 + k_2)\dot{\varepsilon} - \frac{k_2}{c}\sigma + \frac{k_1 k_2}{c}\varepsilon. \tag{13}$$

The above equation governs the response of the SLS model and will be used in the next section to derive expressions for its complex modulus. This value is measurable in an experiment that involves the application of a strain that varies sinusoidally in time, as long as the stress and strain are uniform throughout the specimen.

SLS complex modulus

The SLS parameters of a particular specimen can be obtained via the expressions for the model's complex modulus (obtained from its constitutive equation), by fitting those expressions to the complex modulus behavior observed experimentally for the material under study. To derive the complex modulus of the SLS model, a periodic strain that varies sinusoidally in time with frequency ω is defined as [17,18,25]:

$$\varepsilon = \varepsilon_0^* e^{i\omega t}. \tag{14}$$

When the above strain is applied to the sample, it generates a sinusoidally varying stress of the form

$$\sigma_{\mathrm{ss}} = \sigma_0^* e^{i\omega t}, \tag{15}$$

where both ε_0^* and σ_0^* are complex (strictly speaking, ε_0^* can be real in an experiment, since the phase of the applied strain can be defined as zero) and the subindex ss refers to the steady state condition after all transient responses have disappeared. The complex modulus is now defined as [17,18,25]

$$E^* = \frac{\sigma_0^*}{\varepsilon_0^*} = E' + iE''. \tag{16}$$

To find E' and E'' Equation 14 and Equation 15 are substituted into the SLS constitutive equation, Equation 13. Then $\sigma_0^*/\varepsilon_0^*$ can be solved for, which can be written in the form of Equation 16 and gives

$$E' = \frac{\omega^2\left(k_1 + k_2\right) + \dfrac{k_1 k_2^2}{c^2}}{\omega^2 + \left(\dfrac{k_2}{c}\right)^2}; \tag{17}$$

$$E'' = \frac{\dfrac{\omega k_2^2}{c}}{\omega^2 + \left(\dfrac{k_2}{c}\right)^2}. \tag{18}$$

E' is associated with elastic interactions, while E'' is associated with dissipative interactions [25]. Figure 2 gives examples of plots of the above expressions as a function of frequency for a few sets of parameters. Of the measurable continuum quantities available, the complex modulus is the most appropriate to fit

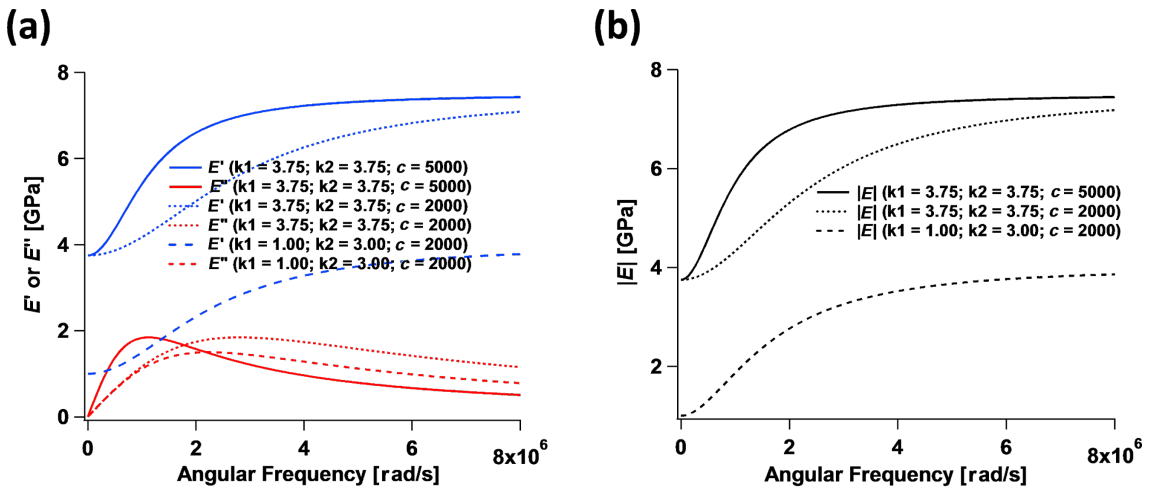

Figure 2: (a) Plots of the complex modulus components, E' and E'' (Equation 17 and Equation 18, respectively), for the sets of model parameters indicated in the graphs. (b) Plots of the absolute value of the complex modulus corresponding to the traces shown in (a). The angular frequency axis is in radians per second, and the maximum axis value of 8×10^6 rad/s corresponds to a frequency of approximately 1.27 MHz, which is nowadays not uncommon in AFM, especially within multifrequency methods [9].

theoretical models to, and is also the most appropriate to draw a connection to within dynamic experimental measurement techniques such as AFM. In contrast, the Young's modulus is not an appropriate measure because it is not well defined in a dynamic measurement (especially as the strain oscillation frequency is increased), and because in the case of viscoelastic materials, the stress and strain are not related by a simple constant as in the elastic case. Furthermore, it must be noted that the complex modulus is only applicable in the context of a continuous periodic measurement, such as the application of a sinusoidal strain ($\varepsilon = \varepsilon_0^* e^{i\omega t}$), as discussed above. Within the context of AFM, this condition can be approximately satisfied only in methods such as CR-AFM or FMOD-AFM [2-6,21]. Therefore, neither the use of the complex modulus nor of quantities derived from it (e.g., the loss tangent, which is the ratio of the loss modulus to the storage modulus) are appropriate for analysis of intermittent-contact AFM measurements (this includes both single- and multifrequency techniques) because, (i) the tip–sample interaction in that mode of imaging is not continuous and therefore the stress response of the material is not able to reach a steady state during the measurement, and (ii) the complex modulus depends on the frequency of the periodic sinusoidal sample deformation, which is not well defined in a tapping-mode experiment (see [26] for a discussion of discrepancies between intermittent-contact and contact-resonance viscoelasticity measurements). Furthermore, the spectrum of the force (stress) and displacement (strain) in intermittent-contact AFM contains a mixture of unknown and difficult to measure frequencies [15,27], and the experiment does not provide a spatial description of the strain distribution throughout the volume of the sample that is instantaneously interacting with the tip (not all sample differential volume elements that interact with the tip at a given instant undergo the same strain history, neither in terms of magnitude nor in terms of strain direction). This is why viscoelastic measurements with AFM are most commonly performed using CR-AFM or FMOD-AFM, where the sample is probed in contact-mode using a single oscillation frequency in the small-amplitude regime. However, even in these most ideal situations, there still exist challenges associated with the shape of the tip, which does not necessarily impart uniform compressive strain, but may cause both compressive and shear strains with an unknown distribution (within CR-AFM and FMOD-AFM measurements it is customary to assume that strains and stresses exist only in the normal direction, but this is only an approximation). Models of the type discussed here could aid in performing such characterizations with greater accuracy.

Regarding the quantification of elastic sample behaviors within periodic dynamic measurements, it is important to point out the two frequency limits for which the response of the 1D SLS model is purely elastic (see Figure 2). At zero frequency (or infinite deformation time scale) the complex modulus is equal to the storage modulus (the loss modulus is zero, so the complex modulus is real), which according to Equation 17 is equal to k_1 and is called the rubbery modulus [25]. At infinite frequency the loss modulus also becomes zero and the complex modulus is again real and reduces to the storage modulus, but with a value of $k_1 + k_2$, called the glassy modulus [25]. Both of these moduli can be appropriate elastic constants to compare experimental AFM results to in the cases of very low or very

high frequencies, if it can be approximately guaranteed that the stress and strain are uniform and their distribution is 1D.

Relationship between sample properties and AFM simulation parameters

Two very important considerations when relating AFM measurements or simulations to sample properties that are consistent with viscoelastic theory concern the uniformity of the deformation (as already stated above) and the units of the model parameters. In the above discussion of the 1D SLS model, it is assumed that the stresses and deformations are uniform throughout the specimen under study, and that the equations are written in terms of strains and stresses. This is why it is appropriate to speak of moduli (note that k_1 and k_2 are referred to above as moduli, and see also Equation 17 and Equation 18, as well as the discussion pertaining to them). However, in AFM one is generally concerned with displacements (indentation depths) and forces [16]. Therefore, in previous publications [14,28] k_1 and k_2 are defined as force constants with units of N/m and not as moduli with units of N/m^2. However, to be consistent with the equations listed above, the relationship between the moduli and the linear force constants of the model are provided here.

Consider the viscoelastic film schematically drawn in Figure 3 and assume that its stress–strain relationship in the vertical (tensile–compressive) direction can be approximated using that of the SLS model (Equation 13). The undeformed film has an initial thickness T_0 but it is then compressed uniformly across its entire area by a distance ΔT. If the film can be treated as a continuum, its strain can be defined as

$$\varepsilon = \frac{\Delta T}{T_0}. \tag{19}$$

Since the film is described by the SLS model, the stress–stress relation of spring k_1 ($\sigma_{k_1} = k_1\varepsilon_{k_1} = k_1\varepsilon$) can be used to write

$$\sigma_{k_1} = k_1\varepsilon = k_1\frac{\Delta T}{T_0} = \left(\frac{k_1}{T_0}\right)\Delta T, \tag{20}$$

where $\hat{k}_1 = k_1 / T_0$ (last term on the right hand side) is defined as a force constant normalized by surface area (with units of force/length^3), whereby $\hat{k}_1$ converts the displacement ΔT into the stress σ_{k_1}. In previous AFM simulations [14,28] a force constant that is not normalized by unit area was simply given, such that multiplication by the displacement gives a force F_{k_1} instead of a stress σ_{k_1}. This is equivalent to assuming that the surface area, A, of the film being compressed under the AFM tip is known, since the total force is equal to the stress multiplied by the total area ($A\sigma_{k_1}$ or $\sigma_{k_1} = F_{k_1} / A$). In the code provided as supplementary information for this paper, the model input parameters are defined as $\hat{k}_1 = k_1 / T_0$, $\hat{k}_2 = k_2 / T_0$, and $\hat{c} = c / T_0$ and have units of N/m/nm^2, N/m/nm^2 and Ns/m/nm^2, respectively. The assumption of homogeneous stress and strain is violated in AFM measurements, where the deformation is minute compared to the dimensions of the sample and the deformation time scale can be short compared to the timescales required for full relaxation. In reality, the appropriate value of T_0 to use in the calculations is not known in an experiment since the deformation may be limited to an unknown region near the surface (the deformed region can be localized, for example, due to cross-linking or layering of the material, which prevents the small deformation imparted at the top of the film from ever reaching the lower end of the specimen in a significant way). It is therefore not possible to establish a direct, rigorous connection between bulk SLS parameters and the SLS parameters to be used in an AFM simulation. Nevertheless, it is illustrative to carry out the exercise of converting model parameters to bulk properties under assumed ideal conditions. For example, consider a 50 nm thick film with $\hat{k}_1 = k_1 / T_0 = 0.075$ N/m·nm^2 as used recently in [22]. In this case, $k_1 = \hat{k}_1 T_0 = 0.075$ N/m·nm^2 × 50 nm = 3.75 GPa, which is in the expected range for a typical polymer film investigated with AFM [10]. For the dissipation coefficient,

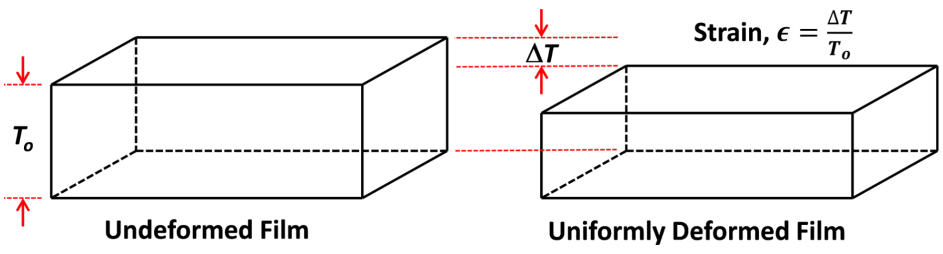

Figure 3: Illustration of the uniform deformation of a viscoelastic film of initial thickness T_0. This type of uniform deformation is not attainable in AFM measurements conducted with standard tips.

$c = 1 \times 10^{-7}$ N s/m·nm^2 × 50 nm = 5000 N s/m^2 as was also used in [22].

Surface effects in nanoscale probe measurements

Surface effects can emerge in AFM measurements when the surface area increases upon indentation by the tip, as this can generate forces in the plane of the surface which seek to reduce the surface area back to the original value. The restoring forces can be caused by the exposure of bulk molecules to the surface, where these molecules will no longer be surrounded by neighbors in all directions and will thus have a reduced number of favorable nearest-neighbor energy interactions [20]. The forces can also be due to elastic effects, such as in the case of a cross-linked or covalently bonded material, which will experience an internal restoring force without undergoing obvious changes in the arrangement of the molecules [19]. Depending on the material, the contribution of each mechanism to the total driving force counteracting increases in surface area can vary [19].

Some of the most striking examples of surface free energy effects are observed in covalent crystals, for which the creation of new surface area by splitting the crystal requires breaking covalent bonds and leaving dangling bonds on the surface [29]. Loosely speaking (that is, without considering reconstruction and/or relaxation), the surface energy correlates with the number of bonds broken per unit area, divided between the two surfaces that are created (the breaking of the bond requires that the appropriate bond energy be supplied and half of the energy cost is assigned to each of the two surfaces created). Often, surfaces undergo structural reconstruction upon the generation of new surface area in order to reduce the overall energy cost [29-31]. Even in the cases where there is no reconstruction, the surface still undergoes some type of relaxation, such that its final structure and specific energy differ from those of the bulk. The degree of crystallinity in viscoelastic surfaces can in general be low compared to that observed in crystals, and adjacent molecules are often not joined by covalent bonds [19]. Frequently, but not always, relatively large molecules are involved and their cohesive energy is governed by dispersion (van der Waals) and electrostatic forces, which are generally weaker than those generated by stretched covalent bonds or electrostatic interactions in ionic crystals, and which allow the molecules to rearrange with relative ease [19,20]. There are also many viscoelastic surfaces which are formed by macromolecules that have cross-linking covalent bonds, such as vulcanized rubber [19], in which case there are restrictions on the relative mobility of adjacent molecules.

From the above discussion, it is clear that the structure of the surface itself is not expected to be the same as that of the bulk, and that the surface structures of viscoelastic surfaces can be very complex and difficult to predict. Additionally, the constituent molecules in a viscoelastic material can exhibit some variation in size (molecular weight and structure), connectivity, distribution of functional groups, etc., such that they are not all necessarily identical [19]. Additionally, the types of surface configurations that are feasible depend on the structure of the source material (e.g., the monomers used and their proportion in a copolymer), the manufacturing process used, and the size (especially thickness in the normal direction) of the specimen under study [19]. For certain ranges of manufacturing conditions, precursor properties (e.g., the time–temperature history or molecular size), or dimensions, the material structure may be "trapped" into different configurations that do not necessarily correspond to a global minimum of energy [19]. Such complexity clearly offers a wider range of morphologies in comparison to a crystal. Figure 4 shows a few examples of AFM images of highly regular polymer surfaces that exhibit significant variability in the horizontal direction, thus precluding a rigorous continuum treatment at the nanoscale.

The existence of a surface energy "penalty" either due to surface free energy or due to elasticity leads to an attempt on the part of the material to reduce its surface area. In the dynamic loading of macroscopic specimens this does not play a role because the surfaces generally remain unchanged (flat) [17,18], but this can be very important in an AFM experiment, where indentation by the tip leads to a curved surface (a curved depression embedded into an otherwise flat surface), whereby the total final area of the cavity created is a function of the curvature of the surface. This is illustrated schematically in Figure 5, which shows two examples of surface profiles caused by interaction of the surface with the tip. The blue profile shown corresponds to a smaller surface area than the red profile. Since the surface free energy and elasticity depend on the material and its configuration, different samples of different materials will exhibit different surface curvature profiles upon indentation by the same AFM tip. As a result, there will be different surface contributions to the total force acting on the AFM tip in each case. This phenomenon can be further complicated by the fact that the proximity of the AFM tip generally leads to favorable nonbonded interactions with the surface, which also affects the surface curvature. Furthermore, additional effects are expected for surfaces that are more cross-linked than the bulk material or surfaces that react with the environment, and also surfaces that absorb or adsorb moisture, which also depends on the environmental temperature and humidity. It is therefore expected that the surface will play an important role in determining the magnitude of the tip–sample forces in viscoelastic materials, which are generally "soft" and for which the indentation is relatively large. For all these reasons, it is not possible to

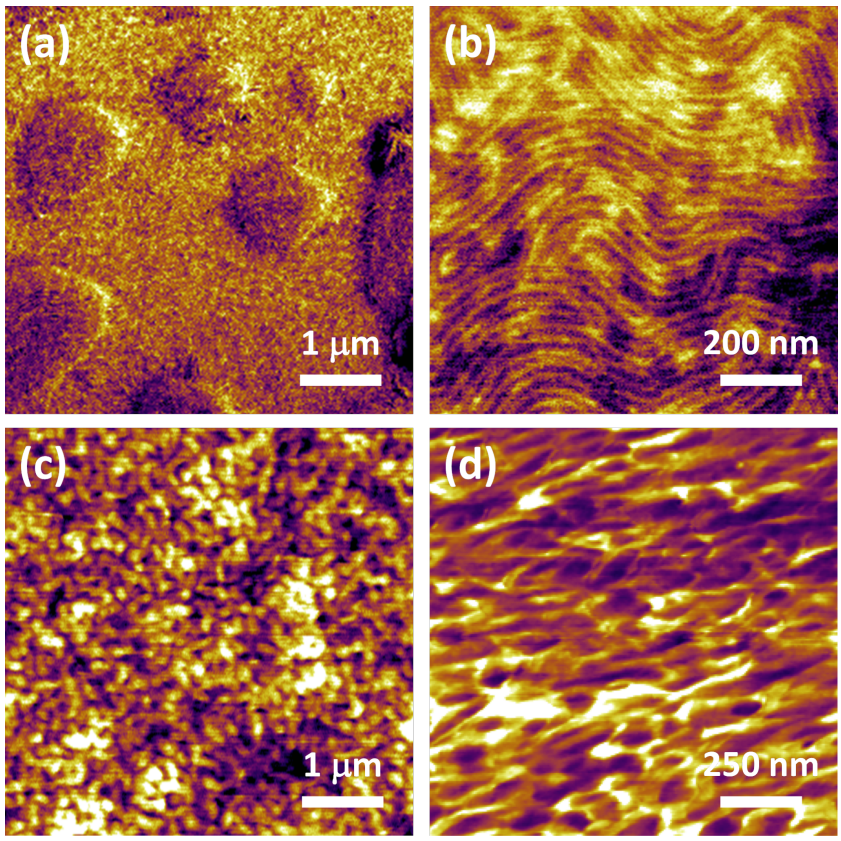

Figure 4: Examples of nanoscale polymer surfaces imaged with AFM. (a,b): Kraton (the height variation in (a) is 30 nm over a scan size of 5 × 5 µm); (c) Nafion (spin-coated thin film); (d) PEDOT:PSS. All images are phase images acquired in tapping-mode AFM. These images are only provided to illustrate typical polymer morphologies and are not related to the model implementation examples provided below.

fully describe the behavior of the surface using elastic–dissipative models in which the internal forces are always normal to the surface, even if they exhibit the correct bulk viscoelastic behavior as in the case of the previously introduced Q3D model (based on the SLS).

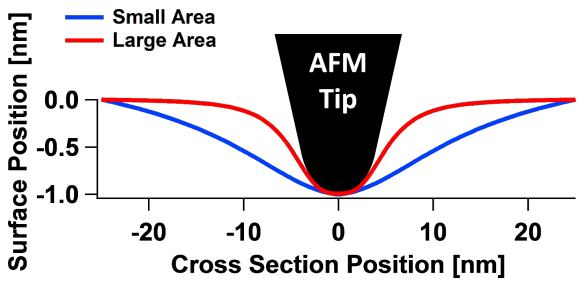

Figure 5: Schematic illustration of two surface profiles caused by indentation with an AFM tip. The blue profile corresponds to a smaller increase in surface area than the red profile.

Results and Discussion

Quasi-three-dimensional SLS model with surface effects

A previous publication [22] introduced a quasi-three-dimensional (Q3D) simulation software implementation of the SLS model. In this work, the surface is partitioned into very small area elements, each of which can undergo displacements in the direction normal to the surface upon interaction with the AFM tip. Figure 6 shows a conceptual representation of the model, with area elements partitioned either in the radial direction to simulate AFM imaging with axisymmetric tips (Figure 6b) or partitioned in the x- and y-directions for general tip shapes (Figure 6c). Within this model, as the tip penetrates deeper into the surface, it interacts with a larger number of viscoelastic elements. This leads to a repulsive tip–sample force curve that exhibits an upward curvature instead of the downward curvature corresponding to the previously used 1D SLS model [14,28] (see Figure 7). Additionally, since within the Q3D model the tip creates a cavity on the surface of the material, the total van der Waals force experienced by the tip depends on the geometry of that cavity, or more specifically, on the number of surface ele-

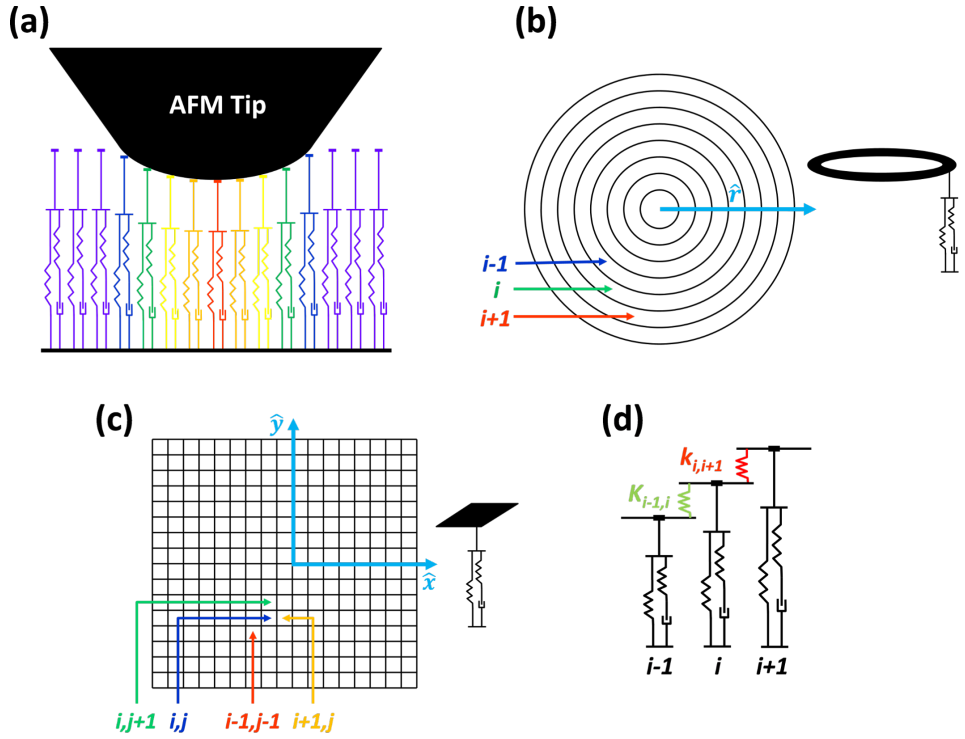

Figure 6: (a) Schematic representation of the Q3D sample model interacting with the AFM tip. (b) Polar coordinates partition of the surface illustrating an individual element (here the SLS parameters of each element differ because their areas differ). (c) Cartesian coordinates partition of the surface illustrating an individual element. (d) Q3D model enhanced with inter-element springs to represent surface effects. In the polar representation of (d) used in this paper, the force constants between adjacent surface elements depend on the contact perimeter between each two elements.

ments that are in close proximity to the tip surface [22]. This is why the maximum attractive force differs for the approach and retract of the Q3D force curve of Figure 7 (note that the model does not currently include other types of forces, besides the force due to the viscoelastic elements and the van der Waals forces).

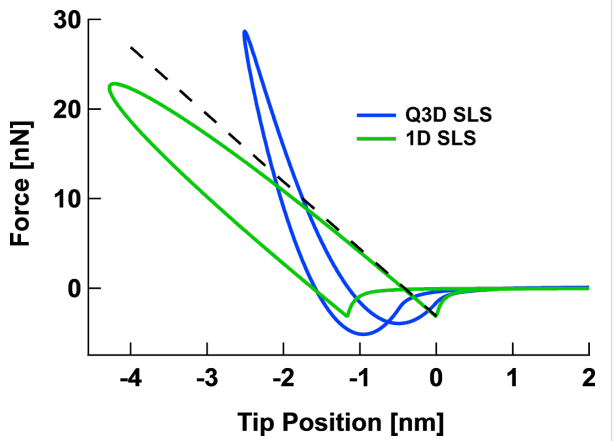

Figure 7: Comparison of typical force curves obtained for the Q3D model and the 1D SLS model in AFM simulations. The force curves for the latter do not exhibit the correct curvature behavior in the repulsive force region.

Since the Q3D model is based on individual 1D SLS elements, it also exhibits the qualitatively correct behavior with respect to creep and stress relaxation. However, in its previous form [22], it lacks interaction between adjacent area elements, and thus, it does not produce a physically correct shape for the surface profiles that emerge upon indentation by the AFM tip. This is because the only area elements that undergo displacement are those directly under the tip, which the tip directly depresses. Thus the Q3D model (in its polar coordinates implementation) has been enhanced by introducing additional linear springs between the adjacent concentric area elements (Figure 6d), which can be loosely related to surface free energy or elasticity. Due to the fact that the area elements in the given model only relax in the vertical direction and not in the horizontal direction, the connection to surface effects is most easily understood in terms of elasticity. In this case, the restoring force can be modeled through an inter-element force constant for the surface, k_s, such that the force between adjacent area elements, i and $i + 1$, displaced by a distance dz with respect to one another, is equal to

$$F_i = -k_{s,i}\,\mathrm{d}z. \tag{21}$$

This equation includes the subindex i in F_i and in $k_{s,i}$ to indicate that the force constant between two area elements varies

with the distance between those elements and the vertical axis of the tip (radial coordinate origin). Additionally, $k_{s,i}$ can be approximately related to the 2D elastic properties of the surface via a 2D stress–strain relation:

$$\sigma^{2D} = \frac{F_i}{2\pi r_i} = E^{2D}\frac{\Delta L}{\Delta r}, \tag{22}$$

where E^{2D} is the 2D Young's modulus of the surface, Δr is the unstrained width of each area element (element size in the partition of the surface area), and $2\pi r_i$ is the perimeter of element i, located at a distance r_i from the vertical axis of the tip. Additionally, ΔL is the increase in the width of the area element, which is proportional to dz via a trigonometric factor of order unity. Therefore, the force constant is approximately equal to

$$k_{s,i} \approx \frac{2\pi r_i E^{2D}}{\Delta r}. \tag{23}$$

For simplicity, in the code provided, the user enters a cohesiveness parameter equal to

$$k_{int} \approx \frac{E^{2D}}{\Delta r}, \tag{24}$$

which can be easily related to $k_{s,i}$ via Equation 23 once Δr is defined (note that Δr can take different values in the code, depending on the desired fineness of the surface partition).

The incorporation of surface free energy effects is mathematically more complex because a simple order of magnitude approximation (as the one used above) is not possible. To see this, consider concentric area element i, which is displaced vertically with respect to element $i + 1$ by a distance dz. In this case, the increase in surface area dA is of the order $\mathrm{d}A \approx 2\pi r_i \mathrm{d}z$ (again, within a trigonometric factor of order unity). This leads to an increase in surface free energy $\mathrm{d}E \approx 2\pi r_i E_s \mathrm{d}z$, where E_s is the specific surface area (energy per unit area). This change in free energy, in turn, generates a force between the two area elements given for element i by

$$F_i = -\frac{\mathrm{d}E}{\mathrm{d}z} \approx -2\pi r_i E_s. \tag{25}$$

In the case of the polar coordinate system considered here, this increases linearly with the distance from the origin, but does not depend on the separation between the area elements, dz (the force acting on element $i + 1$ is of course equal to $-F_i$). Such independence of the force with respect to the displacement (within the approximation considered) leads to discontinuous displacements of the surface area elements and thus gives unphysical results. A more refined approximation is possible by explicit consideration of the surface tilt angles of the various area elements, but that approach results in a much more complex and less efficient calculation. Since this more complex calculation would still not account for the physics of the problem quantitatively due to the limitations inherent to the model (fixed area element width and restriction to motion in the vertical direction), it was not incorporated into the current code.

The enhanced Q3D model is limited in various ways, each of which offers a research opportunity. For example, the presented viscoelastic treatment of the subsurface only considers tensile (compressive) strains, thus neglecting shear. This is common practice in AFM simulation, where 1D models are the norm (e.g., [2,3,10,12-14,16,28]), but neglects the fact that indentation of the tip into a soft material introduces surface curvature and subsurface 3D strain, which can become important as the tip wedges itself further into the material. A second important limitation is that the model offers only a continuum approximation of the sample, which ignores lateral variations in local morphology and topography (see Figure 4), as well as molecular and specimen dimensions. A third shortcoming of the approach presented is that it is based on linear viscoelasticity, which may not be applicable when large forces are rapidly applied to the surface, as in intermittent-contact multifrequency AFM methods [9,28]. In fact, the treatment of the in-plane surface forces is so far only linear elastic. A fourth, related, limitation is that the model assumes uniform material relaxation in the subsurface, which cannot be guaranteed even in one dimension. Adhesion forces other than attractive van der Waals forces are also not considered, although these can be important and may even lead to noticeable upward deformation of the surface. Despite this already comprehensive list of limitations of the Q3D model, it may still offer a qualitative means to begin to develop a richer description of the physics of the surface and subsurface of viscoelastic materials in the specific context of AFM imaging simulation, especially as experimental results become available.

General features of the tip–sample interaction force curve

It is shown in [22] that the previously introduced Q3D model qualitatively reproduces the correct repulsive region curvature and other features of the tip–sample force curve, such as the offset between the position of minimum (most attractive) force during the approach and its position during the retract (see Figure 7). The upward curvature of the force curve results from the fact that the number of surface elements interacting with the tip increases as the latter penetrates deeper into the surface. For

a spherical tip, for example, each SLS element interacting with the tip follows a time-dependent relaxation similar to that of a simple SLS element [14,22], with a time delay for the onset of deformation and with decreasing indentation for each successive element in the radial direction. The offset of the force minima is a consequence of viscoelastic surface relaxation during the tip–sample contact period, as extensively discussed in previous publications [14,22]. The overall features of the force curve do not change when surface effects are introduced via the spring elements illustrated in Figure 6d, but significant differences can be observed in the quantitative behavior of the force curve and surface profiles, as discussed in the next section. Note that in this paper the viscoelastic behaviors of the models are primarily discussed in terms of the corresponding tip–sample force curves (force vs distance). However, it can also be instructive to examine the curves of the tip–sample force plotted against time. An extensive discussion of the qualitative features of such curves for single- and multiple-impact interactions within the SLS model is provided in [14]. The qualitative features of the curves corresponding to the models discussed here are similar.

Surface effects in the tip–sample interaction force curve

The simulations show that the inclusion of surface elasticity via force constants joining adjacent SLS surface elements (Figure 6d) does not necessarily change the overall shape of the force curve features. This, in turn, suggests that the fact that a particular experimental set of spectroscopy data may fit a given analytic function (e.g., a Hertzian curve where the force varies with respect to the indentation with an exponent of 1.5) does not guarantee that the interpretation of the physics is correct. Consider, for example, the results of Figure 8a, where force curves of similar overall appearance are obtained for different values of the 2D Young's modulus of the top surface layer, with the same viscoelasticity parameters in the subsurface. Certainly the curves differ for different moduli, but their overall qualitative appearance is similar and they could be fit with similar analytic functions that do not consider the physics of the surface deformation. In fact, one may be inclined to attribute the variation in the steepness of the curves to variations in bulk elasticity. This would seem to be consistent with the reduced indentation observed (assuming it could be measured) and some small variation in the phase and amplitude of the cantilever oscillation. For the various values of the 2D Young's modulus considered, Figure 8 also illustrates the time-dependent relaxation behavior of the surface element directly under the tip (Figure 8b), the oscillation amplitude and phase (Figure 8c and Figure 8d, respectively), the peak force within one fundamental oscillation (Figure 8e), and the maximum indentation within one fundamental oscillation (Figure 8f).

The cantilever parameters used in Figure 8 were as follows: resonance frequency 150 kHz, force constant 10 N/m, quality factor 150, free oscillation amplitude 100 nm, and tip radius of curvature 20 nm. The cantilever position above the sample was 76 nm for (a) and (b). The subsurface parameters were as follows: $k_1 = \hat{k}_1 / T_0$ = 0.075 N/m·nm^2, $k_2 = \hat{k}_2 / T_0$ = 0.075 N/m·nm^2, and $\hat{c}$ = 1 × 10^{-7} N·s/m·nm^2. The 2D (in-plane) surface Young's modulus E^{2D} is indicated in the legend on the graph in Figure 8a and the color coding of the traces is the same for all graphs. For reference, E^{2D} = 3.1 N/m corresponds to k_{int} = 2.4 × 10^{10} N/m^2 and is approximately equivalent to 1/120 times the 2D Young's modulus of graphene [32].

It is illustrative to examine in more detail the significant effect that a small variation of the 2D surface modulus can have on the results. For example, for the steepest curve in Figure 8b, the 2D modulus of the surface is only 3.1 N/m. If one considers an "effective" surface thickness of ≈1 nm, then one obtains a 3D Young's modulus of approximately (3.1 N/m)/1 nm = 3.1 GPa. This value is comparable to the calculated rubbery and glassy moduli for this simulation, which were on the order of 3.75 GPa and 7.5 GPa, respectively (see previous section for an estimation of the rubbery modulus). The value of 3.1 N/m is particularly small if one considers that the in-plane surface displacements are expected to be small. However, the effect of including surface elasticity in the model is significant because it can drastically change the shape of the indentation profile (Figure 9), softening its curvature and extending the deformation well beyond the area of direct tip–sample contact. This, in turn, leads to the involvement of a larger number of subsurface SLS elements in comparison to the case when the surface elastic modulus is zero. Figure 9 compares the shape of the indentation profiles and their relaxation in time for the case of zero surface elastic modulus (Figure 9a) and a 2D surface elastic modulus of 3.1 N/m (Figure 9b). The latter corresponds to approximately 1/120 of the 2D Young's modulus of graphene [32]. The profiles in Figure 9a and Figure 9b are "snapshots" of the indentation profile (position vs surface element number) observed for different times given as a function of the cantilever oscillation period, while the data in Figure 9c and Figure 9d provide the corresponding positions of the various surface elements along the radial direction, plotted individually as a function of time. In these simulations, the outermost surface element was kept fixed (element number 299, located at a radial distance from the polar coordinates origin equal to 1.9 × (tip radius) = 38 nm).

It is also worth emphasizing the counterintuitive observation that in Figure 8a the force curves corresponding to a larger 2D surface elastic modulus (which Figure 8f indicates lead to shal-

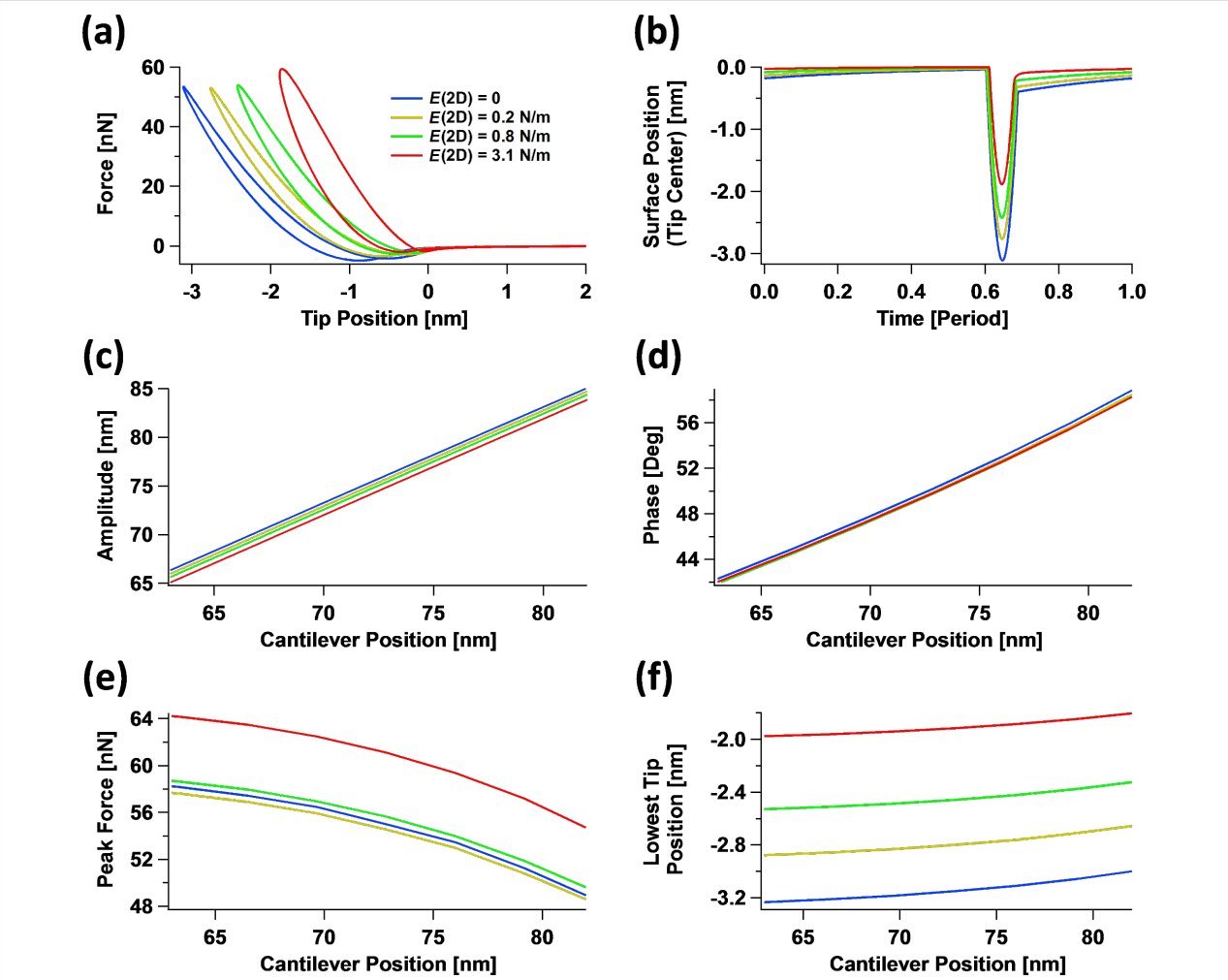

Figure 8: Effect of the 2D surface Young's modulus on tapping-mode AFM: (a) tip–sample force curves; (b) indentation depth vs time (given in cantilever oscillation periods) for the surface element located directly below the center of the AFM tip; and (c–f) tip oscillation amplitude, fundamental phase shift, maximum tip–sample force observed during each cantilever oscillation, and maximum indentation of the surface element located directly below the tip center observed during each cantilever oscillation, respectively, for cantilever positions between 60% and 85% of the free oscillation amplitude (the simulation parameters are given in the text).

lower indentations) exhibit the largest amount of dissipation (they have hysteresis loops of larger area [14]). This is a consequence of the fact that the deformation area is larger when in-plane surface effects are included. This leads to the recruitment of a larger number of SLS elements in the subsurface, thus leading to a larger total dissipated energy. While the explanation is simple, this observation has very significant implications for the interpretation of experiments, for which it is customary to assume that larger amounts of dissipation are expected for samples that are "more viscous" and/or "less elastic". However, the above simulations suggest that the correlation between dissipation and bulk properties can be significantly influenced by in-plane surface forces.

A final subtle observation can be made based on Figure 8c, which indicates that in-plane surface effects lead to changes in the tip oscillation amplitude. This is not unexpected, but is a reminder that topographical measurements in AFM are subject to errors due to changes in material properties. In the case under consideration, the relaxed surface is located at the same position with respect to the cantilever for all simulations labeled with the same cantilever height. However, changes in the surface properties can lead to changes in the amplitude on the order of 1–2 nm for the parameters considered, which will give a comparable error in the topographical measurement.

Interaction between 2D surface elastic modulus and tip geometry

One of the most relevant consequences of having different properties at the surface in comparison to the bulk material is that the interaction of the surface with specific tip geometries becomes more complex. This is illustrated in Figure 10 for an

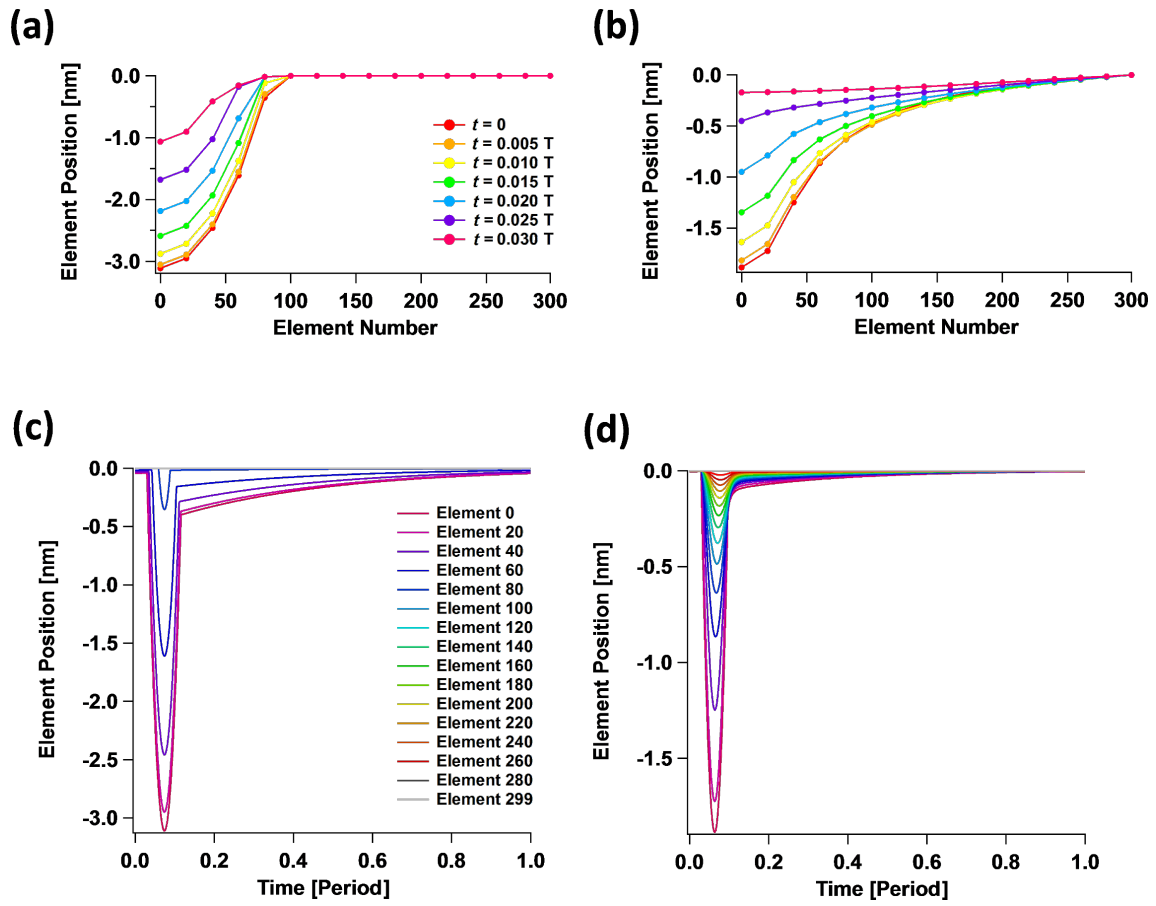

Figure 9: Surface indentation profiles corresponding to the simulations of Figure 8. (a) Indentation of the surface vs distance from the polar coordinate origin in the absence of in-plane surface interactions, for different times given in terms of the tip oscillation period (note how the indented region is limited to the area of direct tip–sample contact). (b) Indentation profiles analogous to those in (a) for a 2D surface Young's modulus of 3.1 N/m. (c) Relaxation of the various surface elements plotted as indentation vs time for the same case as (a). (d) Relaxation of the various surface elements plotted as indentation vs time for the same case as (b). Notice that the relaxation of the various surface elements shown in (c) and (d) exhibits a tip–sample contact region (the deeper part of the plot, on the left) separated by a sharp change in slope from the region of viscoelastic creep, corresponding to relaxation after tip–sample contact has been interrupted. The legend of (b) is the same as that of (a), and the legend of (d) is the same as that of (c).

irregular tip with a protrusion interacting in tapping mode with four surfaces having different values of the 2D surface modulus of elasticity. The force curves (Figure 10b) vary greatly for all four cases not only in simple ways such as steepness differences, but also in overall shape (the corresponding indentation profiles are given in Figure 10c). This happens because there is a gradual evolution between a regime in which the surface is able to interact with both the tip protrusion and the rest of the tip (this happens when in-plane surface elasticity is weak or nonexistent [22]) to a regime in which only the protrusion interacts with the surface (this happens for large in-plane surface stiffness). Notice that there can be a transition between the two regimes as the cantilever position changes, as can be observed by inspection of the green trace in Figure 10d (peak force) and Figure 10e (maximum indentation). It is interesting to observe also that the order of the traces in Figure 10d is not the same as that of Figure 10e (the order of the red and green traces is inverted, in agreement with the force versus distance curves of Figure 10b). Additionally, Figure 10b shows that as the in-plane surface stiffness increases, the force curves resemble those obtained for the 1D SLS model (see Figure 7), since the effect of increasing contact surface area between the tip and the sample with increasing indentation is greatly diminished.

Notice that the peak forces of the green trace in Figure 10d are lower than those of the red trace, despite the fact that the indentation is greater for the green trace, as shown in Figure 10e. This occurs due to the attractive van der Waals interactions between the surface and bulk of the AFM tip, which partially offset the repulsive forces. The simulation parameters are the same as for Figure 8, except for the tip geometry, the 2D

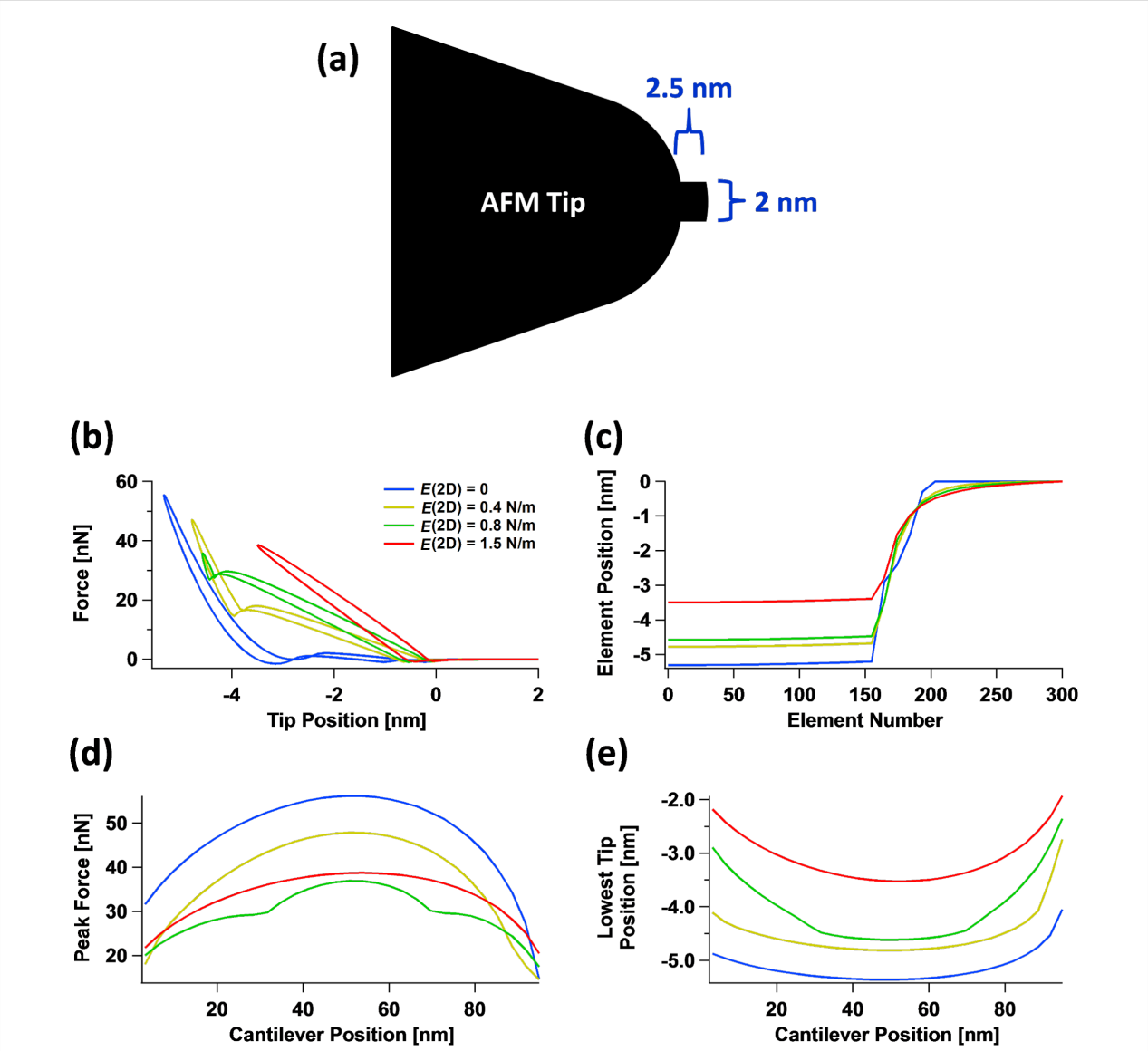

Figure 10: Simulation of the interaction of an AFM tip having an irregular protrusion with surfaces of varying 2D Young's modulus: (a) AFM tip geometry; (b) force curves; (c) surface indentation profiles; (d) peak force observed during one full oscillation of the cantilever versus cantilever position; (e) maximum indentation observed during one full oscillation of the cantilever versus cantilever position. E^{2D} is indicated in the legend of (b) and also applies to graphs (c–e).

Young's modulus values indicated in the legend of Figure 10b, and the cantilever positions indicated on the horizontal axis of Figure 10d,e.

The results of Figure 10 are instructive, but it could be argued that the tip irregularity considered is not common, and although not all tips are perfect, their profiles are often close enough to spherical. However, the simulations show that even in the case of relatively small differences in the tip profile, one can expect significant differences in the tip–sample interaction dynamics. To illustrate this, Figure 11 considers three different tip profiles (Figure 11a), namely spherical, parabolic and quartic. One would expect the variations in the interactions to be relatively small, especially when comparing the spherical and quartic profiles (the parabolic profile is a bit sharper than the other two), but Figure 11b shows that the force curves vary significantly both in steepness and in shape as the in-plane surface elasticity changes. It is interesting to note that not only the steepness and the area of the dissipation hysteresis loop changes, but also the maximum attractive force ("well depth" of the curves) can vary. This is because different tip profiles lead to different proximity between the surface elements and the surface of the tip, thus altering the overall attractive van der Waals interactions. These results suggest that even relatively mild de-

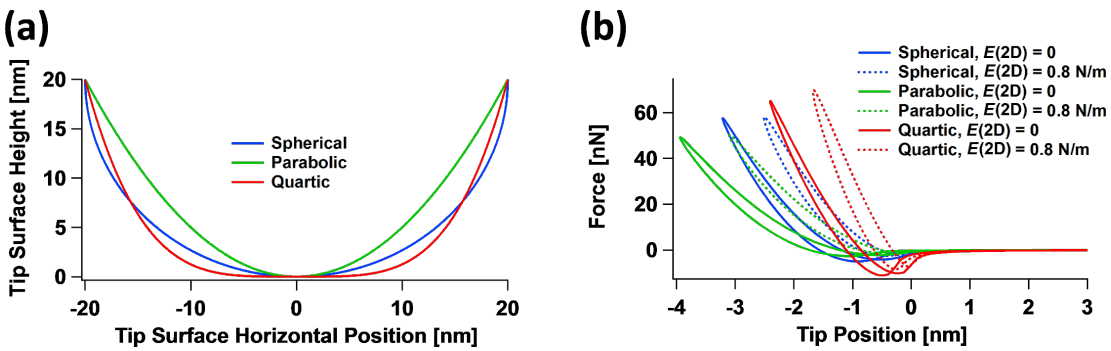

Figure 11: Interaction of tip curvature effects with in-plane surface elasticity effects: (a) three different tip surface profiles (spherical, parabolic and quartic); (b) tip–sample interaction force curves obtained for the profiles in (a) for two different values of the surface 2D Young's modulus. Notice that the magnitude of the maximum attractive force upon approaching the surface differs among the profiles considered because each results in a different proximity between the surface area elements and the tip surface. The simulation parameters, other than the tip profiles shown in (a), the 2D Young's modulus values indicated in the legend of (b) and the cantilever position (located 66 nm above the sample), are the same as for Figure 8.

viations from ideality in the tip shape are important if one wishes to carry out quantitative material property measurements.

The interaction of surface mechanical behaviors with tip geometry effects suggests that the exact tip geometry should not be ignored in a quantitative measurement. Thus interpretations of AFM observables based on 1D models for which the effect of tip geometry can be eliminated from the equations may in some cases lead to an incomplete and, depending on the sample properties, even an incorrect interpretation of the physics.

One final case to consider is the interaction between different tip geometries and the 2D surface Young's modulus within multifrequency AFM imaging [9]. As has been previously discussed [14,28,33], the interaction of the tip with the sample becomes much more complex in this case because multiple tip–sample impacts may occur within a single cycle of the dominant cantilever oscillation (generally the fundamental eigenmode oscillation). A striking example of the complexities and limitations involved is offered by Figure 12. Shown here are multifrequency AFM tip–sample force curves for the same free oscillation amplitude of the first (100 nm) and third eigenmodes (10 nm) for two different positions of the cantilever (80 nm for Figure 12a and 64 nm for Figure 12b), for the spherical and quartic tip profiles of Figure 11. The curves exhibit the expected shape and features, with double-impact loops being clearly discernible in Figure 12b, as well as the expected differences between the various cases considered. The clear differences observed in the nature of the tip–sample interactions are a consequence of intentional variations chosen for the 2D surface Young's modulus and for the tip profiles. However, it may be unexpected that the phase curves for the first eigenmode (Figure 12c) and for the third eigenmode (Figure 12d) are so similar to one another. In fact, the curves are hard to distinguish and may be indistinguishable in a real experiment where noise and other limitations may obscure the differences. This example thus highlights one of the most serious limitations in AFM spectroscopy characterization of nontrivial surfaces: the number of observables, even in multifrequency AFM, can be much smaller than the multiple degrees of freedom that describe the sample's material behavior. The latter may include degrees of freedom related to surface elastic or viscoelastic effects as well as subsurface viscoelastic effects, which may be linear or nonlinear. Each of these effects may require more than one parameter for a proper description, even for each individual Cartesian coordinate (in fact, the 1D SLS model, which is only a linear model, already requires three parameters!). Additionally, the various degrees of freedom of the sample may exhibit different interactions with the tip geometry and imaging parameters. Recall that the number of imaging parameters that the user can vary generally increases with the sophistication of the method; for example, bimodal AFM requires more imaging parameters than single-mode amplitude-modulation AFM [34].

With regards to the complexity in the tip–sample interactions (described in the previous paragraph for multifrequency AFM), it is worth noting that although tip–sample impacts are in principle much simpler for single-frequency AFM, during a scanning experiment, there is an interplay between scanning speed, cantilever oscillation frequency and the recovery time of the surface, such that tip–sample impacts may occur at a location that has not fully relaxed from a previous impact, thus leading to very complex interactions. In general, an experimental viscoelastic study involving intermittent-contact dynamic modes of AFM should consider the physical horizontal distance on the surface between the locations of two successive impacts in

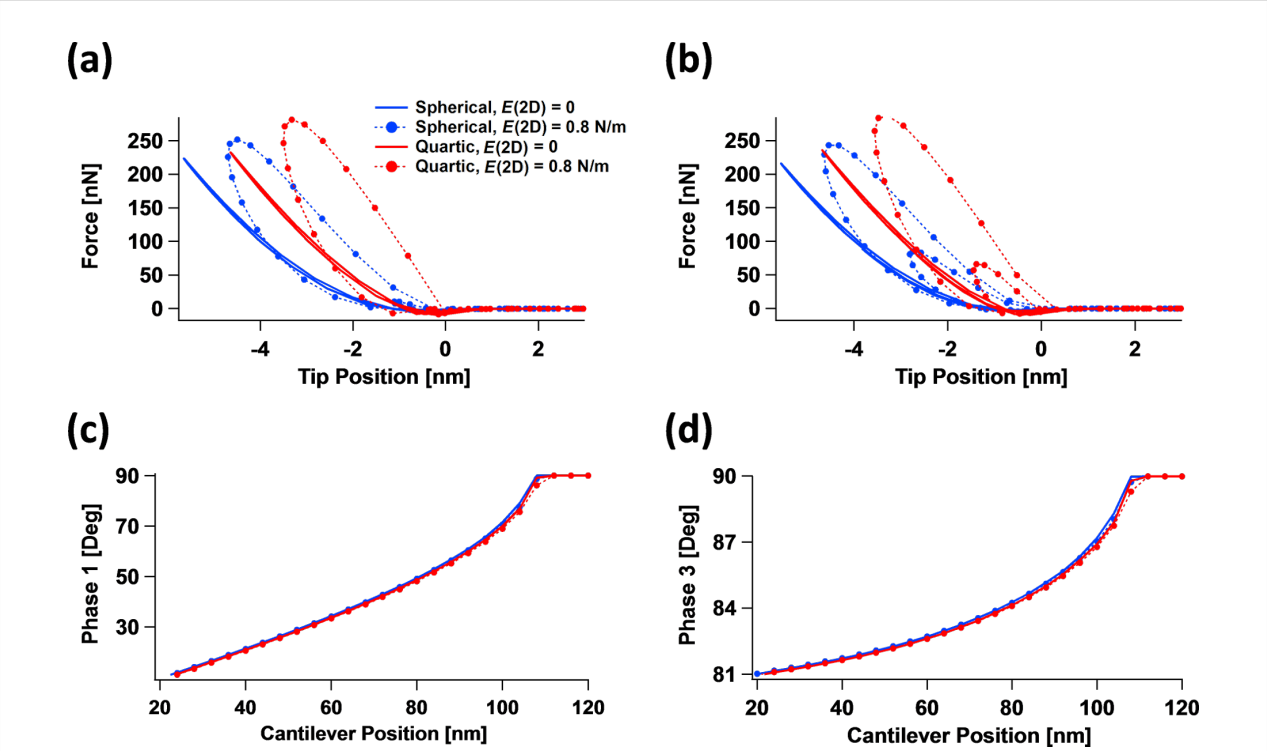

Figure 12: Interaction of tip curvature effects with in-plane surface elasticity effects for bimodal AFM using the first and third eigenmodes for the tip profiles shown in Figure 11a and the 2D surface Young's modulus values indicated in the legend of (a) (same for all graphs): (a) tip–sample interaction force curves for a cantilever position of 80 nm above the surface; (b) tip–sample interaction force curves for a cantilever position of 64 nm above the surface; (c) phase of the first eigenmode vs cantilever position; (d) phase of the third eigenmode vs cantilever position. The sample and first cantilever eigenmode parameters are the same as for Figure 8, except for the cantilever positions given above and in the axes of (c) and (d). The third eigenfrequency was set to 2.64 MHz with a force constant of 3.1 kN/m and the third eigenmode's free amplitude was set to 10 nm.

order to assess whether each impact can be assumed to occur on a fully relaxed region of the sample.

Software tool description

The software tool used for the simulations reported here was written in standard C programming language and is provided as supplementary information. The program performs a spectroscopy curve similar to the program provided with [22], except for the introduction of the 2D surface Young's modulus for the description of in-plane surface forces, as described in the first section of the Results and Discussion above. The code is based on trimodal excitation of the cantilever, whose simulation has been described in previous publications [14,22,23], and is thus not repeated here. The code uses constant-frequency, constant-amplitude excitation of the active eigenmodes, although other schemes or imaging modalities, such as scanning, can be implemented.

Conclusion

A simulation study has been carried out to gain insight into the mechanical behaviors exhibited by viscoelastic materials in the context of AFM imaging. The study is based on an enhanced version of a previously developed quasi-three-dimensional model that treats the surface as a collection of standard-linear-solid viscoelastic elements. It additionally considers the existence of in-plane surface forces via an approximate inclusion of a 2D Young's modulus for the top surface layer. A discussion of linear viscoelasticity concepts is also provided. Simulations are presented for single- and multifrequency intermittent-contact AFM imaging, whereby the corresponding surface indentation profiles and tip–sample interaction force curves, as well as their implications in the context of experimental interpretation are discussed. Where appropriate, discussions relevant to contact-mode-based methods such as contact-resonance and force-modulation AFM are included. A variety of intuitive, but not previously addressed phenomena are examined, which highlight the need for further research in the development of more physically accurate sample models for simulation and interpretation of AFM experiments. Finally, a software tool written in C programming language is provided as supporting information. The software can easily be used by individual researchers or could also be incorporated into existing simulation platforms that offer public access, such as VEDA [35] and dForce [36].

Supporting Information

Supporting Information File 1

Description of software files provided.
Overview of software files content and usage.
[http://www.beilstein-journals.org/bjnano/content/supplementary/2190-4286-7-49-S1.pdf]

Supporting Information File 2

Trimodal AFM with quasi-3D standard linear solid model sample, with in-plane surface effects added.
Software source file written in C programming language.
[http://www.beilstein-journals.org/bjnano/content/supplementary/2190-4286-7-49-S2.zip]

Supporting Information File 3

Parameter input file.
User-defined input parameters.
[http://www.beilstein-journals.org/bjnano/content/supplementary/2190-4286-7-49-S3.zip]

Acknowledgements

The author gratefully acknowledges support from the U.S. Department of Energy, Office of Science, Basic Energy Sciences through award DESC0011912. The author also wishes to thank Babak Eslami for the experimental image shown in Figure 4c, Alfredo Diaz for the experimental image shown in Figure 4d and Enrique López-Guerra for fruitful discussions.

References

1. Cleveland, J. P.; Anczykowski, B.; Schmid, A. E.; Elings, V. B. *Appl. Phys. Lett.* **1998,** *72,* 2163–2165. doi:10.1063/1.121434
2. Rabe, U.; Janser, K.; Arnold, W. *Rev. Sci. Instrum.* **1996,** *67,* 3281–3293. doi:10.1063/1.1147409
3. Yuya, P. A.; Hurley, D. C.; Turner, J. A. *J. Appl. Phys.* **2008,** *104,* No. 074916. doi:10.1063/1.2996259
4. Killgore, J. P.; Yablon, D. G.; Tsou, A. H.; Ganepalli, A.; Yuya, P. A.; Turner, J. A.; Proksch, R.; Hurley, D. C. *Langmuir* **2011,** *27,* 13983–13987. doi:10.1021/la203434w
5. Stan, G.; King, S. W.; Cook, R. F. *Nanotechnology* **2012,** *23,* No. 215703. doi:10.1088/0957-4484/23/21/215703
6. Stan, G.; Solares, S. D.; Pittenger, B.; Erina, N.; Su, C. *Nanoscale* **2014,** *6,* 962–969. doi:10.1039/C3NR04981G
7. Jesse, S.; Kalinin, S. V.; Proksch, R.; Baddorf, A. P.; Rodriguez, B. J. *Nanotechnology* **2007,** *18,* No. 435503. doi:10.1088/0957-4484/18/43/435503
8. Attard, P. *J. Phys.: Condens. Matter* **2007,** *19,* No. 473201. doi:10.1088/0953-8984/19/47/473201
9. Garcia, R.; Herruzo, E. T. *Nat. Nanotechnol.* **2012,** *7,* 217–226. doi:10.1038/nnano.2012.38
10. Herruzo, E. T.; Perrino, A. P.; Garcia, R. *Nat. Commun.* **2014,** *5,* No. 3126. doi:10.1038/ncomms4126
11. Platz, D.; Forchheimer, D.; Tholén, E.; Haviland, D. B. *Nanotechnology* **2012,** *23,* No. 265705. doi:10.1088/0957-4484/23/26/265705
12. Borysov, S. S.; Platz, D.; de Wijn, A. S.; Forchheimer, D.; Tholén, E.; Balatsky, A. V.; Haviland, D. B. *Phys. Rev. B* **2013,** *88,* No. 115405. doi:10.1103/PhysRevB.88.115405
13. López-Guerra, E. A.; Solares, S. D. *Beilstein J. Nanotechnol.* **2014,** *5,* 2149–2163. doi:10.3762/bjnano.5.224
14. Solares, S. D. *Beilstein J. Nanotechnol.* **2014,** *5,* 1649–1663. doi:10.3762/bjnano.5.176
15. Sahin, O.; Magonov, S.; Su, C.; Quate, C. F.; Solgaard, O. *Nat. Nanotechnol.* **2007,** *2,* 507–514. doi:10.1038/nnano.2007.226
16. García, R.; Pérez, R. *Surf. Sci. Rep.* **2002,** *47,* 197–301. doi:10.1016/S0167-5729(02)00077-8
17. Menard, K. P. *Dynamic Mechanical Analysis, A Practical Introduction;* CRC Press LLC: Boca Ration, USA, 1999. doi:10.1201/9781420049183
18. Muraleedharan Nair, T.; Kumaran, M. G.; Unnikrishnan, G.; Pillai, V. B. *J. Appl. Polym. Sci.* **2009,** *112,* 72–81. doi:10.1002/app.29367
19. Rubinstein, M.; Colby, R. H. *Polymer Physics;* Oxford University Press: New York, USA, 2003.
20. Israelachvili, J. *Intermolecular & Surface Forces;* Academic Press: Bury St. Edmunds, UK, 2000.
21. Maivald, P.; Butt, H. J.; Gould, S. A. C.; Prater, C. B.; Drake, B.; Gurley, J. A.; Elings, V. B.; Hansma, P. K. *Nanotechnology* **1991,** *2,* 103–106. doi:10.1088/0957-4484/2/2/004
22. Solares, S. D. *Beilstein J. Nanotechnol.* **2015,** *6,* 2233–2241. doi:10.3762/bjnano.6.229
23. Chyasnavichyus, M.; Young, S. L.; Tsukruk, V. V. *Langmuir* **2014,** *30,* 10566–10582. doi:10.1021/la404925h
24. Vargas Guzman, H. A. Modeling peak interaction forces of soft matter with dynamic AFM in liquid. Ph.D. Thesis, Universidad Autonoma de Madrid, Spain, 2014.
25. Roylance, D. "Engineering viscoelasticity". Massachusets Institute of Technology, 2001; http://ocw.mit.edu/courses/materials-science-and-engineering/3-11-mechanics-of-materials-fall-1999/modules/visco.pdf (accessed Oct 27, 2015).
26. Yablon, D. G.; Grabowski, J.; Chakraborty, I. *Meas. Sci. Technol.* **2014,** *25,* 055402. doi:10.1088/0957-0233/25/5/055402
27. Stark, M.; Stark, R. W.; Heckl, W. M.; Guckenberger, R. *Proc. Natl. Acad. Sci. U. S. A.* **2002,** *99,* 8473–8478. doi:10.1073/pnas.122040599
28. Ebeling, D.; Eslami, B.; Solares, S. D. *ACS Nano* **2013,** *7,* 10387–10396. doi:10.1021/nn404845q
29. Solares, S. D.; Dasgupta, S.; Schultz, P. A.; Kim, Y.-H.; Musgrave, C. B.; Goddard, W. A., III. *Langmuir* **2005,** *21,* 12404–12414. doi:10.1021/la052029s
30. Takayanagi, K.; Tanishiro, Y.; Takahashi, M.; Takahashi, S. *J. Vac. Sci. Technol., A* **1985,** *3,* 1502–1506. doi:10.1116/1.573160
31. Takayanagi, K.; Tanishiro, Y.; Takahashi, S.; Takahashi, M. *Surf. Sci.* **1985,** *164,* 367–392. doi:10.1016/0039-6028(85)90753-8
32. Deng, Z.; Klimov, N. N.; Solares, S. D.; Li, T.; Xu, H.; Cannara, R. J. *Langmuir* **2013,** *29,* 235–243. doi:10.1021/la304079a
33. Solares, S. D.; An, S.; Long, C. J. *Beilstein J. Nanotechnol.* **2014,** *5,* 1637–1648. doi:10.3762/bjnano.5.175
34. Rodríguez, T. R.; García, R. *Appl. Phys. Lett.* **2004,** *84,* 449–451. doi:10.1063/1.1642273
35. Melcher, J.; Hu, S.; Raman, A. *Rev. Sci. Instrum.* **2008,** *79,* 061301. doi:10.1063/1.2938864

36. Guzman, H. V.; Garcia, P. D.; Garcia, R. *Beilstein J. Nanotechnol.* **2015,** *6,* 369–379. doi:10.3762/bjnano.6.36

BEILSTEIN JOURNAL OF NANOTECHNOLOGY

Characterization of spherical domains at the polystyrene thin film–water interface

Khurshid Ahmad[1,2], Xuezeng Zhao[1], Yunlu Pan[*1] and Danish Hussain[3]

Full Research Paper

Open Access

Address:
[1]Key Laboratory of Micro-Systems and Micro-Structures Manufacturing, Ministry of Education and School of Mechatronics Engineering, Harbin Institute of Technology, Harbin 150001, P.R. China, [2]Department of Mechanical Engineering, Main Campus, University of Engineering and Technology, Peshawar, Pakistan and [3]State Key Laboratory of Robotics and Systems and School of Mechatronics Engineering, Harbin Institute of Technology, Harbin 150001, P.R. China

Email:
Yunlu Pan[*] - yunlupan@hit.edu.cn

* Corresponding author

Keywords:
AFM; blisters; contaminants; defects; nanobubbles; water permeation

Beilstein J. Nanotechnol. **2016,** *7,* 581–590.
doi:10.3762/bjnano.7.51

Received: 30 September 2015
Accepted: 05 April 2016
Published: 20 April 2016

This article is part of the Thematic Series "Advanced atomic force microscopy techniques IV".

Guest Editor: T. Glatzel

Abstract

Spherical domains that readily form at the polystyrene (PS)–water interface were studied and characterized using atomic force microscopy (AFM). The study showed that these domains have similar characteristics to micro- and nanobubbles, such as a spherical shape, smaller contact angle, low line tension, and they exhibit phase contrast and the coalescence phenomenon. However, their insensitivity to lateral force, absence of long-range hydrophobic attraction, and the presence of possible contaminants and scratches on these domains suggested that these objects are most likely blisters formed by the stretched PS film. Furthermore, the analysis of the PS film before and after contact with water suggested that the film stretches and deforms after being exposed to water. The permeation of water at the PS–silicon interface, caused by osmosis or defects present on the film, can be a reasonable explanation for the nucleation of these spherical domains.

Introduction

Thin films of several nanometer thickness have long been a topic of interest for researchers. The application of such thin films has been demonstrated in nonvolatile memory devices [1], sensors [2,3], for the modification of emissive properties of glass [4,5], and for the modification of surface properties [6-8] (e.g., hydrophobicity, oleophobicity). The study of the thermal [4], optical [5], mechanical [9,10], and interfacial [6-8] properties of thin films is a broader area of interest. Various physical and chemical processes have been used to produce such films. Polystyrene (PS) is one of the most widely used materials for the preparation of thin films. Thin PS films have been prepared by spin coating [11-15]. So far, these films have been used in different studies related to surface and interface science, for example, to study boundary slip and micro-/nanobubble forma-

tion [15-19]. Nanobubbles are gaseous domains that may be found at a solid–liquid interface. Over the past few decades, dedicated research has been carried out on nanobubbles at the solid–liquid interface. AFM has been proven to be a promising technique for the imaging and analysis of micro-/nanobubbles. Studies have reported surface micro-/nanobubbles on thin PS films immersed in water [15-22]. Bubbles ranging from tens of nanometers to several micrometers have been reported on thin PS films [15-19,21], and the different characteristics of bubbles have been studied by various research groups [15,16,19,23,24]. Studies have shown that the contact angle of the nanoscale gaseous bubbles is smaller than the macroscopic gaseous bubbles (measured from the air side) [15]. It has also been reported that the contact angle of the gaseous bubble increases with the lateral size in each independent size scale [15]. Similarly, increased surface roughness and the influx of gas from the interfacial gas enrichment favors formation of larger gaseous bubbles [15,19]. In addition, other studies have reported different phenomena on the PS-coated surface such as dewetting from the silicon surface and formation of nanoindents and blisters [11,25-28]. It has been shown that the PS film can be dewetted from the silicon surface upon the contact with water [11]. Wang et al. [25] found that the nanobubbles can form nanoindents on the PS-coated surface due to high gas pressure inside the bubble. Additionally, Maebayashi [12] and Berkelaar et al. [26] reported on the nucleation process of blisters on PS films. These studies reveal the possibility that nanobubbles may coexist with blisters on thin PS films. This study employs AFM and optical microscopy to characterize the spherical-shaped domains that readily nucleate on the PS film after immersion in DI water. The radius, height, contact angle (CA) and line tension are analyzed in detail. The coalescence, stiffness and phase contrast analysis were also studied. Moreover, changes in surface topography, before and after the contact with water, have also been discussed.

Experimental

Materials and equipment

The following materials and equipment were used in this study: deionized water purified with a Milli-Q A10 system, silicon dioxide (Lijing, LLC, China), polystyrene beads (average MW ≈350,000; Aldrich, USA), AFM cantilevers (RTESPA, DNP, SNL; Bruker, USA), AFM (Innova; Bruker, USA), digital microscope (KH1300; Hirox, Japan), spin coater (KW-4A; SETCAS Electronics Co. Ltd., Beijing, China), and drop meter (MAIST, Vision, China).

Sample preparation

Polystyrene thin films were spin-coated onto silicon dioxide wafers. Prior to spin coated, the silicon dioxide wafers were cleaned using piranha solution of 3:1 (v/v) sulfuric acid/hydrogen peroxide for 30 min [8]. The wafers were further cleaned with acetone, ethanol and DI water in an ultrasonic sonicator, followed by drying with clean, compressed air. The PS solution (10:1 v/w of toluene/PS) was prepared by dissolving PS beads in toluene. The PS film was spin-coated each of the silicon dioxide wafers at a speed of 3000 rpm. Afterward, the PS-coated surfaces were cured in an electric oven for 4 h at 50 °C. The surfaces were rinsed with DI water and dried with clean, compressed air. In certain cases, the surfaces were not rinsed before scanning with AFM. The CA of the water on the PS-coated surfaces was 85 ± 4°. The surfaces were scanned in air using tapping mode atomic force microscopy (TM-AFM). A typical image of the PS-coated surface is given in Figure 1.

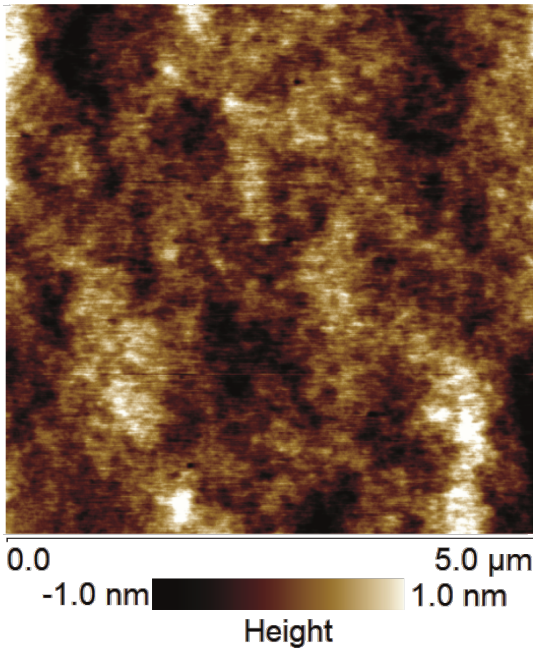

Figure 1: Topographic image of a typical PS-coated surface. The roughness average (R_a) was 0.27 nm, the root mean square (RMS) was 0.35 nm, and the maximum peak-to-valley height of the image (R_{max}) was 2.86 nm.

Atomic force microscopy analysis

The TM-AFM technique was used to analyze the PS-coated surfaces and the spherical domains. A set point ratio of 85 ± 5% of the free air amplitude was used for scanning in the liquid. We used silicon nitride cantilevers with a nominal tip radius of 20 nm and nominal stiffness of 0.05 N/m. The resonance frequency of the cantilever immersed in DI water was 35.0 kHz. Furthermore, an average scan rate of 1 Hz was used to image the surface topography and the micro/nano spherical domains. Moreover, the thickness of the PS film, measured with AFM using the scratch profile method, was 42.0 ± 7 nm.

Results and Discussion

Analysis of radius, lateral size and height of spherical objects on PS thin films

Various-sized spherical or nearly spherical objects were found at the PS–water interface. The size ranged from several hundreds of nanometers to several micrometers, as shown in Figure 2a. The dimensions of the spherical objects were obtained by making the tip correction [15,29]. The apparent radius of curvature (R_{ac}), corrected radius of curvature (R_c), radius of the bubble (R_b), and contact angle (θ) were calculated using the following equations [15,18]:

$$R_{ac} = \left(R_l^2 + h^2\right)/2h \quad (1)$$

$$R_c = R_{ac} - r_t \quad (2)$$

$$R_b = \sqrt{2R_c h - h^2} \quad (3)$$

$$\theta = 2\tan^{-1}\left(\frac{h}{R_b}\right) \quad (4)$$

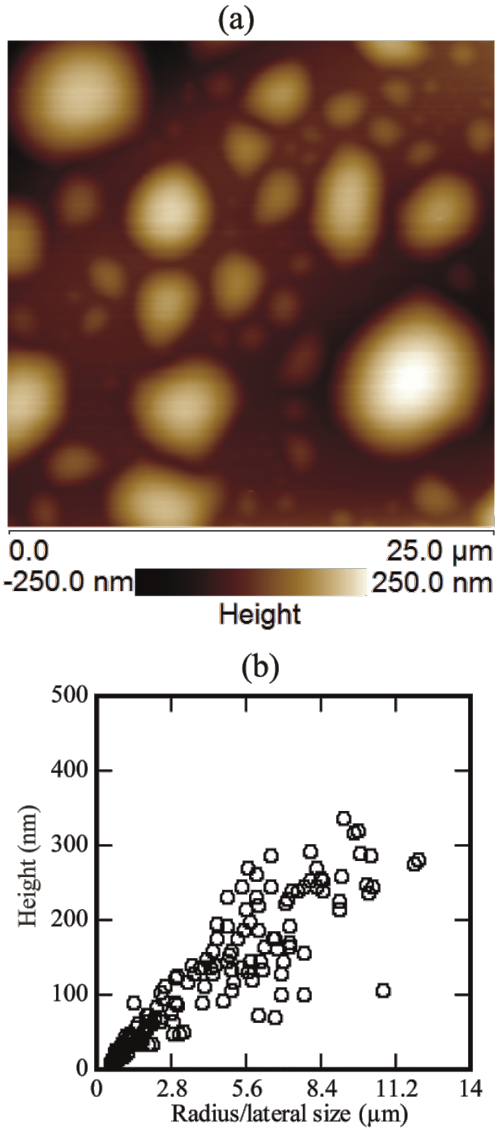

Figure 2: (a) AFM image of micro/nano spherical domains on a PS-coated surface, immersed in DI water. A number of spherical or nearly spherical objects can be seen in the image. (b) Summary of the height and radius/lateral size of the spherical domains. Additional images of the so-called spherical domains are shown in Supporting Information File 1, Figure S1.

where, R_l is the lateral size/radius of the domain without tip correction, h is the height of the spherical domain, and r_t is the nominal radius of the tip. A number of spherical domains were found on different PS-coated surfaces immersed in DI water. A typical image showing a number of spherical or nearly spherical domains is shown in Figure 2a. These domains were analyzed through the Nanoscope analysis software (Bruker, USA). The details of the radius/lateral size and the height were collected. A brief summary is given in Figure 2b. Figure 2b illustrates that the height of the spherical domains changes almost linearly with respect to the radius/lateral size. The lateral size varied between 0.5 and 14.0 µm while the height varied from 7.0 to 300.0 nm.

Analysis of the contact angle

The contact angle of these domains was also analyzed. The analysis showed a very small contact angle when measuring from the inner side of the spherical domain. Generally, the contact angles were approximately in the range of 2.0 to 6.0°. A summary of the contact angles of the spherical domains found on various PS-coated surfaces immersed in DI water is given in Figure 3a. Figure 3a shows that the contact angle changes linearly with respect to radius/lateral size up to 2.0 µm. Beyond this size, the contact angle changes in such a way that an exact correlation becomes difficult.

Analysis of line tension

The line tension is defined as the excess energy per unit length of the three phase contact line [30]. The magnitude of the line tension affects the shape of the bubble [29,31,32]. Negative as well as positive values of line tension have been reported in previous studies [32-34]. Therefore, the sign of the line tension is still a controversial debate [35]. Studies have shown that the magnitude of line tension for nanobubbles ranges from nN to pN [32-35]. The line tension of the spherical domains analyzed in this study was calculated using the following equation [19,33,35]:

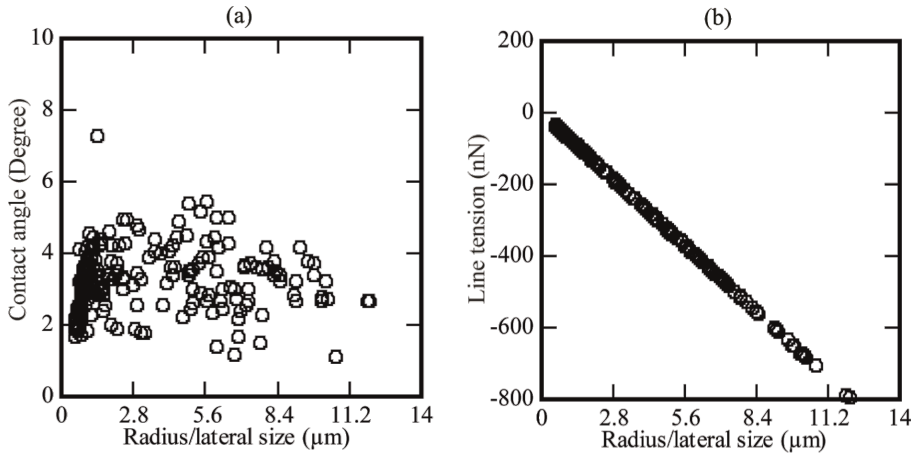

Figure 3: (a) Summary of the contact angle versus the radius/lateral size of the spherical objects. (b) Summary of the line tension of the spherical objects on PS-coated surfaces.

$$\cos\theta = \cos\theta_M - \frac{\tau}{\gamma_{lg} R_b}, \quad (5)$$

where θ is the contact angle of the spherical domains, θ_M is the macroscopic contact angle, τ is the line tension, and γ_{lg} is the surface tension. The results were plotted against the radius of the spherical objects, as shown in Figure 3b. It was found that the line tension varies linearly with the radius/lateral size. This analysis also showed that the magnitude of the line tension of these objects is several orders of magnitude larger (30 nN to 800 nN) than some of the previously reported values of the line tension for nanobubbles [19,33,35]. However, the magnitude is still within the range proposed in other studies (10 pN to 10 μN) [35].

Coalescence of spherical objects

Based on the information collected through AFM, no coalesce was observed. However, coalescence of the objects was observed in optical microscopy (Digital Microscope, KH1300; Hirox, Japan; resolution ≈0.07 μm) experiments. Some examples of the micro-/nano spherical domains are shown in Figure 4a–d.

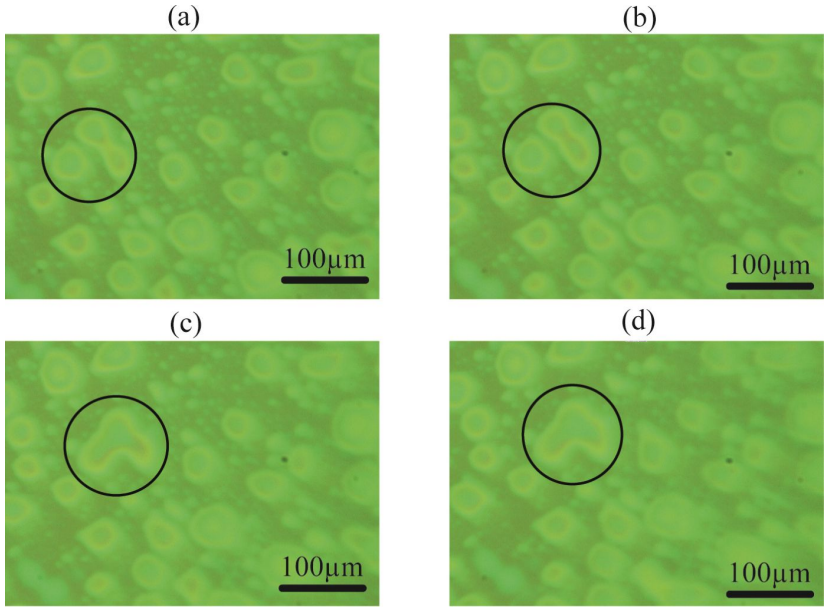

Figure 4: Optical images of the coalescence of spherical domains formed on PS-coated surfaces. (a–d) Time lapse images where the encircled area shows the coalescence of an irregular domain with an approximately spherical domain in the vicinity. Additional examples of coalescence are given in Supporting Information File 1, Figure S2 and Figure S3.

The study suggested that the coalescence might result in spherical and irregular-shaped domains (further information is given in Supporting Information File 1, Figure S2 and Figure S3). The presence of additional domains in the vicinity of the domains merging together can help in growth of these domains. Moreover, the shape of these domains can be affected by the presence of additional domains as well as binding of the PS film to the silicon substrate. The presence of other domains in the surrounding and less tightly bound film might favor coalescence and hence produce larger domains (see Figure 4 above, and Supporting Information File 1, Figure S2 and Figure S3). As pointed out earlier, it is also possible that the coalescence of these domains result in irregular-shaped domains, as shown in Figure 2a. Moreover, the AFM study showed that domains with lateral size ≤1.0 µm (approximately), have an almost spherical shape (see Supporting Information File 1, Figure S1).

Stiffness of the spherical objects

Nanobubbles are softer and the tip–bubble interaction can affect the shape and movement of the bubbles [19,29,36-38]. In order to differentiate the spherical domains from micro-/nanobubbles, the surface was scanned in contact mode AFM (CM-AFM) as well as TM-AFM. The typical images are shown in Figure 5. The section analysis of the spherical domains shown in the Figure 5 is given in Figure 6a–c. In Figure 6a–c there is no evident difference in the shape of the spherical domains scanned with TM-AFM or CM-AFM. It shows that these domains are stiff enough to resist the deformation due to lateral force applied by the tip in CM-AFM. Moreover, in addition to the softer nature, previous studies have also reported that the presence of gaseous bubbles give rise to a long range hydrophobic attraction force [39-41]. Therefore, to analyze this aspect, the approach and retraction force curves were obtained on a bubble as well as the PS-coated surface. The results are shown in Figure 7a,b where it is obvious that there is no clear difference in the approach force curves obtained on the spherical domain or the PS-coated surface. The so-called hydrophobic attraction force was expected in the case of the gaseous bubbles. However, these force curves are identical and suggest that the nature of these objects is not similar to that of bubbles. Moreover, additional force curves obtained on different sized spherical domains are given in Supporting Information File 1, Figure S6.

Analysis of phase contrast and presence of contaminants on the spherical domains

The phase shift is sensitive to the variation in the local surface property [23]. Any change in the surface property can be easily traced through TM-AFM phase contrast analysis. The height images of the spherical domains along with the corresponding phase images are given in Figure 8a,b. The phase contrast in

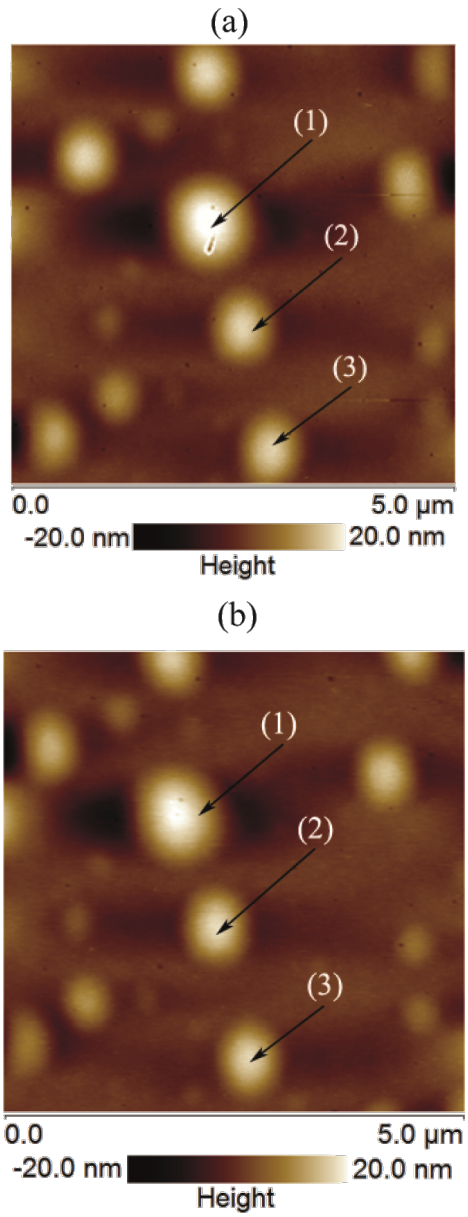

Figure 5: Height images of spherical objects on PS-coated surfaces obtained using (a) contact mode (b) tapping mode at 90% set point ratio.

Figure 8b shows a change in the surface property. Furthermore, the height analysis as well as the phase images of these spherical objects showed the presence of contaminants on the top of these domains (Figure 9a,b). Similarly, in some cases, we also observed scratch-like patterns on these spherical domains (Figure 9b).

The scratches and possible contaminants on these domains bring doubt to the possibility that these might be gaseous bubbles, but rather indicate the likelihood of deformed or stretched PS film [26].

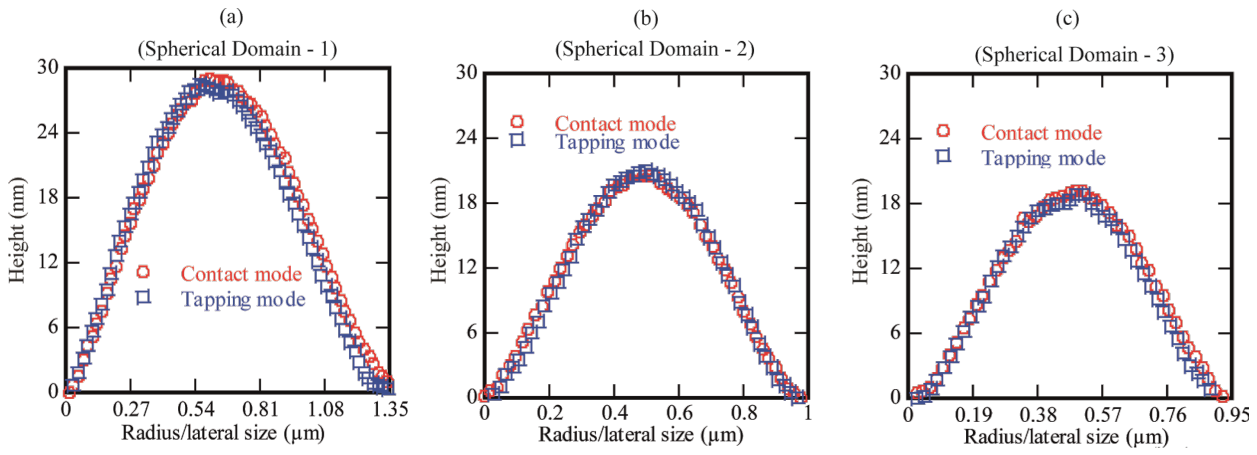

Figure 6: Section analysis of spherical domains imaged in contact mode and tapping mode (shown in Figure 5). (a) Section of spherical domain (1). (b) Section of spherical domain (2). (c) Section of spherical domain (3). The circles show the section of the spherical domain imaged in contact mode while the squares show the section of the spherical domains imaged in tapping mode.

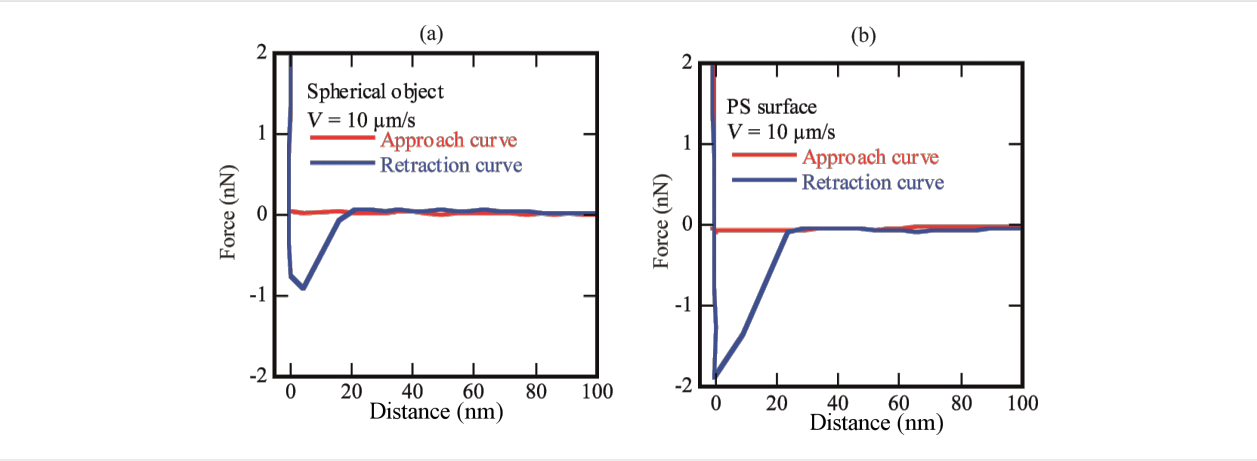

Figure 7: (a) Approach and retraction curves for a spherical object. (b) Approach and retraction curves for a PS-coated surface.

Analysis of the PS film after exposure to water

It is proposed that if these objects are not gaseous bubbles, then they are most likely blisters or deformed PS film due to permeation of water through the film [26]. The permeation of water may stretch the PS film and the footprints might be left behind after the removal of water [26]. Therefore, the topography of the PS film before and after the exposure to DI water was also analyzed. The height images, acquired before and after the exposure to water, are shown in Figure 10a–d.

These Figures show that the topography of the PS-coated surface has changed after coming into contact with water. The height section analysis in Figure 10c,d shows that the asperities on the surface exposed to water are comparatively larger than the dry surface.

Discussion

A series of experiments were conducted in order to characterize the spherical or nearly spherical domains that readily nucleate on the PS-coated surface after immersion in water. The focus of this study was to find out whether the micro-/nanobubbles coexist with the spherical or nearly spherical blisters or if these phenomena occur independently. Micrometer-sized spherical objects were found on the PS-coated surfaces. The phase images clearly showed phase contrast at the locations of these objects (Figure 8b). This suggested a change in the local surface property. However, these objects remained insensitive to contact as well as lateral force. Unlike the micro-/nanobubbles, the force measurements did not show long range hydrophobic attraction (Figure 7a). These objects did not show significant movement or deformation during the CM-AFM measurements (Figure 5a,b). Furthermore, contaminants and scratch-like

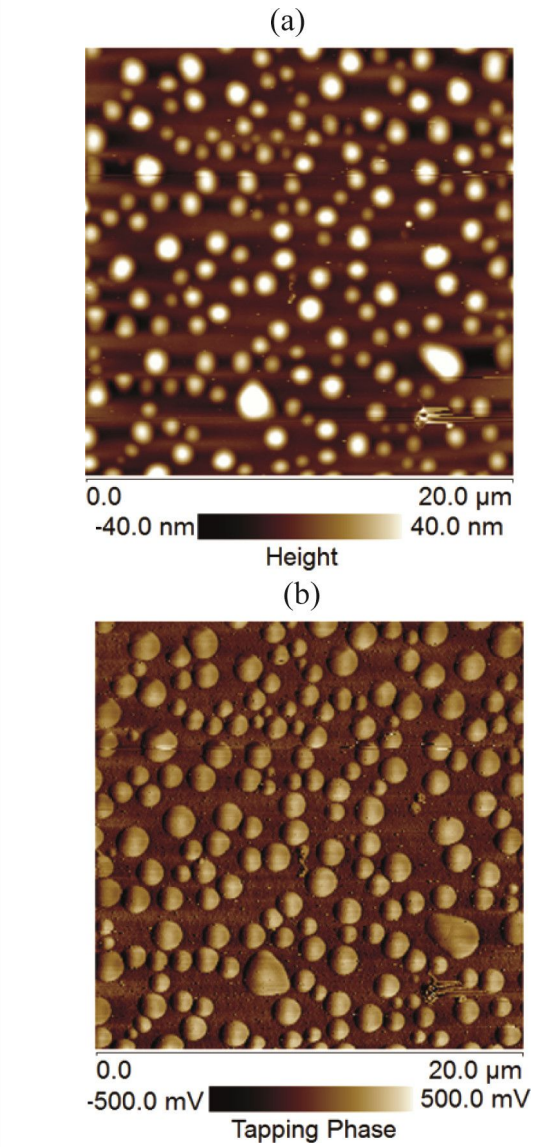

Figure 8: (a) Height image of spherical domains. (b) Phase image of spherical domains. A clear phase contrast can be observed in the image.

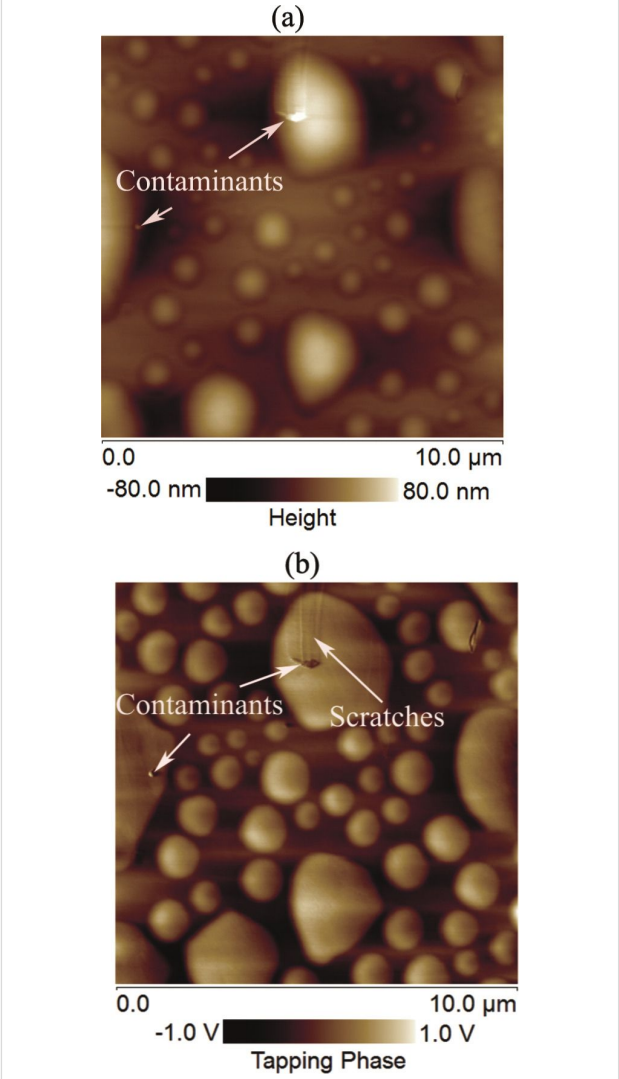

Figure 9: AFM topographic and phase images of PS-coated surfaces obtained in air and water. (a,b) Topographic and phase images, respectively, of the PS-coated surface obtained in DI water. The unknown objects as well as the scratches are clearly visible on the domains. Additional images are given in Supporting Information File 1, Figure S4.

patterns were observed on these spherical objects (Figure 9a,b). To the best of our knowledge, this type of phenomena has not yet been reported for micro-/nanobubbles. In our opinion, contaminants, if present on the surface of the nanobubbles, would not be stable enough to be imaged with CM-AFM or TM-AFM. The presence of the contaminants and scratches highly doubted the idea that these domains could be gaseous bubbles but rather supported the idea that these are the blisters from stretched PS film which appear as spherical micro-/nanobubbles. Additionally, the topographic images obtained before and after contact of water with the PS film showed stretched regions or indents (Figure 10a–d and Supporting Information File 1, Figure S5). A reasonable explanation for the formation of these stretched regions or indents is most likely the penetration of water into the film [26]. As a result, these objects nucleate and leave a footprint as the film dries. Contrary to the optical microscopy study of Berkelaar et al. [26], the proposed blisters were also found upon exposure to ethanol (Figure 11b). Therefore, the hydrophilic silicon surface can further explain the formation of the blisters at the PS–silicon interface. It can be proposed that due to the strong affinity of water towards silicon dioxide, water easily penetrates into the weakly bonded sites of the PS film and the silicon dioxide substrate.

The study of Berkelaar et al. [26] further explained that the smaller water pockets are formed at the defects occurring at the

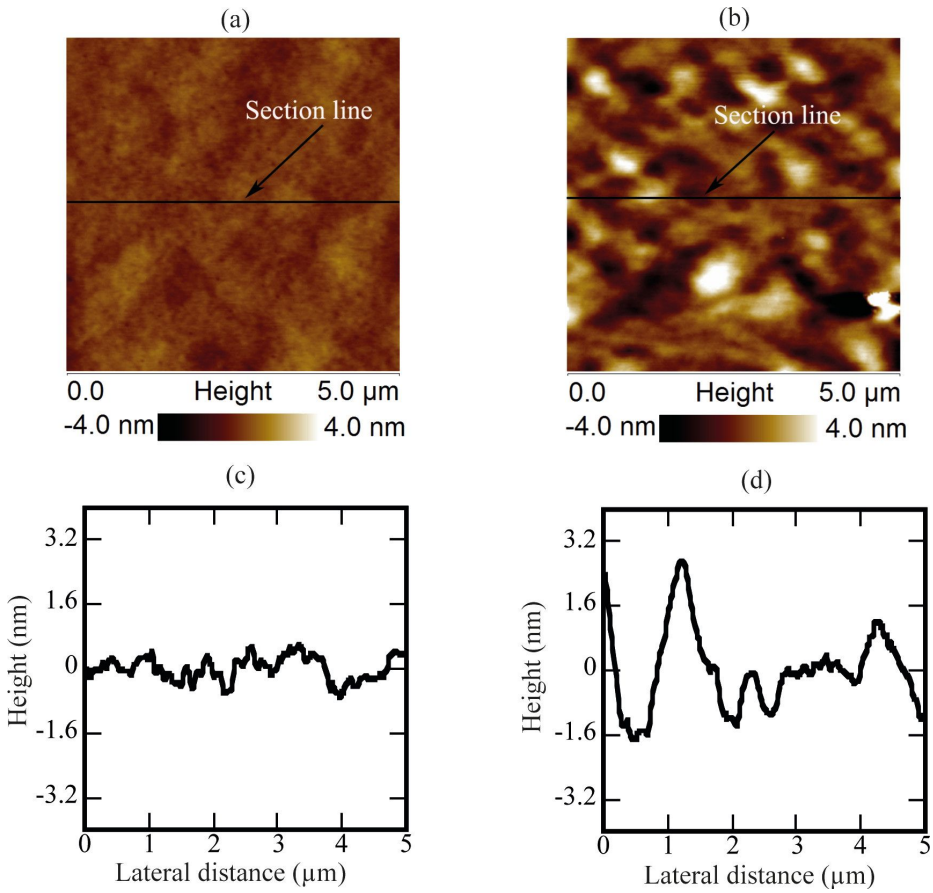

Figure 10: (a,b) AFM images of the PS-coated surface before and after the exposure to water, respectively. (c,d) Height profile analysis of the image of the PS-coated surface before and after the exposure to water. The height profile analysis clearly shows the enhanced features formed on the PS-coated surface. Additional information collected from other surfaces prepared with similar procedures is shown in Supporting Information File 1, Figure S5.

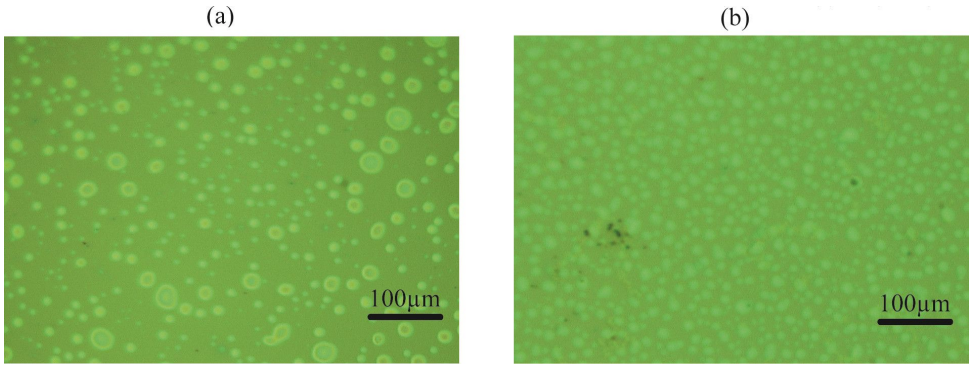

Figure 11: Optical images of blisters formed on a PS-coated surface immersed in (a) DI water and (b) ethanol.

interface of silicon and the PS film. As soon as the osmotic pressure equals the fracture pressure, the PS film detaches from the silicon surface and the blisters begin to form. Their explanation that the water penetrates into the PS–silicon dioxide through defective sites on the PS film is further supported by our study. As was noted, contaminants were present on the blisters as well as on the surface (Figure 9a,b). These defective sites provide a passage for water penetration through the film. This phenomenon leads to the detachment of the PS film from the silicon substrate at the sites that are relatively weakly bonded.

Silicon is hydrophilic in nature, and therefore, in the presence of water, the PS film might easily detach. Furthermore, an additional analysis of these domains was also conducted by taking into account the modulus of elasticity of the PS film and the pressure inside the spherical domains. The results are given in Supporting Information File 1, Figure S7. The analysis showed that the surface excess energy approximately ranges from 3.0 to 72.0 nJ/m^2 for a blister size of 0.5 to 12 μm.

Conclusion

Spherical domains were found on PS-coated surface. The height, contact angle and line tension analysis suggested a close resemblance of these domains to the previously reported micro-/nanobubbles on the PS-coated surfaces. However the analysis of phase images, force curves and the tip–bubble interaction suggested that these objects are different from the so-called micro-/nanobubbles. The absence of long range hydrophobic attraction force, the formation of scratches and the presence of contaminates on these domains strongly suggested that these are blisters that are formed by the stretching and deformation of the PS film in water. It can be concluded that the presence of contaminates and the defect sites on the PS film provide weak points for the penetration of water through the film. This then causes the detachment of the PS film from the silicon dioxide substrate. The strong affinity of silicon surface towards water further enhances the water permeation and the detachment process of the PS film from the silicon substrate. This can further lead to coalescence of the blisters. Furthermore, blisters can also nucleate in ethanol. The results of the present study support the study of Berkelaar et al. [26] and suggests that the spherical objects, which readily form on the PS-coated surface upon contact with water or ethanol, are most likely blisters formed due to the deformation of the PS film and are not micro-/nanobubbles.

Supporting Information

Additional information of spherical domains imaged on various surfaces, coalescence at various locations, contaminants and scratches on the domains, surface topographic images before and after exposure to water, additional force curves obtained on different sized spherical domains, and analysis of surface excess energy per unit area.

Supporting Information File 1

Additional experimental information.
[http://www.beilstein-journals.org/bjnano/content/supplementary/2190-4286-7-51-S1.pdf]

Acknowledgements

This research was supported by the National Natural Science Foundation of China (Grant number: 51475118 and 51505108). K.A. and D.H. acknowledge the support of the Higher Education Commission of Pakistan for study in China.

References

1. Ouyang, J.; Chu, C.-W.; Szmanda, C. R.; Ma, L.; Yang, Y. *Nat. Mater.* **2004,** *3,* 918–922. doi:10.1038/nmat1269
2. Sakai, Y.; Sadaoka, Y.; Matsuguchi, M. *Sens. Actuators, B* **1996,** *35,* 85–90. doi:10.1016/S0925-4005(96)02019-9
3. Lépinay, S.; Kham, K.; Millot, M.-C.; Carbonnier, B. *Chem. Pap.* **2012,** *66,* 340–351. doi:10.2478/s11696-012-0134-6
4. Meszaros, R.; Merle, B.; Wild, M.; Durst, K.; Göken, M.; Wondraczek, L. *Thin Solid Films* **2012,** *520,* 7130–7135. doi:10.1016/j.tsf.2012.07.086
5. Aspnes, D. E. *Thin Solid Films* **1982,** *89,* 249–262. doi:10.1016/0040-6090(82)90590-9
6. Li, Y.; Bhushan, B. *Soft Matter* **2015,** *11,* 7680–7695. doi:10.1039/C5SM00763A
7. Jing, D.; Bhushan, B. *Langmuir* **2013,** *29,* 14691–14700. doi:10.1021/la4030876
8. Ahmad, K.; Zhao, X.; Pan, Y.; Wang, W.; Huang, Y. *J. Phys. Chem. C* **2015,** *119,* 12531–12537. doi:10.1021/acs.jpcc.5b03426
9. Hardwick, D. A. *Thin Solid Films* **1987,** *154,* 109–124. doi:10.1016/0040-6090(87)90357-9
10. Thornton, J. A.; Hoffman, D. W. *Thin Solid Films* **1989,** *171,* 5–31. doi:10.1016/0040-6090(89)90030-8
11. Bonaccurso, E.; Butt, H.-J.; Franz, V.; Graf, K.; Kappl, M.; Loi, S.; Niesenhaus, B.; Chemnitz, S.; Böhm, M.; Petrova, B.; Jonas, U.; Spiess, H. W. *Langmuir* **2002,** *18,* 8056–8061. doi:10.1021/la020429z
12. Maebayashi, M.; Matsuoka, T.; Koda, S.; Hashitani, R.; Nishio, T.; Kimura, S.-i. *Polymer* **2004,** *45,* 7563–7569. doi:10.1016/j.polymer.2004.09.011
13. Neto, C.; Jacobs, K. *Phys. A (Amsterdam, Neth.)* **2004,** *339,* 66–71. doi:10.1016/j.physa.2004.03.049
14. Bhushan, B.; Pan, Y. *Langmuir* **2011,** *27,* 9425–9429. doi:10.1021/la201636g
15. Li, D.; Zhao, X. *Colloids Surf., A* **2014,** *459,* 128–135. doi:10.1016/j.colsurfa.2014.06.022
16. Bhushan, B.; Pan, Y.; Daniels, S. *J. Colloid Interface Sci.* **2013,** *392,* 105–116. doi:10.1016/j.jcis.2012.09.077
17. Agrawal, A.; Park, J.; Ryu, D. Y.; Hammond, P. T.; Russell, T. P.; McKinley, G. H. *Nano Lett.* **2005,** *5,* 1751–1756. doi:10.1021/nl051103o
18. Simonsen, A. C.; Hansen, P. L.; Klösgen, B. *J. Colloid Interface Sci.* **2004,** *273,* 291–299. doi:10.1016/j.jcis.2003.12.035
19. Li, D.; Jing, D.; Pan, Y.; Wang, W.; Zhao, X. *Langmuir* **2014,** *30,* 6079–6088. doi:10.1021/la501262a
20. Wang, Y.; Bhushan, B. *Soft Matter* **2010,** *6,* 29–66. doi:10.1039/B917017K
21. Wang, Y.; Bhushan, B.; Maali, A. *J. Vac. Sci. Technol., A* **2009,** *27,* 754–760. doi:10.1116/1.3086637
22. Wang, Y.; Wang, H.; Bi, S.; Guo, B. *Beilstein J. Nanotechnol.* **2015,** *6,* 952–963. doi:10.3762/bjnano.6.98
23. Ishida, N.; Inoue, T.; Miyahara, M.; Higashitani, K. *Langmuir* **2000,** *16,* 6377–6380. doi:10.1021/la000219r

24. Song, B.; Walczyk, W.; Schönherr, H. *Langmuir* **2011,** *27,* 8223–8232. doi:10.1021/la2014896
25. Wang, Y.; Bhushan, B.; Zhao, X. *Nanotechnology* **2009,** *20,* 045301. doi:10.1088/0957-4484/20/4/045301
26. Berkelaar, R. P.; Bampoulis, P.; Dietrich, E.; Jansen, H. P.; Zhang, X.; Kooij, E. S.; Lohse, D.; Zandvliet, H. J. W. *Langmuir* **2015,** *31,* 1017–1025. doi:10.1021/la504002w
27. Redon, C.; Brzoska, J. B.; Brochard-Wyart, F. *Macromolecules* **1994,** *27,* 468–471. doi:10.1021/ma00080a021
28. Xue, L.; Han, Y. *Prog. Polym. Sci.* **2011,** *36,* 269–293. doi:10.1016/j.progpolymsci.2010.07.004
29. Borkent, B. M.; de Beer, S.; Mugele, F.; Lohse, D. *Langmuir* **2010,** *26,* 260–268. doi:10.1021/la902121x
30. Drelich, J. *Colloids Surf., A* **1996,** *116,* 43–54. doi:10.1016/0927-7757(96)03651-5
31. Craig, V. S. J. *Soft Matter* **2011,** *7,* 40–48. doi:10.1039/C0SM00558D
32. Kameda, N.; Nakabayashi, S. *Chem. Phys. Lett.* **2008,** *461,* 122–126. doi:10.1016/j.cplett.2008.07.012
33. Rangharajan, K. K.; Kwak, K. J.; Conlisk, A. T.; Wu, Y.; Prakash, S. *Soft Matter* **2015,** *11,* 5214–5223. doi:10.1039/C5SM00583C
34. Yang, J.; Duan, J.; Fornasiero, D.; Ralston, J. *J. Phys. Chem. B* **2003,** *107,* 6139–6147. doi:10.1021/jp0224113
35. Peng, H.; Birkett, G. R.; Nguyen, A. V. *Adv. Colloid Interface Sci.* **2015,** *222,* 573–580. doi:10.1016/j.cis.2014.09.004
36. Holmberg, M.; Kühle, A.; Garnæs, J.; Mørch, K. A.; Boisen, A. *Langmuir* **2003,** *19,* 10510–10513. doi:10.1021/la0352669
37. Tyrrell, J. W. G.; Attard, P. *Langmuir* **2002,** *18,* 160–167. doi:10.1021/la0111957
38. Zhao, B.; Song, Y.; Wang, S.; Dai, B.; Zhang, L.; Dong, Y.; Lu, J.; Hu, J. *Soft Matter* **2013,** *9,* 8837–8843. doi:10.1039/c3sm50942g
39. Attard, P. *Adv. Colloid Interface Sci.* **2003,** *104,* 75–91. doi:10.1016/S0001-8686(03)00037-X
40. Parker, J. L.; Claesson, P. M.; Attard, P. *J. Phys. Chem.* **1994,** *98,* 8468–8480. doi:10.1021/j100085a029
41. Attard, P. *Langmuir* **1996,** *12,* 1693–1695. doi:10.1021/la950866w

License and Terms

BEILSTEIN JOURNAL OF NANOTECHNOLOGY

Correlative infrared nanospectroscopic and nanomechanical imaging of block copolymer microdomains

Benjamin Pollard and Markus B. Raschke*

Full Research Paper

Open Access

Address:
Department of Physics, Department of Chemistry, and JILA, University of Colorado, Boulder, Colorado 80309, USA

Email:
Markus B. Raschke* - markus.raschke@colorado.edu

* Corresponding author

Keywords:
block copolymers, force–distance nanomechanical spectroscopy, hybrid imaging, near-field infrared spectroscopy, scanning probe microscopy

Beilstein J. Nanotechnol. **2016,** *7,* 605–612.
doi:10.3762/bjnano.7.53

Received: 18 December 2015
Accepted: 05 April 2016
Published: 22 April 2016

This article is part of the Thematic Series "Advanced atomic force microscopy techniques IV".

Guest Editor: T. Glatzel

Abstract

Intermolecular interactions and nanoscale phase separation govern the properties of many molecular soft-matter systems. Here, we combine infrared vibrational scattering scanning near-field optical microscopy (IR *s*-SNOM) with force–distance spectroscopy for simultaneous characterization of both nanoscale optical and nanomechanical molecular properties through hybrid imaging. The resulting multichannel images and correlative analysis of chemical composition, spectral IR line shape, modulus, adhesion, deformation, and dissipation acquired for a thin film of a nanophase separated block copolymer (PS-*b*-PMMA) reveal complex structural variations, in particular at domain interfaces, not resolved in any individual signal channel alone. These variations suggest that regions of multicomponent chemical composition, such as the interfacial mixing regions between microdomains, are correlated with high spatial heterogeneity in nanoscale material properties.

Introduction

Functional soft-matter and polymer systems often exhibit novel phenomena due to nanoscale chemical heterogeneity and the resulting intermolecular interactions. Infrared vibrational scattering scanning near-field optical microscopy (IR *s*-SNOM) provides a direct, noninvasive, label-free measure of nanoscale chemical composition by localizing the light–matter interaction via a scanning probe tip [1]. Performed most simply with a single-frequency source tuned to a molecular marker resonance [2], IR *s*-SNOM also enables IR spectroscopy on the nanoscale using broadband [3,4] or tunable light sources [5]. Combined with computational imaging to analyze spectral peak position and lineshape, as well as polarization selection, *s*-SNOM can probe intermolecular coupling [6], polymorphism [7], molecular orientation, domain structure [8], and degrees of crystallinity.

However, information beyond nanoscale IR response is sometimes desired for a more complete understanding of molecular

interactions and their relationship to material function. Nanomechanical properties, measured through force spectroscopy, can provide important complimentary information on heterogeneous material systems [9]. By measuring the force on a scanning probe tip as it interacts with the sample, material properties including friction, adhesion, deformation, modulus, and dissipation can be quantified and mapped over nanoscale distances [10-14].

Here, we combine IR *s*-SNOM and force–distance spectroscopy for a multimodal study of heterogeneous molecular thin films. Although *s*-SNOM is commonly already based on intermittent-contact atomic force microscopy (AFM), the enabled compatibility with numerous advanced scanning probe modalities, including force–distance spectroscopy, has not yet been explored in combination with *s*-SNOM. We perform both spatio-spectral *s*-SNOM and force–distance nanoimaging and nanospectroscopy on mesoscopic regions of a block copolymer, providing a multidimensional picture of the variation in material and optical properties between and within polymer microdomains.

Methods

We study a high molecular weight block copolymer of polystyrene-*block*-poly(methyl methacrylate) (PS-*b*-PMMA), with a relative chain length of 270.0-*b*-289.0 $M_n \times 10^3$ (P4443-SMMA, Polymer Source), spin-coated from a 1% w/v solution in toluene onto native-oxide silicon substrates (2 kRPM). The film thickness is ~60 nm, as measured with AFM. The PMMA in this sample is mostly syndiotactic. Long chain lengths result in nonequilibrium, irregularly shaped, microdomain structures with incomplete microphase separation and large interfacial mixing regions [6,15,16]. The size of these microdomains (~60 nm, determined by the radial peak of a 2D Fourier transform of AFM topography) is comparable to the film thickness. Towards equilibrium, differences in the surface energy of PS and PMMA lead to the formation of a top surface layer of PS at the air interface, as PMMA is more polar than PS and tends toward the polar SiO_2 native oxide layer of the Si substrate [17]. Models suggest that this PS surface layer is roughly half the microdomain size when in equilibrium [18], though we can expect nonuniformity and local variations of the surface layer in this case due to the long chain lengths.

We measure the nanomechanical properties of the copolymer film using several modes of scanning force microscopy. We use intermittent contact mode under ambient conditions to map the ordering of block copolymer domains [19]. This modality, especially its phase images, is sensitive to the viscoelastic properties of the sample [20]. To further quantify nanoscale material properties, we also use force–distance spectroscopy (peak force quantitative nanomechanical mapping, PF-QNM) to map spatial variations in modulus, as well as the adhesion, deformation, and dissipation of the tip–sample interaction, simultaneously [12,13]. Corresponding quantitative values can be extracted from calibrated force–distance curves at every pixel to build up a multidimensional force–distance image.

In this work we acquire force–distance curves, as shown in Figure 1a, using a modified commercial AFM (MultiMode 8, Bruker). We calibrate quantiative force values using measurements with the same tip on a Si sample and a rough TiO_2 surface for measuring the deflection sensitivity and tip radius, respectively, as well as tuning curves for measuring the Q-factor using the Sader method [21]. We use commercial Tap150 and Tap525 tips (Bruker) for initial PF-QNM measurements (not shown), and then use those values to calibrate PF-QNM data taken with metallized tips as necessary for *s*-SNOM. Note that the curve in Figure 1a was taken with a different tip and slightly different scan settings than the calibrated data shown below; the curve here is shown only to illustrate the different PF-QNM channels.

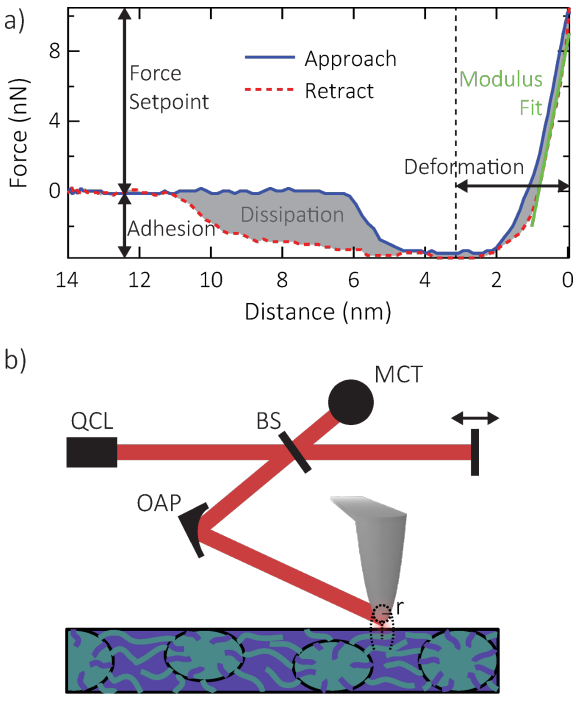

Figure 1: (a) Example force–distance curve from a single force volume at a given force setpoint, showing the properties that are analyzed to create maps of modulus, adhesion, deformation, and dissipation. (b) Schematic of *s*-SNOM setup, showing the quantum cascade laser (QCL), beam splitter (BS), off-axis parabolic (OAP) mirror, mercury–cadmium–telluride (MCT) detector, moving reference arm mirror, and tip–sample interaction confined to the tip radius *r*. Sample feature size exaggerated for visual clarity.

In IR *s*-SNOM, conventional AFM is combined with an optical setup to focus and detect light from a tip-mediated near-field optical interaction confined to a nanoscale volume of the sample surface, as shown schematically in Figure 1b. The localized tip–sample interaction depends on the optical properties of the sample directly below the apex. By scanning the sample, keeping the tip stationary with respect to the laser focus, we can create maps of optical properties of the sample simultaneously with AFM data channels [1].

For our *s*-SNOM experiments, we use a metallized scanning probe tip (11.72 N/m, PtSi–NCH, NanoWorld AG). Mid-infrared light tunable between 1660–1900 cm^{-1} from a quantum cascade laser (QCL, Daylight Solutions) is focused onto the tip, linearly polarized along the surface normal relative to the sample, using an off-axis parabolic mirror (NA = 0.45) with a power density of ≤50 MW cm^{-2}. Tip-scattered light is detected in a confocal epi-illumination/detection geometry with a LN_2-cooled HgCdTe detector (MCT, KLD-0.25/DC/11.5, Kolmar Technologies). The far-field background is suppressed by a lock-in detector (HF2, Zurich Instruments) demodulating at the third harmonic of the tip tapping frequency. Tip-scattered light is recombined at the detector with light of known phase from the reference arm in an asymmetric Michelson interferometer geometry, allowing for the determination of spectral amplitude $A(\bar{\nu})$ and phase $\phi(\bar{\nu})$ of the near-field signal [22].

The vertical sensitivity of *s*-SNOM falls off rapidly into the film over the near-field decay length, which is given by the tip radius to first order [23]. Thus, the probed region penetrates at least in part through a possible nonresonant PS surface layer. Therefore, resonant near-field phase contrast reveals the presence of PMMA microdomains.

A spatio-spectral *s*-SNOM map is acquired over a 500 × 500 nm size region of PS-*b*-PMMA, shown in Figure 2a, as previously described [5,6]. Images are taken over a range of wavelengths spanning the carbonyl stretch mode. The images are 128 × 128 pixels acquired at a rate of 0.3 Hz per line, resulting in a pixel size of 4 × 4 nm and total acquisition time of ~7 min per image. The set of images is analyzed to create nanoscale IR spectra from individual microdomains, as illustrated in Figure 2b. We use the *s*-SNOM spectral phase $\phi(\bar{\nu})$ in our analysis, which for weak molecular oscillators provides a good approximation of the spectral shape of the optical absorption or extinction coefficient $\kappa(\bar{\nu})$[1]. Gaussian resonance curves are computationally fit to the spectra in order to extract peak position $\bar{\nu}_0$ and linewidth Γ based on

$$\phi(\bar{\nu}) = Ae^{-4\ln(2)(\bar{\nu}-\bar{\nu}_0)^2/\Gamma^2} + C, \qquad (1)$$

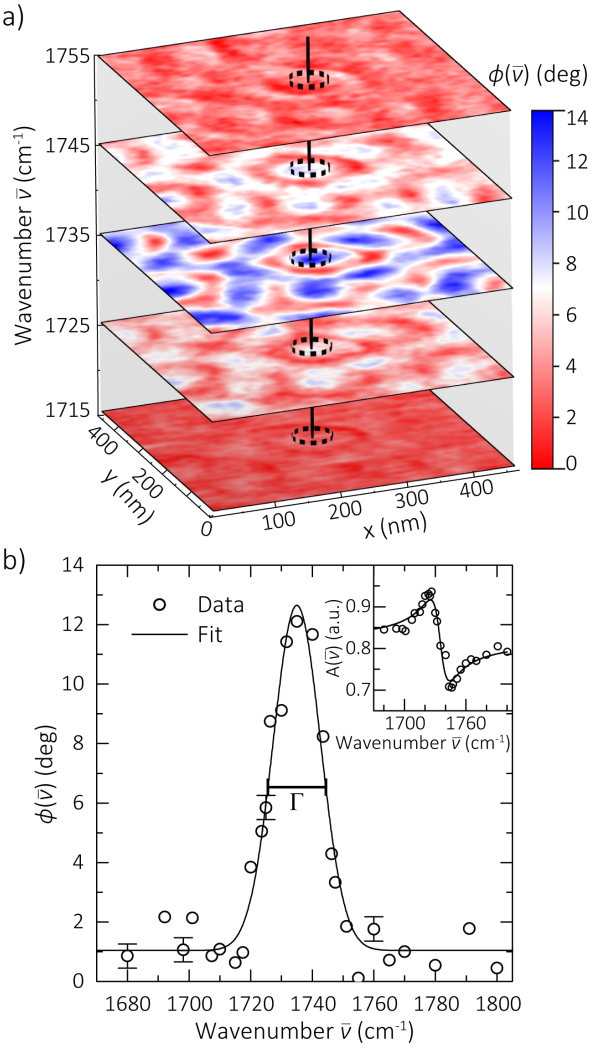

Figure 2: (a) Spatio-spectral *s*-SNOM phase image of PS-*b*-PMMA, with carbonyl mode resonant contrast between PMMA (blue) and PS (red) microdomains. (b) Spectrum extracted from a single PMMA microdomain, as illustrated by the vertical line in (a). Error bars shown on select points as reference, calculated as the standard deviation of the nonresonant baseline datapoints. Peak position and linewidth values Γ are extracted computationally from Gaussian fits to spectra at each pixel. Corresponding amplitude spectrum (inset) also shown for completeness, with fit to a dispersive lineshape as a guide to the eye.

where A and C are frequency-independent scaling and offset constants and Γ is the full width at half maximum (FWHM). For example, the corresponding fit shown in Figure 2b yields a peak position of 1735 ± 1 cm^{-1} and Γ of 18 ± 2 cm^{-1}, with the margin of error representing the 95% confidence interval of the fit parameter. While Lorentzian lineshape fits (not shown) yield similar results, Gaussian lineshapes fit the data slightly better, which indicates that the probed oscillator ensemble is dominated by inhomogeneous broadening. The corresponding amplitude spectrum is shown in the inset with calculated line-

shape (solid line) based on the above fit parameters and is Kramers–Kronig consistent.

As is often encountered in hybrid imaging, maps from force–distance spectroscopy and from *s*-SNOM acquired subsequently with the same tip need to be aligned to compensate for sample drift. The scans are registered by visually comparing ~10 like features in the height images common to both techniques. The different image datasets are then aligned, with few nanometer accuracy, using standard image registration techniques and an affine transform (MATLAB Image Processing Toolbox).

Results and Discussion

Combined *s*-SNOM and force–distance images of a 500 × 500 nm size region of PS-*b*-PMMA are shown in Figure 3 with individual PS and PMMA microdomains and/or surface variations clearly resolved in all imaging channels. The microdomains are ~60 nm in size, and finer features are observed in some channels with an overall spatial resolution of $\lesssim$20 nm. The *s*-SNOM phase in Figure 3a measured on-resonance of the carbonyl stretch mode at 1730 cm^{-1} reflects the nanoscale surface chemical composition. The corresponding trace to the right shows the indicated line profile averaged over a 5-pixel width. The profile starts and ends in a PMMA-rich region and passes through a microdomain surrounded by PS, as indicated by the color bar and profile background. The *s*-SNOM image in Figure 3a is one of many scans in the spatio-spectral dataset used to create the linewidth map shown in Figure 3b. The black regions in Figure 3b represent PS-rich regions where there is insufficient resonant PMMA signal to perform a computational fit and extract a linewidth value. Standard intermittent contact mode topography (Figure 3d) and tapping phase (Figure 3e) channels were collected concurrently during *s*-SNOM scans. The images of modulus (Figure 3c), adhesion (Figure 3f), deformation (Figure 3g), and dissipation (Figure 3h) are defined from the analysis of force–distance curves taken with the same tip over the same region, calibrated as described above.

We present here a preliminary discussion of the polymer properties and interactions probed by our hybrid imaging technique as an illustration of the information made available, while also recognizing that understanding the full complexity of the material system requires more detailed measurements and analysis.

In the resonant *s*-SNOM image (Figure 3a), carbonyl groups in PMMA provide a marker resonance at ~1730 cm^{-1}, resulting in a measured *s*-SNOM phase contrast on the order of 10° compared to the nonresonant PS regions. Within apparent PMMA microdomains, linewidths (Figure 3b) varied between 15 to 20 cm^{-1}. The carbonyl resonance is sensitive to the local chemical environment through intermolcular interactions, resulting in vibrational solvatochromism and line broadening [6]. The varying concentrations of neighboring carbonyl groups in adjacent MMA monomers result in differing levels of intermolecular coupling, changing the measured nanoscale spectral linewidth. In addition, anisotropy within a single PMMA region itself could affect the degree of intermolecular coupling, manifesting in linewidth changes within a single microdomain.

The modulus image (Figure 3c) shows contrast from the differing mechanical properties of PMMA and PS. We observe values around 1–2 GPa in PMMA regions, and 3–4 GPa in PS regions. These values of the DMT modulus [24] are closely related to the Young's modulus, an intrinsic bulk material property of the sample. Measurements of Young's modulus in polymers often exhibit considerable variation and nonlinearity [25]. However, our values generally match the range measured on PS-*b*-PMMA from similar techniques [14,26,27].

The height (Figure 3d), tapping phase (Figure 3e), adhesion (Figure 3f), dissipation (Figure 3g), and deformation (Figure 3h) images represent aspects of the physical tip–sample interaction. For example, we observe a topographic height difference in Figure 3d of ~5 nm between PMMA and PS regions, with PMMA appearing higher, while the tapping phase in Figure 3e is ~15° larger for PMMA than PS. In this case, slight differences in the presence of residual toluene solvent between PMMA and PS, with PMMA retaining slightly more, likely results in PS microdomains shrinking slightly more than PMMA microdomains during spin casting and subsequent drying [28].

The tapping phase is related to the power dissipated by the sample during contact with the tip, and reflects to some extent the viscoelastic properties of the sample [20]. However, the tapping phase is also affected by the intermittent formation of a capillary water neck between tip and sample as the cantilever oscillates, which can lead to either net attractive or net repulsive regimes depending on tapping amplitude, relative humidity, and local curvature of the tip and sample [29,30]. Modeling the formation, evolution, and breaking of the tip–sample water menisci in order to understand the effect on the tapping phase is still a focus of active research [31].

We measure an overall adhesion (Figure 3f) of 0.4 nN on PMMA, and 0.7 nN on PS. We also observe finer structure within regions in the corresponding profile, with an increase of around 0.1 nN in the center of the PMMA microdomain compared to the edges. The adhesion channel measures the minimum force during the force–distance curve, which is sensitive to attractive forces between tip and sample (e.g.,

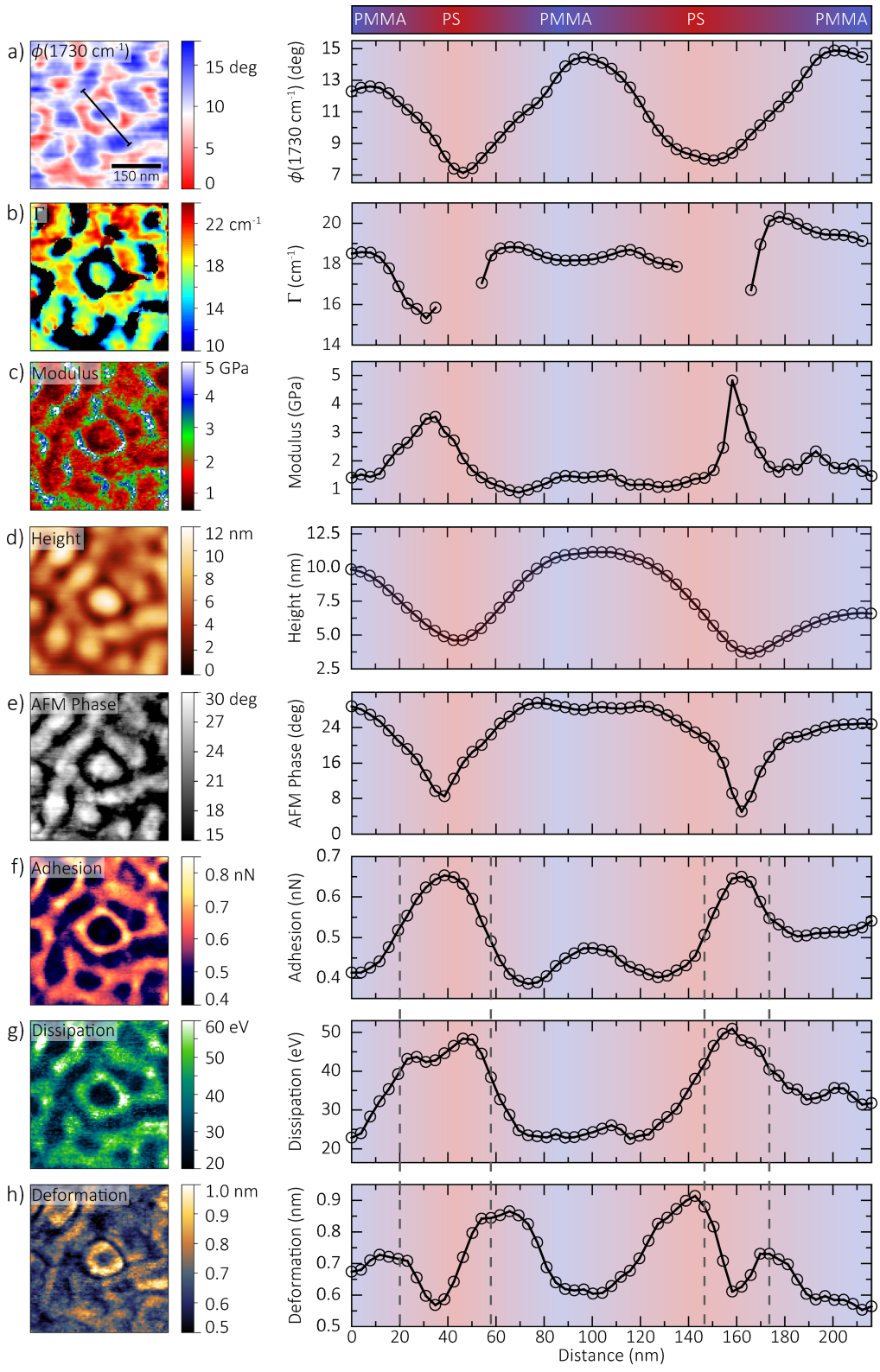

Figure 3: Multidimensional dataset showing maps of PS and PMMA microdomains, with corresponding profiles along the line indicated in (a) averaged over a 5-pixel width. Color bar and profile background suggest regions of high PS or PMMA concentration. (a,b,d,e) measured using spatio-spectral *s*-SNOM and (c,f–h) measured using force–distance spectroscopy. Differences between channels, as highlighted by the dashed lines in (f–h), indicate a complex interplay between crystallinity, composition, and intermolecular interaction between and within single domains.

electrostatic or capillary forces). It can reflect variations in the Hamaker constant of the van der Waals interaction, surface charges, or hydrophilicity [32]. It has been observed in PS-*b*-PMMA that PS preferentially adsorbs onto a gold surface compared to PMMA [33]. Thus, the higher attractive forces over PS domains suggest that our metallized tip interacts with PS similarly to such chemically inert gold substrates. In addition, the polar nature of PMMA makes it more hydrophilic than pure PS [34]. Thus in our block copolymer, the lower attractive forces over PMMA domains possibly indicate that we are operating in the repulsive capillary force regime. Tip–surface capillary forces are most studied in the context of resonant cantilever motion instead of the slower, nonresonant distance modulation employed in PF-QNM. Nonetheless, our modulation amplitude (15 nm), measured tip radius (16–25 nm), and the relative humidity during the measurement (13%) indicate that we are operating near the threshold between attractive and repulsive regimes [30]. The delicate balance between repulsive capillary forces and overall van der Waals interaction could result in the finer variations across the PMMA microdomain.

We measure a dissipation (Figure 3g) of 25 eV over PMMA, and 45 eV over PS. The dissipation channel measures the integrated hysteresis between approach and retract and thus directly measures the energy lost to the sample. For purely elastic behavior, the energy loss is dominated by adhesive forces associated with the tip–surface interaction, while for inelastic deformation, energy is transferred into the sample itself [32] or to the surface water layer through the formation and rupture of the capillary neck at different distances [30]. In the case of PS-*b*-PMMA, the positive correlation between dissipation and adhesion suggests that energy loss is dominated by surface-sensitive adhesive forces.

Our deformation map (Figure 3h) does not correlate directly with chemical composition (e.g., dissipation), as indicated by the dotted lines in the corresponding profile. Instead, it shows larger values, 0.9 nm, at the interfaces between the PS and PMMA domains, compared to 0.6 nm at the domain centers. The deformation measures the maximum penetration of the tip into the polymer during the force–distance cycle, which can be due to both elastic and inelastic behavior, and thus is a measure of both the elasticity and the hardness of the sample [32]. Polymers, including syndiotactic PMMA, tend to pack in a semi-ordered way to minimize the total free energy, though this is highly dependent on tacticity and molecular weight distribution [35]. Crystallinity also creates varying mechanical properties, as greater order and coupling generally suggest stiffer regions at the center of domains [25]. Our deformation profile suggests that the mixing of PMMA and PS significantly disrupts the polymer order and softens the interfacial region.

To further illustrate the relationships between the different image channels, Figure 4 shows several bivariate histograms displaying correlations between two respective channels across the entire image region. They confirm the trends discussed above, as Figure 4a–c show a clear positive correlation of resonant *s*-SNOM phase with Γ, height, and AFM phase, illus-

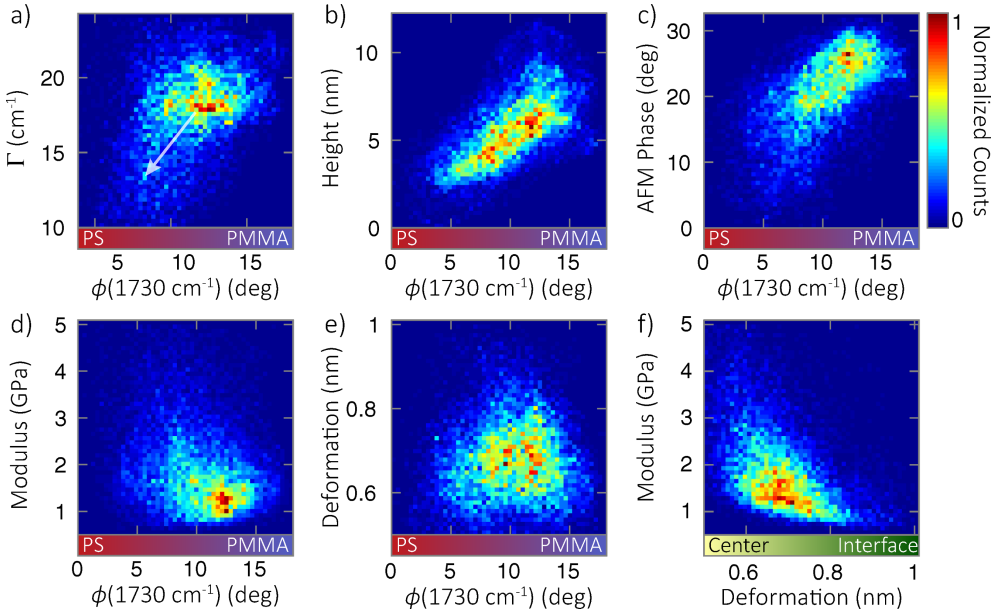

Figure 4: Bivariate histograms, showing the correlations between different signal channels across the entire image region. The arrow in (a) indicates that the correlation is seen to continue towards the lower left until Γ becomes undefined in nonresonant, PS-rich regions. Colored bars along the horizontal axes illustrate the correspondence of the spectral phase with PMMA concentration, or deformation with interfacial mixing (center vs interface).

trating that these channels are predominantly sensitive to differences in relative chemical concentration of PS and PMMA. Note in Figure 4a that Γ is not defined in nonresonant PS regions. However, the correlation with $\phi(1730\ cm^{-1})$ is seen to continue, with decreasing Γ as the PMMA is diluted in the PS phase, and is consistent with earlier results [6]. This relationship is indicated by the arrow in Figure 4a. Modulus and deformation, however, show little correlation with ϕ (Figure 4d,e), instead showing a negative correlation with each other (Figure 4f). Those channels are predominantly sensitive to differences in interfacial mixing between microdomains, suggesting a complex interplay between crystallinity, composition, and intermolecular interactions, especially at microdomain interfaces.

On the other hand, Figure 5 shows strong negative correlations of resonant *s*-SNOM phase with adhesion (Figure 5a,b) and dissipation (Figure 5c,d) channels, which are predominantly sensitive to chemical composition. The bivariate histograms (Figure 5a,c) show a distinct bimodal distribution, more apparent than in the histogram of each channel alone (shown in projection onto respective axes), which is further exemplified by summing diagonally across the direction of correlation to create the coincidence histograms shown in Figure 5b and Figure 5d. The two populations in this distribution represent distinct regions with separate chemical and nanomechanical properties.

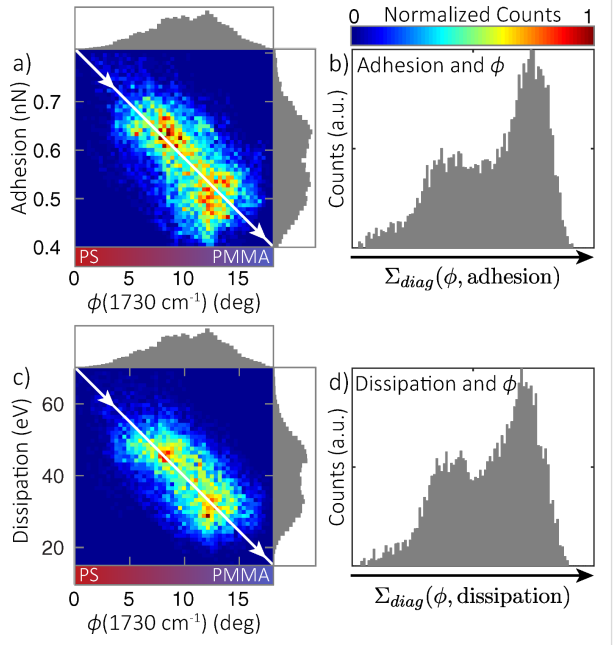

Figure 5: Bivariate and corresponding coincidence histograms showing correlations between adhesion and $\phi(1730\ cm^{-1})$ (a,b), and dissipation and $\phi(1730\ cm^{-1})$ (c,d). Histograms of each single channel are shown along the corresponding axis in (a) and (c). Coincidence histograms (b,d) calculated by summing counts in the bivariate histograms (a,c) along diagonal lines perpendicular to the direction of correlation (solid line). A bimodal distribution is apparent, indicative of separate populations of distinct chemistry and nanomechanical properties.

Conclusion

In summary, we have combined spatio-spectral *s*-SNOM with force–distance spectroscopy to create a multimodal dataset of material and optical properties of nanoscale heterogeneous soft matter. Using a single AFM/*s*-SNOM setup and a metallized scanning probe tip, we produced images of a particular 500 × 500 nm size region of a PS-*b*-PMMA film via IR *s*-SNOM and force–distance spectroscopy analyzed with computational imaging techniques. These maps are sensitive not only to chemical composition, but also to inhomogeneity within domains arising from, for example, varying degrees of crystallinity. The hybrid combination of different imaging modalities established here promises to be a powerful tool for measuring and understanding intermolecular interactions and could address fundamental questions for the study and design of functional nanomaterials.

Acknowledgements

We thank Kyoung-Duck Park for assistance in the preliminary stages of these measurements and Omar Khatib and Eric Muller for valuable discussions at various stages of the data analysis. Funding is gratefully acknowledged from the National Science Foundation (CHE 1306398). This work was also supported by the Soft Materials Research Center under NSF MRSEC Grant DMR-1420736.

References

1. Muller, E. A.; Pollard, B.; Raschke, M. B. *J. Phys. Chem. Lett.* **2015,** *6,* 1275–1284. doi:10.1021/acs.jpclett.5b00108
2. Taubner, T.; Hillenbrand, R.; Keilmann, F. *Appl. Phys. Lett.* **2004,** *85,* 5064–5066. doi:10.1063/1.1827334
3. Huth, F.; Govyadinov, A.; Amarie, S.; Nuansing, W.; Keilmann, F.; Hillenbrand, R. *Nano Lett.* **2012,** *12,* 3973–3978. doi:10.1021/nl301159v
4. Bechtel, H. A.; Muller, E. A.; Olmon, R. L.; Martin, M. C.; Raschke, M. B. *Proc. Natl. Acad. Sci. U. S. A.* **2014,** *111,* 7191–7196. doi:10.1073/pnas.1400502111
5. Berweger, S.; Nguyen, D. M.; Muller, E. A.; Bechtel, H. A.; Perkins, T. T.; Raschke, M. B. *J. Am. Chem. Soc.* **2013,** *135,* 18292–18295. doi:10.1021/ja409815g
6. Pollard, B.; Muller, E. A.; Hinrichs, K.; Raschke, M. B. *Nat. Commun.* **2014,** *5,* 3587. doi:10.1038/ncomms4587
7. Westermeier, C.; Cernescu, A.; Amarie, S.; Liewald, C.; Keilmann, F.; Nickel, B. *Nat. Commun.* **2014,** *5,* 4101. doi:10.1038/ncomms5101
8. Amenabar, I.; Poly, S.; Nuansing, W.; Hubrich, E. H.; Govyadinov, A. A.; Huth, F.; Krutokhvostov, R.; Zhang, L.; Knez, M.; Heberle, J.; Bittner, A. M.; Hillenbrand, R. *Nat. Commun.* **2013,** *4,* 2890. doi:10.1038/ncomms3890

9. Butt, H.-J.; Cappella, B.; Kappl, M. *Surf. Sci. Rep.* **2005,** *59,* 1–152. doi:10.1016/j.surfrep.2005.08.003
10. Radmacher, M.; Tillamnn, R. W.; Fritz, M.; Gaub, H. E. *Science* **1992,** *257,* 1900–1905. doi:10.1126/science.1411505
11. Ton-That, C.; Shard, A. G.; Teare, D. O. H.; Bradley, R. H. *Polymer* **2001,** *42,* 1121–1129. doi:10.1016/S0032-3861(00)00448-1
12. Sweers, K.; van der Werf, K.; Bennink, M.; Subramaniam, V. *Nanoscale Res. Lett.* **2011,** *6,* 270. doi:10.1186/1556-276X-6-270
13. Young, T. J.; Monclus, M. A.; Burnett, T. L.; Broughton, W. R.; Ogin, S. L.; Smith, P. A. *Meas. Sci. Technol.* **2011,** *22,* 125703. doi:10.1088/0957-0233/22/12/125703
14. Herruzo, E. T.; Perrino, A. P.; Garcia, R. *Nat. Commun.* **2014,** *5,* 3126. doi:10.1038/ncomms4126
15. Francis, T. J.; Vogt, B. D.; Wang, M. X.; Watkins, J. J. *Macromolecules* **2007,** *40,* 2515–2519. doi:10.1021/ma062000a
16. Walheim, S.; Böltau, M.; Mlynek, J.; Krausch, G.; Steiner, U. *Macromolecules* **1997,** *30,* 4995–5003. doi:10.1021/ma9619288
17. Green, P. F.; Christensen, T. M.; Russell, T. P.; Jérôme, R. *Macromolecules* **1989,** *22,* 2189–2194. doi:10.1021/ma00195a033
18. Sevink, G. J. A.; Zvelindovsky, A. V.; van Vlimmeren, B. A. C.; Maurits, N. M.; Fraaije, J. G. E. M. *J. Chem. Phys.* **1999,** *110,* 2250. doi:10.1063/1.477837
19. Stenbock-Fermor, A.; Knoll, A. W.; Böker, A.; Tsarkova, L. *Macromolecules* **2014,** *47,* 3059–3067. doi:10.1021/ma500561q
20. Knoll, R.; Magerle, K.; Krausch, G. *Macromolecules* **2001,** *34,* 4159–4165. doi:10.1021/ma001311x
21. Sader, J. E.; Chon, J. W. M.; Mulvaney, P. *Rev. Sci. Instrum.* **1999,** *70,* 3967–3969. doi:10.1063/1.1150021
22. Taubner, T.; Keilmann, F.; Hillenbrand, R. *Nano Lett.* **2004,** *4,* 1669–1672. doi:10.1021/nl0491677
23. Aizpurua, J.; Taubner, T.; García de Abajo, F. J.; Brehm, M.; Hillenbrand, R. *Opt. Express* **2008,** *16,* 1529–1545. doi:10.1364/OE.16.001529
24. Derjaguin, B. V.; Muller, V. M.; Toporov, Yu. P. *Prog. Surf. Sci.* **1994,** *45,* 131–143. doi:10.1016/0079-6816(94)90044-2
25. Humbert, S.; Lame, O.; Séguéla, R.; Vigier, G. *Polymer* **2011,** *52,* 4899–4909. doi:10.1016/j.polymer.2011.07.060
26. Briscoe, B. J.; Fiori, L.; Pelillo, E. *J. Phys. D: Appl. Phys.* **1999,** *31,* 2395–2405. doi:10.1088/0022-3727/31/19/006
27. Jee, A.-Y.; Lee, M. *Polym. Test.* **2010,** *29,* 95–99. doi:10.1016/j.polymertesting.2009.09.009
28. Elbs, H.; Fukunaga, K.; Stadler, R.; Sauer, G.; Magerle, R.; Krausch, G. *Macromolecules* **1999,** *32,* 1204–1211. doi:10.1021/ma981321m
29. Sirghi, L.; Nakagiri, N.; Sugisaki, K.; Sugimura, H.; Takai, O. *Langmuir* **2000,** *16,* 7796–7800. doi:10.1021/la000392n
30. Zitzler, L.; Herminghaus, S.; Mugele, F. *Phys. Rev. B* **2002,** *66,* 155436. doi:10.1103/PhysRevB.66.155436
31. Sirghi, L. *Langmuir* **2012,** *28,* 2558–2566. doi:10.1021/la202917d
32. Pittenger, B.; Erina, N.; Su, C. *Bruker Application Note* **2012,** #*128,* 1–12.
33. Russell, T. P.; Coulon, G.; Deline, V. R.; Miller, D. C. *Macromolecules* **1989,** *22,* 4600–4606. doi:10.1021/ma00202a036
34. Jung, Y. C.; Bhushan, B. *Nanotechnology* **2006,** *17,* 4970–4980. doi:10.1088/0957-4484/17/19/033
35. Fuchs, K.; Friedrich, C.; Weese, J. *Macromolecules* **1996,** *29,* 5893–5901. doi:10.1021/ma951385m

License and Terms

BEILSTEIN JOURNAL OF NANOTECHNOLOGY

Cantilever bending based on humidity-actuated mesoporous silica/silicon bilayers

Christian Ganser[1], Gerhard Fritz-Popovski[1], Roland Morak[1], Parvin Sharifi[1,2], Benedetta Marmiroli[3], Barbara Sartori[3], Heinz Amenitsch[3], Thomas Griesser[4], Christian Teichert[1] and Oskar Paris[*1]

Full Research Paper

Open Access

Address:
[1]Institute of Physics, Montanuniversitaet Leoben, Austria, [2]Max-Planck-Institut für Kohlenforschung, Mülheim an der Ruhr, Germany, [3]Institute of Inorganic Chemistry, Graz University of Technology, Austria and [4]Chair of Chemistry of Polymeric Materials, Montanuniversitaet Leoben, Austria

Email:
Oskar Paris[*] - oskar.paris@unileoben.ac.at

* Corresponding author

Keywords:
AFM cantilever; bilayer bending; grazing incidence small-angle X-ray scattering (GISAXS); mesoporous film; sorption-induced deformation

Beilstein J. Nanotechnol. **2016,** *7,* 637–644.
doi:10.3762/bjnano.7.56

Received: 16 January 2016
Accepted: 12 April 2016
Published: 28 April 2016

This article is part of the Thematic Series "Advanced atomic force microscopy techniques IV".

Guest Editor: T. Glatzel

Abstract

We use a soft templating approach in combination with evaporation induced self-assembly to prepare mesoporous films containing cylindrical pores with elliptical cross-section on an ordered pore lattice. The film is deposited on silicon-based commercial atomic force microscope (AFM) cantilevers using dip coating. This bilayer cantilever is mounted in a humidity controlled AFM, and its deflection is measured as a function of relative humidity. We also investigate a similar film on bulk silicon substrate using grazing-incidence small-angle X-ray scattering (GISAXS), in order to determine nanostructural parameters of the film as well as the water-sorption-induced deformation of the ordered mesopore lattice. The strain of the mesoporous layer is related to the cantilever deflection using simple bilayer bending theory. We also develop a simple quantitative model for cantilever deflection which only requires cantilever geometry and nanostructural parameters of the porous layer as input parameters.

Introduction

Because the bending of a microcantilever can be measured with extremely high accuracy, sensors utilizing this principle are in focus of recent research. Such sensors are able, for instance, to detect molecules adsorbing on the cantilever surface by simply reading out the deflection of a chemically modified cantilever [1]. In order to differentiate a spectrum of molecules, cantilever arrays were used to create an artificial “chemical nose”, leading to sensor systems which are able to detect diabetes in the human breath [2] or cancer [3,4]. The measured deflection is usually very small owing to only very few molecules reaching the surface of the cantilever. In order to use similar principles for actuation purposes, a larger deflection of the cantilever must be reached. One strategy is to increase the number of adsorbed molecules by increasing the total interaction area of molecules

with the surface. This leads to the concept of using bilayer structures, with one of the layers having a large accessible (internal) surface area. In the natural world of plants for instance, humidity-induced bending of bilayer structures is frequently used for actuation purposes. Prominent examples are the opening of tree cones [5], or the complex movement of the dispersal units of wild wheat [6] and ice plants [7]. In all these systems the movement is caused by the bending of bilayer structures that swell anisotropically and differently between the two layers upon the change of relative humidity (RH) [8]. This bilayer principle has been used to build simple artificial actuators based on the swelling of paper–plastic bilayers [9], and also more general routes have been proposed to create directional movement by using swelling of polymers in combination with controllable anisotropy [10]. However, to our knowledge such concepts have not been used so far to create ceramic or metallic bilayer structures, which would have the advantage of their applicability at higher temperatures and in harsh environments. The potential of mesoporous "hard" materials such as nanoporous gold [11] or mesoporous silica [12] for such purposes has recently been highlighted, where the basic idea is to utilize the adsorption-induced deformation of highly porous materials. The simplest way of fabricating an actuator based on such materials would be a bilayer consisting of a thin bulk substrate covered by a film of the mesoporous material. The change of interfacial energies (i.e., solid–liquid and liquid–gas interfaces) during adsorption of a gas into the pore space will lead to a deformation of the porous part of the bilayer [13]. Since the substrate layer is expected to deform considerably less due to its much lower accessible surface area, this will result in a bending movement similar to a bimetal strip in response to a temperature change [9].

Here, we demonstrate for the first time the fabrication and humidity-controlled actuation of a microcantilever based on a mesoporous silica/nonporous silicon bilayer using a commercial AFM cantilever as a substrate. The simplicity and versatility of the approach is promising for applications in several fields where similar systems based on swellable polymers are not applicable.

Experimental

Sample preparation

AFM cantilevers and silicon wafers were coated with a mesoporous silica film using evaporation-induced self-assembly [14-16]. We employed tipless NSG30 cantilevers from NT-MDT (about 130 µm long, 45 µm wide, and about 4.5 µm thick) with a gold reflective coating on one side. The cantilevers were immersed in 2 M NaOH aqueous solution for 40 min, rinsed with ethanol and dried in a flow of inert gas (N_2 or CO_2). In the next step, the gold coating of the cantilever was hydrophobized using self-assembled monolayers (SAM) of dodecanethiol (≥98%, 471364-100ML, Aldrich) in a 1 mM solution in ethanol for 8 h. This hydrophobization was necessary to deposit silica only on the non-hydrophobic side of the cantilever and so that its reflective coating could still be used. The precursor solution for the mesoporous silica coating was prepared in a three-step process. First, 1.75 g of tetraethyl orthosilicate (TEOS) and 1.25 g of ethanol was mixed with 1.25 g of aqueous 10 M HCl solution and was stirred for 1 h. Second, 580 mg of the block copolymer P123 (435465-250ML, Aldrich) were dissolved in 26.85 g ethanol and stirred for 1 h, followed by adding the first solution. In the third step, 1.9 g of aqueous 1 M HCl solution was added to the mixture prepared in the second step. This final precursor solution was then stirred for 2 h. The precursor solution was deposited on the cantilever by dip coating with a withdrawal speed of 2 mm/s. After letting the film rest at room temperature for one day, the sample was calcined at a temperature of 450 °C. The temperature was increased by 1 °C/min, held at 450 °C for 2 h, and cooled down to room temperature at the same rate. The silicon wafers were prepared with the identical protocol as the cantilever samples, only the hydrophobization step with the SAMs was skipped.

AFM

The atomic force microscope in use was an Asylum Research MFP-3D, of which only the cantilever deflection was read-out and recorded as a function of the time. The deflection read-out was performed by the light-beam method, where a laser beam is reflected from the gold coating of the cantilever onto a split photodiode (Figure 1a). The control of relative humidity was achieved with a custom-built setup where a nitrogen stream is saturated with water in a bubbler and mixed with a dry nitrogen stream [17]. By manually adjusting the flow rates of the two streams, the relative humidity can be continuously controlled. The AFM cantilever was mounted inside a closed commercial fluid cell with a volume of about 10 mL. In addition, a Sensirion SHT21 sensor, which records the relative humidity as well as the temperature, is mounted in the fluid cell. Relative humidity and temperature were recorded as a function of time. This allows for correlating the cantilever deflection with the relative humidity. To properly quantify the cantilever response to the change in relative humidity as a deflection, the cantilever needs to be calibrated. The thermal sweep method [18] was used to calibrate the cantilevers and was performed directly before every measurement. In order to start every experiment under the same conditions, the first step was to reduce RH to the lowest possible value (around 5%). The cantilever was left in these conditions for several hours to equilibrate RH and the cantilever deflection to a stationary value. From this point, the adsorption curve followed by the desorption curve were recorded stepwise with 30–45 min equilibration time before

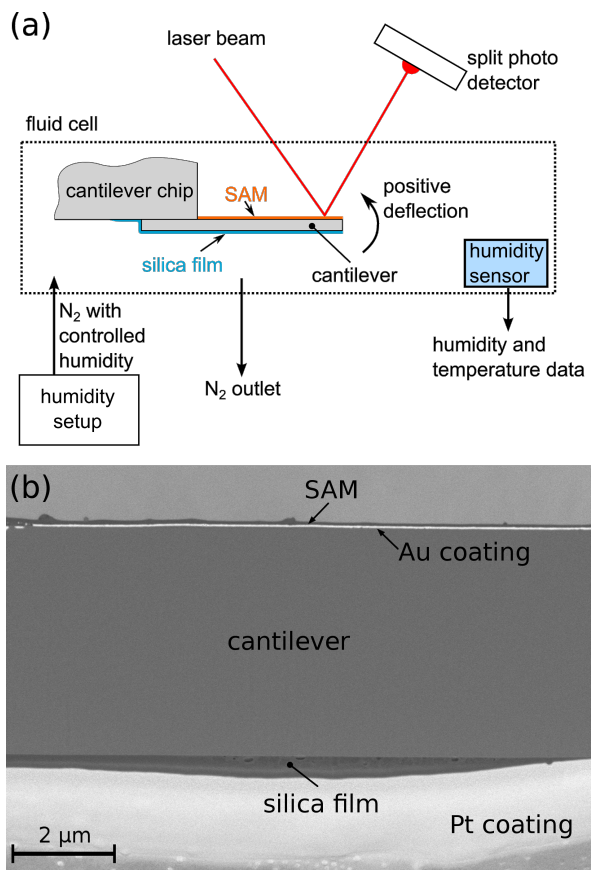

Figure 1: (a) Scheme of an AFM cantilever coated with a porous silica film in the fluid cell with deflection readout. (b) Backscattered electron SEM image of the cross section of a silica-coated cantilever.

reading out the cantilever deflection for each step. A cross section of the AFM cantilever after the actuation experiment was prepared with focused ion beam (FIB) cutting using an AURIGA Crossbeam Workstation (Zeiss). Scanning electron microscopy (SEM) images of the sample cross-section were taken with the same instrument with the electron microscope operated at a voltage of 2 keV.

GISAXS: measurements and data evaluation

GISAXS measurements of the films prepared on Si wafers were performed at the Austrian SAXS beamline at the synchrotron radiation source ELETTRA in Trieste, Italy [19]. The wavelength was $\lambda = 0.154$ nm and 2D GISAXS data were collected with a Pilatus 1M detector (Dectris, Baden Switzerland) at a distance of 1502 mm. For the in situ water sorption measurements, a custom-built humidity cell with Kapton X-ray windows was used. The working principle is very similar to the humidity chamber for AFM described above with a humidity range between about 10 and 90% RH (for more information on the humidity cell, see [20]). In contrast to the AFM measurements, RH was changed continuously during the GISAXS measurements with a nominal rate of 0.5% per minute. The GISAXS measurement time was one minute per frame. After reaching the highest humidity (typically 92–93%), the sample was kept at this RH for 30 min and a desorption cycle with the same rate of RH and the same measurement time was started. Silver behenate was mounted as a standard on the sample cell.

Instabilities of the primary beam position were corrected by computing the center of the silver behenate rings for each frame. Changes of the incidence angle were monitored by the position of the specular reflection. Peak positions were computed as centers of gravity in cuts parallel and normal to the wafer surface after subtraction of a linear background. The obtained positions were corrected for refraction effects [21].

Results and Discussion

Cantilever deflection

In Figure 1a, the scheme of the coated cantilever is shown and in Figure 1b, the successful coating is demonstrated by an SEM image of the cantilever cross-section after the actuation experiment within the AFM. The different materials can easily be distinguished by the backscattered electron contrast, revealing bright contrast for the Au coating at the top, and the additional Pt coating required for clean FIB cutting at the bottom of the image. A compact silica film with only few defects formed on the bottom (hydrophilic) side of the silicon substrate. This film is thickest (approx. 500 nm) in the center of the cantilever cross section and becomes thinner towards the edges, with an average thickness of roughly 300 nm. The top (hydrophobized) side shows that a very thin silica film was formed also on the Au coating, which means that the hydrophobization with SAMs did not work as perfectly as planned. However, the mesoporous silica film is much thicker (by a factor of 8–10) at the bottom side without the SAMs. Therefore, the top silica film was not taken further into account.

When the cantilever was placed in the AFM, a clear response to a change in relative humidity was evident. This response is shown as the cantilever deflection in Figure 2 during an adsorption cycle followed by a desorption cycle. The difference between minimum and maximum deflection was found to be about 140 nm, with a slight offset (about 20 nm) between the deflections before adsorption and after desorption. Such an offset points to an only partially reversible process and perhaps also to slight drift problems. A clear hysteresis is evident between the adsorption and desorption curves above RH = 50%. This hysteresis in cantilever deflection agrees with the hysteresis seen in water sorption isotherms measured for similar materials, indicating the different pressures for capillary condensation during adsorption and capillary evaporation during desorption, respectively, in pores with quite monodis-

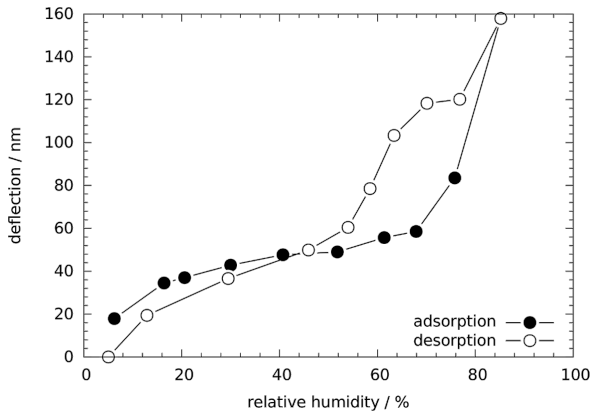

Figure 2: Cantilever deflection as a function of the relative humidity.

perse size distributions [22]. It is well known that adsorption and desorption of fluids leads to a non-monotonous deformation of mesoporous materials [12,13]. In particular the so-called strain-isotherm, i.e., the deformation of the porous material as a function of relative fluid pressure, exhibits a similar hysteresis as the sorption isotherm. The observed cantilever bending is most likely induced by the sorption-induced deformation of the mesoporous film. Therefore, we attribute the strong change in the slope of the curves seen in Figure 2 (about 70% RH for adsorption and about 55% RH for desorption) to the transition from film formation on the pore walls to the spontaneous filling/emptying (capillary condensation/evaporation) of the pores with water.

Because the change of the relative humidity of air will also change its index of refraction (IOR), n, and the deflection readout was done via a laser beam reflected from the cantilever, we have checked whether this can influence our results. The IOR change between dry air and air fully saturated with water is given by $\Delta n \approx 1 \cdot 10^{-4}$ [23]. Taking this into account, a detected deflection of 200 nm would be artificially increased due to the IOR change by only 0.2%, which can be neglected. This fact was also verified experimentally by placing an uncoated, pristine cantilever in the fluid cell and increasing the relative humidity from 5 to 90% while recording the cantilever deflection. In this experiment, only a drift of the deflection of approximately 5 nm was found but no significant change in deflection. Therefore, the data shown in Figure 2 reflect the cantilever deflection due to the change in humidity with an accuracy better than 5%.

Characterization of mesoporous films

A mesoporous film on silicon substrate was prepared in the same way as the film on AFM cantilever to obtain a macroscopically extended film for the nanostructure characterization using GISAXS. The nanostructure of this material consists of quite monodisperse cylindrical pores ordered on 2D pore lattice [24]. The GISAXS pattern of the corresponding sample shown in Figure 3 reveals sharp Bragg reflections from this pore lattice.

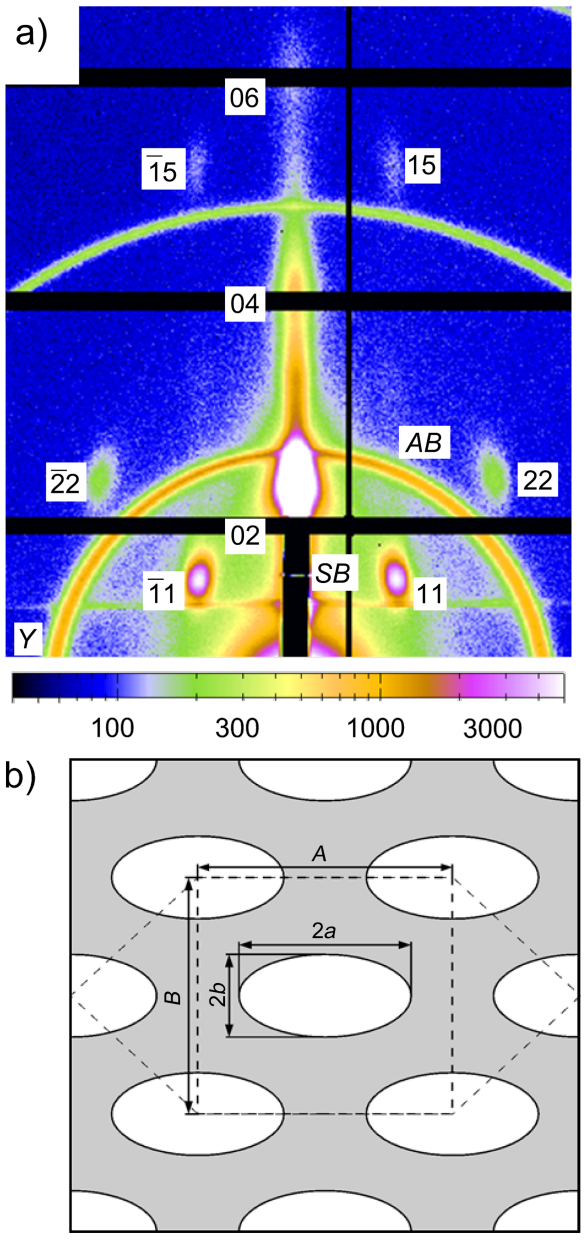

Figure 3: (a) GISAXS pattern of mesoporous silica film on a silicon substrate. The rings (marked AB) are from a silver behenate internal standard, and the black lines are dead areas of the detector. The numbers denote the Miller indices of the reflections of a centered rectangular 2D lattice, *Y* is the Yoneda peak, and *SB* the specular reflected beam. The grazing angle was 0.384°. (b) Unit cell of the 2D pore lattice reconstructed from the positions of the GISAXS reflections with lattice parameter A = 15.08 nm and B = 14.01 nm, and pore size parameters estimated from the intensities of the reflections assuming an elliptical cross-section of the cylindrical pores; $2a$ = 10.2 nm and $2b$ = 4.90 nm. Please note that the cylindrical pores lie preferentially within the film plane.

The fact that these reflections are not azimuthally smeared means that the long axis of the cylindrical pores expected from this type of materials shows a high degree of alignment to the substrate. The pattern reveals fiber symmetry around the film normal, which means that the orientation of the cylinder axes within the plane of the film is random. From the positions of the diffraction peaks, the lattice symmetry can easily be deduced. As reported already in earlier work [24], this symmetry deviates considerably from the 2D hexagonal lattice found for powder SBA-15 materials [25]. This is understood by the fact that the silicon substrate induces a strong mechanical constraint to the silica film. For an infinitely extended thin film tightly attached to a rigid substrate, film shrinkage would only be possible perpendicular to the substrate, but not parallel to it. This was demonstrated recently on similar samples for the water-sorption-induced deformation of the silica films [20]. Even much stronger deformation is expected during drying and calcination of the as synthesized films, causing the pore lattice to strongly shrink in the direction perpendicular to the substrate, while it is kept almost constant in the direction parallel to the substrate. As a consequence, the originally hexagonal pore lattice is strongly deformed. Figure 3b illustrates this by showing the centered rectangular unit cell of the 2D pore lattice extracted from the GISAXS data. While for a hexagonal symmetry the lattice parameters A and B would be related by $B = \sqrt{3}A$, Figure 3b rather suggests $B \approx A$. This is of course only possible, if also the cross-section of the cylindrical pores changes from originally circular to elliptical. A detailed analysis of the intensities of the individual reflections in the GISAXS pattern can be used to obtain an estimate for the two half axes a and b of the elliptical pore cross-section, which are given in Figure 3b. Together with the lattice parameters A and B of the centered rectangular unit cell, the pore volume fraction (porosity) of the film can easily be calculated by $\phi = (2ab\pi)/(AB) = 0.37$. Moreover, the mean curvature of the pore cross-section can be determined by $\kappa = 0.5(1/a + 1/b)$, which leads to a mean radius of curvature $r = 1/\kappa = 3.31$ nm [26].

GISAXS patterns were collected in situ while changing the RH. From the shift of the Bragg peaks as a function of the RH, the pore lattice strain can be obtained [12,27,28]. Similar to our previous work [20], this strain was found to be much smaller in-plane (i.e., parallel to the surface) as compared to the out-of-plane direction perpendicular to the surface. Figure 4 shows the pore lattice strain obtained from the shift of the 02 reflection as a function of the RH during adsorption. Unfortunately, the corresponding desorption run could not be evaluated due to problems with humidity equilibration within the restricted time available for the synchrotron radiation experiment. Nonetheless, for the adsorption branch the pore lattice strain ε measured at the level of the individual pores can now be compared with the macroscopic cantilever deflection δ shown in Figure 2. Both quantities increase more gently at low RH, and become considerably steeper above 70%, where the onset of capillary condensation is expected. Indeed, the shape of the cantilever deflection vs RH curve in Figure 2 is very similar to the strain vs RH curve of Figure 4, suggesting a linear relationship between these two quantities.

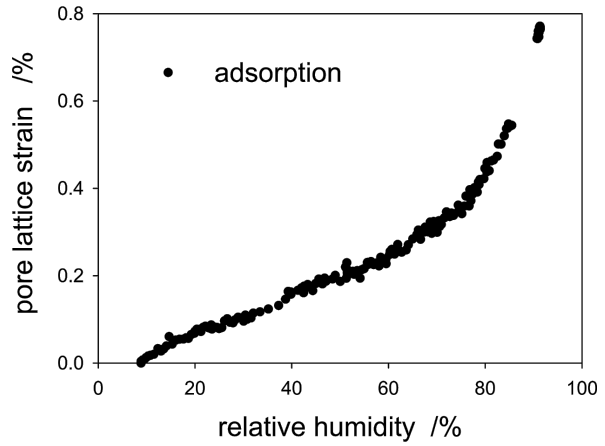

Figure 4: Strain isotherm from in situ GISAXS derived from the shift of the out-of-plane 02 reflection in Figure 3a. Only the adsorption branch could be measured reliably with the humidity setup used.

Quantitative description of cantilever deflection

In the following we attempt to describe the measured deflection of the cantilever on a quantitative basis. For this, we consider only the maximum measured deflection between the "dry" sample (i.e., below 10% humidity) and the "wet" sample. Since the deflection of the cantilever was only measured up to 85% RH, we take the same RH interval for the measured pore lattice strain. Table 1 summarizes the parameters used in the following.

The linear deflection δ of a bilayer cantilever (i.e., a film F on a substrate S) with length l and total thickness $d = d_F + d_S$ clamped at one end is given for small deflections (δ << bending radius) by [9]

$$\delta = \varepsilon \cdot \frac{l^2}{2d} \cdot f(n,m), \qquad (1)$$

where ε is the strain difference (i.e., the difference in the relative expansion) between the two layers. The function $f = 6(1+m)^2/[3(1+m)^2 + (1+mn)(m^2 + 1/mn)]$ depends on the thickness ratio $n = d_F/d_S$ of the two layers, and on the ratio of their Young's moduli $m = E_F/E_S$ [31]. In our case both ratios

Table 1: Maximum cantilever deflection δ and maximum pore lattice strain ε, both at RH = 85%; pore mean radius of curvature r, pore volume fraction ϕ, effective cantilever length l, silicon substrate thickness d_S, average film thickness d_F, Young's modulus of silica E_S, and change of surface energy Δγ of silica upon full wetting with water.

	δ (nm)	ε (%)	r (nm)	ϕ (%)	l (μm)	d_S (μm)	d_F (μm)	E_S (GPa)	Δγ (J/m^2)
value	140	0. 55	3.31	37	130	4.5	0.3	130	0.12
reference	AFM	GISAXS	GISAXS	GISAXS	SEM	SEM	SEM	[29]	[30]

are much smaller than one and f reduces to $f = 6mn$, which after approximating d_S by d leads to a very simple expression for Equation 1.

$$\delta \approx 3\varepsilon \frac{E_F}{E_S} \frac{l^2}{d^2} d_F \,. \tag{2}$$

Since the silicon substrate can be regarded as rigid, ε is given by the strain in the silica film, which was measured experimentally by GISAXS (Table 1). Equation 2 confirms the linear relationship between the sorption-induced strain and the cantilever deflection. If we have a reliable estimate for the Young's modulus E_F of the film, the expected deflection can be predicted from the experimentally measured strain (see Figure 4). However, E_F is not known experimentally for our film. On the other hand, if we know both, the cantilever deflection and the sorption-induced strain from experiment, Equation 2 can be used to estimate the Young's modulus of the porous film. Inserting the experimental values of δ and ε together with the other known parameters (Table 1) we obtain $E_F \approx 5.0$ GPa. Literature reports values of the order of 30–40 GPa for the bulk Young's modulus E_F^{solid} in nanostructured amorphous silica systems [32,33]. If we assume quadratic scaling of the Young's modulus with density $E_F^{solid} = E_F / (1-\phi)^2$ [34], E_F would be expected to be of the order of 12–16 GPa, which is higher by a factor of 2–3 than the value obtained from Equation 2. This discrepancy can be resolved when considering that the pore volume fraction obtained from GISAXS (Table 1) does not include any micropores (i.e., pores smaller than 2 nm) within the walls of the mesopores. It is well known that wall microporosity plays an important role in mesoporous silica prepared from P123 [35,36]. The value of $E_F \approx 5.0$ GPa obtained from Equation 2 agrees indeed fairly well with the one found in SBA-15 ($E_F \approx 6$ GPa) with a similar volume fraction of mesopores [27].

Now we try to estimate the maximum sorption-induced deformation ε and thus, the cantilever deflection, on a more fundamental basis. Gor and Neimark [13] introduced an analytical model based on the Derjaguin–Broekhoff–de Boer theory, which is able to derive the pressure P within a mesopore from a rigorous thermodynamic treatment of the liquid–solid and the liquid–gas interfaces involved. Knowing the pressure within the pores the resulting surface and bulk stresses in the solid pore walls can be calculated and, by using elasticity theory, the strains of the porous material can be obtained. This step is generally not a simple task as it depends critically on the geometry of the pore network. For cylindrical pores on a hexagonal pore lattice it was found recently that the pore lattice strain can be approximated by the radial strain within the wall of a cylindrical pore subjected to an internal pressure P [27,37]. Following [37], the strain within a thick cylinder with pore volume fraction ϕ, pore wall Young's modulus E_F^{solid}, and corresponding Poisson's ratio ν is given by

$$\begin{aligned} \varepsilon(\mathrm{RH}) &= \frac{2\phi}{1-\phi} \frac{(1-\nu^2)}{E_F^{solid}} P(\mathrm{RH}) \\ &\approx \frac{2\phi}{1-\phi} \frac{1}{E_F^{solid}} \left(\frac{\gamma_{SL}(\mathrm{RH})}{r} - P_L(\mathrm{RH}) \right), \end{aligned} \tag{3}$$

where P(RH) is the humidity-dependent pressure within the pore. To derive the right side of Equation 3, we have used the fact that ν is smaller than 0.2 for silica, and therefore $(1 - \nu^2) \approx 1$. The first pressure term on the right hand side depends on the mean radius of curvature of the pores, r, and the absolute value of the solid–liquid interfacial energy, γ_{SL}(RH), which is determined by the amount of water adsorbed during successive pore filling [13,30,38]. In addition to the solid–liquid interfacial energy, both, the curved liquid–vapor interface during adsorption, and the formation of a hemispherical meniscus at the pore ends after capillary condensation lead to a Laplace pressure P_L(RH). While the change of γ_{SL} gives rise to an increase of ε with increasing RH, P_L is opposite in sign. This leads to the often observed non-monotonous shape of the strain isotherms [13,27,37], with a sudden drop of the strain at capillary condensation. The reason, why there is no such strain drop seen in Figure 4 (and Figure 2) at the pressure of capillary condensation (RH ≈ 70%) is not fully clear. Theoretical calculations [13,39] and experiments with water in SBA-15 [40] show that this drop may be rather small for the adsorption branch. There should be, however, a clear increase in slope above

capillary condensation, which is seen in both, the strain isotherm (Figure 4) and the cantilever deflection (Figure 2) at RH ≈ 70–80%.

To come to an estimate for the measured cantilever deflection, we assume for simplicity all mesopores being fully empty for the lowest RH (RH < 10%) and fully saturated with water without any menisci (meaning $P_L = 0$ in Equation 3) for the highest RH (RH ≈ 85%). Then, $\gamma_{SL} = \Delta\gamma$ is the difference between the surface energy of silica and the interfacial energy of bulk silica fully wetted with water, which is known from literature (Table 1). If we make the additional assumption that the Young's modulus of the porous silica has a quadratic dependence on its density, i.e., $E_F = E_F^{solid}(1-\phi)^2$ [34] and insert the simplified Equation 3 into Equation 2 we obtain

$$\delta \approx 6\frac{\phi(1-\phi)}{r}\frac{\Delta\gamma}{E_S}\frac{l^2}{d^2}d_F\,. \qquad (4)$$

Most interestingly, within this model the cantilever deflection does not depend anymore on the elastic properties of the porous film, but only on the Young's modulus of the silicon substrate, which is well known (Table 1). Hence, Equation 4 can be used to estimate the deflection δ from parameters derived from the nanostructure of the film and from the cantilever geometry only. Inserting the values summarized in Table 1 into Equation 4 yields a calculated deflection of δ = 86 nm, which is in fair agreement with the measured value of about 140 nm, given all the assumptions made to derive this result. The largest uncertainty comes certainly from the film thickness, which is not homogeneous within the cross section (see Figure 1b). As a final remark we note that the expression $\phi(1-\phi)/r$ in Equation 4 is closely related to the total volume specific surface area of the mesoporous material comprising the film. Hence, in the limit of thin compliant films as compared to the substrate, the deflection increases linearly with the specific surface area and with film thickness, and quadratically with the length/thickness ratio of the cantilever. In particular, it is noted that when a 1 μm thick substrate would be used instead of the 4.5 μm thick substrate of the present work, a deflection of roughly a factor 20 larger as compared to the current work can be expected.

Conclusion

We have demonstrated the fabrication and humidity-induced deflection of a microcantilever based on a mesoporous silica/nonporous silicon bilayer. The principle of humidity-induced deformation of mesoporous silica is utilized to create a strain in the porous film, which leads to a reversible cantilever deflection of roughly 140 nm measured with an AFM. Grazing-incidence small-angle scattering (GISAXS) is used to determine nanostructural parameters of the pores such as their volume fraction and their mean curvature radius. Measurement of the RH-dependent pore lattice strain with GISAXS and comparison with the cantilever deflection using classical bilayer bending theory allows for estimating the Young's modulus of the porous film. This is remarkable insofar, as the determination of elastic properties of highly porous thin films is quite important and not at all trivial [41-43]. We also develop a simple model to describe the cantilever deflection quantitatively. The model includes the determination of the sorption-induced strain from nanostructural parameters of the porous film, following the rigorous thermodynamic treatment of sorption-induced deformation introduced by Gor and Neimark [13]. It is shown that the maximum cantilever deflection at high RH depends on geometrical parameters (cantilever length and thickness of film and substrate) and on nanostructural parameters of the film (mean curvature and volume fraction). The only material-dependent properties entering are the Young's modulus of the substrate and the change of the surface energy of the pore wall material with wetting, which for the silica–water interface is well known. Within certain limits, all the mentioned parameters may be varied to quantitatively control the deflection of the presented simple bilayer actuator in order to tailor its response to a humidity change. In combination with cantilever arrays, this concept could be used for complex, humidity-controlled switching operations.

Acknowledgements

Financial support from the Federal Government of Styria in the Framework of the Human Technology Interface: Sensors for Medical Applications (HTI:SMApp) initiative under contract A3-22.M-5/2012-32 is gratefully acknowledged. G.P., R.M. and O.P. also acknowledge financial support from the K2 Competence Centre MPPE in the framework of the Austrian COMET Competence Centre Program, project A2.19. We are grateful for receiving beam time at the ELETTRA-Sincrotrone Trieste (proposal 20140234) via the Austrian beam time contingent at the SAXS beamline. We thank B. Sartory (Materials Center Leoben) for FIB sample preparation and for SEM measurements, and E. Bucher (Chair of Physical Chemistry, Montanuniversitaet Leoben) for the calcination of the samples.

References

1. Lang, H. P.; Baller, M. K.; Berger, R.; Gerber, C.; Gimzewski, J. K.; Battiston, F. M.; Fornaro, P.; Ramseyer, J. P.; Meyer, E.; Güntherodt, H. J. *Anal. Chim. Acta* **1999,** *393,* 59–65. doi:10.1016/S0003-2670(99)00283-4
2. Lang, H. P.; Ramseyer, J. P.; Grange, W.; Braun, T.; Schmid, D.; Hunziker, P.; Jung, C.; Hegner, M.; Gerber, C. *J. Phys.: Conf. Ser.* **2007,** *61,* 663–667. doi:10.1088/1742-6596/61/1/133
3. Huber, F.; Lang, H. P.; Backmann, N.; Rimoldi, D.; Gerber, C. *Nat. Nanotechnol.* **2013,** *8,* 125–129. doi:10.1038/nnano.2012.263

4. Huber, F.; Lang, H. P.; Zhang, J.; Rimoldi, D.; Gerber, C. *Swiss Med. Wkly.* **2015,** *145,* w14092. doi:10.4414/smw.2015.14092
5. Dawson, C.; Vincent, J. F. V.; Rocca, A.-M. *Nature* **1997,** *390,* 668. doi:10.1038/37745
6. Elbaum, R.; Zaltzman, L.; Burgert, I.; Fratzl, P. *Science* **2007,** *316,* 884–886. doi:10.1126/science.1140097
7. Harrington, M. J.; Razghandi, K.; Ditsch, F.; Guiducci, L.; Rueggeberg, M.; Dunlop, J. W. C.; Fratzl, P.; Neinhuis, C.; Burgert, I. *Nat. Commun.* **2011,** *2,* 337. doi:10.1038/ncomms1336
8. Paris, O.; Burgert, I.; Fratzl, P. *MRS Bull.* **2010,** *35,* 219–225. doi:10.1557/mrs2010.655
9. Reyssat, E.; Mahadevan, L. *J. R. Soc., Interface* **2009,** *6,* 951–957. doi:10.1098/rsif.2009.0184
10. Erb, R. M.; Sander, J. S.; Grisch, R.; Studart, A. R. *Nat. Commun.* **2013,** *4,* 1712. doi:10.1038/ncomms2666
11. Xue, Y.; Markmann, J.; Duan, H.; Weissmüller, J.; Huber, P. *Nat. Commun.* **2014,** *5,* 4237. doi:10.1038/ncomms5237
12. Balzer, C.; Morak, R.; Erko, M.; Triatafillidis, C.; Hüsing, N.; Reichenauer, G.; Paris, O. *Z. Phys. Chem.* **2015,** *229,* 1189–1209. doi:10.1515/zpch-2014-0542
13. Gor, G. Yu.; Neimark, A. V. *Langmuir* **2010,** *26,* 13021–13027. doi:10.1021/la1019247
14. Brinker, C. J.; Lu, Y.; Sellinger, A.; Fan, H. *Adv. Mater.* **1999,** *11,* 579–585. doi:10.1002/(SICI)1521-4095(199905)11:7<579::AID-ADMA579>3.0.CO;2-R
15. Dourdain, S.; Bardeau, J.-F.; Colas, M.; Smarsly, B.; Mehdi, A.; Ocko, B. M.; Gibaud, A. *Appl. Phys. Lett.* **2005,** *86,* 113108. doi:10.1063/1.1887821
16. Yan, M.; Henderson, M. J.; Gibaud, A. *Appl. Phys. Lett.* **2007,** *91,* 023104. doi:10.1063/1.2755722
17. Ganser, C.; Hirn, U.; Rohm, S.; Schennach, R.; Teichert, C. *Holzforschung* **2014,** *68,* 53–60. doi:10.1515/hf-2013-0014
18. Hutter, J. L.; Bechhoefer, J. *Rev. Sci. Instrum.* **1993,** *64,* 1868–1873. doi:10.1063/1.1143970
19. Amenitsch, H.; Rappolt, M.; Kriechbaum, M.; Mio, H.; Laggner, P.; Bernstorff, S. *J. Synchrotron Radiat.* **1998,** *5,* 506–508. doi:10.1107/S090904959800137X
20. Sharifi, P.; Marmiroli, B.; Sartori, B.; Cacho-Nerin, F.; Keckes, J.; Amenitsch, H.; Paris, O. *Bioinspired, Biomimetic Nanobiomater.* **2014,** *3,* 183–190. doi:10.1680/bbn.14.00017
21. Tate, M. P.; Urade, V. N.; Kowalski, J. D.; Wei, T.-c.; Hamilton, B. D.; Eggiman, B. W.; Hillhouse, H. W. *J. Phys. Chem. B* **2006,** *110,* 9882–9892. doi:10.1021/jp0566008
22. Erko, M.; Wallacher, D.; Brandt, A.; Paris, O. *J. Appl. Crystallogr.* **2010,** *43,* 1–7. doi:10.1107/S0021889809044112
23. Ciddor, P. E. *Appl. Opt.* **1996,** *35,* 1566–1573. doi:10.1364/AO.35.001566
24. Grosso, D.; Balkenende, A. R.; Albouy, P. A.; Ayral, A.; Amenitsch, H.; Babonneau, F. *Chem. Mater.* **2001,** *13,* 1848–1856. doi:10.1021/cm001225b
25. Zhao, D.; Feng, J.; Huo, Q.; Melosh, N.; Fredrickson, G. H.; Chmelka, B. F.; Stucky, G. D. *Science* **1998,** *279,* 548–552. doi:10.1126/science.279.5350.548
26. Boissiere, C.; Grosso, D.; Lepoutre, S.; Nicole, L.; Bruneau, A. B.; Sanchez, C. *Langmuir* **2005,** *21,* 12362–12371. doi:10.1021/la050981z
27. Prass, J.; Müter, D.; Fratzl, P.; Paris, O. *Appl. Phys. Lett.* **2009,** *95,* 083121. doi:10.1063/1.3213564
28. Günther, G.; Prass, J.; Paris, O.; Schoen, M. *Phys. Rev. Lett.* **2008,** *101,* 086104. doi:10.1103/PhysRevLett.101.086104
29. Hopcroft, M. A.; Nix, W. D.; Kenny, T. W. *J. Microelectromech. Syst.* **2010,** *19,* 229–238. doi:10.1109/JMEMS.2009.2039697
30. Scherer, G. W. *J. Am. Ceram. Soc.* **1986,** *69,* 473–480. doi:10.1111/j.1151-2916.1986.tb07448.x
31. Timoshenko, S. *J. Opt. Soc. Am.* **1925,** *11,* 233–255. doi:10.1364/JOSA.11.000233
32. Fritz-Popovski, G.; Morak, R.; Schöberl, T.; Van Opdenbosch, D.; Zollfrank, C.; Paris, O. *Bioinspired, Biomimetic Nanobiomater.* **2014,** *3,* 160–168. doi:10.1680/bbn.14.00012
33. Zlotnikov, I.; Shilo, D.; Dauphin, Y.; Blumtritt, H.; Werner, P.; Zolotoyabko, E.; Fratzl, P. *RSC Adv.* **2013,** *3,* 5798. doi:10.1039/c3ra40574e
34. Gibson, L. J.; Ashby, M. F. *Cellular Solids, Structure and Properties;* Cambridge University Press: Cambridge, United Kingdom, 1999.
35. Ryoo, R.; Ko, C. H.; Kruk, M.; Antochshuk, V.; Jaroniec, M. *J. Phys. Chem. B* **2000,** *104,* 11465–11471. doi:10.1021/jp002597a
36. Müter, D.; Jähnert, S.; Dunlop, J. W. C.; Findenegg, G. H.; Paris, O. *J. Phys. Chem. C* **2009,** *113,* 15211–15217. doi:10.1021/jp810040k
37. Gor, G. Y.; Bertinetti, L.; Bernstein, N.; Hofmann, T.; Fratzl, P.; Huber, P. *Appl. Phys. Lett.* **2015,** *106,* 261901. doi:10.1063/1.4923240
38. Bangham, D. H.; Fakhoury, N. *J. Chem. Soc.* **1931,** 1324–1333. doi:10.1039/JR9310001324
39. Gor, G. Yu.; Paris, O.; Prass, J.; Russo, P. A.; Ribeiro Carrott, M. M. L.; Neimark, A. V. *Langmuir* **2013,** *29,* 8601–8608. doi:10.1021/la401513n
40. Prass, J. Ph.D. Thesis, Humboldt-Universität, Berlin, Germany, 2011.
41. Mogilnikov, K. P.; Baklanov, M. R. *Electrochem. Solid-State Lett.* **2002,** *5,* F29. doi:10.1149/1.1517771
42. Fan, H.; Hartshorn, C.; Buchheit, T.; Tallant, D.; Assink, R.; Simpson, R.; Kissel, D. J.; Lacks, D. J.; Torquato, S.; Brinker, C. J. *Nat. Mater.* **2007,** *6,* 418–423. doi:10.1038/nmat1913
43. Dourdain, S.; Britton, D. T.; Reichert, H.; Gibaud, A. *Appl. Phys. Lett.* **2008,** *93,* 183108. doi:10.1063/1.2996412

License and Terms

BEILSTEIN JOURNAL OF NANOTECHNOLOGY

Coupled molecular and cantilever dynamics model for frequency-modulated atomic force microscopy

Michael Klocke and Dietrich E. Wolf*

Full Research Paper

Open Access

Address:
Department of Physics, University of Duisburg-Essen and CeNIDE, D-47048 Duisburg, Germany

Email:
Dietrich E. Wolf* - dietrich.wolf@uni-due.de

* Corresponding author

Keywords:
atomic force microscopy; frequency-modulated atomic force microscopy (FM-AFM); energy dissipation

Beilstein J. Nanotechnol. **2016,** *7,* 708–720.
doi:10.3762/bjnano.7.63

Received: 10 September 2015
Accepted: 05 April 2016
Published: 17 May 2016

This article is part of the Thematic Series "Advanced atomic force microscopy techniques IV".

Guest Editor: T. Glatzel

Abstract

A molecular dynamics model is presented, which adds harmonic potentials to the atomic interactions to mimic the elastic properties of an AFM cantilever. It gives new insight into the correlation between the experimentally monitored frequency shift and cantilever damping due to the interaction between tip atoms and scanned surface. Applying the model to ionic crystals with rock salt structure two damping mechanisms are investigated, which occur separately or simultaneously depending on the tip position. These mechanisms are adhesion hysteresis on the one hand and lateral excitations of the cantilever on the other. We find that the short range Lennard-Jones part of the atomic interaction alone is sufficient for changing the predominant mechanism. When the long range ionic interaction is switched off, the two damping mechanisms occur with a completely different pattern, which is explained by the energy landscape for the apex atom of the tip. In this case the adhesion hysteresis is always associated with a distinct lateral displacement of the tip. It is shown how this may lead to a systematic shift between the periodic patterns obtained from the frequency and from the damping signal, respectively.

Introduction

The physical background of the dissipation signal in frequency-modulated atomic force microscopy (FM-AFM) was unclear for a long time, and different effects had been discussed, before it was shown that the main contribution comes from adhesion hysteresis [1-3]. However, agreement between theoretical predictions and experimental dissipation rates has remained a challenge [4] in many cases. The detailed reaction path for a given system can be quite complicated, involving different types of hysteresis [5] and additional effects such as lateral tip displacements [6,7].

Computer simulations have been indispensable to disentangle concurrent complex processes that determine the imaging data, i.e., cantilever damping and frequency shift. Roughly, two types of simulations can be distinguished. First, there are simulations of the dynamics of the whole measurement setup [8,9]. They are

crucial for understanding experimental parameters and procedures. These virtual AFMs provide a link between a known surface–tip interaction and the resulting images [10-13]. A simplified version of this modeling approach are phenomenological point-mass models of the tip. Their purpose is to clarify basic effects, such as the alternating presence or absence of adhesion hysteresis, if the dissipated energy is not replenished fast enough [14], or the effects of lateral tip displacements on the frequency shift [15] and on the cantilever damping [7]. In all these models, adhesion hysteresis can only be incorporated a priori, e.g., by using different forces on approach and retraction of the tip [16,17].

The second type of simulation models focuses on the atomic dissipation mechanisms of the interaction between tip and sample. Small regions of tip and sample, where the interaction takes place, are simulated with atomic resolution. Some of these models use ab initio molecular dynamics or DFT methods [2,18,19], which represent the material properties most reliably. Their computational demand is very high, though, so that the force between tip and sample surface is usually calculated for a quasistatic tip. Molecular dynamics (MD) simulations [1] with material specific interatomic potentials are computationally less demanding. They can take the finite frequency of the approach and retraction of the tip into account [20,21] and have also been applied to torsional cantilever oscillations, where the tip moves parallel to the sample surface [6]. In these simulations the tip motion is represented in a parametric way, e.g., by prescribing a sinusoidal trajectory normal or parallel to the surface.

Recently situations attracted interest, where "the back-action of the tip–sample force on the cantilever can no longer be ignored" [22]. This is for instance the case, when adhesion hysteresis, lateral and normal cantilever oscillations are coupled with each other, which is the focus of the present paper. Then models such as the one in [22] are needed that are placed in between the above two extremes. To this end, we include the dynamics of the tip in an atomistic simulation. Instead of being guided along a predefined curve, the tip atoms move in a harmonic potential representing the elastic restoring force of the bent cantilever. This has several advantages. The frequency shift and the cantilever damping are simulated directly, and their coupling can be studied. Moreover, the dynamic response of the tip due to its interaction with the substrate allows for the excitation of lateral degrees of freedom, which were suppressed, if the tip trajectory was fixed. They can give rise to a significant contribution to the dissipation signal.

These results can already be obtained for the first cycle of the cantilever oscillation. Focussing on the first cycle allows for a microcanonical approach that is complementary to the common MD simulations, which couple the system to a thermostat. A microcanonical MD simulation has advantages in our case: First, one can avoid the numerical integration of a force hysteresis, so that one gets numerically more accurate values for the dissipated energy. Second, in order to distinguish the two damping mechanisms in a system coupled to a thermostat, one would have to check, if the force hysteresis integrals of the three cartesian components add up to zero (corresponding to energy transfer into lateral degrees of freedom) or not (corresponding to adhesion hysteresis). This is more elaborate and likely more error-prone than monitoring the energies directly.

Simulation method

It is not feasible to include the full extent of an AFM cantilever nor that of a substrate within an atomistic simulation. As in previous studies [1,6,20-22] the simulation must be restricted to a small volume around the crucial region of interaction between the tip and the substrate. This is sketched in Figure 1. The substrate is reduced to a simple cuboid, and the tip to a cube. Compared to the crystallographic orientation of the substrate, the tip cube is rotated such that one of its diagonal axes is parallel to the z-axis. The crystals considered in this paper have face-centered cubic (fcc) or NaCl structure. The z-axis corresponds to the [100]-direction in the substrate and the [111]-direction in the tip. There is exactly one apex atom closest to the substrate.

Atoms are treated as point masses with potentials defined between pairs of atoms. They move according to Newton's equations of motion, which are solved numerically by the velocity Verlet algorithm [23]. The atoms are initially placed according to the stable crystal structure (see below for details). Their movement reflects the collective motion of the tip as a whole, as well as the fluctuations induced by the tip–substrate interaction. This is achieved by several harmonic potentials corresponding to the different modes of the cantilever, and by effective masses of part of the simulated atoms, as described in the next paragraphs.

The bending mode of the cantilever (in the absence of the substrate) can be regarded as a harmonic oscillation. Higher harmonics can usually be neglected as long as they are not excited on purpose [24-26]. Therefore it suffices to let the z-component of the center of mass, z_s, of the simulated tip move in a harmonic potential, $V_z = \frac{1}{2}k_z\left(z_s - z_0\right)^2$. The equilibrium position of the center of mass is denoted by z_0, and k_z is the stiffness of the bending mode of the cantilever. This potential is applied to each atom of the tip.

As the simulated tip mass M is only a small portion of the real cantilever, the experimental values for k_z would lead to an enor-

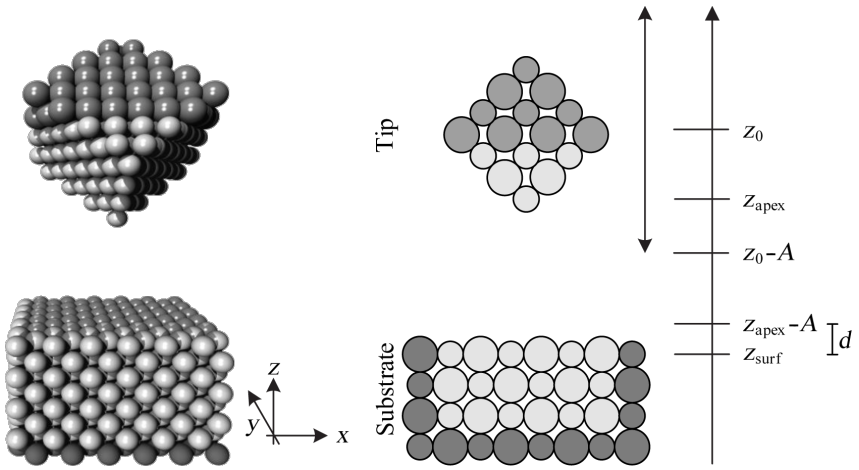

Figure 1: Three-dimensional plot (left) and schematic representation (right) of simulation setup. The tip is represented by a cube, the substrate by a rectangular solid.

mously enhanced frequency of the tip oscillation $\omega_z = \sqrt{k_z / M}$. To obtain a correct frequency of the cantilever, we augment the total mass of the tip M by making some atoms "heavier". However, any impact on the interaction between tip and substrate should be avoided, so that the mass of atoms that are close to the substrate must not be augmented. Therefore the atoms of the tip are divided in two groups, the heavy "head atoms" (dark shade in Figure 1) and the others with normal mass. The mass of the head atoms is augmented by a factor that follows from k_z, ω_z, the normal atomic masses, and the number of head atoms.

The lateral modes can be modeled in a similar fashion. Let x_s and y_s denote the x- and y-component of the center of mass of the tip and x_0 and y_0 the associated equilibrium positions. The potential

$$V_l = \frac{1}{2} k_x \left((x_s - x_0)^2 + (y_s - y_0)^2 \right)$$

is applied to all atoms of the simulated tip, where k_x denotes the stiffness for the oscillation parallel to the x–y-plane. Correspondingly, the frequency of the lateral oscillations is given by $\omega_x = \sqrt{k_x / M}$. ($M$ is the total mass of the tip including the augmentation factor determined by the calibration of ω_z.) Lateral motion of the tip can be due to torsion of the cantilever axis. The corresponding rotation of the tip around the cantilever axis would imply a slight increase of z_s, correlated to the lateral displacement. However, as the lateral amplitudes are very small compared to the length of the tip, it is justified to neglect this effect.

Due to the rotational invariance of the lateral potential V_l, a restoring torque is missing, when the tip is twisted around the z-axis. Therefore, a third harmonic potential is needed that drags all atoms back into their original position relative to the center of mass. In contrast to the other two potentials, this one is only applied to the head atoms. Otherwise it might affect the actual interaction between tip and substrate. For head atom i the potential reads

$$V_{s,i} = \frac{1}{2} k_s \left(\left(\vec{r}_i - \vec{r}_{i,0} \right) - \left(\vec{r}_s - \vec{r}_{s,0} \right) \right)^2 .$$

Here, $\vec{r}_s$ and $\vec{r}_{s,0}$ are, respectively, the current center of mass position and the one at the start of the simulation. Likewise, $\vec{r}_i$ and $\vec{r}_{i,0}$ are the current position of atom i and the one at the start of the simulation, respectively. Obviously, the potential favors atomic displacements parallel to the one of the center of mass. The stiffness k_s should generally be much larger than k_z and k_x.

Prior to the simulation, the initial configuration is obtained in the following way: First, we set up a system that consists only of the substrate atoms. For the Lennard-Jones crystal, these were placed on regular fcc lattice sites with (100)-surfaces. Then all atoms were allowed to relax according to the finite size of the substrate. Only the z-coordinates of the atoms in the bottom layer were fixed. For the (slightly smaller) ionic crystals a relaxation with free boundaries would lead to stronger surface curvature than for the Lennard-Jones crystal. Therefore, a different procedure turned out to be more favorable. For the ionic crystals the substrate ions were placed on a regular NaCl lattice with a lattice constant characteristic for the finite crystal size. Then the positions of all surface atoms apart from those facing the tip were fixed. Note that there is no thermostated layer between the fixed boundary atoms and the ones obeying Newton's law. In this respect, our simulation differs from the common approach [20].

Next, we set up a system that consists only of the tip atoms. The procedure is the same as used for the substrate with two differences: The tip is rotated as described at the beginning of the section and there are no fixed boundaries. Finally, we assemble the two separate systems by placing the uppermost tip atoms at certain positions relative to the bottom layer of the substrate, while relaxing all emerging stresses. These positions are determined such that the lower apex atom of the tip has the desired lateral position and distance $A + d$ from the substrate surface z_{surf} (Figure 1). We set the equilibrium positions of the harmonic potentials V_z and V_l to the position of the center of mass, and choose the initial velocity of all tip atoms such that the tip would oscillate with amplitude A, if the interaction between tip and substrate was switched off. The closest approach to the surface without any interaction between tip and substrate is the nominal distance d. If the interaction is switched on, the closest approach will be different.

In this paper we present results for two kinds of atomic interactions. First the Lennard-Jones potential serves as a reference case. Then, a Coulomb interaction is added in order to simulate KBr, which has been studied extensively in experiments [24,27,28].

Lennard-Jones crystals

If one uses the Lennard-Jones potential,

$$V_{ij}(r) = 4\varepsilon\left(\left(\sigma/r_{ij}\right)^{12} - \left(\sigma/r_{ij}\right)^{6}\right), \qquad (1)$$

for simulating dynamic force microscopy, the tip in Figure 1 in general does not remain intact, but may loose its apex atom, if it comes too close to the substrate. This can be shown simply by comparing the adsorption energy (the energy, the system gains when an atom is attached to the surface) and the dissociation energy of the apex atom (the energy necessary to detach it from the tip). If the dissociation energy is overcompensated by the adsorption energy, it is more favorable for the apex atom to remain on the substrate. To calculate these energies, we place a single atom onto the surface of the substrate and perform an equilibration run by applying the conjugate gradient algorithm. The difference between the total energy of the relaxed system with and without the atom is the adsorption energy. For a substrate with a size of 6 × 6 × 4 unit cells, we get an adsorption energy of $E_a = -5.89\varepsilon$. Similarly, the dissociation energy $E_d = 4.35\varepsilon$ is obtained as difference between the total energy of an isolated tip with and without the apex atom. This shows that the system lowers its energy, if the apex atom detaches from the tip and stays on the surface of the substrate. This is not the case for the potential of KBr described below.

If Lennard-Jones potentials are used exclusively, one way to stabilize the tip is to assume a larger ε parameter for the tip atoms than for the substrate atoms, $\varepsilon_t > \varepsilon_s$. For the interaction between tip and substrate atoms we use the Lorentz–Bertheloth mixing rule: $\varepsilon_{ts} = \sqrt{\varepsilon_t \cdot \varepsilon_s}$. Stability requires that $\left|E_a'\right| = 5.89\varepsilon_{ts} < 4.35\varepsilon_t = E_d'$, or $\varepsilon_t > 1.84\varepsilon_s$. To be on the safe side we use $\varepsilon_t = 2\varepsilon_s$. All basic parameters for the simulation with Lennard-Jones potentials are shown in reduced units in Table 1. A schematic top view of the substrate surface for this simulation is given in Figure 2.

Table 1: Parameter set used for Lennard-Jones case, given in reduced units.

parameter	value
σ	1
m	1
ε_t	2
ε_s	1
k_x	$2.9\cdot10^{-5}$
k_z	$4.6\cdot10^{-7}$
k_s	10^4
ω_x	$3.4\cdot10^{-4}$
ω_z	$4.3\cdot10^{-5}$
A	5
substrate size	6 × 6 × 4 unit cells (576 atoms)
tip size	4 × 4 × 4 unit cells (256 atoms)

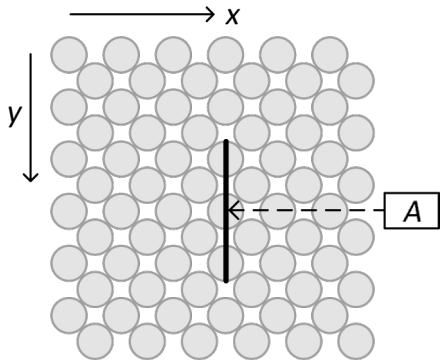

Figure 2: Top view of the substrate surface for the Lennard-Jones case. Distance dependence is probed at position A, whereas constant height scans are performed along the sketched line.

Ionic crystals: Lennard-Jones plus Coulomb

As a simple model for ionic crystals, we add the Coulomb interaction to the Lennard-Jones potential as in [15]:

$$V_{ij}(r) = \frac{q_i q_j}{4\pi\varepsilon_0 r_{ij}} + 4\varepsilon\left(\left(\sigma/r_{ij}\right)^{12} - \left(\sigma/r_{ij}\right)^{6}\right). \qquad (2)$$

Here, it is not necessary to use different Lennard-Jones parameters for the tip and the substrate, because the dissociation energy for the apex atom is not overcompensated by the adsorption energy. The parameters are chosen such that the lattice constant of a KBr crystal is reproduced, and that the error of the cohesive energy is less than 5%. They are given in Table 2, this time in SI units in order to facilitate comparison with previous works and experimental findings. Figure 3 provides the corresponding schematic top view of the substrate surface.

Table 2: Parameter set used for the ionic case.

parameter	value
σ	0.361 nm
ε	0.011 eV
m_K	39 u
m_{Br}	79 u
k_x	64 N/m
k_z	4 N/m
k_s	$4.8{\cdot}10^4$ N/m
f_x	400 MHz
f_z	1600 MHz
A	1.8 nm
substrate size	5 × 5 × 3 unit cells (600 atoms)
tip size	3 × 3 × 3 unit cells (216 atoms)

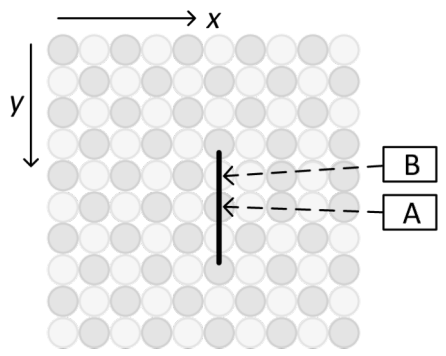

Figure 3: Top view of the substrate surface for the ionic crystal. Distance dependence is probed at position A with oppositely charged apex and projection atom and at position B with same charges. Constant height scans are performed along the sketched line.

Equation 2 is a very simple potential for ionic crystals. Often, more sophisticated Buckingham-type pair potentials [21] are used, which have an exponential short range repulsive part instead of the one with the 12th power in Equation 2. Also, the parameters are different for K–K, Br–Br and K–Br interactions. A further refinement takes the electronic polarization into account via a shell model replacing the rigid ions [29]. It must be kept in mind, though, that the atomic interaction is only one among several important factors that influence FM-AFM simulations. For example the shape of the tip can change the dissipation rate by as much as 100% [21]. For our present purpose, to investigate qualitatively, what the effect of concurring adhesion hysteresis and lateral excitations is, the simple potential is justified.

Determination of dissipation rate Δ*E* and frequency shift Δ*f*

Experimentally the dissipation rate is determined as the amount of energy necessary to maintain a fixed amplitude of the cantilever oscillation. Correspondingly we monitor the energy of the normal oscillation of the center of mass of the tip, z_s, during the half cycle, when it approaches and retracts from the substrate surface. At $t = 0$ the tip starts at the equilibrium position $z_s = z_0$ and returns to the same z-coordinate at $t = t_{\text{end}}$. The damping of the normal cantilever oscillation per cycle is then given by

$$\Delta E = \frac{1}{2M}\left[\left(\sum_{i\in\text{tip}} m_i v_{z,i}\left(t=0\right)\right)^2 - \left(\sum_{i\in\text{tip}} m_i v_{z,i}\left(t_{\text{end}}\right)\right)^2\right]. \quad (3)$$

As the calculations are microcanonical, the energy of the whole system is conserved. Δ*E* must be balanced by an increase of energy in another part. As far as dissipation is concerned, this part would be the inner degrees of freedom of the crystal (that is, substrate and tip are heating up). It is also possible that the energy of another macroscopic degree of freedom is increased, e.g., by a lateral excitation of the tip. For this reason, Δ*E* is called “damping” rather than “dissipation”.

The frequency shift is evaluated as

$$\Delta f = \frac{1}{t_{\text{end}} + T/2} - \frac{1}{T} \quad (4)$$

with the unperturbed oscillation period $T = 1/f_z$.

Results and Discussion

Lennard-Jones crystal

Figure 4 shows the dissipation and the frequency shift as a function of the nominal distance d between tip and surface for a Lennard-Jones crystal. The apex atom is directly above an atom of the substrate (position A in Figure 2). Energy dissipation sets in abruptly as soon as the nominal distance drops below $d < 1.2$ and is basically constant for smaller distances. This is a typical sign for adhesion hysteresis: The sudden configurational change happens only if the tip comes close enough to the surface. Once it happened, the system will go through the hysteresis loop upon retraction of the tip (as shown in Figure 5). The hysteresis is in-

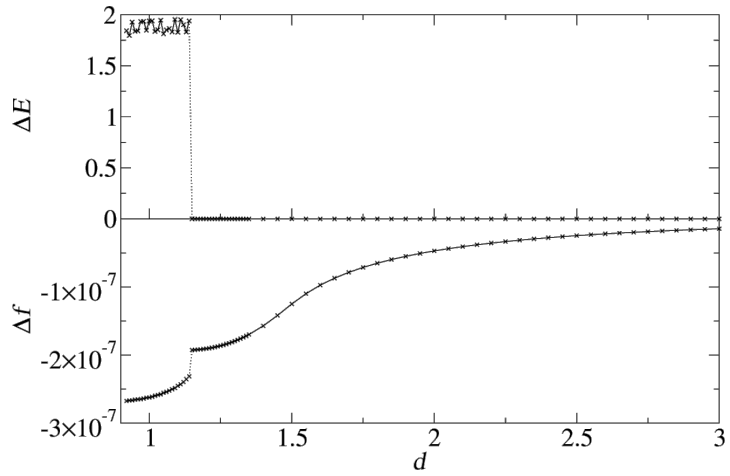

Figure 4: Energy dissipation and frequency shift as a function of the nominal distance. Each point is calculated by a single simulation run with shifted z_0. Lateral tip position is set to A of Figure 2.

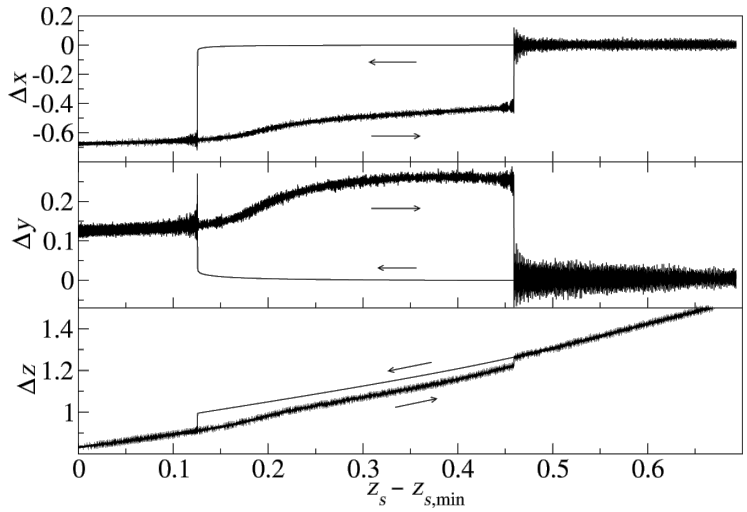

Figure 5: Trajectory of the apex atom at tip position A (Figure 2). Δ*x* and Δ*y* are its *x*- and *y*-coordinates relative to their values at time *t* = 0. The *z*-coordinate Δ*z* is given relative to z_{surf}.

dependent of the smooth, elastic deformation of the configuration, when the tip approaches the surface further before being retracted. Therefore the dissipation is independent of the closest approach. The onset of dissipation can be seen so clearly here, because substrate and tip start with zero temperature at $t = 0$. At finite temperatures the onset of dissipation becomes smeared out due to thermal fluctuations.

One strength of the present model is that it allows for a direct determination of the frequency shift. As expected, a decrease of the nominal distance reduces the frequency (the shift is negative), because of the attraction between tip and surface. It has been predicted [16,18] that the beginning of the dissipation also leads to a change in frequency shift. This is confirmed by the lower plot of Figure 4: The frequency shift shows a discontinuity at the nominal distance where dissipation sets in. The sharp jump will be smeared out for higher temperatures. Comparing the size of the discontinuity to the continuous part of the frequency shift, it can be estimated that adhesion hysteresis is responsible for approximately 20% of the frequency shift. This is rather large, and although the precise ratio clearly depends on the potential used, it is important to realize that the frequency shift is generally not independent of the dissipation signal.

This coupling between the dissipation and the topology signal has further consequences, which are observable experimentally. In order to explain them, a closer inspection of the energy land-

scape of the apex atom is needed. Figure 5 shows the coordinates of the apex atom for a tip oscillating with a nominal distance of $d = 1.05$ above point A in Figure 2. The actual minimal distance is smaller than d due to the attractive forces between tip and substrate. The trajectory shows a hysteresis loop with significant displacements in all three dimensions.

As the tip starts with zero temperature, the apex coordinates first do not fluctuate, when the tip approaches the substrate. However, as soon as the apex atom jumps into its new stable position, the released energy is dissipated, heating the substrate and the tip. From then on the apex coordinates fluctuate. On retraction, the apex atom jumps back, when its original position becomes more favorable again and the energy barrier between the two minima becomes small enough. The energy difference between the two minima is dissipated again, enhancing the apex fluctuations further.

In order to analyze the configurational change associated with the adhesion hysteresis, we probe the potential landscape by relocating the apex atom parallel to the x–y-plane (Figure 1), while the rest of the configuration remains fixed (in particular the distance between tip and substrate). In the first panel of Figure 6, tip and substrate are far apart. The diagram shows a contour plot of the energy landscape in the x–y-plane with origin at position A (Figure 2). High energy values are cut in such a way that the strongly repulsive regions appear as large white areas (these belong to the next neighbors of the apex atom). Beneath the contour plot, the energy variation along the y-axis for $x = 0$ is shown. As expected, the total minimum can be found at $y = 0$. Analogous plots are shown in the second panel of Figure 6, but calculated in an x–y-plane very close to the surface of the substrate. As we have placed the apex atom directly above an atom of the substrate, one finds a strong repulsion at $x = 0$, $y = 0$.

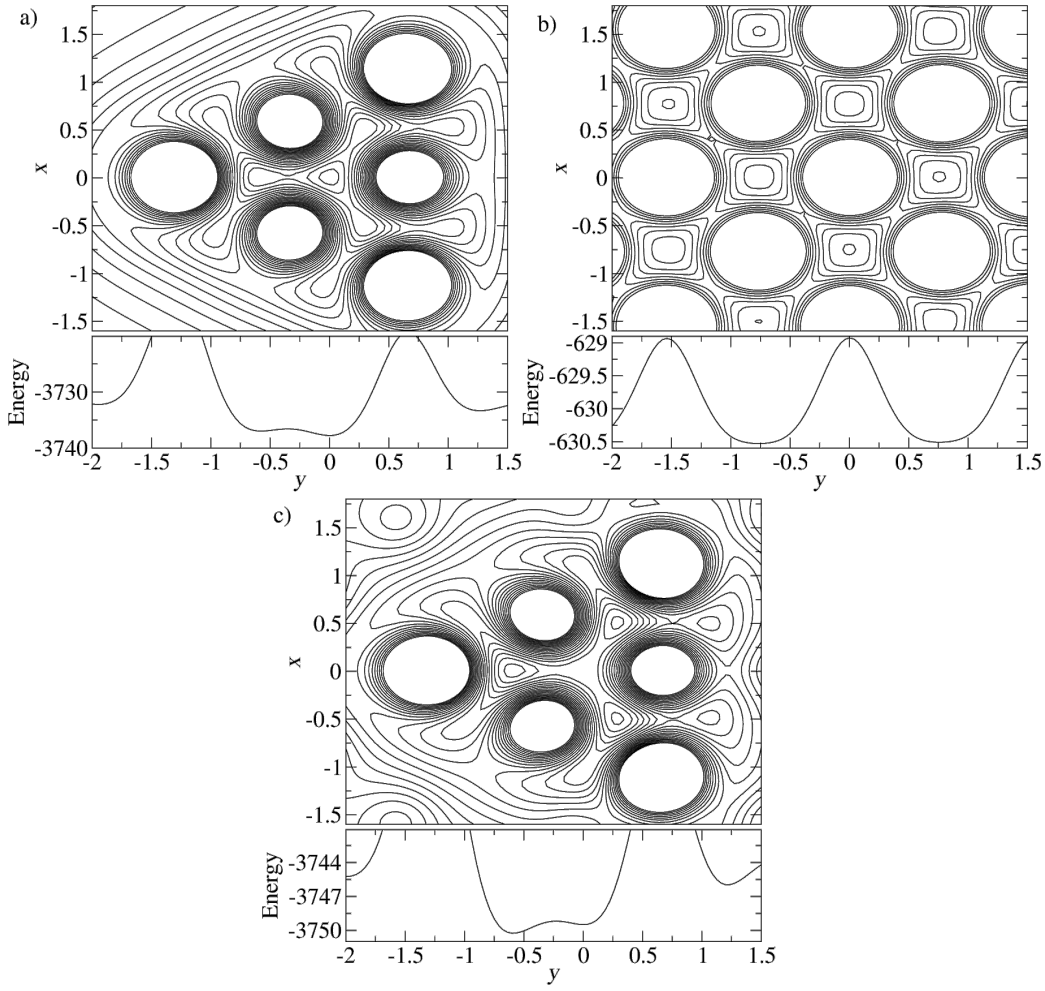

Figure 6: Potential energy surface a) in the (111)-plane of the apex atom, when the tip is far away from the substrate; b) for an adatom in a plane above the substrate; c) in the (111)-plane of the apex atom when the tip is near the substrate ($d = 1.05$). The graphs under the contour plots show the corresponding cross-section of the potential energy surface for $x = 0$.

Not so close, but still at a small distance to the substrate, one obtains the last panel of Figure 6. The energy landscape changes distinctly as both substrate and tip contributions are important. One can roughly view this energy landscape as the sum of the two previous ones. With this picture, the instability leading to the hysteresis gets more clear: While the original apex position at the center becomes unstable due to the repulsion by the substrate atom, the other minima are less affected, as they are rather near a regular lattice site for an adatom on the surface. This explains why the minimum of the energy landscape for the apex atom at $x = 0$, $y \approx -0.6$ is now lower than the one at $x = 0$, $y = 0$ (see the graph under panel c of Figure 6). However, this is not the minimum the apex atom jumps to. It is off the y-axis roughly in (61−1)-direction as concluded from Figure 5.

The coupling between the dissipation and the topography signals combined with the lateral displacement in the adhesion hysteresis explains an effect that has been a puzzle for some time [30]: A systematic discrepancy between the positions of frequency and dissipation maxima, even for a system as simple as the Lennard-Jones crystal considered here. We performed simulations of a scan, where the tip probes many y-positions within an interval of three lattice constants (as shown in Figure 2). The nominal distance d was kept fixed during such a scan (similar to the "constant height"-mode of an AFM).

In Figure 7 the frequency shift and the dissipation (with atomic resolution) are compared for three such scans with different nominal distances d. For the largest distance, $d = 1.30$, the hysteresis is not present. Hence the damping is only minute (note the different ΔE-scale compared to the panels for the other two d-values). It is due to an energy transfer into the lateral degree of freedom. A signature of this effect is that it is nearly equally strong on both sides of the points of strongest attraction between tip and substrate, so that the scan has two dissipation maxima per lattice constant, but only one frequency minimum. In the next section, an example will be discussed, where this effect is stronger.

Figure 7b shows the scan lines for $d = 1.22$. The closer approach of the tip implies a stronger attraction, hence a lower frequency. Moreover, adhesion hysteresis is present in a fraction of the unit cell. It leads to more than 100 times stronger dissipation maxima than in the first panel. Whereas outside the y-intervals with significant dissipation the qualitative y-dependence of the frequency is unchanged, it is strongly reduced, where adhesion hysteresis occurs. This means that the system jumps into a configuration with enhanced attraction. The asymmetric shape of the dissipation curve can be understood with the help of the potential energy surfaces shown in Figure 6a,b. Consider the tip at position $y = 0$, which is directly above a substrate atom A. The attraction between tip and substrate is minimal, because the

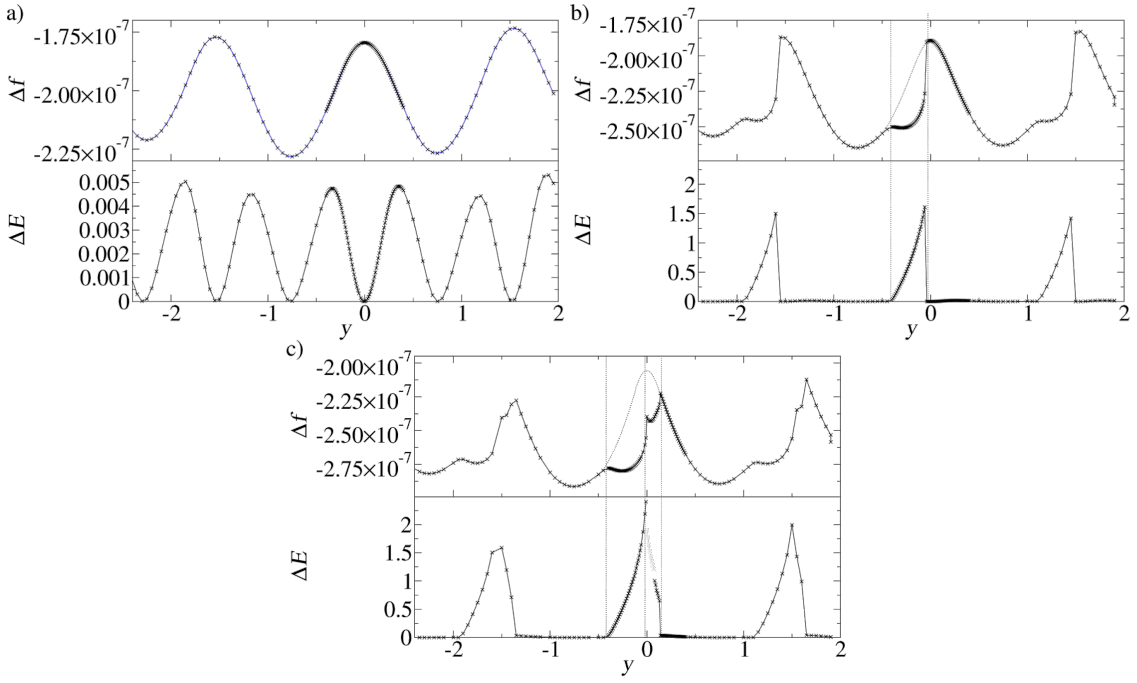

Figure 7: Simulated constant-height scans along the line shown in Figure 2 for a Lennard-Jones system (position A at $y = 0$). The nominal distances are a) $d = 1.30$, b) $d = 1.22$, c) $d = 1.12$. Frequency shift and damping of the cantilever are shown. For b) and c) adhesion hysteresis occurs near position A. The dissipation signal is correlated with a frequency drop. For c) there is an interval to the right of position A, where the atomic configuration of the tip changes irreversibly (grey), i.e., ΔE is the energy dissipated in the first cycle only.

apex atom is far from an fcc binding site to the substrate. As the tip moves in *y*-direction, the fcc binding site to the right of atom A moves towards the center of the triangle of the potential energy surface in Figure 6a, stabilizing the apex atom. When the tip has passed the fcc binding site, the secondary potential minimum left of the apex position benefits from it. This is when the bistability of the apex atom emerges, first with a very small hysteresis. However, the hysteresis increases, as the tip moves towards the substrate atom to the right of A, and the lateral jump of the apex atom into the substrate-induced minimum becomes larger and larger. This explains why the maximal dissipation is reached almost at the point of weakest attraction between tip and substrate. The asymmetry of the dissipation curve is a direct consequence of the mismatch between the triangular potential landscape of the tip and the square one of the substrate.

In Figure 7c the tip is even closer to the substrate, with a nominal distance of d = 1.12. In the *y*-interval, where dissipation occurred already in the previous panel, the curves for dissipation and frequency remain qualitatively the same. However, dissipation extends now also further to the right. The adhesion hysteresis here takes place on the other side of the point of weakest attraction between tip and substrate, and has the opposite asymmetry than before. The explanation is, that now the secondary minima in Figure 6a, which are off the *y*-axis, are the jump destinations. This adhesion hysteresis again causes a frequency reduction. Due to the inverted symmetry, the position of maximal adhesion hysteresis is no longer close to the frequency maximum. It can be assumed that this effect is rather general, whenever adhesion hysteresis involves lateral displacements in different directions. A systematic shift between dissipation and frequency shift has indeed been observed in experiments [30,31].

Ionic crystal

In order to link the conceptual findings of the previous section to a real system, an ionic crystal KBr, we include a long-range Coulomb part in the potential (Equation 2) and give all parameters and results in SI units. The system setup is similar to the one of the previous section.

Figure 3 shows the surface of the ionic crystal. First we let the tip descend over position A, where the apex atom and the projection atom directly underneath are oppositely charged. The results, Figure 8, are clear indication of adhesion hysteresis: energy dissipation sets in abruptly as soon as the tip approaches the substrate closer than (nominally) 5.4 Å. At that point, also the reduced frequency shift $\gamma = (\Delta f/f_z)k_z A^{3/2}$ changes abruptly. (The reduced frequency shift is commonly used instead of Δf in order to minimize the dependence on system parameters such as f_z or k_z. This is helpful in the simulation context, because molecular dynamics simulations are only feasible with exaggerated frequencies f_z [32]). As in Figure 4, the dissipated energy ΔE fluctuates around a roughly constant value, if the tip approaches the substrate close enough that the adhesion hysteresis occurs. The reason is the same: The simulation starts with zero temperature. After the sudden configurational change during the tip approach the temperature increases, so that the position, at which the original configuration is resumed upon retraction of the tip, has thermal fluctuations.

The results for frequency shift and dissipation are similar to those discussed for the simple Lennard-Jones system in Figure 4, although the configurational changes are completely different: Here it is the projection atom that undergoes a significant displacement. The hysteresis loop for the apex atom is much smaller. Another difference is the lack of lateral displacement. This can be understood by the local potential, which the

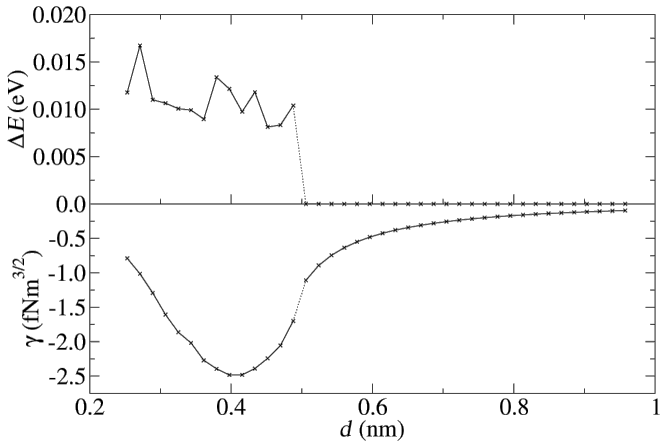

Figure 8: Damping and reduced frequency shift as a function of the nominal distance *d* for position A (apex atom and projection atom are oppositely charged).

apex atom sees in the rock salt structure. The (111) atomic plane (parallel to the (100) substrate surface) next to the apex atom consists of only three atoms of opposite charge, in contrast to the fcc structure (Figure 6a), where it consists of six atoms. Besides the potential minimum, in which the apex atom of a KBr tip sits, there are no secondary minima, which could become favorable due to the substrate influence. Hence the asymmetry of the tip with respect to the substrate has little dynamical effect. This explains, why no lateral displacement can be observed at positions A and B, where the apex atom descends directly above an attractive (A) or repulsive (B) substrate atom.

Along the line connecting the positions A and B of Figure 3 both the hysteresis as well as the lateral excitation occur, separately or simultaneously to varying degrees. This is the conclusion drawn from Figure 9. The first panel shows the positional dependence of the reduced frequency shift obtained with the parameters of Table 2 and d = 0.4. The second panel shows the damping of the cantilever for the same simulations. In order to discriminate between the two damping mechanisms, the third panel displays the energy ending up in the lateral degrees of freedom x_s and y_s of the center of mass of the tip. It nearly vanishes, if the apex atom is above a substrate atom, but has pronounced maxima in between. Subtracting the third from the second panel, one obtains the energy dissipated due to adhesion hysteresis, panel four. It is the dominant mechanism around tip position A, but vanishes near tip position B. The regions, where both mechanisms are present, overlap. There, both mechanisms contribute to the damping on the same order of magnitude.

This raises the question, whether or not the two damping mechanisms enhance or inhibit each other. In order to answer this question we repeated the simulation with the only difference that the lateral stiffness k_x was enhanced by a factor of 10^4, thereby essentially suppressing the excitation of lateral oscillations. Then the cantilever damping is solely determined by the adhesion hysteresis. It is also shown in the fourth panel of Figure 9. Within the numerical errors it agrees with the difference curve obtained from the second and third panel. This

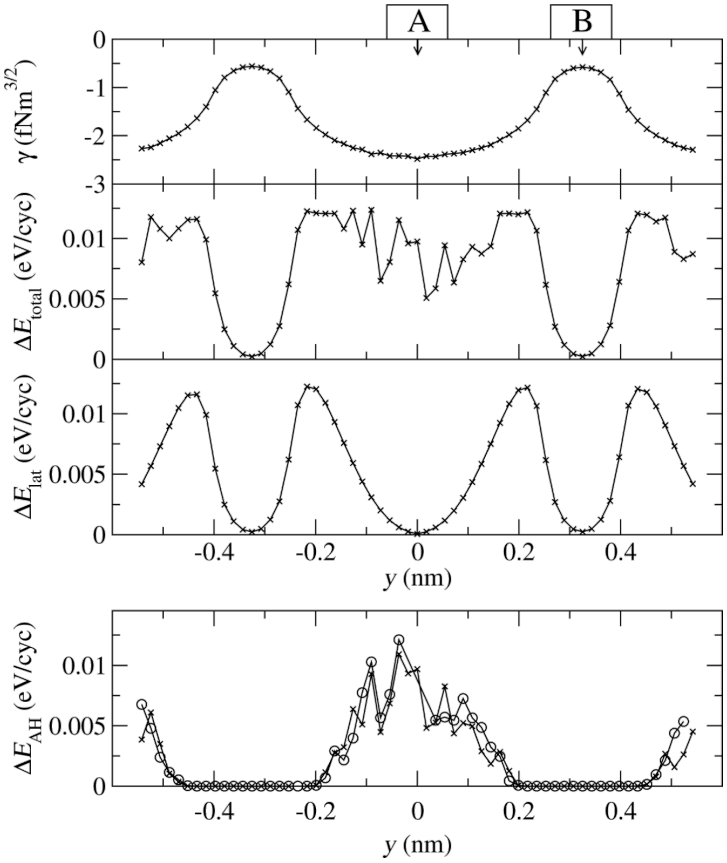

Figure 9: Simulated constant-height scan (d = 0.4 nm) for KBr along the line shown in Figure 3. The first panel shows the frequency shift, the second shows the total damping rate ΔE_{total}, which is composed of the damping rate due to lateral oscillations (ΔE_{lat} shown in the third panel) and due to adhesion hysteresis (ΔE_{AH} shown in the fourth panel). The fourth panel also shows the dissipation rate, if the excitation of lateral oscillations is suppressed (open circles).

proves that adhesion hysteresis is not affected significantly by the excitation of lateral oscillations, at least in the present case of KBr.

Now the tip is placed at position $y = 0.243$, where according to Figure 9 exclusively lateral excitations are responsible for the cantilever damping. Figure 10 shows a completely different d-dependence of the dissipation behavior. It is not step-like as in Figure 8. The excitation of the lateral oscillation of the tip continuously becomes stronger when the nominal distance between tip and substrate decreases. Previously, we pointed out the conceptual difference between the damping of the tip motion and an actual dissipation (see [7] for a detailed discussion). If we evaluate the dissipation directly (the energy of the internal degrees of freedom without the motion of the tip as a whole), we find that it actually vanishes. This shows that the energy is transferred into the macroscopic lateral modes rather than being distributed randomly among the internal degrees of freedom.

The cantilever damping is determined by the energy landscape of the system and therefore depends on the parameter ε in Equation 2, which quantifies the relative strength of the short-range Lennard-Jones interaction compared to the long-range Coulomb interaction. It will vary for different ionic crystals with rock salt structure.

The ε-dependence of the cantilever damping at point A of Figure 3 for a nominal distance $d = 0.4$ nm is shown in Figure 11. The figure shows also the dissipation, which accounts only for a part of the damping. The difference is the energy transferred into the lateral degrees of freedom. For increasing ε the damping becomes weaker first, nearly vanishes near $\varepsilon \approx 0.05$ eV, but then increases again. This remarkable re-occurring damping can be traced back to the two different damping mechanisms (adhesion hysteresis or lateral excitation). Up to $\varepsilon \approx 0.05$ the damping is entirely due to adhesion hysteresis. As already discussed for KBr, lateral modes are not excited in significant amounts. However, the adhesion hysteresis becomes weaker and ultimately ceases to exist: The increased short-range attraction makes it more and more difficult to let the projection atom jump from the substrate towards the approaching tip. The high coordination number wins over the point-like long distance attraction between apex and projection atom.

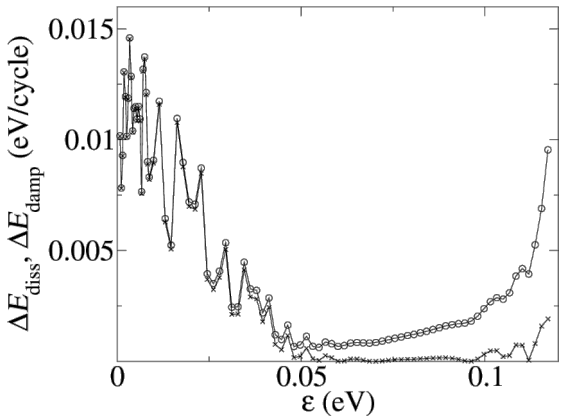

Figure 11: Damping rate (upper curve) and dissipation rate (lower curve) as a function of the strength ε of the short range part of the potential. Below 0.05 eV the cantilever damping is due to adhesion hysteresis. Above, it is mainly due to the transfer of energy from the normal into the lateral oscillation modes.

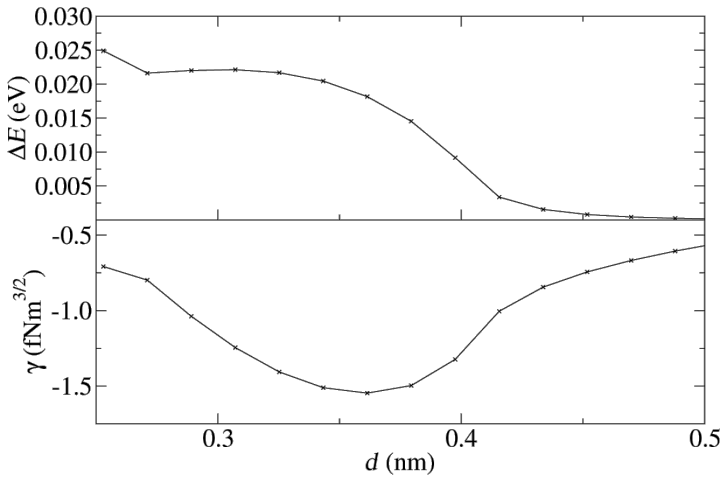

Figure 10: Damping and reduced frequency shift as a function of the nominal distance d for position $y = 0.243$ nm, where the damping is exclusively due to lateral excitations.

For larger ε, the damping of the normal cantilever oscillation is dominated by its coupling to the lateral modes. Dissipation of energy to the internal degrees of freedom hardly occurs. How can this finding be reconciled with the argument presented above, that no lateral excitation should be possible at point A? The essence of that argument was that the apex atom of the tip sits in a deep potential well without secondary local minima around, so that its position in the *x*–*y*-plane remains essentially unchanged, when the interaction between tip and substrate is switched on. However, the point contact force between tip and substrate also increases with ε, hence also its lateral components, if there are any. In fact the total potential energy of substrate and tip has a lower symmetry than for the substrate or the tip separately. This leads to a lateral excitation of the tip without adhesion hysteresis.

Conclusion

Simulating the motion of the cantilever together with the atomistic dynamics led to several new insights relevant for frequency-modulated atomic force microscopy. Specifically, we considered ionic crystals with rock salt structure. The interaction between pairs of ions was modeled by the Coulomb potential plus a short range contribution of the Lennard-Jones type. The AFM tip and the substrate were of the same material. The (100)-surface was probed by a cubic portion of the tip (with (100) faces). The tip was turned such that its diagonal direction was normal to the sample surface.

This class of models shows adhesion hysteresis, when the apex ion of the tip is directly above an oppositely charged ion of the substrate surface. However, the dissipation becomes weaker, if the short range attraction between the atoms is increased, and vanishes above a critical Lennard-Jones parameter $\varepsilon \approx 0.05$ eV. Then a different mechanism of the cantilever damping takes over: Energy is transferred from the normal cantilever oscillation into the lateral modes without any adhesion hysteresis. This transition from one damping mechanism to another one can only be simulated with a molecular dynamics model that includes the dynamics of the cantilever.

The two damping mechanisms can be distinguished by their dependence on the nominal distance d between the tip and the substrate. For the adhesion hysteresis the dissipation sets in abruptly as soon as d becomes small enough and remains roughly constant below. At the same time, the frequency of the cantilever oscillation changes discontinuously. If the normal cantilever oscillation is damped, for lateral oscillations get excited, the energy transfer increases smoothly with decreasing d, due to the increasing lateral forces, and the normal frequency has no discontinuity. This correlated behavior of the frequency shift and the damping rate can be observed in experiments.

For a KBr (100) surface we could show that there exist different tip positions, where either one of the two damping mechanisms dominates, and those, where both occur simultaneously. Adhesion hysteresis was found at and around the tip position, where the apex atom of the tip faces a substrate ion of opposite charge. These correspond to binding sites of the ionic crystal. Lateral cantilever excitation was found in an annulus around the position where these charges are equal. In between, both mechanisms contribute significantly to the cantilever damping.

Even the simple Lennard-Jones crystal shows adhesion hysteresis. In contrast to KBr, the adhesion hysteresis does not occur close to the binding sites of the substrate, but at the least attractive positions. It is always connected with lateral displacement of the apex atom. A careful analysis of the potential landscape for the apex atom explains this behavior and reveals the reason, why the dissipation signal is sometimes systematically shifted by a fraction of a lattice constant into one direction compared to the frequency signal. Turning the argument around, this observation gives indirect information about the combined energy landscape of tip and substrate, and hence about the tip geometry.

These results show that the combined simulation of atomic and cantilever dynamics is very instructive and leads to a better understanding of frequency modulated atomic force microscopy. In this paper we studied KBr type systems, because such ionic crystals were among the earliest samples where the mechanism of adhesion hysteresis was investigated experimentally [33] and theoretically [1]. However, by now, many more examples are known with distinct adhesion hysteresis, notably also organic molecules with covalent bonds [34]. These systems are chemically more complex, but the principal mechanism of adhesion hysteresis is the same as for a simple KBr surface. Also, lateral displacements of the tip should not only occur in ionic crystals. Therefore a combination of both causes for cantilever damping should be expected for other systems, as well. When interpreting the experimental data one has to be aware of this.

Acknowledgements

This work was supported by the German Research Society (DFG) within SFB 616 “Energy Dissipation at Surfaces”. We like to thank M. Schleberger, R. Möller, M. Lange and T. Roll for discussing their experiments with us.

References

1. Trevethan, T.; Kantorovic, L. *Nanotechnology* **2006,** *17,* S205–S212. doi:10.1088/0957-4484/17/7/S18
2. Kantorovich, L.; Hobbs, C. *Phys. Rev. B* **2006,** *73,* 245420. doi:10.1103/PhysRevB.73.245420

3. Sugimoto, Y.; Pou, P.; Custance, O.; Jelinek, P.; Abe, M.; Perez, R.; Morita, S. *Science* **2008,** *322,* 413. doi:10.1126/science.1160601
4. Martínez, N. F.; Kamiński, W.; Gómez, C. J.; Albonetti, C.; Biscarini, F.; Pérez, R.; García, R. *Nanotechnology* **2009,** *20,* 434021. doi:10.1088/0957-4484/20/43/434021
5. Bamidele, J.; Li, Y. J.; Jarvis, S.; Naitoh, Y.; Sugawara, Y.; Kantorovich, L. *Phys. Chem. Chem. Phys.* **2012,** *14,* 16250–16257. doi:10.1039/C2CP43121A
6. Canova, F. F.; Kawai, S.; de Capitani, C.; Kan'no, K.-i.; Glatzel, T.; Such, B.; Foster, A. S.; Meyer, E. *Phys. Rev. Lett.* **2013,** *110,* 203203. doi:10.1103/PhysRevLett.110.203203
7. Klocke, M.; Wolf, D. E. *Beilstein J. Nanotechnol.* **2014,** *5,* 2048–2057. doi:10.3762/bjnano.5.213
8. Kokavecz, J.; Tóth, Z.; Horváth, Z. L.; Heszler, P.; Mechler, Á. *Nanotechnology* **2006,** *17,* S173. doi:10.1088/0957-4484/17/7/S12
9. Nony, L.; Baratoff, A.; Schär, D.; Pfeiffer, O.; Wetzel, A.; Meyer, E. *Phys. Rev. B* **2006,** *74,* 235439. doi:10.1103/PhysRevB.74.235439
10. Livshits, A. I.; Shluger, A.; Rohl, A. L.; Foster, A. S. *Phys. Rev. B* **1999,** *59,* 2436–2448. doi:10.1103/PhysRevB.59.2436
11. Polesel-Maris, J.; Gauthier, S. *J. Appl. Phys.* **2005,** *97,* 044902. doi:10.1063/1.1841462
12. Watkins, M.; Trevethan, T.; Shluger, A. L.; Kantorovich, L. N. *Phys. Rev. B* **2007,** *76,* 245421. doi:10.1103/PhysRevB.76.245421
13. Melcher, J.; Hu, S.; Raman, A. *Rev. Sci. Instrum.* **2008,** *79,* 061301. doi:10.1063/1.2938864
14. Sahagún, E.; Sáenz, J. J. *Phys. Rev. B* **2012,** *85,* 235412. doi:10.1103/PhysRevB.85.235412
15. Uluutku, B.; Baykara, M. Z. *J. Vac. Sci. Technol., B* **2013,** *31,* 041801. doi:10.1116/1.4807376
16. Sasaki, N.; Tsukada, M. *Jpn. J. Appl. Phys.* **2000,** *39,* L1334–L1337. doi:10.1143/JJAP.39.L1334
17. Hölscher, H.; Gotsmann, B.; Allers, W.; Schwarz, U. D.; Wiesendanger, R. *Phys. Rev. B* **2001,** *64,* 075402. doi:10.1103/PhysRevB.64.075402
18. Oyabu, N.; Pou, P.; Sugimoto, Y.; Jelinek, P.; Abe, M.; Morita, S.; Pérez, R.; Custance, O. *Phys. Rev. Lett.* **2006,** *96,* 106101. doi:10.1103/PhysRevLett.96.106101
19. Sugimoto, Y.; Pou, P.; Abe, M.; Jelinek, P.; Pérez, R.; Morita, S.; Custance, O. *Nature* **2007,** *446,* 64–67. doi:10.1038/nature05530
20. Pishkenari, H. N.; Meghdati, A. *Physica E* **2010,** *42,* 2069–2077. doi:10.1016/j.physe.2010.03.030
21. Kawai, S.; Canova, F. F.; Glatzel, T.; Foster, A. S.; Meyer, E. *Phys. Rev. B* **2011,** *84,* 115415. doi:10.1103/PhysRevB.84.115415
22. Castanie, F.; Nony, L.; Gauthier, S.; Bouju, X. *J. Phys. Chem. C* **2013,** *117,* 10492. doi:10.1021/jp400948a
23. Swope, W. C.; Andersen, H. C.; Berens, P. H.; Wilson, K. R. *J. Chem. Phys.* **1982,** *76,* 637–649. doi:10.1063/1.442716
24. Kunstmann, T.; Schlarb, A.; Fendrich, M.; Paulkowski, D.; Wagner, T.; Möller, R. *Appl. Phys. Lett.* **2006,** *88,* 153112. doi:10.1063/1.2194367
25. Reinstädtler, M.; Kasai, T.; Rabe, U.; Bhushan, B.; Arnold, W. *J. Phys. D: Appl. Phys.* **2005,** *38,* R269. doi:10.1088/0022-3727/38/18/R01
26. Kawai, S.; Sasaki, N.; Kawakatsu, H. *Phys. Rev. B* **2009,** *79,* 195412. doi:10.1103/PhysRevB.79.195412
27. Kawai, S.; Glatzel, T.; Such, B.; Koch, S.; Baratoff, A.; Meyer, E. *Phys. Rev. B* **2012,** *86,* 245419. doi:10.1103/PhysRevB.86.245419
28. Fremy, S.; Kawai, S.; Pawlak, R.; Glatzel, T.; Baratoff, A.; Meyer, E. *Nanotechnology* **2012,** *23,* 055401. doi:10.1088/0957-4484/23/5/055401
29. Lindan, P. J. D.; Gillan, M. J. *J. Phys.: Condens. Matter* **1993,** *5,* 1019. doi:10.1088/0953-8984/5/8/005
30. Baykara, M. Z.; Schwendemann, T. C.; Altman, E. I.; Schwarz, U. D. *Adv. Mater.* **2010,** *22,* 2838–2853. doi:10.1002/adma.200903909
31. Fendrich, M.; Kunstmann, T.; Paulkowski, D.; Möller, R. *Nanotechnology* **2007,** *18,* 084004. doi:10.1088/0957-4484/18/8/084004
32. García, R.; Pérez, R. *Surf. Sci. Rep.* **2002,** *47,* 197–301. doi:10.1016/S0167-5729(02)00077-8
33. Ruschmeier, K.; Schirmeisen, A.; Hoffmann, R. *Phys. Rev. Lett.* **2008,** *101,* 156102. doi:10.1103/PhysRevLett.101.156102
34. Langewisch, G.; Kamiński, W.; Braun, D.-A.; Möller, R.; Fuchs, H.; Schirmeisen, A.; Pérez, R. *Small* **2012,** *8,* 602–611. doi:10.1002/smll.201101919

License and Terms

The definitive version of this article is the electronic one which can be found at: doi:10.3762/bjnano.7.63

BEILSTEIN JOURNAL OF NANOTECHNOLOGY

High-resolution noncontact AFM and Kelvin probe force microscopy investigations of self-assembled photovoltaic donor–acceptor dyads

Benjamin Grévin[*1,2,3], Pierre-Olivier Schwartz[4,5], Laure Biniek[6], Martin Brinkmann[6], Nicolas Leclerc[7], Elena Zaborova[7] and Stéphane Méry[*4]

Full Research Paper

Open Access

Address:
[1]University Grenoble Alpes, INAC-SPrAM, 38000 Grenoble, France, [2]CNRS Alpes, INAC-SPrAM, 38000 Grenoble, France, [3]CEA, INAC-SPrAM, 38000 Grenoble, France, [4]Institut de Physique et de Chimie des Matériaux de Strasbourg, Université de Strasbourg, CNRS UMR 7504, 23 rue du Loess, BP 43, 67034 Strasbourg Cedex 2, France, [5]Institut für Organische Chemie II und Neue Materialien, Ulm Universität, Albert-Einstein-Allee 11, Ulm, Germany, [6]Institut Charles Sadron, CNRS, Université de Strasbourg, 23 rue du Loess, BP 84047, 67034 Strasbourg Cedex 2, France, and [7]Institut de Chimie et Procédés pour l'Energie, l'Environnement et la santé (ICPEES), Université de Strasbourg, CNRS UMR 7515, ECPM, 25 rue Becquerel, 67087 Strasbourg Cedex 2, France

Email:
Benjamin Grévin[*] - benjamin.grevin@cea.fr; Stéphane Méry[*] - stephane.mery@ipcms.unistra.fr

* Corresponding author

Keywords:
donor–acceptor co-oligomers; donor–acceptor lamellae; donor–acceptor-ordered bulk heterojunction; Kelvin probe force microscopy (KPFM); noncontact atomic force microscopy (nc-AFM); organic photovoltaics; surface photo-voltage (SPV)

Beilstein J. Nanotechnol. **2016,** *7,* 799–808.
doi:10.3762/bjnano.7.71

Received: 01 February 2016
Accepted: 22 May 2016
Published: 03 June 2016

This article is part of the Thematic Series "Advanced atomic force microscopy techniques IV".

Guest Editor: T. Glatzel

Abstract

Self-assembled donor–acceptor dyads are used as model nanostructured heterojunctions for local investigations by noncontact atomic force microscopy (nc-AFM) and Kelvin probe force microscopy (KPFM). With the aim to probe the photo-induced charge carrier generation, thin films deposited on transparent indium tin oxide substrates are investigated in dark conditions and upon illumination. The topographic and contact potential difference (CPD) images taken under dark conditions are analysed in view of the results of complementary transmission electron microscopy (TEM) experiments. After in situ annealing, it is shown that the dyads with longer donor blocks essentially lead to standing acceptor–donor lamellae, where the acceptor and donor groups are π-stacked in an edge-on configuration. The existence of strong CPD and surface photo-voltage (SPV) contrasts shows that structural variations occur within the bulk of the edge-on stacks. SPV images with a very high lateral resolution are achieved, which allows for the resolution of local photo-charging contrasts at the scale of single edge-on lamella. This work paves the way for local investigations of the optoelectronic properties of donor–acceptor supramolecular architectures down to the elementary building block level.

Introduction

Nowadays, with power conversion efficiency records of over 10% [1,2], solution-processed organic solar cells are regarded as a promising alternative to conventional silicon-based photovoltaic devices. Bulk heterojunction (BHJ) organic solar cells rely on blends of electron-donor (D) and electron-acceptor (A) materials, arranged in interpenetrated networks at the 10 nm scale to efficiently separate the excitons into free charges at the D–A interface. In the past decade, several studies demonstrated that Kelvin probe force microscopy (KPFM) can be powerfully combined with atomic force microscopy (AFM) to simultaneously probe the nanostructure and the optoelectronic properties of organic and hybrid, photoactive thin films and devices [3-9]. Particularly, the local surface photo-voltage (SPV) of organic blends [3,4,6,7] can be mapped in KPFM by analysing the surface potential (or contact potential difference, CPD) shift upon illumination. Nevertheless, analysing the SPV contrasts in relation with the nanostructure remains a challenge due to the complex morphology of nano-phase segregated D–A blends. Achieving a clear identification of the D–A interfaces in optimized, nano-phase segregated blends (i.e., at the 10nm scale) using KPFM continues to be a challenge. Moreover, recent studies have shown that pure donor and acceptor domains may often coexist with intermixed or co-crystallized phases [10,11]. In such structures, the donor and acceptor can be intimately mixed at the sub-10 nm scale. To establish the resolution limits of SPV imaging by KPFM, there is now a crucial need to investigate model D–A interfaces with better defined structural and electronic properties.

In that context, several groups have used the "microphase separation ability" of D–A block copolymers [12] or oligomers to elaborate well-defined, nanostructured D–A interfaces. Most of these supramolecular architectures rely on the use of fullerenes [13-15] or perylene-3,4,9,10-tetracarboxylic acid diimide (PDI) [16-20] as the acceptor components. However, to date, very few KPFM studies have focused on such self-assembled D–A networks [20].

In this study, we investigate a new class of PDI-based acceptor–donor block co-oligomers [19,21]. More precisely, the acceptor block (A) is PDI, whereas the donor block (D) is made of a combination of thiophene, fluorene, and 2,1,3-benzothia-

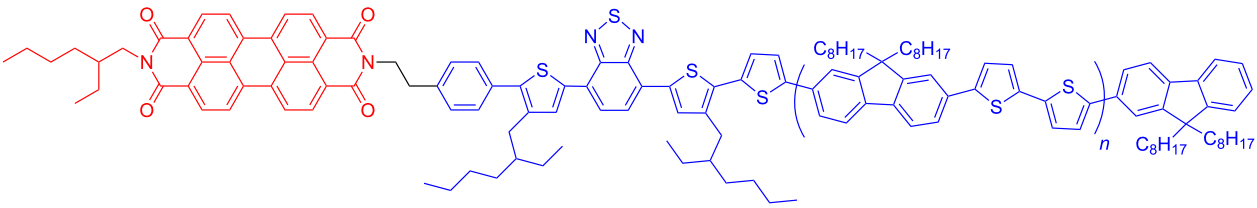

Figure 1: Molecular structures of the investigated A–D_n co-oligomers (in this study n = 1 or n = 3).

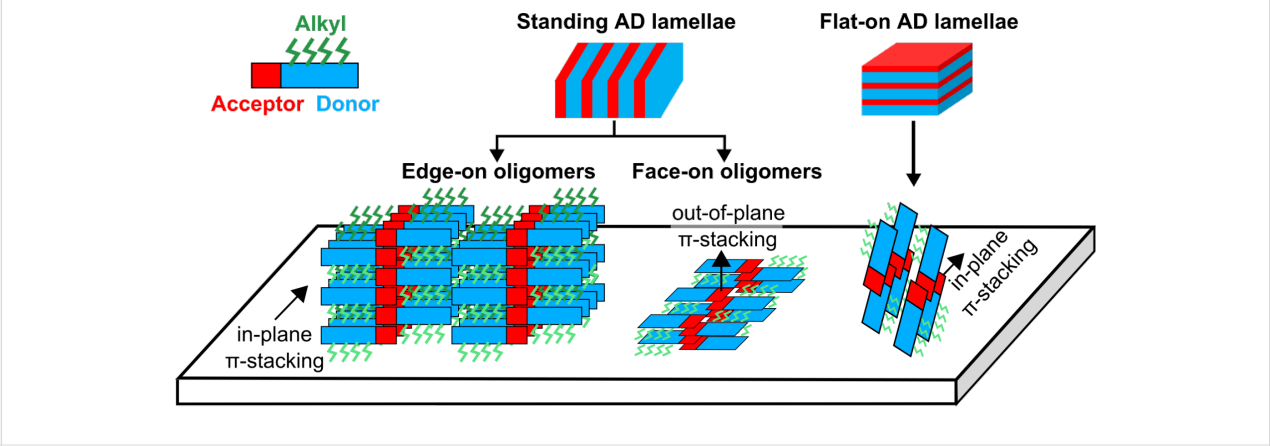

Figure 2: Schematic view of the self-assembled acceptor–donor (A–D) lamellar structures and the observed orientations on the substrate. In the present study, A–D films are composed of mostly standing lamellae with co-oligomers oriented in an edge-on configuration. In these domains, the molecules are π-stacked with a strong overlap of both the PDI and donor segments, and the π-stacking direction is parallel to the plane of the substrate (for more details see [19]). A minority of face-on co-oligomer molecules are also observed in standing A–D lamellae. Flat-on A–D lamellae are formed by co-oligomers oriented normal to the film surface.

diazole derivatives (Figure 1). The donor length can be varied by repeating the number, n, of bithiophene-dioctyl-fluorene segments.

Recent transmission electron microscopy (TEM) and X-ray diffraction (XRD) studies [19,21] have shown that these co-oligomers can form lamellar mesophases on various substrates (e.g., glass, SiO_2, indium tin oxide, oriented poly(tetrafluoroethylene)). The D–A co-oligomers self-assemble in a zipper-like structure such that the donor groups and the PDI units form distinct D and A lamellae. In thin films, both standing and flat-on lamellae were evidenced as illustrated in the schematic of Figure 2.

For standing lamellae, the long axis of the molecules lies in the plane of the substrate whereas for the flat-on lamellae, the molecules are oriented approximately normal to the film plane. The ratio between standing and flat-on lamellae is a function of the donor block length as well as the processing conditions. Flat-on lamellae were obtained on oriented substrates of poly(tetrafluoroethylene) (PTFE) [21], while the films deposited on glass, SiO_2 or indium tin oxide are mainly composed of standing lamellae. In these standing lamellae, two molecular orientations of the D–A oligomers with respect to the substrate are evidenced. They correspond to (i) edge-on co-oligomer orientation (π-stacking direction in the substrate plane) and (ii) face-on co-oligomer orientation with the π-stacking direction normal to the substrate. Both these molecular orientations coexist in the standing lamellae but with a majority of edge-on co-oligomers.

In this work, two samples with $n = 1$ (AD1) and $n = 3$ (AD3) were investigated by nc-AFM and KPFM in the form of thin films (a few tens of nm thick) deposited on functionalized indium tin oxide substrates. Most of the surface photo-voltage investigations were carried out on the AD3 sample, while the AD1 was mainly used in a first step to check the influence of the donor segment length on the film morphology. TEM measurements were carried out on other AD3 samples processed with similar conditions.

The manuscript will focus successively on i) the morphology characterization using AFM and TEM, ii) the analysis of the surface electrostatic contrast in dark conditions, and finally, iii) the surface photo-voltage characterization of the films under illumination.

Methods

The nc-AFM experiments were performed in frequency modulation (FM) mode with an Omicron VT-AFM setup under UHV at room temperature. For each image, the frequency shift, Δf, and vibration amplitude, A_{Vib}, are indicated in the corresponding figure caption. Silicon cantilevers (SuperSharpSilicon, Nanosensors, n+-doped, stiffness 40 N/m, resonance frequency in the 280–300 kHz range) were Ar-sputtered in vacuum to remove the oxide layer and possible contaminants. KPFM measurements were performed in FM mode with the modulation bias V_{AC} (typically 1 V peak-to-peak at 900 Hz) and the compensation voltage V_{DC} applied to the cantilever (tip bias $V_{tip} = V_{DC}$). In that configuration, the contact potential difference (CPD) is equal to $-V_{DC}$. In this work, the potentiometric data are presented as compensation bias ($V_{tip} = -$CPD) images (also called CPD images, KPFM potential or surface potential images). Surface photo-voltage (SPV) images were calculated as the difference between the compensation bias images recorded under selective illumination and in dark conditions, SPV $= V_{tip}^{illum} - V_{tip}^{dark}$. The SPV images were smoothed by applying a Gaussian filter (raw data display the same features but with a slightly higher noise level, see Figures S6, S7, and S8 in Supporting Information File 1).

The lateral lag (due to thermal drift and piezoelectric actuator creep) between the set of images used for the SPV calculation was corrected by using the lattice tool of the WsXM software [22] (see Figure S9 in Supporting Information File 1). After correcting the images, the residual lateral error in the alignment was estimated by comparing topographic cross-section profiles extracted with the multiple profile tool of WsXM (see Supporting Information File 1 for more details). The estimated lateral resolution is indicated for each SPV image in the corresponding figure caption.

Dyads thin films (50 ± 5 nm thick, determined from intermittent-contact AFM measurements, not shown) were deposited from toluene solutions (10 mg/mL) via spin-coating on indium–tin–oxide (ITO) functionalized with PEDOT:PSS (thickness 40 ± 5 nm). In this study, PEDOT:PSS was primarily used to reduce the roughness of the substrate. In situ sample annealing (60 min at 200 °C for AD1 and at 215 °C for AD3) has been performed at pressures of 10^{-10} mbar and under temperature control with an optical pyrometer. Similar results (not shown in this report) were obtained on thin films annealed at a slightly lower temperature (180 °C).

A triple laser source emitting at λ = 405 nm, 515 nm and 685 nm (spot beam diameter ≈0.8 mm) with variable light intensity (OmicronLaser, Germany) was used for sample illumination (through an optical viewport of the UHV chamber). The sample was illuminated with a backside geometry (Figure 3) using specifically designed sample holders with on-board mirrors. The surface photo-voltage of the dyads was investigated as a function of the illumination wavelength, confirming the absence of any photo-voltage related to the silicon cantilever

itself (see Figure S5 in Supporting Information File 1). In the following, all KPFM measurements under illumination were performed at a wavelength of 515 nm with an optical power of 15 mW.

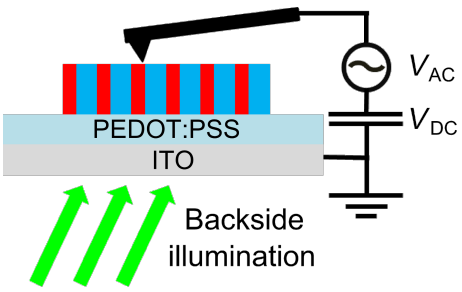

Figure 3: Geometry of the experimental setup for KPFM. The sample is illuminated in backside geometry. The modulation and compensation bias are applied to the tip, while the ITO substrate is grounded.

For TEM investigations, the thin films were coated with a thin amorphous carbon film and removed from the glass substrate by floating on a diluted aqueous HF solution (10 wt %) and subsequent recovery on TEM copper grids. TEM was performed in bright field, high-resolution and diffraction modes using a CM12 Philips microscope equipped with a MVIII (Soft Imaging System) CCD camera. In order to avoid beam damage to the thin films, after focusing and correction of astigmatism, the electron beam was blanked with a shutter and a nearby area was selected to record the HRTEM image. Image treatment was performed by using the AnalySIS software (Soft Imaging System).

Results and Discussion

Surface morphology

Figure 4a,b shows the surface morphology of AD1 and AD3 films after in situ annealing. The topographic images reveal a lamellar self-organization with modulation periodicities (mean values deduced from FFT images, not shown) of ≈9.5 and 15 nm for AD1 and AD3, respectively. These values are fully consistent with the structural model proposed by Schwarz et al. [19] for standing A–D lamellae consisting of edge-on co-oligomers (Figure 2 and Figure 5d). We note that the higher level of damping recorded over the standing domains may be reasonably attributed to the influence of the lateral alkyl side groups, which point out of the surface in the case of the edge-on oligomers (see Figure 2).

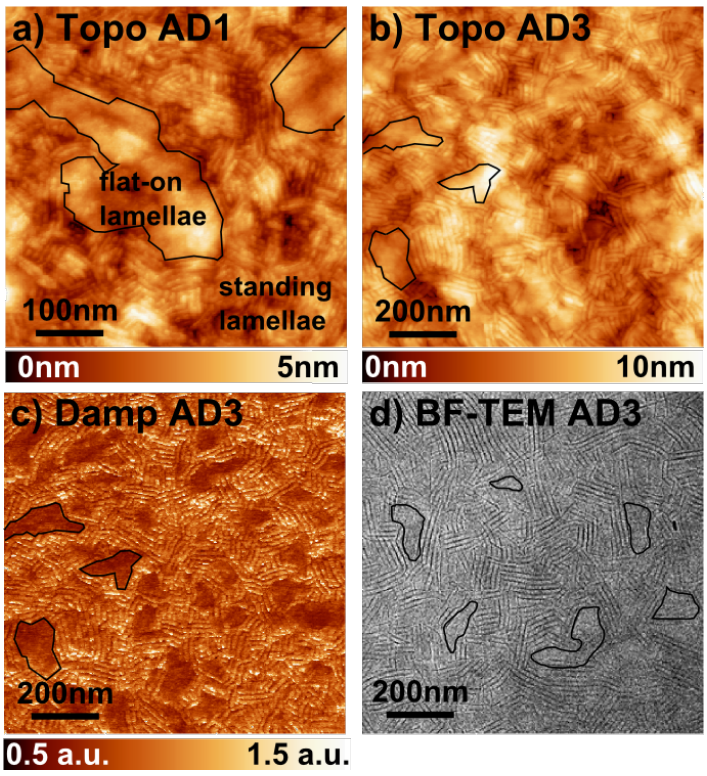

Figure 4: (a) nc-AFM topographic image (500 × 500 nm) of the AD1 film on ITO/PEDOT:PSS (Δf = −55 Hz, A_{Vib} = 14 nm). (b,c) nc-AFM topographic (b) and damping (c) images (1000 × 1000 nm) of the AD3 film on ITO/PEDOT:PSS (Δf = −20 Hz, A_{Vib} = 20 nm). (d) Bright field TEM image of an AD3 film. The area corresponding to some flat-on lamellae are highlighted by black contours in (a–d).

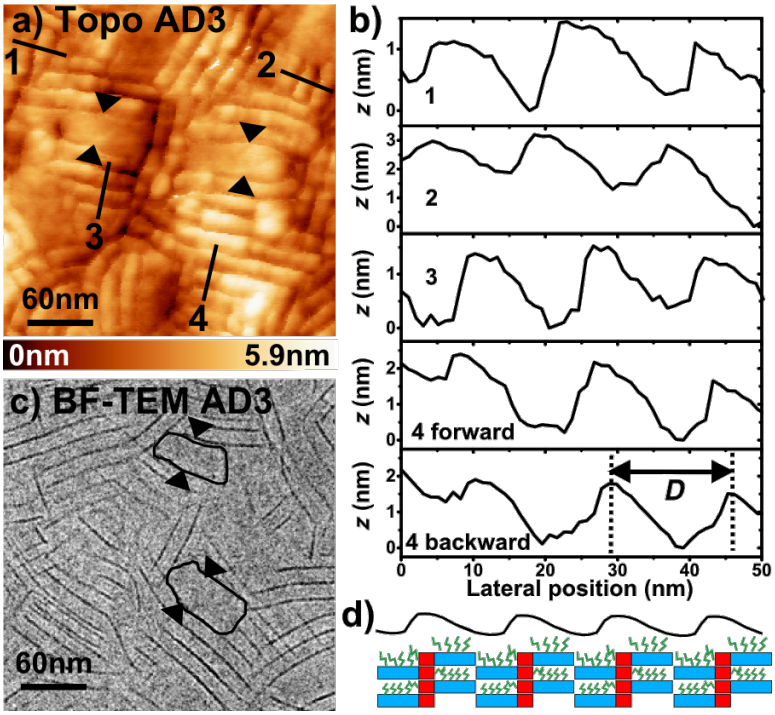

Figure 5: (a) 300 × 300 nm nc-AFM topographic image of the AD3 film (Δf = −10 Hz, A_{Vib} = 20 nm). (b) Topographic profile corresponding to the path highlighted by the black line in (a).The two arrows pinpoint the location of a structural defect. (c) Bright field TEM image of an AD3 film showing identical defects. (d) Schematic side view of the edge-on lamellae, showing how the zipper-like organization results in the appearance of asymmetric AFM topographic profiles (black line).

It is also clear that the standing lamellae coexist with other domains (highlighted in Figure 4a–c) giving rise to a strong contrast in the dissipation images, as shown by Figure 4c. In these parts of the surface, the supramolecular packing cannot be directly resolved from the nc-AFM data. In turn, the similarity between the damping and TEM images is remarkable when comparing Figure 4c and Figure 4d. Actually, XRD and TEM investigations [19,21] have shown that these other domains consist of flat-on lamellae (see Figure 2) and that their proportion in the film is inversely proportional to the length of the donor blocks. This last result is consistent with the surface morphology probed by nc-AFM (compare Figure S1a and Figure S1b in Supporting Information File 1). In the case of the longer AD3 dyad, a statistical analysis performed on large-scale damping images (by using the "flooding" tool of the WSxM software [22], not shown) shows that less than 16% of the surface is apparently covered by flat-on domains. Thus, the AD3 films are mostly composed of standing lamellae, which can be used as model A–D networks for local surface photo-voltage investigations by KPFM. They provide a benchmark to check the ability to resolve the contributions to the SPV contrasts of donor and acceptor units.

Interestingly, the topographic profiles acquired over the standing lamellae (Figure 5a,b) reveal not only a periodic modulation, but also a characteristic asymmetry in the section profile as shown in Figure 5b. This phenomenon is observed both for the forward and backward scans, and is independent of the scanning direction relative to the lamellar in-plane orientation. Moreover, this has been observed by using different cantilevers (not shown). As depicted in Figure 5d, this asymmetry is consistent with the structural model [21] for the standing lamellae with edge-on co-oligomers. Indeed the zipper-like stacking results in a factory roof profile as observed by AFM. Besides, structural defects within the edge-on stacks are revealed in nc-AFM (Figure 5a) and TEM (Figure 5c) images, and appear as local doubling of the lamellar periodicity. They may exist either as small face-on domains or inclined lamellae.

Electrostatic contrasts under dark conditions

Further insight into the structural organization can be achieved by analysing the contact potential images in dark conditions (Figure 6a). In principle, for these undoped oligomers, one expects no permanent charges under dark conditions, with the exception of molecular dipoles and interface dipoles at the dyad–substrate interface.

Firstly, we note the absence of any significant CPD contrast within the flat-on lamellae (blue contours in Figure 6), which is consistent because the tip probes the top surface consisting ex-

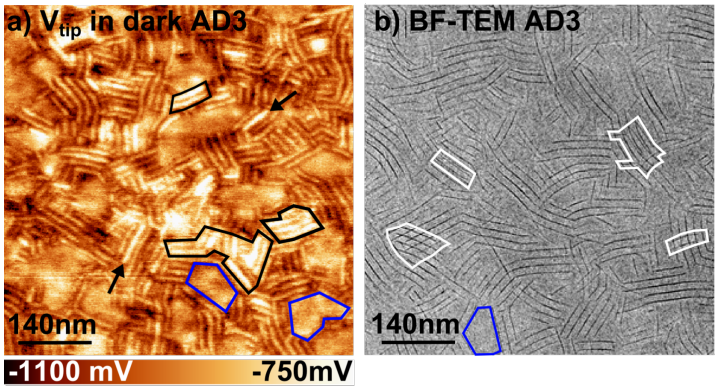

Figure 6: (a) KPFM potential image of the AD3 film recorded in dark (670 × 670 nm, Δf = −20 Hz, A_{Vib} = 20 nm). (b) Bright field TEM image of another AD3 film at the same scale. In both images, flat-on lamellae are highlighted by blue contours. The edge-on lamellae with a high KPFM potential level and the cross-hatch patterns are highlighted by black and white contours in (a) and (b), respectively. Black arrows in (a) pinpoint individual lamellae with higher surface potentials.

clusively of donor groups. Besides, the mean potential level is nearly the same over all flat-on domains. This last point reveals the absence of structural variations within the bulk of the film. In such a case, the CPD originates only from the interface dipole at the recessed dyad–PEDOT:PSS interface.

In turn, the KPFM potential displays modulations over the edge-on domains, in correspondence with the topography and damping channels (see Figure S2 in Supporting Information File 1). Moreover, the KPFM potential image shows additional features not apparent in the other channels. These features correspond essentially to individual or a few A–D lamellae with strong potentiometric contrasts, mostly in the form of brighter stripes in the CPD images. The absence of equivalent features in topography and dissipation images (Figure S2 in Supporting Information File 1) proves the absence of artefacts at the origin of these CPD contrasts, which therefore originate from uneven charge distributions within the edge-on domains.

The most likely explanation is that structural variations occur below the surface of the standing lamellae. These defects impact the molecular dipoles at the surface of the film, due to the mutual polarization effects and wave function overlap with the recessed layers.

Especially, the top layers may cover recessed edge-on stacks displaying a different π-stacking direction, or eventually subsurface flat-on domains. The first hypothesis is particularly supported by the existence of cross-hatch patterns in the TEM images (Figure 6b), clearly revealing that lamellae with different π-stacking directions overlap in some parts of the film. The TEM bright field images correspond to 2D projections of a 3D film morphology. Hence, cross-hatched patterns indicate that two layers of standing lamellae with two different azimuthal orientations are superposed (Figure S3 in Supporting Information File 1).

Here, we stress that in many cases, the size of the "bright CPD patches" is compatible with that found for the cross-hatched areas (compare Figure 6a and Figure 6b). With regards to the contrasts displayed at the scale of individual lamellae (highlighted by black arrows in Figure 6a), one could consider the existence of standing lamellae with face-on co-oligomer orientation. However, this hypothesis is excluded by the analysis of topographic profiles extracted from high-resolution images (see Figure S2 in Supporting Information File 1). Hence, these features most probably reflect underlying structural defects in the bulk of the standing lamellae.

All in all, these results support a picture in which flat-on domains percolate through the whole film thickness without significant structural changes, while edge-on domains present structural variations in the bulk of the sample.

Photo-voltage imaging

In the following, we focus on the analysis of the surface photovoltage (SPV) images acquired on the AD3 sample. At the mesoscopic scale (Figure 7), it can be clearly seen that the surface potential shifts downwards upon illumination, resulting in a negative surface photo-voltage. The potential shift is completely reversible (Figure S4 in Supporting Information File 1), revealing the absence of permanent charge trapping effects in these samples.

The SPV displays a logarithmic dependence as a function of the illumination intensity [4], which is related to the electron–hole recombination kinetics [23]. More precisely, the slope of the SPV as a function of the natural logarithm of the intensity

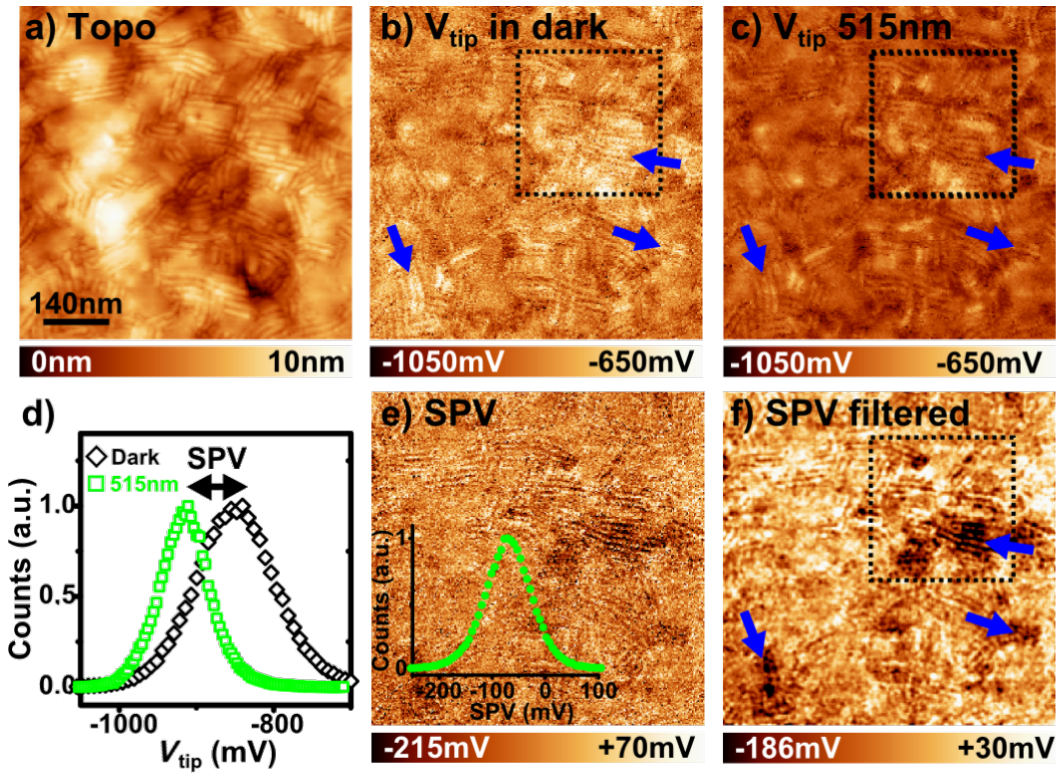

Figure 7: (a–c) nc-AFM/KPFM images (712 × 712 nm) of the AD3 film (Δf = −10 Hz, A_{Vib} = 20 nm) recorded in dark conditions (a,b) and under illumination (c). (d) Histograms of the surface potential values calculated from (b) and (c). (e) SPV image calculated as the difference between (c) and (b). Lateral resolution: ≈5 nm (see Figure S6 in Supporting Information File 1). The corresponding SPV histogram is given in the inset. (f) SPV image filtered with a Gaussian smoothing function. The blue arrows in (b,c,f) indicate some areas where the potential collected under dark conditions is higher and the SPV is more negative. The black dotted squares indicate the location corresponding to the high-resolution images (shown later in Figure 9a,b).

(see Figure S4 in Supporting Information File 1) is equal to k_BT/e = 25 mV, which shows that the recombination is bimolecular [23]. Besides, the photo-voltage response as a function of the illumination wavelength is consistent with the absorption spectrum of the dyads (see Figure S5 in Supporting Information File 1).

In organic donor–acceptor solar cells, the SPV measures the splitting of the quasi-Fermi levels of the holes and electrons under illumination across the donor–acceptor interface [8]. In operating devices, the quasi-Fermi levels of the holes and electrons are nearly aligned with the Fermi levels of the anode and cathode, respectively. The SPV matches the open circuit voltage and is negative when the anode is grounded. Here, the situation is more complicated. The ITO substrate is also grounded, but in the absence of a top metallic cathode, both donor and acceptor units can contribute to the local SPV measured at the surface of the film. However, it can be simply shown that the average SPV remains negative. In order to prove this, we consider the case of the idealized D–A network depicted in Figure 8. In the dark condition state, the Fermi level of the donor units is pinned by the substrate, while the acceptor blocks display a flat band alignment. Under illumination, the holes quasi-Fermi level remains aligned with the Fermi level of the grounded substrate, while the quasi-Fermi level of the electrons is located near the lowest unoccupied orbital level (LUMO) of the acceptor units. As a consequence, the local vacuum level remains constant over the donor units, and is shifted upward over the acceptor segments, resulting in a global downward shift of the surface potential (i.e., a negative SPV).

Now, the question that presents itself is whether this argument still holds in the case of more complex sample morphologies. In our case, it has been previously shown that the AD3 film consists mainly of standing lamellae constituted by edge-on molecules. Then, bi-continuous A–D networks will percolate through a large fraction of the whole film thickness, resulting in a negative SPV (on average).

Moreover, the SPV image displays well-marked contrast over the edge-on stacks (see Figure 7f), most of time in the form of dark patches. Actually, these local SPV minima occur over the lamellae appearing as bright stripes in the CPD images collected under dark conditions (see Figure 7 and Figure S7 in

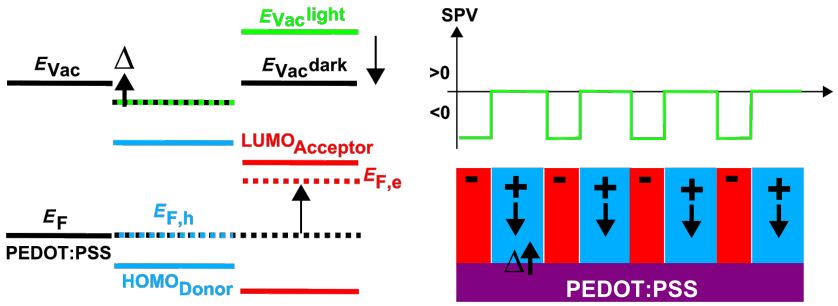

Figure 8: Schematic representation of an idealized D–A network and its band alignment with respect to the substrate. Here, we assume a Fermi level pinning of the donor blocks after charge transfer to the substrate (resulting in the existence of an interface dipole, Δ), and a flat band alignment (in dark) of the acceptor segments. Under illumination, the local vacuum level (E_{Vac}) remains constant over the donor segments while it is shifted upward over the acceptor segments, resulting in a negative shift of the surface potential in average. E_F: Fermi level. $E_{F,h}$ ($E_{F,e}$): quasi-Fermi level of holes (electrons).

Supporting Information File 1). Again, we stress that the size of these dark SPV patches is compatible with that found for the cross-hatched areas in TEM images. Therefore, these last observations reinforce the hypothesis of structural variations within the bulk of the standing lamellae.

Here, it is mandatory to check that the local photo-potential contrasts have a physical origin and do not result from a misalignment of the set of source images used for the SPV calculation. In the case of the image displayed in Figure 7f, the analysis of topographic profiles recorded simultaneously with the KPFM data in dark and under illumination (Figure S6, Supporting Information File 1) shows that the lateral misalignment is at a maximum of 5 nm. This value falls well below the lateral extension of the area displaying a lower photo-voltage (highlighted by blue arrows in Figure 7), which is on the order of 100 nm. Therefore, the lateral resolution is sufficient to establish that the SPV contrasts are related to heterogeneities in the photo-carrier distribution under illumination.

Besides the bright and dark mesoscopic patches, high-resolution SPV images (Figure 9) also display dark stripes corresponding to individual A–D lamellae. The image analysis reveals that these local SPV contrasts are actually correlated with the supramolecular lattice. One lamella, displaying an SPV lower than its neighbour, is highlighted in Figure 9b,c and Figure 9e,f. For the latter data sets (Figure 9e,f), the lateral resolution falls (on average) below 1 nm (see Figure S8 in Supporting Information File 1), unambiguously demonstrating that the lower SPV is intrinsically related to the charging state of a single lamella.

Now we briefly discuss the origin of the observed SPV contrasts. As mentioned above, it is likely that the local SPV minima (in other words, the “dark” SPV patches) reflect the existence of recessed defects within the bulk of the film. Especially, stacking several layers of edge-on oligomers with different orientations should dramatically impact the electron delocalization through the bulk of the film by breaking the continuity of the subnetwork formed by the acceptor units. In turn, the hole transport will be less affected, due to the longer length of the donor segments. Then, disorder-induced electron localization could be the origin of the local negative SPV contrasts.

At this stage, we cannot definitely conclude this – particularly since the structural organization of the recessed layers remains partially unknown. Further experiments, such as mapping the morphology and SPV for films of different thicknesses (down to a few monolayers), will be needed to conclusively address this issue. Local measurements of the recombination rates [24] may also help to establish a more comprehensive picture of the local photo-transport mechanisms in these self-assembled D–A architectures.

A final topic we want to address is the ability to resolve the contributions to the SPV contrasts of donor and acceptor units within a single A–D lamella. Numeric zoom within high-resolution SPV images shows that the minima of the topography match approximatively with the maxima of the surface potential (Figure S10 in Supporting Information File 1), and vice versa. This contrast inversion seems, in a first approximation, consistent with the structural model envisioned for the edge-on lamellae. Indeed, if one takes into account the dynamic motion of the lateral alkyl side groups, the topographic maxima should be close to the location of the negatively charged PDI units. However, a direct visualisation of the donor and acceptor segments remains beyond the limits of resolution of our experiment. At room temperature, the thermal fluctuations of the alkyl segments prevent more precise resolution at the supramolecular scale. We anticipate that cryogenic nc-AFM/KPFM experiments [25] will help to reveal the exact nature of SPV contrasts at the submolecular scale in these self-assembled dyads.

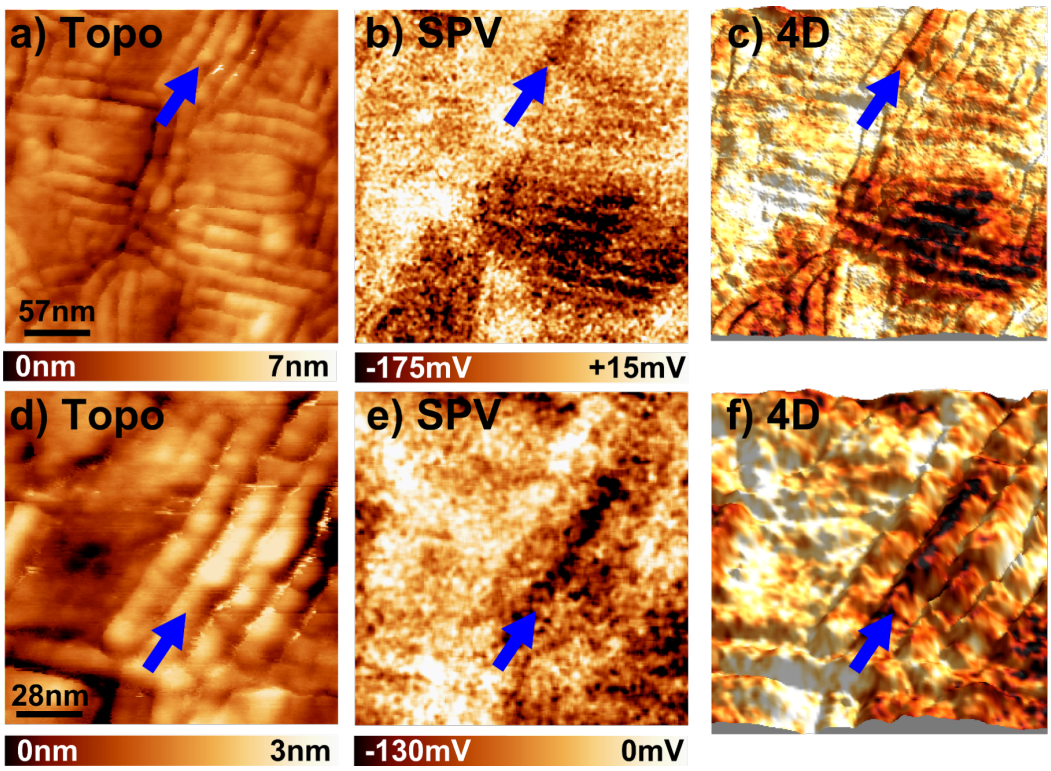

Figure 9: (a) 286 × 286 nm nc-AFM topographic image of the AD3 film. (b) SPV image calculated as the difference between the KPFM images recorded under illumination and in dark (see Figure S7 in Supporting Information File 1). Lateral resolution: ≈2 nm. (c) 4D textured image (topography + SPV) obtained by applying the color code used for the photo-potential values of the SPV image onto a 3D representation of the topography. (d) High-resolution 145 × 145 nm nc-AFM topographic image. (e) Calculated SPV image. Lateral resolution: ≈1 nm (see Figure S8 in Supporting Information File 1). (f) 4D textured image. The blue arrows pinpoint a supramolecular stack displaying a lower (i.e., more negative) SPV than its neighbors.

Conclusion

Self-assembled thin films of donor–acceptor dyads have been investigated by noncontact atomic force microscopy and Kelvin probe force microscopy. Consistent with the results of transmission electron microscopy, the nc-AFM images reveal that the dyads self-assemble primarily as edge-on lamellae, and to a lesser extent, as flat-on domains. The comparison with the TEM results suggests that structural variations within the bulk of the edge-on domains could be at the origin of the electrostatic contrasts probed by KPFM.

Specific features observed in KPFM and SPV images may to some extend be related to structural defects evidenced by TEM in the bulk of the films such as cross-hatched layers. SPV imaging reveals that structural defects in A–D co-oligomers affect the carrier photo-transport, and hence, the global photovoltaic properties of corresponding devices. Lastly, SPV contrasts were resolved at the scale of single edge-on lamellae, which is an important step towards local investigations of photovoltaic self-assembled donor–acceptor heterojunctions at the submolecular scale.

Supporting Information

Comparison of nc-AFM topographic images of the AD1 and AD3 films. nc-AFM/KPFM images (topography, damping, CPD) of the AD3 film recorded in dark conditions. 3D representation of two lamellae with different in-plane π-stacking directions. Surface photo-voltage as a function of the illumination intensity. KPFM potential images recorded in dark and under illumination at 685 nm, 515 nm and 405 nm. Estimation of the SPV lateral resolution (3 series of topographic and KPFM potential images recorded in dark and under illumination). Correction procedure used for the SPV image calculation. High-resolution topographic and SPV cross sections over an edge-on lamellae.

Supporting Information File 1

Additional experimental results.
[http://www.beilstein-journals.org/bjnano/content/supplementary/2190-4286-7-71-S1.pdf]

Acknowledgements

Financial support by the Agence Nationale de la Recherche (France) with the NANOKAN (ANR-11-BS10-0004) and PICASSO (ANR-11-BS08-0009) projects is gratefully acknowledged. We thank Florent Caffy (SPrAM) for his help in the processing of the dyad films on ITO/PEDOT:PSS substrates.

References

1. Chen, J.-D.; Cui, C.; Li, Y.-Q.; Zhou, L.; Ou, Q.-D.; Li, C.; Li, Y.; Tang, J.-X. *Adv. Mater.* **2015,** *27,* 1035–1041. doi:10.1002/adma.201404535
2. Liu, Y.; Zhao, J.; Li, Z.; Mu, C.; Ma, W.; Hu, H.; Jiang, K.; Lin, H.; Ade, H.; Yan, H. *Nat. Commun.* **2014,** *5,* 5293. doi:10.1038/ncomms6293
3. Hoppe, H.; Glatzel, T.; Niggemann, M.; Hinsch, A.; Lux-Steiner, M. C.; Sariciftci, N. S. *Nano Lett.* **2005,** *5,* 269–274. doi:10.1021/nl048176c
4. Chiesa, M.; Bürgi, L.; Kim, J.-S.; Shikler, R.; Friend, R. H.; Sirringhaus, H. *Nano Lett.* **2005,** *5,* 559–563. doi:10.1021/nl047929s
5. Glatzel, T.; Rusu, M.; Sadewasser, S.; Lux-Steiner, M. C. *Nanotechnology* **2008,** *19,* 145705. doi:10.1088/0957-4484/19/14/145705
6. Maturová, K.; Kemerink, M.; Wienk, M. M.; Charrier, D. S. H.; Janssen, R. A. J. *Adv. Funct. Mater.* **2009,** *19,* 1379–1386. doi:10.1002/adfm.200801283
7. Fuchs, F.; Caffy, F.; Demadrille, R.; Mélin, T.; Grévin, B. *ACS Nano* **2016,** *10,* 739–746. doi:10.1021/acsnano.5b05810
8. Ellison, D. J.; Kim, J. Y.; Stevens, D. M.; Frisbie, C. D. *J. Am. Chem. Soc.* **2011,** *133,* 13802–13805. doi:10.1021/ja2034574
9. Henning, A.; Günzburger, G.; Jöhr, R.; Rosenwaks, Y.; Bozic-Weber, B.; Housecroft, C. E.; Constable, E. C.; Meyer, E.; Glatzel, T. *Beilstein J. Nanotechnol.* **2013,** *4,* 418–428. doi:10.3762/bjnano.4.49
10. Westacott, P.; Tumbleston, J. R.; Shoaee, S.; Fearn, S.; Bannock, J. H.; Gilchrist, J. B.; Heutz, S.; deMello, J.; Heeney, M.; Ade, H.; Durrant, J.; McPhail, D. S.; Stingelin, N. *Energy Environ. Sci.* **2013,** *6,* 2756–2764. doi:10.1039/c3ee41821a
11. Scarongella, M.; Paraecattil, A. A.; Buchaca-Domingo, E.; Douglas, J. D.; Beaupré, S.; McCarthy-Ward, T.; Heeney, M.; Moser, J.-E.; Leclerc, M.; Fréchet, J. M. J.; Stingelin, N.; Banerji, N. *J. Mater. Chem. A* **2014,** *2,* 6218–6230. doi:10.1039/C3TA15112C
12. Ku, S.-Y.; Kramer, E. J.; Brady, M. A.; Treat, N. D.; Cochran, J. E.; Robb, M. J.; Chabinyc, M. L.; Hawker, C. J. *J. Am. Chem. Soc.* **2012,** *134,* 16040–16046. doi:10.1021/ja307431k
13. Nishizawa, T.; Tajima, K.; Hashimoto, K. *J. Mater. Chem.* **2007,** *17,* 2440–2445. doi:10.1039/B701438D
14. Nishizawa, T.; Tajima, K.; Hashimoto, K. *Nanotechnology* **2008,** *19,* 424017. doi:10.1088/0957-4484/19/42/424017
15. Li, W.-S.; Yamamoto, Y.; Fukushima, T.; Saeki, A.; Seki, S.; Tagawa, S.; Masunaga, H.; Sasaki, S.; Takata, M.; Aida, T. *J. Am. Chem. Soc.* **2008,** *130,* 8886–8887. doi:10.1021/ja802757w
16. Bu, L.; Guo, X.; Yu, B.; Qu, Y.; Xie, Z.; Yan, D.; Geng, Y.; Wang, F. *J. Am. Chem. Soc.* **2009,** *131,* 13242–13243. doi:10.1021/ja905980w
17. Li, W.-S.; Saeki, A.; Yamamoto, Y.; Fukushima, T.; Seki, S.; Ishii, N.; Kato, K.; Takata, M.; Aida, T. *Chem. – Asian J.* **2010,** *5,* 1566–1572. doi:10.1002/asia.201000111
18. Qu, J.; Gao, B.; Tian, H.; Zhang, X.; Wang, Y.; Xie, Z.; Wang, H.; Geng, Y.; Wang, F. *J. Mater. Chem. A* **2014,** *2,* 3632–3640. doi:10.1039/c3ta14701k
19. Schwarz, P.-O.; Biniek, L.; Zaborova, E.; Heinrich, B.; Brinkmann, M.; Leclerc, N.; Méry, S. *J. Am. Chem. Soc.* **2014,** *136,* 5981–5992. doi:10.1021/ja4129108
20. Fuchs, F.; Linares, M.; de Vet, C.; Leclère, P.; Demadrille, R.; Grévin, B. *Adv. Mater.* **2014,** *26,* 6416–6422. doi:10.1002/adma.201401221
21. Biniek, L.; Schwarz, P.-O.; Zaborova, E.; Heinrich, B.; Leclerc, N.; Méry, S.; Brinkmann, M. *J. Mater. Chem. C* **2015,** *3,* 3342–3349. doi:10.1039/C5TC00221D
22. Horcas, I.; Fernández, R.; Gómez-Rodríguez, J. M.; Colchero, J.; Gómez-Herrero, J.; Baro, A. M. *Rev. Sci. Instrum.* **2007,** *78,* 013705. doi:10.1063/1.2432410
23. Cowan, S. R.; Roy, A.; Heeger, A. J. *Phys. Rev. B* **2010,** *82,* 245207. doi:10.1103/PhysRevB.82.245207
24. Shao, G.; Glaz, M. S.; Ma, F.; Ju, H.; Ginger, D. S. *ACS Nano* **2014,** *8,* 10799–10807. doi:10.1021/nn5045867
25. Schuler, B.; Liu, S.-X.; Geng, Y.; Decurtins, S.; Meyer, G.; Gross, L. *Nano Lett.* **2014,** *14,* 3342–3346. doi:10.1021/nl500805x

License and Terms

BEILSTEIN JOURNAL OF NANOTECHNOLOGY

Understanding interferometry for micro-cantilever displacement detection

Alexander von Schmidsfeld*, Tobias Nörenberg, Matthias Temmen and Michael Reichling

Full Research Paper

Open Access

Address:
Fachbereich Physik, Universität Osnabrück, Barbarastraße 7, 49076 Osnabrück, Germany

Email:
Alexander von Schmidsfeld* - avonschm@uos.de

* Corresponding author

Keywords:
displacement noise spectral density; interferometer; non-contact atomic force microscope (NC-AFM); opto-mechanic effects

Beilstein J. Nanotechnol. **2016,** *7,* 841–851.
doi:10.3762/bjnano.7.76

Received: 19 February 2016
Accepted: 22 May 2016
Published: 10 June 2016

This article is part of the Thematic Series "Advanced atomic force microscopy techniques IV".

Guest Editor: T. Glatzel

Abstract

Interferometric displacement detection in a cantilever-based non-contact atomic force microscope (NC-AFM) operated in ultra-high vacuum is demonstrated for the Michelson and Fabry–Pérot modes of operation. Each mode is addressed by appropriately adjusting the distance between the fiber end delivering and collecting light and a highly reflective micro-cantilever, both together forming the interferometric cavity. For a precise measurement of the cantilever displacement, the relative positioning of fiber and cantilever is of critical importance. We describe a systematic approach for accurate alignment as well as the implications of deficient fiber–cantilever configurations. In the Fabry–Pérot regime, the displacement noise spectral density strongly decreases with decreasing distance between the fiber-end and the cantilever, yielding a noise floor of 24 fm/Hz$^{0.5}$ under optimum conditions.

Introduction

A common method for measuring the displacement of a micro-cantilever or another micro-mechanical device is interferometric displacement detection. The most basic interferometer setup is the Michelson interferometer using two mirrors for the superposition of two light beams [1,2]. A related interferometric setup based on multi-beam interference in an optical cavity is the Fabry-Pérot interferometer typically used in form of an etalon in spectroscopy, lasers, and optical telecommunication [3] for precise wavelength selection within a certain free spectral range [4]. The Fabry–Pérot interferometer is characterized by the finesse $\mathcal{F}$, defined as the ratio between the spectral selectivity and the free spectral range [5]. Both types of interferometers are suitable for precisely detecting small movements of one of the involved mirrors [6]. The high precision and sensitivity of calibrated position measurement makes the interferometer a suitable system for displacement detection in a cantilever based non-contact atomic force microscope (NC-AFM) [7]. In contrast to a classical interferometer, the setup commonly involving a fiber end and a cantilever is characterized by a significant beam divergence and a small mirror area. Such a system is

susceptible to misalignment resulting in increased optical loss in the cavity and a strongly reduced signal-to-noise performance. In a previous publication, we have shown that using the bare, cleaved fiber end allows one to change the characteristics of the interferometer from Fabry–Pérot to Michelson interference by adjusting the distance between the fiber end and the cantilever [8].

The micro-cantilever used for force detection in an interferometry-based NC-AFM is a lightweight oscillating mirror, which is part of an optical cavity and, therefore, its movement can be affected by forces originating from the radiation pressure acting on the cantilever [9]. Under conditions of Fabry–Pérot interference, this yields an optical spring effect, i.e., an effective cantilever stiffness that is increased or lowered depending on the slope of the interference fringe [10,11]. In previous work, we have shown that the variation of the distance between the fiber end and the cantilever allows for a control of the opto-mechanical interaction between the cavity light field and the cantilever [8]. The type and quality of interference can be straightforwardly assessed by measuring the Fabry–Pérot enhancement factor $\tilde{\mathcal{F}}$, which is defined as

$$\tilde{\mathcal{F}} = \frac{P_{\max} - P_{\min}}{P_{\text{ref}}} \cdot e^{\left(\frac{P_{\max} - P_{\min} - 2P_{\text{ref}}}{P_{\text{ref}}}\right)}, \qquad (1)$$

In case of negligible optical loss at very small distances d, $\tilde{\mathcal{F}}$ is related to the cavity finesse $\mathcal{F}$ by

$$\mathcal{F} \approx \frac{R_f}{1-R_f}\frac{\pi}{2}\left(\tilde{\mathcal{F}} - 1\right) \text{ for } d \to 0\,. \qquad (2)$$

Here, we discuss the beams involved in generating the interference pattern in a typical cantilever setup and describe a systematic approach for optimum adjustment based on the externally measurable optical signals. This comprises fine-tuning the fiber–cantilever distance such that the resting position of the cantilever is exactly at the steepest point of the cavity response function, yielding maximum signal response for any given deflection.

To further optimize the signal, we introduce a method for positioning the fiber precisely in the optimal lateral position and examine the importance of this positioning. Finally, we investigate the impact of the interferometric signal on the effective modal spring constant $k_0^{\pm}$ and the modal Q-factor Q_0^{eff} of the cantilever, as well as on the noise floor $d_{ds}^{z\pm}(f)$ of the deflection measurement.

Experimental

Experiments are performed with a NC-AFM body operated in an ultra-high vacuum (UHV) environment with a base pressure of 3×10^{-11} mbar. The main components of the interferometer are shown in Figure 1, while all further details of the NC-AFM setup are described in [12]. The cantilever, I, with its support chip is mounted on a dove-tail cantilever holder, II, clamped into position inside two side braces on a piezo stage, III, facilitating cantilever excitation. The cantilever holder has an angle of $\alpha = 15°$ with respect to the horizontally aligned sample surface to make sure that the tip at the cantilever end approaches the sample surface first. For the studies reported here, the sample is, however, always retracted so that the cantilever displacement is affected only by the cavity light field but not by any tip–sample interaction.

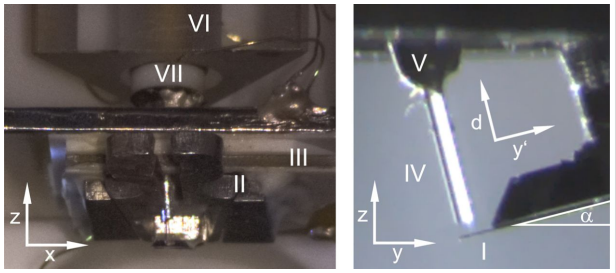

Figure 1: Details of the NC-AFM measuring head in a front and side view showing the interferometric setup with the cantilever, I, mounted on a dove-tail cantilever holder, II, inserted in a holding mechanism on the piezo stage, III. The fiber, IV, is mounted in the ferrule, V, glued in the tube piezo, VII, used for fine-positioning and scanning the fiber. The tube-scanner piezo is embedded in the sapphire prism, VI, which is part of the coarse-approach mechanism. The side view shows the fiber retracted by 200 µm from the cantilever.

The optical fiber, IV, is glued in a ferrule, V, which is bent by 15° with respect to the vertical axis to match the cantilever angle. The fiber end is coarse-approached from the top with a piezoelectric actuator moving the triangular sapphire prism, VI, along the z-axis towards the cantilever in steps of 0.4 µm. The actuator is electrically driven by a PMC100 stepper control system (RHK Technology Inc., Troy(MI) USA). The tube piezo, VII, inside the prism allows for positioning the fiber end in x-, y- and z-directions and, specifically, for scanning laterally over an area of 20 µm × 20 µm. A SPM1000 scan controller (RHK Technology Inc., Troy(MI) USA) is used to drive the scanning tube piezo, while a custom-built, low-noise power supply is used to position the fiber exactly at the optimal position.

Most experiments are performed with three aluminium-coated silicon micro-cantilevers taken from one batch (type NCLR, NanoWorld AG, Neuchâtel, Switzerland) further on referred to

as cantilever 1, 2 and 3. They have a reflectivity of $R_c \approx 90\%$ for light with a wavelength of $\lambda = 782$ nm, a length of 220 µm, a width of 40 µm and a thickness of 7 µm. Cantilever 3, which exhibits the best results, is used for dynamic measurements involving oscillation at its eigenfrequency of $f_0 = 164{,}999$ Hz at a measuring head temperature of $T = 29.3$ °C. Some measurements are performed with cantilever 4 (type NCHR, NanoWorld AG, Neuchâtel, Switzerland) having similar properties as the others, but a length of 125 µm, a width of 30 µm and a thickness of 4 µm.

The optical setup shown in Figure 2 consist of a stabilized laser light source (type 48TA-1-42037, Schäfter + Kirchhoff GmbH, Hamburg, Germany) operated at a wavelength of $\lambda = 782$ nm with the output power being optimized for low-noise operation. The power of the light coupled into the interferometer is optically adjusted by a variable absorber. A single-mode optical fiber with a core diameter of 4.0 µm (type Hi780, Corning Inc., Corning, New York, USA) optimized for transmission of light of the utilized wavelength is used to transmit the light from the source to the components of the interferometer setup. The fiber end placed above the cantilever is cleaved with great care to achieve a high interface reflectivity R_f. The reflectivity is determined by procedures outlined below and we regularly obtain R_f values higher than 3.5%. The best value obtained is $R_f = (3.9 \pm 0.3)\%$, which is –within experimental error– identical to the maximum possible value of 3.84% determined by the diffraction index of the core material of the fiber ($n = 1.48$ at 800 nm according to the data sheet). No coating to increase the reflectivity has been applied to the cleaved end, resulting in a strongly asymmetric optical cavity that allows us to tune the interferometer from Fabry–Pérot to Michelson characteristics [8].

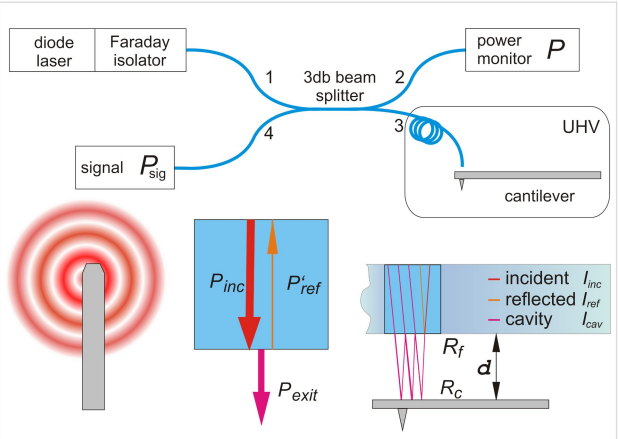

Figure 2: Schematic representation of the interferometer setup, signal path and cavity parameters. Signal power P_{sig} and power monitor P are either measured with a power meter or processed with a balanced photo detector for low-noise detection of dynamic signals.

The laser is decoupled from the interferometric detection system through a Faraday isolator feeding the light into port 1 of the 3 dB coupler that divides the beam in two parts with identical light power P exiting at ports 2 and 3. The 3 dB splitting is confirmed by a measurement with an optical power meter (type TQ8210, Advantest, Tokyo, Japan). Port 2 is used as the power monitor while light from port 3 is directed onto the cantilever via the optical fiber guiding the light into the UHV chamber. To determine the optical loss in the feed line of the fiber occurring after the 3 dB coupler to the microscope, the fiber is completely retracted from the cantilever ($d \approx 40$ mm) so that only a negligible amount of light reflected from the cantilever is collected by the fiber. The light with power P_{inc} incident on the fiber end is split into a fraction of power P_{exit} exiting the fiber and a fraction of light with power P_{ref} that is reflected back inside the fiber (see Figure 2) forming the reference beam for Michelson interference. As P_{inc} cannot be measured directly, we introduce the loss factor $f_{loss} = P_{inc}/P$ describing the optical loss in the fiber on the way from the beam splitter to the fiber end. The power P_{exit} is measured with the power meter after the fiber is cleaved but before it is glued into the ferrule. The back-reflected light with power P_{ref} attenuated in the fiber by the factor f_{loss} and measured as power P_{sig}^{∞} at port 4 of the 3 dB coupler. In this configuration, we find as the relation between the three measured power values:

$$P_{exit} = f_{loss} P - \frac{P_{sig}^{\infty}}{f_{loss}}. \tag{3}$$

By visual inspection, we find that the amount of light scattered at the fiber end is negligible. Because light absorption at the fiber end can also be neglected, it is straightforward to determine $f_{loss} = 0.44 \pm 0.02$ for the experiments reported here. The high loss is presumably occurring in the tightly wound reserve coil inside the vacuum, containing about 3 m of fiber for cleaving new fiber ends and for repairs.

Using this result, we calculate the reflectivity of a fiber end as

$$R_f = \frac{1}{(f_{loss})^2} \frac{P_{sig}^{\infty}}{P}. \tag{4}$$

After the determination of the properties of the fiber, d is decreased to a distance of approx. 30 µm, estimated through observation with a video camera. The distance is further decreased in single steps until the fiber end is in contact with the cantilever. During the approach, P_{sig} is monitored and exhibits

interference oscillations. Fiber–cantilever contact is reached when P_{sig} does not vary over several steps of approach. Note, that an actual contact between the fiber core and the cantilever is very unlikely, because much more likely, the 125 µm thick fiber cladding surrounding the core will be in contact with the cantilever due to a small unavoidable inclination between the cleavage face and the cantilever. Afterwards, the fiber is retracted by 5–10 µm to protect it against hitting the cantilever during lateral positioning. At this distance, interferometric patterns are observed, which are generated by light with the intensity $I_{inc} - I_{ref}$ exiting the fiber and entering the interferometric cavity. Inside the cavity, light is reflected back from the cantilever and the fiber-end yielding multi-beam interference inside the cavity where I_{cav} is the intensity of the light acting on the cantilever. The actual value of I_{cav} depends on the optical losses in the cavity and cannot be determined directly [8].

Part of the light in the cavity is coupled back into the fiber core where it interferes with I_{ref} to form the intensity in the signal arm I_{sig}. The diameter of the fiber core is about five times the wavelength of the light resulting in a light intensity distribution dominated by pinhole diffraction and a diffraction-limited aperture opening angle of 9°. This ensures that the measured values for the optical power represent the respective intensities. The corresponding power value P_{sig} is measured by the power meter that can be read out via an analog monitoring port. For dynamic measurements, the intensity is converted into a proportional voltage signal V_{sig} via either a custom-built detector-diode/pre-amplifier combination for low-frequency signals or a balanced photo detector (Nirvana detector Model 2007, Newport Corporation, Irvine, USA) processing P_{sig} at the signal input and P at the reference input.

After the approach, the fiber is aligned into the optimal lateral position that is the position of maximum interference signal. For a precise alignment, the lateral cantilever position as well as the alignment angle are crucial. Three types of misalignment resulting in excessive optical loss are shown in Figure 3. A deviation to the cantilever long (Figure 3a) and short (Figure 3b) side can be compensated by adjustment in the *xy*-plane with the fiber piezo. Tilt as shown in Figure 3c can not be compensated by the fiber piezo, but is of minor concern for tilt angles below 4° because of the divergent nature of the beam.

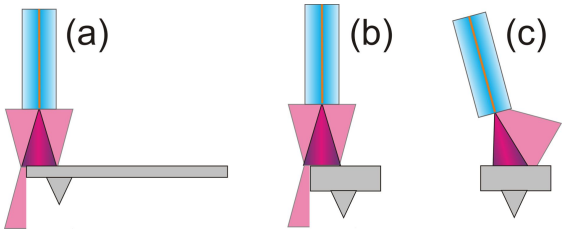

Figure 3: Schematic representation of three common types of misalignment of fiber and cantilever; (a) lateral in length, (b) to the side and (c) tilt of the fiber with respect to the cantilever.

Lateral positioning of the fiber with the tube piezo for alignment and scanning is inevitably accompanied by a tilt of the fiber. The 54 mm long piezo/fiber assembly can be displaced by a maximum of ±10 µm resulting in a maximum tilt angle of 38" and a maximum variation of the distance between fiber end and cantilever of d = 4.6 Å. Therefore, we can exclude that the tilt of the fiber changes the interference pattern significantly.

Figure 4 is a sketch of the first few interferometric fringes obtained upon retracting the fiber end from the contact position. Practically, only a few fringes can be scanned, limited by the maximum extension of the scanner tube. Starting from the contact point with unknown minimum distance, the signal power varies approximately sinusoidally as a function of d between local maxima P_{sig}^{max} and minima P_{sig}^{min} with a distance of λ/2. The optical loss increases with d and results in a decrease of the mean value $P_{sig}^{mean} = \left(P_{sig}^{max} + P_{sig}^{min}\right)/2$ but also of the visibility $M = \left(P_{sig}^{max} - P_{sig}^{min}\right)/P_{sig}^{mean}$, thus being a measure for the Fabry–Pérot enhancement factor $\tilde{\mathcal{F}}$ [8].

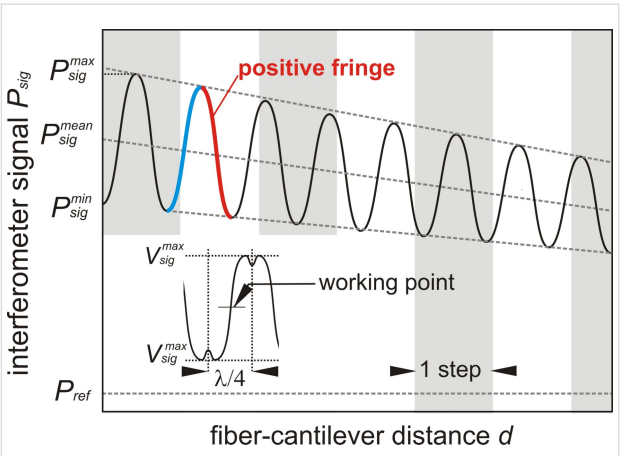

Figure 4: Schematic representation of the interferometer signal P_{sig} as a function of the fiber–cantilever distance d. Coarse-approach piezo steps are marked as gray boxes. The inset schematically shows the oscilloscope trace of V_{sig} for a cantilever excited to an amplitude of larger than λ/8.

We define positive and negative fringes so that a positive fringe covers a region of rising light intensity when the fiber is approached towards the cantilever. This is compatible with the more general definition that, for a positive fringe, the force gradient experienced by the cantilever in the cavity light field due to the opto-mechanical coupling points in the same direction as the radiation pressure.

In dynamic operation, the cantilever is excited to oscillation with an amplitude of typically 5–20 nm. To yield the maximum deflection signal, d is adjusted so that the zero-crossing of the periodic cantilever displacement coincides with the point of maximum slope for the selected fringe. To find this optimum working point (see inset in Figure 4), the z-extension of the fiber piezo is modulated with a frequency of 30 Hz and an amplitude of about 120 nm ≥ λ/8, while V_{sig} is observed with an oscilloscope similar to procedures suggested in [13]. The modulation frequency is chosen to avoid mechanical resonances and piezo creep. Dips appear at positions of maximum and minimum V_{sig} as schematically illustrated in the inset of Figure 4, as the oscillation extends into neighbouring fringes. If the interference pattern is found not to be symmetric, the z-piezo offset voltage is adjusted such that the two dips appear symmetrically. In that way, minimum and maximum voltage levels precisely define the voltage amplitude $V_{sig}^{\lambda/8}$ corresponding to a cantilever oscillation amplitude of λ/8. The measured maximum voltage $V_{sig}^{\lambda/8}$ in combination with the wavelength is used for amplitude calibration by applying an arcsine function to account for the approximately sinusoidal modulation of the interferometric fringes as a function of d. For a cavity with low $\mathcal{F}$, this is a good approximation. Any amplitude A below $\lambda/8$ can be determined via

$$A = \frac{\lambda}{8} \cdot \frac{2}{\pi} \arcsin\left(\frac{V_{sig}}{V_{sig}^{\lambda/8}}\right). \tag{5}$$

or the commonly used approximation for $A \ll \lambda/8$.

$$A \approx \frac{\lambda}{12} \frac{V_{sig}}{V_{sig}^{\lambda/8}}. \tag{6}$$

To fine-tune the working point under measurement conditions where the fiber position is fixed, the cantilever oscillation amplitude is adjusted to oscillation with an amplitude of about 10 nm where V_{sig} is a quasi-linear function of d and the z-piezo offset voltage is adjusted such that the maximum peak-to-peak voltage is obtained. Such fine-tuning can be carefully repeated during a series of measurements to compensate for thermal drift. Note, that the measured amplitude corresponds to the position of the light spot on the cantilever, that may differ from the tip position that is relevant for NC-AFM measurements.

Results

Cantilever alignment

Signal quality crucially depends on the relative alignment of optical fiber and cantilever, which is in first place determined by the precision in gluing the cantilever support chip on the cantilever holder. Misalignment of the types illustrated in Figure 3 can only partially be corrected by positioning the fiber with the fiber piezo, however, the quality of the cantilever alignment can easily be checked by measuring the signal power P_{sig} as a function of d revealing the optical loss of the cavity [8]. For such a measurement, the fiber is first positioned in contact with the cantilever and then d is increased over a large range via the coarse-positioning stepper in increments of 0.4 µm. Note, that these steps are much larger than one interferometric fringe leading to an aliasing of the interference signal.

In Figure 5, respective measurements are shown for cantilevers 1, 2 and 3 exhibiting different alignment quality. Generally, the increasing optical loss results in an overall decline of the signal when increasing d and the signal power P_{sig} asymptotically approaches P_{ref}. For all three cantilevers, two characteristic regimes of interference are visible. At small distances with low cavity loss, Fabry–Pérot interference dominates the signal while for larger distances, Michelson interference dominates the signal. In the distance region between these regimes where no modulation is visible, the interferometric signal is effectively quenched as the light beams originating from Fabry–Pérot and Michelson interference have a similar amplitude but 180° phase shift. As a result of the multi-beam interference, the signal visibility M in the Fabry–Pérot regime is up to 14 times larger than that in the Michelson regime.

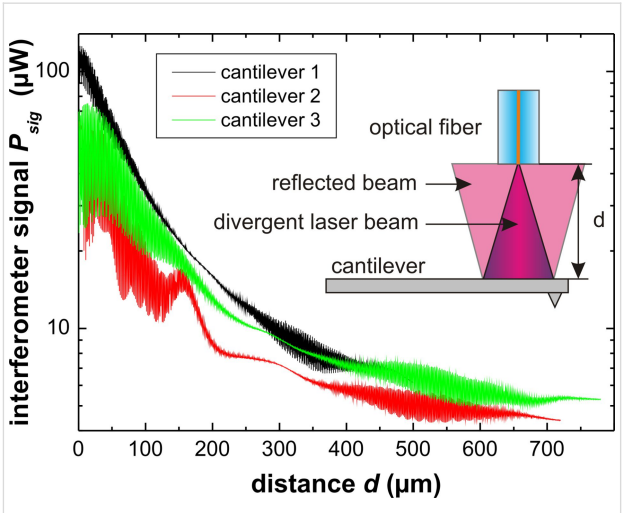

Figure 5: Signal power over distance measurements for three differently positioned cantilevers. Cantilever 1 has high optical loss, cantilever 2 is positioned to the side of the fiber, cantilever 3 is positioned close to the optimum.

Cantilever 1 (black curve) exhibits a high overall signal strength, however, the modulation depth is low. This means that the light is reflected back from the cantilever but is lost for the

next cavity round trip. This may be caused by the fiber being positioned at the tip of the cantilever as indicated in Figure 3a in combination with a large tilt shown in Figure 3c. Because such a configuration results in a high cavity loss for multiple-beam interference, although a large amount of light reflected back from the cantilever surface enters the fiber. This is in line with the early onset of Michelson interference observed for this cantilever since the high loss results in a strong reduction of multi-beam interference. Cantilever 2 (red curve) is hit close to the side as schematically shown in Figure 3b, effectively decreasing the mirror area for close distances and thus the amount of light reflected back. This results in erratic and low performance of the interference under Fabry–Pérot conditions. Because of the beam divergence, the cantilever is performing better for distances above 300 µm when the entire cantilever is hit by the light resulting in a good signal strength and modulation depth for Michelson interference. Cantilever 3 (green curve) demonstrates close to optimum alignment as the modulation depth is large in both modes of operation. The non-monotonous slope of $P_{\mathrm{sig}}^{\mathrm{mean}}$ around $d = 300$ µm, however, points to a slight misalignment also for this cantilever. All three examined cantilevers show similar performance in Michelson interference and are equally suited for usage in this regime. However, only cantilever 3 exhibits a performance suitable for further experiments in the Fabry–Pérot regime.

Fiber positioning

For a perfectly aligned fiber and an infinitely extended mirror surface, there should be no signal variation when scanning the fiber parallel to the mirror surface, as the fiber is the source and the collector of the light. The pattern is expected to exhibit variations with a period of $\lambda/2$ upon a variation in d. However, the limited area of the cantilever mirror as well as an unavoidable misalignment result in variations for movement parallel to the cantilever surface and, therefore, one can search for the optimal lateral position with minimal optical loss and minimal phase difference between the cavity light beam and the reference beam reflected back inside the fiber.

To study alignment effects, the interferometer signal is recorded while laterally scanning the fiber over an area of 20 µm × 20 µm for a fixed z. Such patterns are recorded for 512 equidistant slices with z ranging from 0 to 5 µm generating a 3D intensity map. From the 3D data, it is straightforward to extract a profile of the interferometric pattern in any plane (see Supporting Information File 1). Results from respective experiments performed with cantilever 4 are shown in Figure 6. The interference pattern for a scan in the xy-plane is recorded for (a) Fabry–Pérot interference at $d = 25$ µm, (b) interferometric quenching at $d = 300$ µm and (c) Michelson interference at $d = 500$ µm.

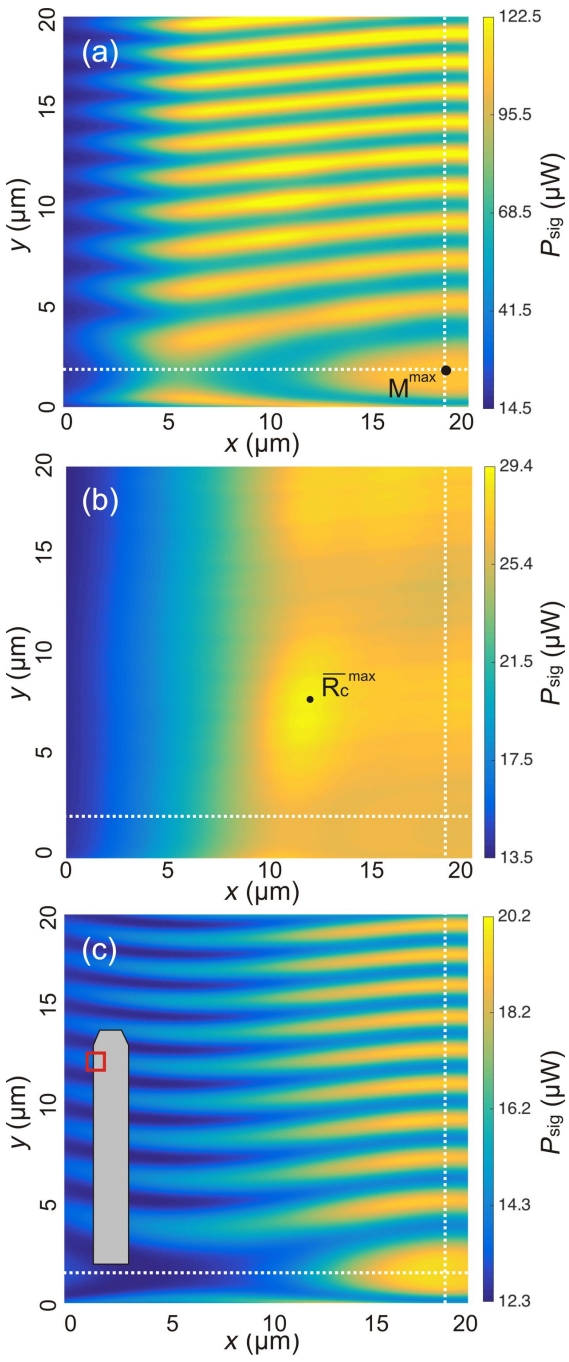

Figure 6: Lateral interference patterns for cantilever 4 scanned by the fiber-positioning piezo for (a) Fabry–Pérot interference $d = 25$ µm, (b) interferometric quenching at $d = 300$ µm and (c) Michelson interference at $d = 500$ µm. The inset shows a sketch of the scanned area in relation to the cantilever. For a full account of the interference pattern, see Supporting Information File 1.

Apparently, there is a signal variation in all images representing different effects. The left side appears darker in all intensity maps, which is the result of a loss of light due to cantilever misalignment as shown in Figure 3b. The most prominent features are, however, the lateral stripes appearing in Figure 6a

and Figure 6c. These are a result of d changing by scanning along the y-axis, which is inclined with respect to the the y'-axis as illustrated in Figure 1. Scanning a distance Δy along the y-axis results in a distance change of

$$\Delta d = \sin(\alpha)\Delta y. \tag{7}$$

For the fiber positioned close to the cantilever, the interference is dominated by Fabry–Pérot interference represented by Figure 6a. The intensity map is basically a stripe pattern where stripes are aligned parallel to the x-axis, as movement parallel to this axis does not change d. The small deviation from the alignment is due to a slight misalignment of the cantilever or the fiber. Overall, the stripe pattern is rather even. However, we identify one distinct point of maximum fringe visibility $M^{\max}$ at x = 19 µm and y = 2 µm. For Michelson-dominated interference represented by Figure 6c, the resulting pattern is similar to that for Fabry–Pérot interference with $M^{\max}$ found at the same lateral position. In contrast to the Fabry–Pérot case, here the pattern continues into the wider area of low intensity. At this distance more of the divergent beam hits the cantilever producing interference than in the Fabry–Pérot case where the fiber end is much closer to the cantilever. Furthermore, the light collected by the fiber core is integrated over a larger cantilever area compared to the Fabry–Pérot case, resulting in an overall smoother interference pattern.

The stripe pattern cannot be seen in Figure 6b due to the effective quenching of the interference patterns in the transition regime. Here, the image represents the intensity of the light reflected from the cantilever and the intensity drop at the left side is most pronounced. Note that the overall intensity maximum representing the cantilever reflectivity maximum $\overline{R_c}^{\max}$ of the cantilever located at x = 12 µm and y = 7 µm is different from the position of $M^{\max}$. In a similar fashion, we generate profiles in the yz-plane shown with constant x = 19 µm in Figure 7a–c and profiles in the xz-plane with constant y = 2 µm shown in Figure 7d–f. The cuts have been positioned so that both intersect with $M^{\max}$.

In the yz-slices (Figure 7a–c) the diagonal lines represent lines of constant d and are inclined by an angle α (see Figure 1) with respect to the y-axis. This is utilized to calibrate the sensitivity of the tube piezo in y- and z-direction. We calibrate by measuring the distance between a local maximum and the $(n + 1)$-th maximum along the y- and z-directions and use λ as a length standard to obtain the piezo calibration factors C_y and C_z:

$$C_y = \frac{1}{2\sin(\alpha)}\frac{n\lambda}{\Delta V_y(n\lambda)}, \tag{8}$$

$$C_z = \frac{1}{2\cos(\alpha)}\frac{n\lambda}{\Delta V_z(n\lambda)}. \tag{9}$$

The quantities ΔV_y and ΔV_z denote the difference of voltages applied to the tube piezo corresponding to the positions of the maxima. Analyzing Figure 7a and Figure 7c, we find C_y = 45 ± 4 nm/V and C_z = 10.5 ± 1 nm/V. The calibration in x-direction can be assumed to be identical to the one in y-direction but can not be measured by this method. At the y-position of $M^{\max}$ at y = 2 µm, the direction of the diagonal lines changes. We attribute this to a small deviation of the orthogonal positioning between fiber and cantilever resulting in a position of minimal displacement at $\Delta y' = 0$ and a surrounding pattern with $(\Delta y)^2 = (\Delta y')^2 + (\Delta d)^2$.

For the slices in the xz-plane (Figure 7d–f), we observe almost horizontal lines with the expected sinusoidal signal modulation. The slight tilt of the lines with respect to the horizontal axis is a result of a small cantilever rotation in the xy-plane resulting in a movement nominally in x-direction having a small component in y'-direction. Otherwise, these images can be interpreted as the ones from the other series. The fiber should be positioned for minimum optical loss to maximize the absolute signal strength as well as modulation depth. For cantilever 4, we find this position to be in the Fabry–Pérot mode of operation at x = 19 µm, y = 2 µm and z = 1.7 µm. The lateral position of this point of lowest optical loss is generally found to be the same for all distances, depending only on the cantilever misalignment. To illustrate the impact of lateral positioning on the signal quality, we measure P_{sig} over d for cantilever 1 analogously to the measurements shown in Figure 5 for the optimum position and a position shifted by $\Delta y' = \lambda$, respective results are shown in Figure 8 where the positions are marked in the inset. Cantilever 1 is chosen for this purpose since it exhibits the highest optical loss and thus is most sensitive to lateral positioning.

Starting at identical intensities in the Fabry–Pérot region the curves significantly differ from each other for larger distances. However, both curves exhibit identical values for $P_{\text{sig}}^{\max}$ and $P_{\text{sig}}^{\min}$ in the maximum of the Michelson mode at d = 295 µm and d = 340 µm, respectively. This can be explained straightforwardly by an increased optical loss. In the maximum of the Michelson interference, I_{cav} collected by the fiber is of the order of I_{ref}. The increased loss due to the lateral miscalibration is responsible for a faster decrease of I_{cav}, which directly translates in a compression of the entire interference pattern to smaller d. The amount of this compression varies with the cavity loss of the order of 2–12%.

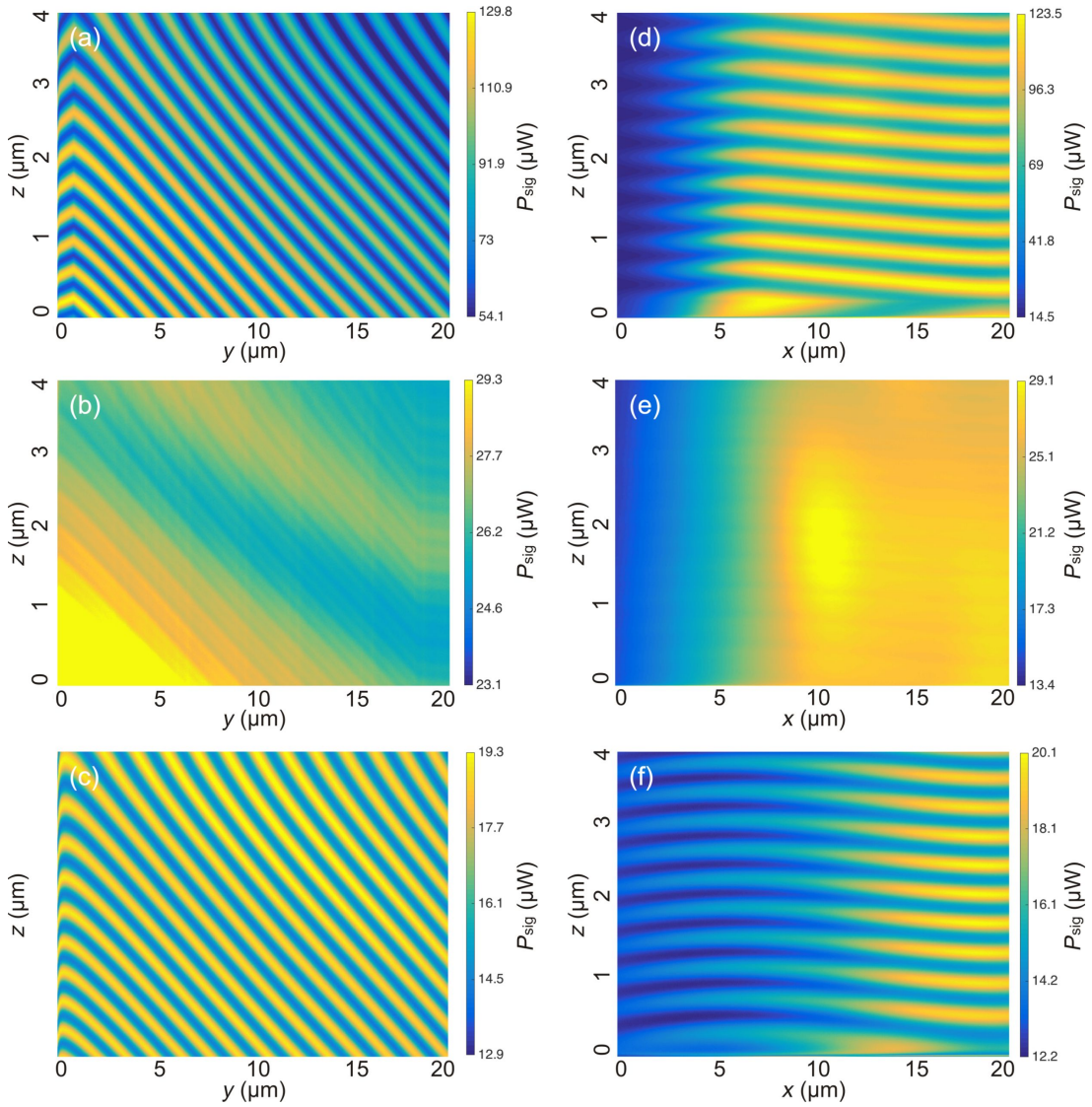

Figure 7: Interference patterns for cantilever 4 generated from the 3D intensity map data for (a,d) Fabry–Pérot interference d = 25µm, (b,e) interferometric quenching at d = 300 µm and (c,f) Michelson interference at d = 500 µm. The yz-profiles (a,b,c) where generated for a fixed position x = 19 µm, the xz-profiles (d,e,f) for a fixed position y = 1 µm. For a full account of the interference pattern, see Supporting Information File 1.

Cantilever and system noise characterization

For cantilever 3, we investigate the influence of fiber positioning on the effective parameters of the cantilever and the noise performance of the system. Measurements are performed with the balanced detector to yield the best possible noise performance. To characterize the cantilevers and the noise performance of the detection system, we use well-established methods based on the spectral analysis of displacement fluctuations of a thermally excited cantilever [14,15]. For that purpose, the signal spectral density $d^{V_{\mathrm{sig}}}(f)$ is measured around the eigenfrequency f_0 for the thermally excited cantilever using a HF2 spectral analyzer (Zurich Instruments, Zürich, Switzerland). Results for the effective cantilever parameters are compiled in Table 1. The fringe-dependent effective cantilever stiffness $k^{\pm}$ is determined by a method relating the intrinsic stiffness to the optical spring constant as described in detail in [8].

Table 1: Effective modal Q-factor $Q_0^{th\pm}$, effective modal cantilever stiffness $k_0^{\pm}$ and noise floor $d_{ds}^{z\pm}$ for the positive and negative fringe for 400 µW under conditions of optimal Fabry–Pérot (FP) and Michelson (M) configuration.

d [µm]	$Q_0^{th\pm}$	$k_0^{\pm}[N/m]$	$d_{ds}^{z\pm}\left[\mathrm{fm}/\sqrt{\mathrm{Hz}}\right]$
18 (FP +)	18031	55.4	33
18 (FP −)	18925	53.3	44
510 (M +)	17911	54.5	988
510 (M −)	19081	54.4	1065

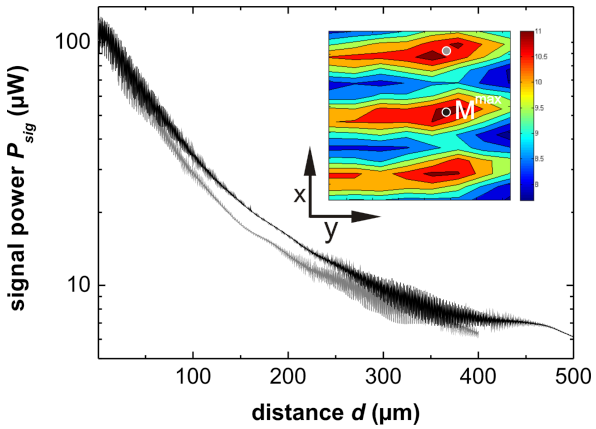

Figure 8: Interferometer signal power P_{sig} of the main maximum (black) and a side maximum (gray) measured for cantilever 1 as a function of *d*. The inset shows the pattern in the *xy*-plane around the main maximum for the fiber–cantilever distance *d* = 330 µm, with the positions of the distance-dependent measurements marked with black and gray circles, respectively.

In a series of measurements, we determine the noise floor by measuring the displacement noise spectral density $d_{ds}^{z\pm}(f)$ around the eigenfrequency of the fundamental mode f_0 for a laser power of P = 400 µW and different values of the fiber–cantilever distance in the range of d = 6–660 µm with a step size of 6 µm. The amplitude is calibrated at every position to translate the observed voltage noise spectral density into the displacement noise spectral density $d_{ds}^{z\pm}(f)$. The corresponding results are shown in Figure 9. For d = 18 µm, we additionally determine the noise floor as a function of P with the results being shown in the inset.

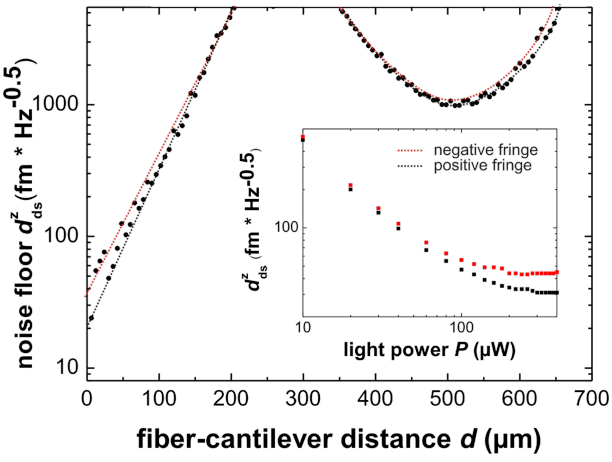

Figure 9: Displacement spectral density d_{ds}^{z} of the noise floor of the interferometer signal as a function of the fiber–cantilever distance *d* for *P* = 400 µW measured for cantilever 3. The inset shows the noise floor for positive and negative fringes at *d* = 18 µm as a function of the light power *P*.

For the Fabry–Pérot regime ($d \leq 200$ µm), we find an exponential increase of the noise level with distance from a minimum equivalent displacement noise spectral density of 24 fm/$\sqrt{\text{Hz}}$ for d = 6 µm to over 4000 fm/$\sqrt{\text{Hz}}$ at 200 µm. Hence, the interferometer exhibits excellent noise figures when operated in the Fabry–Pérot regime with high $\tilde{\mathcal{F}}$.

The dramatic increase of the noise level can be explained by the interference signal V_{sig} dramatically decreasing with d according to the results shown in Figure 5 and Figure 8. For $d \leq 100$ µm, where $\tilde{\mathcal{F}} \geq 3$, we observe a splitting of the curve into two branches corresponding to positive and negative fringes. The splitting is confirmed by measuring the noise floor for d = 18 µm as a function of the light power P as shown in the inset of Figure 9. The observation of the splitting for $P \geq 50$ µW clearly points to opto-mechanical coupling influencing the stochastic cantilever motion in this regime. The fact that this value is different for neighboring positive and negative fringes with identical values of $P_{\text{sig}}^{\text{max}}$ and $P_{\text{sig}}^{\text{min}}$ strongly suggests that this limit is not caused by the noise of the laser, the photo diode or following electronics, but is at least partially a result of the opto-mechanical interaction in the cantilever system. Although, the details of this interaction remain to be explored, we find that opto-mechanical coupling is apparently the limiting factor for the noise performance of our system.

In the distance regime between Fabry–Pérot and Michelson operation (200 to 350 µm) the modulation of the interferometer signal is too small to detect a meaningful cantilever oscillation. Above d = 350 µm, Michelson interference is dominant and the noise level drops to a value of about 1000 fm/$\sqrt{\text{Hz}}$ for the optimum Michelson configuration at d = 510 µm. Contrary to the Fabry-Pérot regime, we find that the interferometer is not well suited for low-noise measurements in the Michelson mode in the present configuration of an asymmetric cavity.

To investigate the impact of opto-mechanical coupling on other oscillatory properties of the cantilever, two neighboring fringes with identical values for $P_{\text{sig}}^{\text{max}}$ and $P_{\text{sig}}^{\text{min}}$ are investigated for the optimal Fabry–Pérot as well the optimal Michelson configurations when determining the effective modal Q-factors $Q_0^{th\pm}$ and effective cantilever stiffnesses $k_0^{\pm}$ (Table 1) by procedures described in [8,14,15]. The opto-mechanical effects are observable in the cantilever stiffness $k_0^{\pm}$ exhibiting the characteristic split between the fringes due to the optical spring effect of up to 4% as expected from our previous studies [8]. For small amplitudes and a negative fringe, the Q-factor is up to 6% larger than for the positive fringe. Although, this variation is significant within the statistical error, it is much less than the typical tolerance of commercial cantilevers and the impact of the mounting system [16]. Overall, we find that the oscillatory cantilever

properties are not heavily affected by the interferometric detection while operating the interferometer in the Fabry–Pérot mode with high $\tilde{\mathcal{F}}$.

Discussion

Interferometric detection is a straightforward and highly sensitive method for measuring displacement in a cantilever-based NC-AFM. This has been realized already in the early days of frequency-modulation force microscopy [2,7,13,17,18]. By instrumental development and optimization, the detection sensitivity has constantly been improved over two decades of development and a force sensitivity in the attonewton range has been claimed for measurements with an ultra-soft cantilever in conjunction with interferometric detection [19]. Although, other variants have been introduced [20-22], the fiber-optic interferometer [23-26] is the most commonly used optical setup for measuring cantilever displacement. This type of interferometer is based on guiding the light entirely through optical fibers and utilizes a 3 dB beam splitter for routing light beams while one cleaved fiber end and the cantilever act as mirrors producing interfering light beams. A ramification of this concept is that light is always delivered and collected through the same aperture defined by the core of the fiber, which typically has a diameter of a few micrometers. Therefore, the vast majority of the sampled light stems from the center of the interference pattern and the challenge in signal detection is just to monitor light intensity variations with the lowest possible noise. The details of interference signal generation can, however, be predetermined by appropriately manipulating the optical reflectivities of fiber end and cantilever with reflective coatings. According to the preference of the experimentalist, signal generation can be based predominantly on two-beam interference of Michelson-type or multi-beam interference of Fabry–Pérot-type, the latter with either low or high finesse. While a Michelson-type interferometer is simple in adjustment and robust in operation [27,28], the high-finesse cavity of a Fabry–Pérot interferometer yields high optical signal amplification but requires a sophisticated cavity design or active stabilization [29-31].

Here, we described an interferometer with a strongly asymmetric low-finesse cavity combining the high reflectivity of a metal-coated cantilever with the low reflectivity of the bare, cleaved fiber end, which is a simple design previously adapted by several authors [17,18,32,33]. In previous work, we have shown that this allows for a smooth transition from predominant Fabry–Pérot operation to predominant Michelson operation by adjusting the gap between the fiber end and the cantilever, effectively controlling the cavity optical loss [8]. For the case of multi-beam interference, the interaction between the cavity-amplified optical field and the cantilever results in opto-mechanical coupling and a shift of several parameters of the cantilever oscillation to fringe-dependent effective values. This allows, for instance, for a simple determination of the effective cantilever stiffness for operation in positive and negative fringes as well as the intrinsic cantilever stiffness. We find that the Fabry–Pérot mode of operation with the smallest fiber–cantilever gap allows for displacement detection with a very low detection-system noise floor of 24 $\mathrm{fm}/\sqrt{\mathrm{Hz}}$ promising a high sensitivity in force detection even for the relatively stiff cantilevers used in the present study. Apparently, the system noise is affected by opto-mechanical coupling and we find that measuring on a positive fringe is the best choice with regard to noise. However, in future work the opto-mechanical coupling might also be used to advantageously manipulate the cantilever dynamics for improved force detection and measurement stability.

Supporting Information

Supporting Information File 1

Profile of interferometric patterns in all planes.
[http://www.beilstein-journals.org/bjnano/content/supplementary/2190-4286-7-76-S1.mp4]

Acknowledgements

The authors are grateful to Alexander Schwarz, Tjeerd Bollmann, Julian Stirling, Yigit Uysalli and Ahmet Oral for most fruitful discussions.

References

1. Saulson, P. R. *Phys. Rev. D* **1990,** *42,* 2437. doi:10.1103/PhysRevD.42.2437
2. Putman, C. A. J.; de Grooth, B. G.; van Hulst, N. F.; Greve, J. *Ultramicroscopy* **1992,** *42–44,* 1509. doi:10.1016/0304-3991(92)90474-X
3. Boucher, R.; Villeneuve, B.; Breton, M.; Tetu, M. *IEEE Photonics Technol. Lett.* **1992,** *4,* 801. doi:10.1109/68.145277
4. Stone, J.; Stulz, L. W. *Electron. Lett.* **1987,** *15,* 781. doi:10.1049/el:19870554
5. Hernandez, G. *Fabry–Perot Interferometers;* Cambridge University Press: Cambridge, MA, U.S.A., 1986.
6. Shyu, L.-H.; Chang, C.-P.; Wang, Y.-C. *Rev. Sci. Instrum.* **2011,** *82,* 063103. doi:10.1063/1.3596451
7. Kracke, B.; Damaschke, B. *Rev. Sci. Instrum.* **1996,** *67,* 2957. doi:10.1063/1.1147079
8. von Schmidsfeld, A.; Reichling, M. *Appl. Phys. Lett.* **2015,** *107,* 123111. doi:10.1063/1.4931702
9. Kippenberg, T. J.; Vahala, K. J. *Science* **2008,** *321,* 1172. doi:10.1126/science.1156032
10. Braginsky, V. B.; Strigin, S. E.; Vyatchanin, S. P. *Phys. Lett. A* **2001,** *287,* 331. doi:10.1016/S0375-9601(01)00510-2
11. Kippenberg, T. J.; Rokhsari, H.; Carmon, T.; Scherer, A.; Vahala, K. J. *Phys. Rev. Lett.* **2005,** *95,* 033901. doi:10.1103/PhysRevLett.95.033901

12. Troeger, L. *Aufbau eines Tieftemperatur-Rasterkraftmikroskopes;* Sierke Verlag: Göttingen, Germany, 2009.
13. Moser, A.; Hug, H. J.; Jung, T.; Schwarz, U. D.; Güntherodt, H.-J. *Meas. Sci. Technol.* **1993,** *4,* 769. doi:10.1088/0957-0233/4/7/009
14. Lübbe, J.; Temmen, M.; Rahe, P.; Kühnle, A.; Reichling, M. *Beilstein J. Nanotechnol.* **2013,** *4,* 227. doi:10.3762/bjnano.4.23
15. Lübbe, J.; Temmen, M.; Rode, S.; Rahe, P.; Kühnle, A.; Reichling, M. *Beilstein J. Nanotechnol.* **2013,** *4,* 32. doi:10.3762/bjnano.4.4
16. Lübbe, J.; Tröger, L.; Torbrügge, S.; Bechstein, R.; Richter, C.; Kühnle, A.; Reichling, M. *Meas. Sci. Technol.* **2010,** *21,* 125501. doi:10.1088/0957-0233/21/12/125501
17. Rugar, D.; Mamin, H. J.; Guethner, P. *Appl. Phys. Lett.* **1989,** *55,* 2588. doi:10.1063/1.101987
18. Albrecht, T. R.; Grütter, P.; Horne, D.; Rugar, D. *J. Appl. Phys.* **1991,** *69,* 668. doi:10.1063/1.347347
19. Stowe, T. D.; Yasumura, K.; Kenny, T. W.; Botkin, D.; Wago, K.; Rugar, D. *Appl. Phys. Lett.* **1997,** *71,* 288. doi:10.1063/1.119522
20. Hug, H. J.; Stiefel, B.; van Schendel, P. J. A.; Moser, A.; Martin, S.; Güntherodt, H.-J. *Rev. Sci. Instrum.* **1999,** *70,* 3625. doi:10.1063/1.1149970
21. Hoogenboom, B. W.; Frederix, P. L. T. M.; Yang, J. L.; Martin, S.; Pellmont, Y.; Steinacher, M.; Zäch, S.; Langenbach, E.; Heimbeck, H.-J.; Engel, A.; Hug, H. J. *Appl. Phys. Lett.* **2005,** *86,* 074101. doi:10.1063/1.1866229
22. Oral, A.; Grimble, R. A.; Özer, H. Ö.; Pethica, J. B. *Rev. Sci. Instrum.* **2003,** *74,* 3656. doi:10.1063/1.1593786
23. Rugar, D.; Mamin, H. J.; Erlandsson, R.; Stern, J. E.; Terris, B. D. *Rev. Sci. Instrum.* **1988,** *59,* 2337. doi:10.1063/1.1139958
24. Morita, K.; Sugimoto, Y.; Sasagawa, Y.; Abe, M.; Morita, S. *Nanotechnology* **2010,** *21,* 305704. doi:10.1088/0957-4484/21/30/305704
25. Albrecht, T. R.; Grütter, P.; Rugar, D.; Smith, D. P. E. *Ultramicroscopy* **1992,** *42–44,* 1638. doi:10.1016/0304-3991(92)90498-9
26. Metzger, C. H.; Karrai, K. *Nature* **2004,** *432,* 1002. doi:10.1038/nature03118
27. Allers, W.; Schwarz, A.; Schwarz, U. D.; Wiesendanger, R. *Rev. Sci. Instrum.* **1998,** *69,* 221. doi:10.1063/1.1148499
28. Schwarz, A.; Schwarz, U. D.; Langkat, S.; Hölscher, H.; Allers, W.; Wiesendanger, R. *Appl. Surf. Sci.* **2002,** *188,* 245. doi:10.1016/S0169-4332(02)00146-0
29. Hogenboom, B. W.; Frederix, P. L. T. M.; Fotaidis, D.; Hug, H. J.; Engel, A. *Nanotechnology* **2008,** *19,* 384019. doi:10.1088/0957-4484/19/38/384019
30. Patil, S.; Matei, G.; Dong, H.; Hoffmann, P. M.; Karaköse, M.; Oral, A. *Rev. Sci. Instrum.* **2005,** *76,* 103705. doi:10.1063/1.2083147
31. Karci, O.; Dede, M.; Oral, A. *Rev. Sci. Instrum.* **2014,** *85,* 103705. doi:10.1063/1.4897147
32. Hölscher, H.; Milde, P.; Zerweck, U.; Eng, L. M.; Hoffmann, R. *Appl. Phys. Lett.* **2009,** *94,* 223514. doi:10.1063/1.3149700
33. Vogel, M.; Mooser, C.; Karrai, K.; Warburton, R. J. *Appl. Phys. Lett.* **2003,** *83,* 1337. doi:10.1063/1.1600513

License and Terms

BEILSTEIN JOURNAL OF NANOTECHNOLOGY

Generalized Hertz model for bimodal nanomechanical mapping

Aleksander Labuda*, Marta Kocuń, Waiman Meinhold, Deron Walters and Roger Proksch

Full Research Paper

Open Access

Address:
Asylum Research, an Oxford Instruments company, Santa Barbara, CA, 93117, USA

Email:
Aleksander Labuda* - aleks.labuda@oxinst.com

* Corresponding author

Keywords:
bimodal atomic force microscopy; bimodal spectroscopy; contact mechanics; multifrequency; nanomechanical mapping; nanomechanics

Beilstein J. Nanotechnol. **2016,** *7,* 970–982.
doi:10.3762/bjnano.7.89

Received: 28 March 2016
Accepted: 15 June 2016
Published: 05 July 2016

This article is part of the Thematic Series "Advanced atomic force microscopy techniques IV".

Guest Editor: T. Glatzel

Abstract

Bimodal atomic force microscopy uses a cantilever that is simultaneously driven at two of its eigenmodes (resonant modes). Parameters associated with both resonances can be measured and used to extract quantitative nanomechanical information about the sample surface. Driving the first eigenmode at a large amplitude and a higher eigenmode at a small amplitude simultaneously provides four independent observables that are sensitive to the tip–sample nanomechanical interaction parameters. To demonstrate this, a generalized theoretical framework for extracting nanomechanical sample properties from bimodal experiments is presented based on Hertzian contact mechanics. Three modes of operation for measuring cantilever parameters are considered: amplitude, phase, and frequency modulation. The experimental equivalence of all three modes is demonstrated on measurements of the second eigenmode parameters. The contact mechanics theory is then extended to power-law tip shape geometries, which is applied to analyze the experimental data and extract a shape and size of the tip interacting with a polystyrene surface.

Introduction

Over the decades since its invention [1] the atomic force microscope (AFM) has been used in a variety of modes to characterize micro- and nanoscale heterogeneous structures in composites and other advanced materials. The AFM can provide high resolution topographic and mechanical properties mapping using techniques such as force curves [2,3], contact resonance [4,5], force modulation [6,7], phase imaging [8,9], loss tangent imaging [10], friction force microscopy [11], creep compliance [12], shear modulation force microscopy [13], pulsed force microscopy [14] and torsional approaches [15]. These techniques can be broadly classified as either “parametric” or “spectroscopic” techniques.

In parametric nanomechanical techniques, the sample properties are deduced from changes in the parameters of a driven cantilever that is oscillating in a (quasi) steady state while interacting with the sample surface. For example, tapping-mode AFM [16,17] (also known as amplitude-modulation (AM) AFM

[18-20]), is one of the most commonly used parametric techniques, where the cantilever is driven on resonance and the cantilever–sample distance is adjusted by a feedback loop to maintain a constant oscillation amplitude at every image pixel. The time required for the cantilever to reach a steady state defines the acquisition speed, allowing tapping-mode imaging to achieve very high speeds ultimately only limited by the cantilever bandwidth. However, the small number of tapping-mode observables (amplitude and phase) limits the extraction of absolute storage and loss moduli, as they cannot be distinguished from changes in indentation depth. In tapping mode, only the *ratio* of the storage to loss modulus can be measured [10,21,22]. The same limitation applies to many other parametric techniques, such as force modulation [6,7] and other single-frequency imaging modes, such as frequency-modulation (FM) AFM [23]. Separating the storage and loss moduli, and quantifying them, requires either additional independent observables or the use of spectroscopic methods.

Spectroscopic techniques rely on changing the operating conditions of the cantilever to provide the necessary information to extract nanomechanical properties of the sample for a given image pixel. This can be achieved by changing the cantilever–sample distance [24] or sweeping the drive frequency [25], amongst others [26]. Examples of well-established spectroscopic techniques are nanoindentation [27] and force curves as well as dynamic force curves performed with an oscillated cantilever. The time-varying cantilever response serves as input to a model for extracting nanomechanical properties of the sample at any location. These techniques are by nature slow for imaging, as they measure time-varying changes of the cantilever at every pixel.

Recently, parametric techniques have been extended by driving two or more cantilever resonances simultaneously in order to increase the number of observables, which is required to quantify the storage and loss moduli. Advances in this direction include bimodal [28-33], trimodal [34] or more generally multimodal/multifrequency [35] techniques, and have demonstrated quantitative mapping without compromising on the high speeds that define parametric imaging techniques. Currently, state-of-the-art bimodal methodologies are mostly based on FM-AFM techniques that rely on elaborate mathematical theories [36-41], involving fractional calculus and Laplace transforms for relating AFM observables to nanomechanical properties. The mathematical complexity of these techniques can obscure physically intuitive understanding of the cantilever dynamics in bimodal AFM experiments.

Here, we present a simplified theory for bimodal AFM with a *large* fundamental resonance oscillation amplitude and *small* higher resonance amplitude. The theory is based on a binomial approximation of the weight function for extracting the interaction stiffness for both resonant modes, each yielding a simple analytical expression. These two independent pieces of information are refactored to provide information about modulus and indentation depth. While the theory is generally applicable to a wide range of tip–sample interaction models, the derivation here begins in the context of a Hertzian contact with a paraboloidal tip and is then generalized to any tip shape described by a power-law profile. This theory is then experimentally applied to three variations of bimodal AFM involving different dynamic AFM modes of operation [42,43], namely amplitude modulation (AM) [1,18,19], phase modulation (PM) [43-46] and frequency modulation (FM) [23,36,47]. Finally, a method for extracting the tip size and tip shape from bimodal AFM approach curves is presented and demonstrated on a polystyrene sample. Figure 1 provides a diagram of the theory presented in the following three sections.

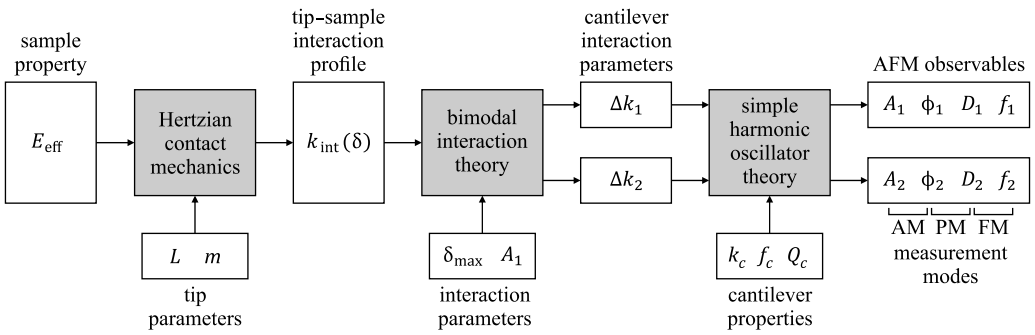

Figure 1: Diagram of the theory presented in this paper, showing relationship between inherent sample properties and tip geometry parameters to the AFM observables for bimodal AFM in the context of Hertzian contact mechanics. The tip shape is assumed to have a power-law profile with size parameter *L* and shape parameter *m*.

Methods

Hertzian contact mechanics

The Hertzian contact model involves the interaction stiffness k_{int} versus indentation depth δ between a paraboloidal tip of radius R and a flat sample as

$$k_{\text{int}}(\delta) = 2E_{\text{eff}}\sqrt{R\delta}, \tag{1}$$

where the effective Young's modulus E_{eff} combines deformation of the tip and sample [48]. Similar expressions can be derived for a tip in the shape of a punch or a cone [49].

Here, these three special cases are generalized to any axisymmetric tip shape whose cross-sectional radius r, as a function of height z, is governed by the power law

$$r(z) = L^{2-m}z^{m-1}, \tag{2}$$

where the characteristic length scale L and the exponent parameter $m \in [1,2]$ fully define the tip size and shape, respectively. Figure 2a illustrates Equation 2 for five values of m, including the three special cases of punch, paraboloid, and cone. Note that "sphere" is used as a shorthand for "paraboloid" in the scientific vernacular.

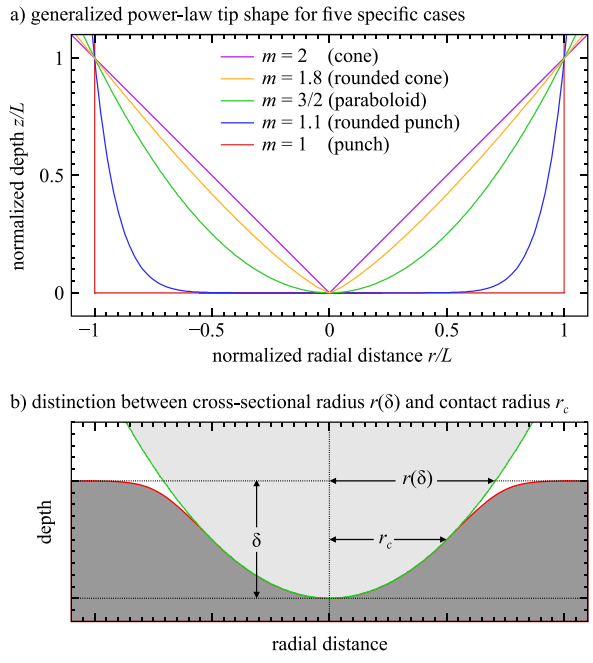

Figure 2: a) The generalized tip shape is drawn for various values of m. b) The indentation of a paraboloidal indenter into an elastic surface illustrates the distinction between the cross-sectional indentation radius versus the true contact radius.

Upon purely elastic indentation of such a power-law indenter into a sample surface to an indentation depth δ, the true contact radius r_c is smaller than the cross-sectional radius $r(\delta)$ because of deformation of the surface, as can be understood from Figure 2b. The exception is the punch model for $m = 1$, where no reduction in radius occurs. The contact radius correction factor α_c quantifies the reduction in contact radius r_c with respect to $r(\delta)$ by

$$r_c = \alpha_c r(\delta) = \alpha_c L^{2-m}\delta^{m-1}. \tag{3}$$

As expected, $\alpha_c = 1$ for $m = 1$ (punch), and then α_c monotonically decreases to $\alpha_c = 2/\pi \approx 0.64$ for $m = 2$ (cone). The mathematical form of α_c is presented in the Appendix (b).

Importantly, it is the true contact radius r_c that defines the tip–sample interaction stiffness, as derived by Oliver and Pharr [27]:

$$k_{\text{int}} = 2E_{\text{eff}}r_c. \tag{4}$$

Substituting in the expression for r_c leads to the general form

$$k_{\text{int}} = 2E_{\text{eff}}\alpha_c L^{2-m}\delta^{m-1}. \tag{5}$$

The interaction stiffness in Equation 5 is plotted for three special cases in Figure 3. For the punch model with $m = 1$, the length scale parameter L is equal to the punch radius R. For the paraboloidal indenter model with $m = 3/2$, L is the effective "sphere" diameter $2R$. For the conical indenter with $m = 2$, L drops out and the cone half-angle $\theta = 45°$. (Given the loss of the length scale parameter L in the degenerate case $m = 2$ (cone), a half-angle parameter θ may be introduced by multiplying k_{int} by $(\tan\theta)^{-1}$ to fully define the geometry of the conical indenter, if necessary.)

Bimodal interaction theory

This section first describes how the tip–sample interaction stiffness of a paraboloidal ("spherical") tip affects the changes in effective stiffness of the first and second eigenmodes of the cantilever. Then, the results are generalized to a power-law tip shape.

Paraboloidal tip

For the first eigenmode driven with a *large* oscillation amplitude A_1, the change in stiffness of the interacting cantilever Δk_1 averaged over one cycle can be computed by integrating $k_{\text{int}}(\delta)$ with a semi-circular weight function that spans the peak-to-peak

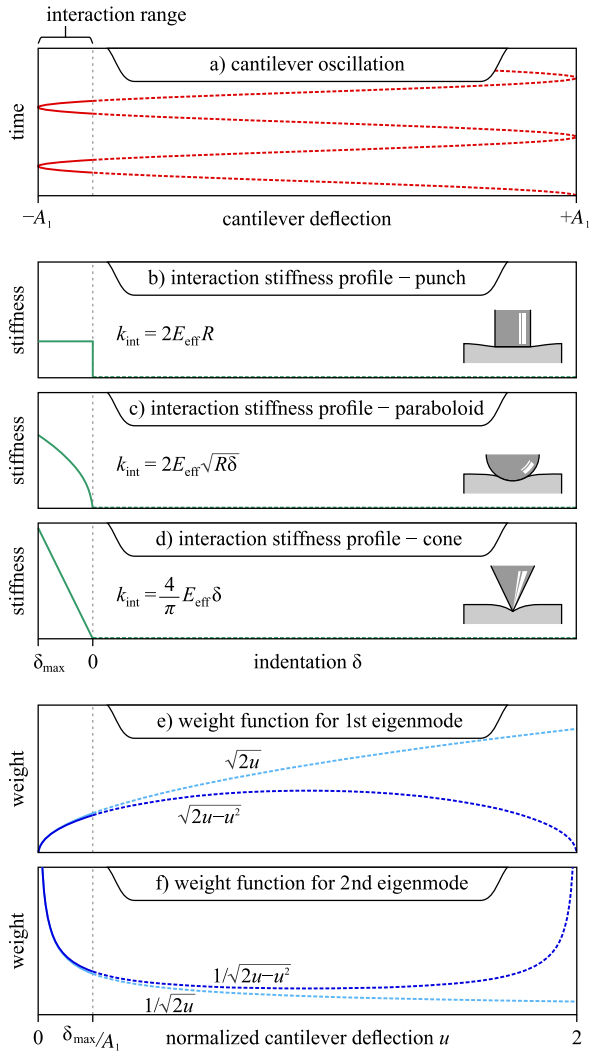

Figure 3: a) The cantilever motion during oscillation in bimodal imaging with only a small portion interacting with the sample. Note that the oscillation of the second eigenmode cannot be seen, as it is assumed infinitely small by the model proposed here. The stiffness profile of the interacting tip is plotted for three tip shapes: b) punch, c) paraboloid, d) cone. The weight functions used for integrating these stiffness profiles are shown for e) the first eigenmode (assuming a large amplitude) and f) the second eigenmode (assuming a small amplitude). The weight function for the second eigenmode diverges where the interaction stiffness is nonzero, reflecting the sensitivity of bimodal AFM to nanomechanical properties. The $\sqrt{2u-u^2} \approx \sqrt{2u}$ binomial approximation is illustrated for both weight functions; they are very accurate approximations in the interaction range, and can be used to derive a simple analytical solution for bimodal imaging. Note: the three different *x*-axes shown in these plots are interchangeable; they reflect the most appropriate parameterization of the tip position in each case.

cantilever oscillation [50], as represented in Figure 3. Mathematically,

$$\Delta k_1 = \frac{2}{\pi}\int_0^2 k_{int}\left(\delta_{max} - uA_1\right)\sqrt{2u-u^2}\,du, \qquad (6)$$

where δ_{max} is the maximum indentation depth and the normalized distance $u = (\delta_{max} - \delta)/A_1$. It is worth noting the distinction between $k_{int}(\delta)$, which is the instantaneous stiffness *profile* experienced by the oscillating cantilever tip, and Δk_1, which is the time-averaged effective change in stiffness of the cantilever–tip–sample system that is experimentally measurable by the AFM user. Measuring Δk_1 is the topic of Section 'Simple harmonic oscillator theory', presented later.

In the limit that the fundamental amplitude A_1 is much larger than the interaction length scale, the stiffness profile $k_{int}(\delta)$ only affects a small portion of the cantilever sinusoidal oscillation where the tip indents the sample, as shown in Figure 3a. Therefore, the integration limits in Equation 6 reduce to $[0, \delta_{max}/A_1]$ such that $u << 1$ throughout the integration. Consequently, the weight function can be approximated very accurately with the first term in the binomial expansion, $\sqrt{2u-u^2} \approx \sqrt{2u}$. This approximation, used previously [51], is graphically illustrated in Figure 3e,f. Applying it to Equation 6 results in

$$\Delta k_1 \approx \frac{2}{\pi}\int_0^2 k_{int}\left(\delta_{max} - uA_1\right)\sqrt{2u}\,du, \qquad (7)$$

which can be easily integrated for a paraboloidal indenter to give

$$\Delta k_1 \approx \sqrt{\frac{R}{2A_1^3}}E_{eff}\delta_{max}^2. \qquad (8)$$

The relative error in Δk_1 introduced by the binomial approximation is quantified in Figure 4; it typically falls on the order of 1% in large-amplitude dynamic AFM, where the interaction amplitude A_1 greatly exceeds δ_{max}.

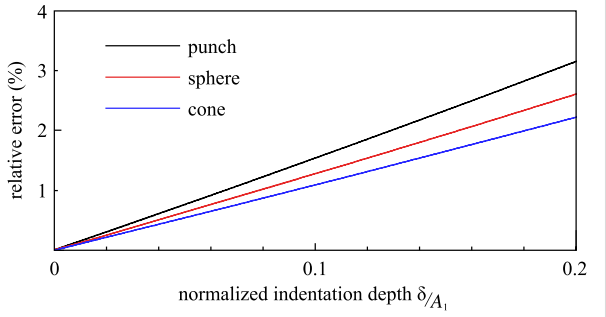

Figure 4: The relative error introduced in the calculation of Δk_1 because of the $\sqrt{2u-u^2} \approx \sqrt{2u}$ approximation applied to Equation 6 in the case of a punch, paraboloid, and cone contact model. The $1/\sqrt{2u-u^2} \approx 1/\sqrt{2u}$ approximation applied to Equation 10 results in a similar, albeit negative, error.

Meanwhile, the second (or higher) eigenmode is deliberately driven at a *small* amplitude A_2, such that the interaction stiffness it experiences is roughly constant throughout one of the higher eigenmode oscillation cycles. However, the instantaneous interaction stiffness experienced by the second eigenmode slowly changes along the trajectory of the first eigenmode. Because the second mode rides along the slower sinusoidal motion of the first mode, its time-averaged change in interaction stiffness Δk_2 can be calculated by

$$\Delta k_2 = \frac{1}{T}\int_0^T k_{\text{int}}\left(\delta(t)\right)dt, \tag{9}$$

where T is the oscillation period of the first eigenmode. A rigorous derivation of Equation 9 is provided in Appendix (a). Parametrizing this time integral with respect to distance by the substitution $t = \cos^{-1}(u)/\omega_1$ results in

$$\Delta k_2 = \frac{1}{\pi}\int_0^2 k_{\text{int}}\left(\delta_{\max} - uA_1\right)\frac{1}{\sqrt{2u-u^2}}du. \tag{10}$$

Similarly to the approach taken with the first eigenmode, this integral can be solved analytically for a paraboloidal indenter after applying the binomial approximation $1/\sqrt{2u-u^2} \approx 1/\sqrt{2u}$ such that

$$\Delta k_2 \approx \sqrt{\frac{R}{2A_1}}E_{\text{eff}}\delta_{\max}. \tag{11}$$

Note that the second-mode change in stiffness scales linearly with indentation depth, $\Delta k_2 \propto \delta_{\max}$, while the first mode stiffness scales with the square of the indentation depth, $\Delta k_1 \propto \delta_{\max}^2$. These scaling laws have been verified experimentally for a paraboloidal indenter [39]. The system of two equations (Equation 8 and Equation 11) can be solved for two unknowns, namely

$$\delta_{\max} = A_1\frac{\Delta k_1}{\Delta k_2} \tag{12}$$

and

$$E_{\text{eff}} = \sqrt{\frac{2}{RA_1}}\frac{\Delta k_2^2}{\Delta k_1}. \tag{13}$$

This operation is central to bimodal imaging, as it separates the changes in modulus from changes in indentation depth. This distinction cannot be made in single-mode dynamic AFM imaging.

The key to bimodal nanomechanical imaging is that the *same* stiffness profile is measured simultaneously by two different eigenmodes with different weight functions: $\sqrt{2u}$ and $1/\sqrt{2u}$. The fact that these weight functions are related by a derivative operation results in independent measures of nanomechanical properties by both eigenmodes while imaging. Notably, the fact that the weight function of the second eigenmode increases drastically as the tip approaches the sample, as seen in Figure 3f, explains the high sensitivity and increased spatial resolution of bimodal imaging noted in the past [52].

Power-law tip

The derivation so far revolved about a paraboloidal indenter. Applying the same approach used in Equations 6–13 to the generalized stiffness profile of Equation 5 result in the generalized indentation and modulus equations

$$\delta_{\max} = \frac{A_1}{2}\frac{\Delta k_1}{\Delta k_2}\left[m+\frac{1}{2}\right] \tag{14}$$

and

$$E_{\text{eff}} = \frac{\beta}{\alpha_c}\frac{L^{m-2}}{A_1^{m-1}}\frac{\Delta k_2^{m+1/2}}{\Delta k_1^{m-1/2}}, \tag{15}$$

where β is a scaling constant that depends only on m and is mathematically defined in the Appendix (c). As expected, choosing m = 3/2 in Equation 14 and Equation 15 recovers Eqution 12 and Equation 13.

The tip shape exponent m is a free parameter in the generalized stiffness profile. It can be inferred experimentally by measuring changes in Δk_1 and Δk_2 for a fixed A_1 and relating them to Equation 15 by the scaling law

$$\Delta k_2 \propto \Delta k_1^{\frac{m-1/2}{m+1/2}}, \tag{16}$$

as will be demonstrated later.

Simple harmonic oscillator theory

Measurements of Δk_1 and Δk_2 are necessary for calculating $\delta_{\max}$ and E_{eff} in Equation 12 and Equation 13 or Equation 14 and Equation 15.

A single equation that extracts Δk from a driven eigenmode (on and off resonance) with any number of changing AFM observables is presented in the Appendix (d). The derivation assumes the eigenmode in question can be modeled as a simple harmonic oscillator (SHO) within the range of interactions explored in the experiment. Here, three special cases (AM, PM, FM) for starting an experiment on-resonance were extracted from the general SHO solution for simplicity. These special cases are presented in Table 1, and described in the following subsections. The constant-excitation FM mode (CEFM) is also included in Table 1 for completeness.

Table 1: Using an automatic-gain-controller (AGC) and/or phase-locked-loop (PLL) to control the cantilever amplitude and frequency, respectively, leads to four combinations of measurement modes: amplitude modulation (AM), phase modulation (PM), frequency modulation (FM), and constant-excitation frequency modulation (CEFM). Using these modes for measuring Δk_1 and Δk_2 of a cantilever independently leads to 16 bimodal configurations: AM-AM, AM-PM, AM-FM, FM-FM, etc.

		Phase-locked-loop (PLL)	
		OFF	ON
Automatic-Gain-Controller (AGC)	OFF	AM mode	CEFM mode
	ON	PM mode	FM mode

The last subsection extends the SHO theory to measuring two eigenmodes simultaneously, as required for bimodal AFM.

Amplitude modulation (AM) mode

For an eigenmode driven in AM mode, the corresponding time-averaged interaction stiffness can be calculated from the measured interaction amplitude A and interaction phase ϕ, as in

$$\Delta k^{\mathrm{AM}} = \frac{k_{\mathrm{c}}}{Q_{\mathrm{c}}}\frac{A_{\mathrm{r}}}{A}\cos\phi, \tag{17}$$

while the cantilever quality factor Q_{c}, the cantilever stiffness k_{c}, and the reference amplitude A_{r} are all measured in the absence of tip–sample interactions (A_{r} is often referred to as the "free amplitude").

Phase modulation (PM) mode

Alternatively, PM mode uses an automatic-gain-controller (AGC) to maintain a constant cantilever amplitude A by varying the drive amplitude D; meanwhile, the drive frequency remains fixed just as in AM mode. In this mode,

$$\Delta k^{\mathrm{PM}} = \frac{k_{\mathrm{c}}}{Q_{\mathrm{c}}}\frac{D}{D_{\mathrm{r}}}\cos\phi. \tag{18}$$

Note that an AGC is especially beneficial for use on the second eigenmode, because A_2 is often chosen close to the detection limit and may drop substantially in AM mode when the resonance frequency shifts upon interaction with the sample. The AGC in the PM mode assures that A_2 remains above the detection limit throughout the experiment.

Frequency modulation (FM) mode

If FM mode is employed for any of the eigenmodes, where the resonance frequency f_{c} is tracked with a phase-locked-loop (PLL), the measured frequency shift Δf can be used to estimate the interaction stiffness by the approximation

$$\Delta k^{\mathrm{FM}} \approx 2k_{\mathrm{c}}\frac{\Delta f}{f_{\mathrm{c}}}. \tag{19}$$

In this mode, the oscillation amplitude is held constant with an AGC. The use of an AGC will be assumed for "FM mode" henceforth.

Alternatively, constant-excitation FM mode (CEFM) employs a PLL but does not use an AGC [53,54]; therefore, the oscillation amplitude is not necessarily constant throughout the tip–sample interaction. This less-common technique is not explored in this article.

Bimodal configurations

In bimodal AFM, both eigenmodes behave like independent SHO's because the first mode is driven in the large-amplitude limit and the second is driven in the small-amplitude limit. An empirical verification of this independence will be performed and discussed later.

In principle, both Δk_1 and Δk_2 can be measured with any of the four measurement modes described so far, leading to 16 possible configurations: AM-AM, AM-PM, AM-FM, FM-FM, etc. As an example, the first experimental bimodal measurements were taken in the AM-AM configuration [33]. In their pioneering work, Heruzzo and Garcia demonstrated FM-FM measurements [39,55]. Here, the AM-AM, AM-PM and AM-FM configurations are explored in detail. Practical considerations for these choices will be discussed later.

Results

A polystyrene surface was probed with bimodal approach curves (also known as "force–distance" curves), where the bimodally oscillating cantilever approaches the sample with a constant velocity. The experiment is described in the first subsection, where the AM-AM, AM-PM, and AM-FM configurations are compared to investigate the validity of the SHO

model assumed by the bimodal theory. Then, multiple approach curves are used to extract the shape and size of the tip. Finally, the newly defined tip geometry is used to extract the modulus from all the approach curves to assess consistency of the results and their dependence on imaging parameters.

Experiment

The experiment was performed on a Cypher AFM with an ASYELEC-02 cantilever, which has a Ti/Ir-coated tip of nominal tip radius $R = 28 \pm 10$ nm. Photothermal excitation [56] was used, which ensures stable imaging [57] and accurate FM tracking [58-60]. An automated calibration method [61] was used to obtain the stiffness of the first eigenmode ($k_{c1} = 43.2$ N/m), which was then used as a basis of calibration for the second eigenmode stiffness $k_{c2} = 818$ N/m by a recently established calibration protocol [62]. Next, a thermal power spectral density [63] of the cantilever was acquired close to the surface (within a few hundred nanometers) to determine the remaining cantilever properties ($f_{c1}, f_{c2}, Q_{c1}, Q_{c2}$). For this calibration step, the proximity to the surface is important. Performing it far from the surface incorrectly introduces long-range cantilever–sample interactions into the final measurement. Finally, the equipartition theorem was used to convert the amplitudes of both eigenmodes into nanometers [64-66].

Figure 5 shows approach curves acquired in the AM-AM, AM-PM, and AM-FM configurations. Equations 17–19 were used to recover values of Δk_1 and Δk_2 where appropriate. The excellent agreement between all three bimodal configurations across the entire approach curve suggests that the simple

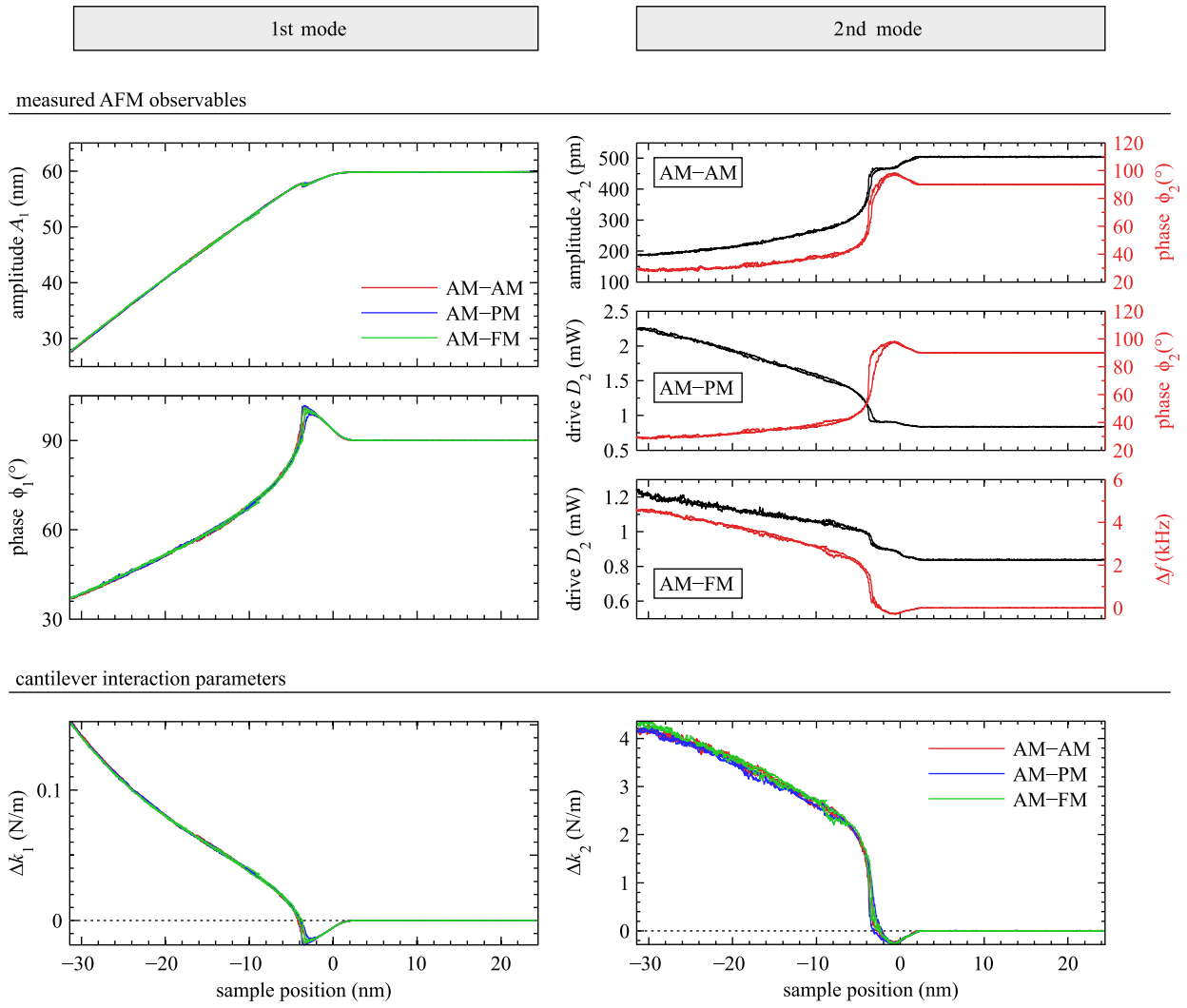

Figure 5: Experimental results from three consecutive approach curves on polystyrene using AM-AM, AM-PM, AM-FM configurations for the first mode (left) and second mode (right). The changes in effective cantilever stiffness for both modes (below) calculated from the observables of each mode (above) by using Equations 17–19, respectively (reference amplitude $A_{r1} = 60$ nm).

harmonic oscillator is a valid model to describe the second eigenmode of the cantilever in this experiment.

Calibration of the tip shape and size

When driving the first eigenmode in the AM mode, large variations in indentation depth can be achieved by varying the reference amplitude A_{r1} ("free amplitude") while keeping A_1 fixed. Varying the reference amplitude is more effective than changing A_1 which carries a weak dependence on indentation for a setpoint around $A_1/A_{r1} \approx 0.5$. Consecutive bimodal approach curves on a polystyrene sample were performed while varying the reference amplitude A_{r1} between 50 nm and 91 nm in 21 increments. The AM-AM, AM-PM, and AM-FM configurations were alternated. A total of 63 approach curves were performed within 45 min.

The values of Δk_1 and Δk_2 at a fixed amplitude (A_1 = 40 nm) were used to determine the tip shape using the scaling law in Equation 16. The results are shown in Figure 6, where the exponent m values for each bimodal configuration were extracted from a power-law fit and shown to be equal within error; they averaged to $m = 1.24 \pm 0.04$. This measurement of the tip shape (m) can now be used to calculate the tip size (L), which is uniquely determined if the sample modulus is known. Fitting Equation 15 to the data and setting E_{eff} = 3 GPa (as approximately expected for polystyrene [67]) results in a value for the tip length scale L = 32 nm. This tip characterization suggests a tip shaped as a rounded punch, somewhere between a punch of radius R = 32 nm and a paraboloid of radius R = 16 nm.

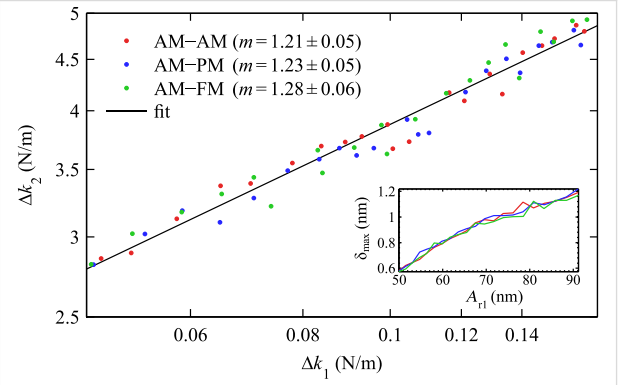

Figure 6: The set of approach curves in Figure 5 was repeated 21 times at various drive amplitudes. The values of Δk_1 and Δk_2 extracted at A_1 = 40 nm from all 63 approach curves are plotted on a log–log scale. The line represents a power-law fit to the entire data, which can be used to determine the tip shape (m = 1.24) by Equation 16 and the tip size (L = 32 nm) by Equation 15. The inset shows the range of indentation depths probed in this experiment.

With a defined exponent m value, the absolute indentation depth at the various A_{r1} can be calculated by Equation 15, as shown in the inset of Figure 6. The calibration of the tip shape and size is expected to be valid for the explored range of indentations (between 0.6 nm and 1.2 nm in this case).

Measurement of modulus

With a modeled tip shape and size (m = 1.24, L = 32 nm), the modulus E_{eff} was extracted from all 63 approach curves, as shown in Figure 7. At A_1 = 40 nm, the average modulus must be 3 GPa because this was the assumed value from which the tip size was extracted. Notably, the modulus appears to be independent of both A_1 and bimodal configuration, as will be discussed in the next section.

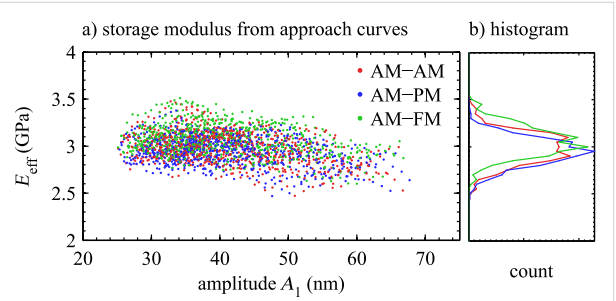

Figure 7: a) The modulus E_{eff} for all 63 approach curves from Figure 6 was extracted as a function of oscillation amplitude A_1. Not only is E_{eff} independent of interaction amplitude A_1 and reference amplitude A_{r1} (free amplitude), the three configurations (AM-AM, AM-PM, AM-FM) yield the same results within error. Note that a value of E_{eff} was only extracted for values A_1/A_{r1} < 0.75 to ensure that repulsive interactions dominate.

Discussion

Independence of imaging parameters

The approach curves in Figure 7 span indentation depths from 0.6 nm to 1.2 nm, interaction amplitudes from 25 nm to 70 nm, and reference amplitudes between 50 nm and 91 nm. The modulus values at A_1 = 40 nm are constrained to match 3 GPa by the tip shape and size calibration. However, throughout this range of imaging parameters, the modulus also remains within a 0.15 GPa standard deviation (5%) of 3 GPa, with no obvious trend. In addition, the three bimodal configurations agree to better than this standard deviation.

The independence on imaging parameters provides confidence that the system was accurately modeled by a rounded punch of shape m = 1.24 and size L = 32 nm. In contrast, assuming a paraboloidal tip (m = 1.5) results in increased variability in the modulus, as well as noticeable dependence on imaging parameters. Also, assuming a paraboloidal tip results in a tip radius R = 93 nm for these experiments, which is far from the nominal radius for this cantilever tip (R = 28 ± 10 nm).

These results lead to the conclusion that calibrating the tip shape and size provided a more accurate picture of the tip–sam-

ple contact mechanics, which led in turn to improved accuracy in extracting the modulus of polystyrene over a wider range of imaging parameters.

Given that the bimodal AFM theory was derived in the context of Hertzian contact mechanics where only repulsive interactions are considered, only data where $A_1/A_{r1} < 0.75$ were analyzed to ensure that repulsive forces dominate over attractive and adhesive forces. This criterion is somewhat arbitrary and specific to the current dataset; other samples and tip geometries may require different threshold values of A_1/A_{r1} or may require more elaborate models.

AM/PM/FM equivalence

The agreement between AM, PM and FM modes of operation for Δk_2 shown in Figure 5 validates the mathematical framework leading up to Equations 17–19 that assumes SHO behavior of the cantilever. This agreement is reassuring, as a sinusoidally-driven SHO model was used for both eigenmodes to derive the bimodal interaction theory that relates the cantilever parameters to the interaction profile. Furthermore, the agreement between the modes of operation suggests that the feedback loops used for the PM and FM modes tracked changes in the cantilever eigenmode appropriately.

Large and small amplitude approximations

The amplitude of the first mode was modeled in the large limit, while the amplitude of the second mode was modeled in the small limit. The validity of these assumptions was implicitly verified in the dataset acquired for this experiment, as described herein.

The analysis in Figure 7 suggests that the variations in interaction amplitude (25 nm < A_1 < 70 nm) do not affect the outcome of the measured E_{eff}. This suggests that the large-amplitude limit for the first mode was fulfilled across the range of explored amplitudes.

The small-amplitude limit for A_2 is tested by the comparison of experimental configurations. Whereas the second mode amplitude A_2 for AM-AM drops significantly (from 500 pm to 200 pm) during a single approach curve, A_2 for AM-PM and AM-FM is held fixed by the AGC. The fact that all three configurations lead to the same extracted E_{eff} suggests that the small-amplitude limit for the second mode was fulfilled.

Sensitivity of bimodal AFM

The high sensitivity of bimodal AFM was predicted in the theory described in Section 'Bimodal interaction theory' and attributed to the introduction of an additional eigenmode driven at a small amplitude. The argument was based on the fact that the weight function of the second eigenmode $\left(1/\sqrt{2u}\right)$ rises quickly as the tip approach the sample, as shown in Figure 3f.

This fact is demonstrated experimentally in the data of Figure 5, where Δk_2 is 20× to 50× larger than Δk_1. Whereas both Δk_1 and Δk_2 are weighted integrals of the identical stiffness profile $k_{int}(\delta)$, the weight function of the second mode captures much more of the interaction stiffness for small indentations.

This illustrates the benefit of introducing a small-amplitude second eigenmode into the measurement: it provides a high-sensitivity channel of information, without disrupting the measurement as explained in the previous section.

Error from binomial approximation

The error introduced by the $\sqrt{2u-u^2} \approx \sqrt{2u}$ approximation that allowed the analytical closed-form in Equation 14 and Equation 15 is now calculated. In the worst case scenario for this experiment with δ_{max} = 1.2 nm and A_1 = 40 nm, a relative error of 0.5% is caused by the approximation $\sqrt{2u-u^2} \approx \sqrt{2u}$. In turn, this results in an overestimation of 0.9% in indentation depth, and an underestimation of 1.0% in modulus as far as Equation 14 and Equation 15 are concerned. These errors from approximation are negligible compared with experimental variability and absolute calibration error.

Importantly, applying Equation 19 to both eigenmodes results in FM-FM equations that are identical to those derived by Herruzo et al. [38,39]. This leads to the conclusion that the $\sqrt{2u-u^2} \approx \sqrt{2u}$ approximation is sufficient for deriving analytical equations for bimodal FM-FM and other bimodal configurations. In other words, the use of fractional calculus, Laplace transforms, Padé approximants, and Bessel functions can be avoided with no loss in accuracy when deriving bimodal AFM theory.

Merits of AM-FM

Although the three configurations of bimodal methods tested in Figure 5 were equally accurate, the AM-AM method has the disadvantage of potentially having more noise relative to AM-PM, which in turn may have more noise relative to AM-FM. In AM-AM and AM-PM, the second eigenmode drive frequency is held fixed. In that case, when the second eigenmode resonance frequency shifts by more than its bandwidth ($f_c/2Q_c$), the signal-to-noise ratio degrades because the signal drops relative to the noise floor. Furthermore, in AM-AM operation, A_2 decreases upon interaction with the surface – further aggravating the drop in signal-to-noise ratio. It is therefore often advisable to operate the second eigenmode in FM mode in practical situations.

On the other hand, the first eigenmode typically undergoes more modest changes in resonance frequency upon interaction with the surface. Also, these changes are controllable by the AFM user by the setting of an amplitude setpoint. For this reason, AM operation on the first eigenmode does not cause the same decrease in signal-to-noise ratio often observed on the second eigenmode. More importantly, dynamic AFM imaging in ambient conditions has relied on the robustness of AM (tapping-mode) imaging, mostly attributable to the monotonicity of the amplitude versus distance relationship, for stable operation and topography tracking.

For these two reasons, the authors generally recommend the use of AM-FM over the other configurations (AM-PM, FM-FM, etc.), as it is the most robust, versatile and sensitive configuration for bimodal nanomechanical mapping in a wide range of imaging conditions.

Conclusion

An analysis framework for bimodal AFM with a power-law tip and Hertzian contact was presented. The derived theory was used to extract the tip shape and size for an experiment on a polystyrene sample. For a wide range of imaging parameters, the experimental data returned a nearly constant modulus of the material when analyzed with this model. Three configurations (AM-AM, AM-PM, AM-FM) were tested and shown to provide equally accurate results, thereby supporting our assumption that the cantilever second eigenmode can be modeled as a simple harmonic oscillator for the range of interactions explored in the experiment.

The approximations used for deriving an analytical closed-form solution for bimodal AFM were also investigated. Both the first mode large-amplitude approximation and the second mode small-amplitude approximation were verified to be accurate for typical imaging conditions. Notably, the fact that the weight function of the second eigenmode increases drastically as the tip approaches the sample explains the high sensitivity and spatial resolution of bimodal imaging. The binomial approximation of the stiffness weight function ($\sqrt{2u-u^2} \approx \sqrt{2u}$) was shown to introduce negligible error (<1%), yet it can be used to derive bimodal AFM theory without invoking the use of fractional calculus.

The experimental in situ determination of the tip shape and size is a pivotal step towards absolute quantitative nanomechanical measurements in a variety of techniques. This work demonstrates the benefits of tip characterization in the context of bimodal nanomechanical mapping, which improves the accuracy of fast parametric techniques such as AM-FM nanomechanical mapping.

Appendix

a. Correction factor for contact radius: α_c

The correction factor that accounts for deformation of the sample that leads to a true contact radius different from the nominal contact radius [68,69] is given by

$$\alpha_c = \left[\frac{2}{\sqrt{\pi}}[m-1]\frac{\Gamma\left(\frac{m}{2(m-1)}\right)}{\Gamma\left(\frac{1}{2(m-1)}\right)}\right]^{m-1}, \qquad (20)$$

where Γ is the gamma function. Figure 1 graphs α_c for values between m = 1 and m = 2. Note that obtaining α_c = 1 at the value at m = 1 requires a taking a limit.

b. Weighted interaction stiffness of the higher eigenmode

The weighted integral used to average the interaction stiffness across one oscillation cycle of the first eigenmode (Equation 6) also applies to higher eigenmodes; it can be rewritten as

$$\Delta k_2 = \frac{2}{\pi}\int_0^2 k_{\text{int}}\left(\delta(t)-u'A_2\right)\sqrt{2u'-u'^2}\,du', \qquad (21)$$

where u' is the normalized deflection of the higher eigenmode in this context. The major distinction between Equation 6 and Equation 21 is the substitution $\delta_{max} \rightarrow \delta(t)$ which accounts for the non-zero amplitude of the first eigenmode A_1 that introduces a time-varying component to the k_{int} experienced by the higher mode. For a first-mode period $T = 1/f_{c1}$, this effect can be averaged over a full cycle by

$$\Delta k_2 = \frac{1}{T}\int_0^T \frac{2}{\pi}\int_0^2 k_{\text{int}}\left(\delta(t)-u'A_2\right)\sqrt{2u'-u'^2}\,du'\,dt. \qquad (22)$$

In the limit that $A_2 \rightarrow 0$ and $f_{c2}/f_{c1} \rightarrow \infty$, k_{int} remains constant throughout any full oscillation cycle of the second mode, such that Equation 22 solves to

$$\Delta k_2 = \frac{1}{T}\int_0^T k_{\text{int}}\left(\delta(t)\right)dt. \qquad (23)$$

Notably, this integral that determines Δk_2 only depends on the trajectory of the first eigenmode because A_2 is assumed small.

c. Correction factor for power-law force model: β

When integrating $k_{int}(\delta)$ in Equation 6 and Equation 10 to obtain Δk_1 and Δk_2, respectively, for a power-law model $k_{int} \propto \delta^{m-1}$ as defined by Equation 5, gamma functions emerge due to the integration of non-integer powers. They are summarized here as

$$\beta = \frac{2^{m-1}\sqrt{\pi}}{\Gamma(m)} \frac{\Gamma\left(m+\frac{1}{2}\right)^{m+\frac{1}{2}}}{\Gamma\left(m+\frac{3}{2}\right)^{m-\frac{1}{2}}}. \quad (24)$$

Note that the gamma functions that compose α_c in Appendix a relate to deformation of the sample and have no direct relationship to the gamma functions of β, which relate to the effects of power-law stiffness profiles affecting the cantilever parameters.

d. Generalized SHO equation

The on-resonance Equations 17–19 are special cases of the general solution to a simple harmonic oscillator model, which can be driven on or off resonance with concurrent changes in drive frequency, phase, oscillation amplitude and drive amplitude. This section derives a general equation that makes no assumption about which of these variables is held fixed upon interaction with the sample.

The response of a freely vibrating cantilever with effective stiffness k_c, mass m_c, and damping b_c can be described by the complex-valued cantilever impedance [70]

$$\mathcal{C}^{-1}(\omega) = k_c - m_c\omega^2 + i\omega b_c, \quad (25)$$

where the angular frequency is defined as $\omega = 2\pi f$. The subscript "c" reminds that k_c, m_c, b_c are properties of the cantilever (prior to the tip–sample interaction) that do not change throughout the experiment.

A "reference" measurement of this cantilever impedance can be made prior to tip–sample interaction by exciting the cantilever sinusoidally with some reference driving force F_r at some reference drive frequency ω_r, which results in a reference oscillation amplitude A_r and a reference phase ϕ_r:

$$\mathcal{C}^{-1}(\omega_r) = \frac{F_r}{A_r} e^{i\phi_r}. \quad (26)$$

The reference driving force can be defined by isolating the imaginary components of both equations and solving for the driving force:

$$F_r = \frac{A_r \omega_r b_c}{\sin\phi_r}. \quad (27)$$

In the presence of some interaction, the cantilever impedance is subject to a time-averaged change in stiffness Δk and a time-averaged change in damping Δb, such that the interaction impedance

$$\mathcal{C}_{int}^{-1}(\omega) = k_c + \Delta k - m_c\omega^2 + i\omega(b_c + \Delta b). \quad (28)$$

The interaction impedance is inferred during the experiment by

$$\mathcal{C}_{int}^{-1}(\omega) = \frac{F}{A} e^{i\phi}. \quad (29)$$

where the drive force F, the drive frequency ω, the oscillation amplitude A and the phase response ϕ are measured during tip–sample interaction.

Subtracting the reference measurement $\mathcal{C}^{-1}(\omega_r)$ from the interaction measurement $\mathcal{C}_{int}^{-1}(\omega)$, then isolating the real components and solving for Δk leads to

$$\Delta k = m_c\left(\omega^2 - \omega_r^2\right) + \frac{F}{A}\cos\phi - \frac{F_r}{A_r}\cos\phi_r. \quad (30)$$

Assuming that the drive force F is proportional to the drive amplitude D and that their relationship is frequency-independent implies that

$$F = F_r \frac{D}{D_r}. \quad (31)$$

Substituting Equation 27 and Equation 31 into Equation 30 results in

$$\Delta k = m_c\left(\omega^2 - \omega_r^2\right) + \omega_r b_c\left(\frac{A_r}{A}\frac{D}{D_r}\frac{\cos\phi}{\sin\phi_r} - \frac{\cos\phi_r}{\sin\phi_r}\right). \quad (32)$$

With the substitutions

$$m_c = \frac{k_c}{\omega_c^2} \quad (33)$$

and

$$b_c = \frac{k_c}{\omega_c Q_c}, \tag{34}$$

that introduce the cantilever resonance frequency ω_c and the quality factor Q_c, Equation 32 can be rewritten in a more experimentally friendly form as

$$\Delta k = \frac{k_c}{\omega_c^2}\left(\omega^2 - \omega_r^2\right) + \frac{\omega_r k_c}{\omega_c Q_c}\left(\frac{A_r}{A}\frac{D}{D_r}\frac{\cos\phi}{\sin\phi_r} - \frac{\cos\phi_r}{\sin\phi_r}\right). \tag{35}$$

Lastly, driving the cantilever on resonance prior to tip sample interactions ($\omega_r = \omega_c$; $\phi_r = 90°$) simplifies the result to

$$\Delta k = k_c\left(\frac{\omega^2}{\omega_c^2} - 1\right) + \frac{k_c}{Q_c}\left(\frac{A_r}{A}\frac{D}{D_r}\cos\phi\right). \tag{36}$$

For AM operation, setting $D = D_r$ and $\omega = \omega_c$ results in Equation 17.

For PM operation, setting $A = A_r$ and $\omega = \omega_c$ results in Equation 18.

For FM operation, setting $A = A_r$, enforcing $\phi = 90°$, and applying a binomial approximation results in Equation 19.

References

1. Binnig, G.; Quate, C. F.; Gerber, C. *Phys. Rev. Lett.* **1986,** *56,* 930. doi:10.1103/PhysRevLett.56.930
2. Butt, H.-J.; Cappella, B.; Kappl, M. *Surf. Sci. Rep.* **2005,** *59,* 1. doi:10.1016/j.surfrep.2005.08.003
3. Cappella, B.; Dietler, G. *Surf. Sci. Rep.* **1999,** *34,* 1. doi:10.1016/S0167-5729(99)00003-5
4. Killgore, J. P.; Yablon, D. G.; Tsou, A. H.; Gannepalli, A.; Yuya, P. A.; Turner, J. A.; Proksch, R.; Hurley, D. C. *Langmuir* **2011,** *27,* 13983. doi:10.1021/la203434w
5. Rabe, U.; Amelio, S.; Kester, E.; Scherer, V.; Hirsekorn, S.; Arnold, W. *Ultrasonics* **2000,** *38,* 430. doi:10.1016/S0041-624X(99)00207-3
6. Maivald, P.; Butt, H. J.; Gould, S. A. C.; Prater, C. B.; Drake, B.; Gurley, J. A.; Elings, V. B.; Hansma, P. K. *Nanotechnology* **1991,** *2,* 103. doi:10.1088/0957-4484/2/2/004
7. Radmacher, M.; Tillmann, R. W.; Gaub, H. E. *Biophys. J.* **1993,** *64,* 735. doi:10.1016/S0006-3495(93)81433-4
8. Tamayo, J.; García, R. *Langmuir* **1996,** *12,* 4430. doi:10.1021/la960189l
9. Magonov, S. N.; Elings, V.; Whangbo, M.-H. *Surf. Sci.* **1997,** *375,* L385. doi:10.1016/S0039-6028(96)01591-9
10. Proksch, R.; Yablon, D. G. *Appl. Phys. Lett.* **2012,** *100,* 073106. doi:10.1063/1.3675836
11. Carpick, R. W.; Salmeron, M. *Chem. Rev.* **1997,** *97,* 1163. doi:10.1021/cr960068q
12. Braunsmann, C.; Proksch, R.; Revenko, I.; Schäffer, T. E. *Polymer* **2014,** *55,* 219. doi:10.1016/j.polymer.2013.11.029
13. Ge, S.; Pu, Y.; Zhang, W.; Rafailovich, M.; Sokolov, J.; Buenviaje, C.; Buckmaster, R.; Overney, R. M. *Phys. Rev. Lett.* **2000,** *85,* 2340. doi:10.1103/PhysRevLett.85.2340
14. Rosa-Zeiser, A.; Weilandt, E.; Hild, S.; Marti, O. *Meas. Sci. Technol.* **1997,** *8,* 1333. doi:10.1088/0957-0233/8/11/020
15. Sahin, O.; Magonov, S.; Su, C.; Quate, C. F.; Solgaard, O. *Nat. Nanotechnol.* **2007,** *2,* 507. doi:10.1038/nnano.2007.226
16. Hu, S.; Raman, A. *Nanotechnology* **2008,** *19,* 375704. doi:10.1088/0957-4484/19/37/375704
17. Zhong, Q.; Inniss, D.; Kjoller, K.; Elings, V. B. *Surf. Sci.* **1993,** *290,* L688. doi:10.1016/0167-2584(93)90906-Y
18. Hölscher, H. *Appl. Phys. Lett.* **2006,** *89,* 123109. doi:10.1063/1.2355437
19. Katan, A. J.; van Es, M. H.; Oosterkamp, T. H. *Nanotechnology* **2009,** *20,* 165703. doi:10.1088/0957-4484/20/16/165703
20. Lee, M.; Jhe, W. *Phys. Rev. Lett.* **2006,** *97,* 036104. doi:10.1103/PhysRevLett.97.036104
21. Cleveland, J. P.; Anczykowski, B.; Schmid, A. E.; Elings, V. B. *Appl. Phys. Lett.* **1998,** *72,* 2613. doi:10.1063/1.121434
22. San Paulo, Á.; García, R. *Phys. Rev. B* **2002,** *66,* 041406. doi:10.1103/PhysRevB.66.041406
23. Albrecht, T. R.; Grütter, P.; Horne, D.; Rugar, D. *J. Appl. Phys.* **1991,** *69,* 668. doi:10.1063/1.347347
24. Martin, Y.; Williams, C. C.; Wickramasinghe, H. K. *J. Appl. Phys.* **1987,** *61,* 4723. doi:10.1063/1.338807
25. Jesse, S.; Kalinin, S. V.; Proksch, R.; Baddorf, A. P.; Rodriguez, B. J. *Nanotechnology* **2007,** *18,* 435503. doi:10.1088/0957-4484/18/43/435503
26. Forchheimer, D.; Platz, D.; Tholén, E. A.; Haviland, D. B. *Phys. Rev. B* **2012,** *85,* 195449. doi:10.1103/PhysRevB.85.195449
27. Oliver, W. C.; Pharr, G. M. *J. Mater. Res.* **1992,** *7,* 1564. doi:10.1557/JMR.1992.1564
28. Kawai, S.; Glatzel, T.; Koch, S.; Such, B.; Baratoff, A.; Meyer, E. *Phys. Rev. Lett.* **2009,** *103,* 220801. doi:10.1103/PhysRevLett.103.220801
29. Li, J. W.; Cleveland, J. P.; Proksch, R. *Appl. Phys. Lett.* **2009,** *94,* 163118. doi:10.1063/1.3126521
30. Stark, R. W. *Appl. Phys. Lett.* **2009,** *94,* 063109. doi:10.1063/1.3080209
31. Ebeling, D.; Solares, S. D. *Nanotechnology* **2013,** *24,* 135702. doi:10.1088/0957-4484/24/13/135702
32. Rodríguez, T. R.; García, R. *Appl. Phys. Lett.* **2004,** *84,* 449. doi:10.1063/1.1642273
33. Proksch, R. *Appl. Phys. Lett.* **2006,** *89,* 113121. doi:10.1063/1.2345593
34. Solares, S. D.; Chawla, G. *Meas. Sci. Technol.* **2010,** *21,* 125502. doi:10.1088/0957-0233/21/12/125502
35. Lozano, J. R.; Garcia, R. *Phys. Rev. Lett.* **2008,** *100,* 076102. doi:10.1103/PhysRevLett.100.076102
36. Sader, J. E.; Jarvis, S. P. *Appl. Phys. Lett.* **2004,** *84,* 1801. doi:10.1063/1.1667267
37. Herruzo, E. T.; Garcia, R. *Appl. Phys. Lett.* **2007,** *91,* 143113. doi:10.1063/1.2794426
38. Herruzo, E. T.; Garcia, R. *Beilstein J. Nanotechnol.* **2012,** *3,* 198. doi:10.3762/bjnano.3.22
39. Herruzo, E. T.; Perrino, A. P.; Garcia, R. *Nat. Commun.* **2014,** *5,* 3126. doi:10.1038/ncomms4126

40. Sader, J. E.; Uchihashi, T.; Higgins, M. J.; Farrell, A.; Nakayama, Y.; Jarvis, S. P. *Nanotechnology* **2005,** *16,* S94. doi:10.1088/0957-4484/16/3/018
41. Aksoy, M. D.; Atalar, A. *Phys. Rev. B* **2011,** *83,* 075416. doi:10.1103/PhysRevB.83.075416
42. García, R.; Pérez, R. *Surf. Sci. Rep.* **2002,** *47,* 197. doi:10.1016/S0167-5729(02)00077-8
43. Labuda, A.; Kobayashi, K.; Kiracofe, D.; Suzuki, K.; Grütter, P. H.; Yamada, H. *AIP Adv.* **2011,** *1,* 022136. doi:10.1063/1.3601872
44. Fukuma, T.; Kilpatrick, J. I.; Jarvis, S. P. *Rev. Sci. Instrum.* **2006,** *77,* 123703. doi:10.1063/1.2405361
45. Hölscher, H. *J. Appl. Phys.* **2008,** *103,* 064317. doi:10.1063/1.2896450
46. Sugawara, Y.; Kobayashi, N.; Kawakami, M.; Li, Y. J.; Naitoh, Y.; Kageshima, M. *Appl. Phys. Lett.* **2007,** *90,* 194104. doi:10.1063/1.2737907
47. Labuda, A.; Miyahara, Y.; Cockins, L.; Grütter, P. H. *Phys. Rev. B* **2011,** *84,* 125433. doi:10.1103/PhysRevB.84.125433
48. Johnson, K. L. *Contact Mechanics;* Cambridge University Press: Cambridge, United Kingdom, 1985.
49. Sneddon, I. N. *Int. J. Eng. Sci.* **1965,** *3,* 47. doi:10.1016/0020-7225(65)90019-4
50. Giessibl, F. J. *Appl. Phys. Lett.* **2001,** *78,* 123. doi:10.1063/1.1335546
51. Dürig, U. *Appl. Phys. Lett.* **2000,** *76,* 1203. doi:10.1063/1.125983
52. Martinez, N. F.; Patil, S.; Lozano, J. R.; Garcia, R. *Appl. Phys. Lett.* **2006,** *89,* 153115. doi:10.1063/1.2360894
53. Gotsmann, B.; Fuchs, H. *Appl. Surf. Sci.* **2002,** *188,* 355. doi:10.1016/S0169-4332(01)00950-3
54. Ebeling, D.; Solares, S. D. *Beilstein J. Nanotechnol.* **2013,** *4,* 198. doi:10.3762/bjnano.4.20
55. Garcia, R.; Herruzo, E. T. *Nat. Nanotechnol.* **2012,** *7,* 217. doi:10.1038/nnano.2012.38
56. Labuda, A.; Cleveland, J.; Geisse, N.; Kocun, M.; Ohler, B.; Proksch, R.; Viani, M.; Walters, D. *Microsc. Anal.* **2014,** *28,* 23.
57. Labuda, A.; Kobayashi, K.; Miyahara, Y.; Grütter, P. *Rev. Sci. Instrum.* **2012,** *83,* 053703. doi:10.1063/1.4712286
58. Proksch, R.; Kalinin, S. V. *Nanotechnology* **2010,** *21,* 455705. doi:10.1088/0957-4484/21/45/455705
59. Labuda, A.; Brastaviceanu, T.; Pavlov, I.; Paul, W.; Rassier, D. E. *Rev. Sci. Instrum.* **2011,** *82,* 013701. doi:10.1063/1.3527913
60. Kobayashi, K.; Yamada, H.; Matsushige, K. *Rev. Sci. Instrum.* **2011,** *82,* 033702. doi:10.1063/1.3557416
61. Sader, J. E.; Sanelli, J. A.; Adamson, B. D.; Monty, J. P.; Wei, X.; Crawford, S. A.; Friend, J. R.; Marusic, I.; Mulvaney, P.; Bieske, E. J. *Rev. Sci. Instrum.* **2012,** *83,* 103705. doi:10.1063/1.4757398
62. Labuda, A.; Kocun, M.; Lysy, M.; Walsh, T.; Meinhold, J.; Proksch, T.; Meinhold, W.; Anderson, C.; Proksch, R. *Rev. Sci. Instrum.* **2016,** *87,* in press. doi:10.1063/1.4955122
63. Labuda, A. *Rev. Sci. Instrum.* **2016,** *87,* 033704. doi:10.1063/1.4943292
64. Hutter, J. L.; Bechhoefer, J. *Rev. Sci. Instrum.* **1993,** *64,* 1868. doi:10.1063/1.1143970
65. Butt, H.-J.; Jaschke, M. *Nanotechnology* **1995,** *6,* 1. doi:10.1088/0957-4484/6/1/001
66. Higgins, M. J.; Proksch, R.; Sader, J. E.; Polcik, M.; Mc Endoo, S.; Cleveland, J. P.; Jarvis, S. P. *Rev. Sci. Instrum.* **2006,** *77,* 013701. doi:10.1063/1.2162455
67. Miyake, K.; Satomi, N.; Sasaki, S. *Appl. Phys. Lett.* **2006,** *89,* 031925. doi:10.1063/1.2234648
68. Popov, V. L. *Friction* **2013,** *1,* 41. doi:10.1007/s40544-013-0005-3
69. Heß, M. *Phys. Mesomech.* **2012,** *15,* 264. doi:10.1134/S1029959912030034
70. Labuda, A.; Grütter, P. *Langmuir* **2012,** *28,* 5319. doi:10.1021/la300557u

License and Terms

BEILSTEIN JOURNAL OF NANOTECHNOLOGY

Signal enhancement in cantilever magnetometry based on a co-resonantly coupled sensor

Julia Körner[1], Christopher F. Reiche[1], Thomas Gemming[1], Bernd Büchner[1,2], Gerald Gerlach[3] and Thomas Mühl[*1]

Full Research Paper

Open Access

Address:
[1]Leibniz Institute for Solid State and Materials Research IFW Dresden, Helmholtzstr. 20, 01069 Dresden, Germany, [2]Institut für Festkörperphysik, Technische Universität Dresden, 01062 Dresden, Germany and [3]Institut für Festkörperelektronik, Technische Universität Dresden, 01062 Dresden, Germany

Email:
Thomas Mühl[*] - t.muehl@ifw-dresden.de

* Corresponding author

Keywords:
cantilever magnetometry; coupled oscillator; iron-filled carbon nanotube; magnetometry; signal enhancement

Beilstein J. Nanotechnol. **2016,** *7,* 1033–1043.
doi:10.3762/bjnano.7.96

Received: 02 March 2016
Accepted: 06 July 2016
Published: 18 July 2016

This article is part of the Thematic Series "Advanced atomic force microscopy techniques IV".

Guest Editor: T. Glatzel

Abstract

Cantilever magnetometry is a measurement technique used to study magnetic nanoparticles. With decreasing sample size, the signal strength is significantly reduced, requiring advances of the technique. Ultrathin and slender cantilevers can address this challenge but lead to increased complexity of detection. We present an approach based on the co-resonant coupling of a micro- and a nanometer-sized cantilever. Via matching of the resonance frequencies of the two subsystems we induce a strong interplay between the oscillations of the two cantilevers, allowing for a detection of interactions between the sensitive nanocantilever and external influences in the amplitude response curve of the microcantilever. In our magnetometry experiment we used an iron-filled carbon nanotube acting simultaneously as nanocantilever and magnetic sample. Measurements revealed an enhancement of the commonly used frequency shift signal by five orders of magnitude compared to conventional cantilever magnetometry experiments with similar nanomagnets. With this experiment we do not only demonstrate the functionality of our sensor design but also its potential for very sensitive magnetometry measurements while maintaining a facile oscillation detection with a conventional microcantilever setup.

Introduction

Over the last decade, magnetic objects of micro- and nanometer size have come into focus of researchers, since they offer a wide range of possible applications. These include magnetic storage techniques and spintronics [1], as well as the study of magnetic microorganisms in biology, for example for applications in hypothermia treatment [2]. A technique to investigate such magnetic particles and samples is cantilever magnetometry. The measurement setup is based on a cantilever oscillating at or close to its resonance frequency, with the sample placed at the free end of the cantilever. When an external magnetic field is applied to the setup, the magnetic interaction of the sample with the field alters the resonance frequency of the can-

tilever by creating a torque [3]. The resulting frequency shift can be used as measurement signal to derive information on the properties of the sample. In most cases the motion of the cantilever is detected optically, for example via laser deflection or laser interferometry [4]. With decreasing sample size, the cantilever has to be adapted to compensate the weaker magnetic interaction and, therefore, the loss in signal strength of the frequency shift. This is usually achieved through geometric changes, making the cantilever itself very small and thin.

An oscillating cantilever beam can be represented by a harmonic oscillator model for each flexural eigenmode of the beam [5]. Considering an external force gradient as an additional spring constant Δk, the eigenfrequency of the cantilever as a harmonic oscillator is given by:

$$f_0^{\Delta k} = \frac{1}{2\pi}\sqrt{\frac{k+\Delta k}{m_{\text{eff}}}} \tag{1}$$

with the spring constant k and effective mass m_{eff} of the cantilever. Please note that the eigenfrequency f_0 and the resonance frequency f_0' of a harmonic oscillator should in principle be distinguished. They are connected by the relation $f_0'^2 = f_0^2(1-1/(2Q)^2)$. However, it is obvious that in the limit of small dissipation or correspondingly a high quality factor of the cantilever these frequencies coincide well. The resonance frequency of a beam can easily be determined from amplitude response curves and, since all our discussions will be based on such curves, we will be using the term resonance frequency throughout the remainder of this publication.

For magnetometry experiments, the mass of the cantilever with the magnetic sample remains unchanged throughout the experiment, making it unnecessary to consider the influence of mass changes on the resonance frequency of the cantilever. The magnetic interaction between sample and external magnetic field acts as the additional spring constant Δk, altering the resonance frequency of the cantilever. The frequency shift Δf induced by these interactions can be derived from Equation 1 as:

$$\Delta f = f_0^{\Delta k} - f_0 \approx \frac{f_0}{2k}\Delta k. \tag{2}$$

In the case of cantilever magnetometry, Δk does not only depend on the interaction of the magnetic moment m of the sample with the external magnetic field H but also on the effective length of the cantilever L_{eff} [6,7]. Furthermore, by assuming a simple Stoner–Wohlfarth single domain particle, the magnetic interaction is related to the anisotropy field of the sample H_{a}, so Equation 2 reads:

$$\Delta f \approx \frac{1}{2}\frac{f_0\mu_0 H_{\text{ext}}}{k_0 L_{\text{eff}}^2}\cdot m \cdot \frac{H_{\text{a}}}{H_{\text{ext}}+H_{\text{a}}}. \tag{3}$$

This equation can be used as a good approximation for the iron-filled carbon nanotube samples which are presented in this publication. However, please note that other samples might exhibit more complex magnetic configurations, as for example multiple particles or domains, which then need a more elaborate description.

From Equation 3 it is evident that small magnetic samples require a low stiffness as well as a short length of the cantilever which can be achieved by decreasing all of the dimensions of the cantilever as already mentioned above. As an instructive example to understand this, a simple cantilever with constant rectangular cross section with the width w, the thickness t and the length L can be considered. According to Euler–Bernoulli beam theory, the spring constant and resonance frequency for this kind of beam are given by $k \propto wt^3/L^3$ and $f \propto t/L^2$[6]. By combining this with Equation 3 for the frequency shift signal in cantilever magnetometry, it can be derived that $\Delta f \propto 1/wt^2L$. Therefore, a decrease of all dimensions of the rectangular cantilever is favorable to increase the signal strength. Please note that while this simple derivation is only valid for cantilevers with rectangular cross section, similar considerations can be applied to other cantilever geometries.

However, ultrathin and small cantilevers are difficult to produce and handle and furthermore still need a feature to allow for the use of optical detection methods. This is usually realized by a paddle-shaped structure positioned somewhere along the length of the cantilever [4,8]. Still, the detection capability limits the decrease in size. Conclusively, there are two competing conditions: on the one hand, the stiffness and length of the cantilever should be very low in order to obtain a strong signal even with very small magnetic samples. On the other hand, detection becomes increasingly difficult when the size of the cantilever is reduced to dimensions on the nanoscale.

Our recently introduced sensor concept addresses these difficulties by co-resonant coupling of a micro- and a nanocantilever where the latter allows for very high sensitivity and the micrometer size part for an easy detection [9]. We will only briefly review the theoretical considerations regarding the sensor concept since it is discussed in depth elsewhere [9]. The main focus of this publication is to demonstrate the applicability of the concept for cantilever magnetometry by deriving magnetic information of an iron nanowire and comparing them to the results of other measurements. In our experiment we use a commercially available silicon cantilever of micrometer dimensions

and an iron-filled carbon nanotube (FeCNT), the latter with two out of three dimensions on the nanometer scale and therefore with low stiffness and low effective mass. Typical diameters of the iron filling are (15–30) nm and the nanotube length ranges from (15–45) µm [10,11]. The FeCNT not only features favorable geometric and material properties [12] but the iron filling allows for a magnetometry measurement as well and, therefore, for a demonstration of the functionality of our sensor. The remainder of this publication is structured as follows: first we will introduce the main ideas of the co-resonant sensor concept. Next, we will discuss the fabrication of such a sensor and then evaluate a magnetometry measurement and derive magnetic properties of an iron nanowire in order to prove the applicability of the concept and to indicate its potential for signal enhancement in magnetometry.

Experimental

Co-resonant concept

By applying the harmonic oscillator model for both subsystems of our sensor approach, the simple model of a coupled harmonic oscillating system is derived as depicted in Figure 1. It consists of a spring, a mass and a damping element for each subsystem. Furthermore, there are an additional spring k_3 and a damping element d_3, modeling interactions between the coupled system and external influences. The oscillation of the coupled system is driven by a periodic force applied to the bigger subsystem.

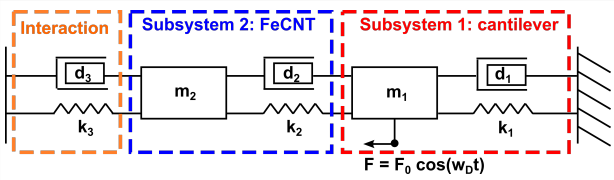

Figure 1: Simple model for two coupled harmonic oscillators, each represented by a mass (m_1, m_2), a sping (k_1, k_2) and a damping element (d_1, d_2). The system is excited to oscillations by a periodic force with the driving angular frequency $\omega_D = 2\pi f_D$ applied to the first subsystem. Interactions between the system and external influences are modeled by an additional spring k_3 and the damping element d_3. For the described sensor setup, subsystem 1 corresponds to the cantilever and subsystem 2 to a FeCNT.

In our case, subsystem 1 represents the silicon cantilever and subsystem 2 the FeCNT and, since the cantilever is the part of the sensor that will be used for detection, we will discuss the behaviour of the coupled system accordingly. Please note that all the following considerations are valid for the FeCNT as well. Theoretically, if coupled beams are each represented by a harmonic oscillator model which is only valid for one resonance mode of the beam, the amplitude response of each subsystem should exhibit a number of resonance frequencies according to the number of subsystems. Applied to our system it means that two resonance peaks should occur in the amplitude response of the subsystem representing the cantilever. However, if the resonance frequencies of cantilever and FeCNT are far apart, the amplitude of the second peak in the amplitude response of the cantilever will be well below the limit of almost every detection method. Figure 2 depicts a calculated amplitude response of the cantilever based on typical values for our system as summarized in Table 1. With the resonance frequencies of the subsystem far apart, i.e., very weak interplay, the amplitude response curve of the harmonic oscillator representing the cantilever only shows one prominent resonance peak, coinciding well with the resonance frequency of the uncoupled cantilever. The amplitude for the second peak caused by the FeCNT is by several orders of magnitude smaller and therefore not shown in Figure 2.

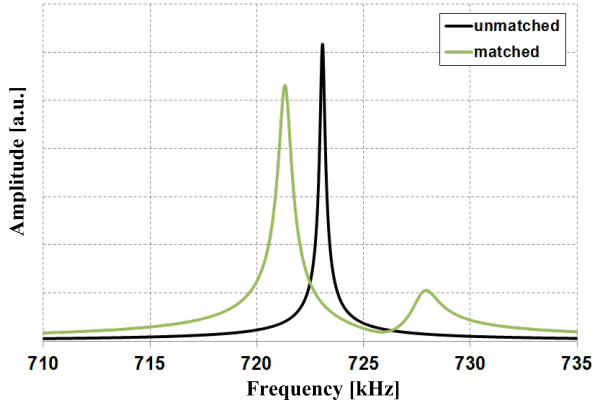

Figure 2: Calculated amplitude response for the cantilever (subsystem 1) with and without frequency matching between the two subsystems. The calculation is based on typical values for cantilever and FeCNT (see Table 1) and d_3 and k_3 are set to zero, assuming a system without interaction.

Table 1: Properties of cantilever and FeCNT constituting the coupled sensor.

Parameter	Cantilever (1)	FeCNT (2)
spring constant k_i	133.8 N/m	0.0086 N/m
effective mass $m_{eff,i}$	$6.5 \cdot 10^{-12}$ kg	$4.1 \cdot 10^{-16}$ kg
quality factor Q_i	3390	450
resonance frequency f_i before matching	723080 Hz	2082080 Hz
resonance frequency f_i after matching	723080 Hz	725610 Hz

This picture changes drastically when the resonance frequency of the FeCNT is adjusted close to the value of the cantilever. In that case, we observe two clear resonance peaks in the amplitude response of the cantilever (Figure 2). Furthermore, due to strong interplay between the subsystems induced by the co-resonant frequency matching, the two resonance frequencies

of the coupled system are shifted compared to the resonance frequencies of the single subsystems. We will therefore use f_a and f_b for the resonance frequencies of the coupled system and f_1 and f_2 for the individual resonance frequencies of cantilever and FeCNT, respectively, in the following. Futher details on the behaviour of a co-resonantly coupled system can be found elsewhere [9], so we will only summarize the main points here:

1. A strong interplay is induced between the two subsystems due to the matching of the resonance frequencies, even for two highly asymmetric subsystems.
2. Interactions between FeCNT and an external influence alter the oscillation of the FeCNT. Through the co-resonant coupling this changes the resonance frequencies of the coupled system and can be detected at the cantilever.
3. Small interactions result in rather large frequency shifts due to the low stiffness, i.e., high sensitivity of the nanoscale oscillator, and can be measured with a rather insensitive cantilever.

Sensor fabrication

Based on the theoretical considerations we fabricated a magnetometry sensor consisting of a commercially available tipless silicon cantilever and an iron-filled carbon nanotube. All productions steps were carried out in a Zeiss FIB CrossBeam 1540 XB under high vacuum (≈10^{-5} mbar). First, the cantilever was shortened via focused ion beam milling to increase its resonance frequency. This step also increased the stiffness of the cantilever to about 133.8 N/m (see Table 1) which is rather high compared to typical values in cantilever magnetometry. In a second step, an individual nanotube was picked from a forest of FeCNTs grown by chemical vapor deposition [10] by a Kleindiek micromanipulator and placed at the free end of the cantilever. Electron beam-induced deposition of amorphous carbon on the contact point between FeCNT and cantilever ensures a strong attachment of the nanotube. Next, amorphous carbon was also deposited at the free end of the FeCNT to lower its resonance frequency from above 2 MHz close to that of the cantilever. Throughout the process of carbon deposition, the oscillation of the FeCNT was observed with SEM to ensure close matching of the two resonance frequencies by employing a custom-made vibration stage. When the resonance frequencies of the subsystem are approaching each other, the resonance frequencies of the coupled system do not coincide with them anymore, as discussed above. In order to still measure the single resonance frequency of each subsystem we used a tungsten tip to hold the respective other subsystem, therefore detuning the coupled system. Figure 3 shows the sensor and magnified images of the free of the FeCNT end before and after frequency matching. Furthermore, the co-resonant oscillation of the nanotube is depicted.

Another feature of the co-resonant coupling is the amplitude amplification [13] of the free end of the oscillating nanotube as it is evident in Figure 3d. The free end of the FeCNT exhibits an amplitude of more than 2 µm, whereas the cantilever and the other end of the FeCNT conntected to the cantilever only oscillate in the range of a few nanometers.

Magnetometry measurement

All magnetometry measurements were carried out in a NanoScan AG hr-MFM at room temperature and under high vacuum (≈10^{-5} mbar). The machine employs a piezo actuator for oscillating the cantilever and a laser deflection detection system with a sectioned photo diode to determine its oscillation. We measured the amplitude response of the cantilever by sweeping the excitation frequency at a constant amplitude of the AC piezo voltage.

In order to generate a magnetic field parallel to the long axis of the FeCNT inside the measurement chamber, we used commercially available NdFeB magnets [14], positioned on a sample

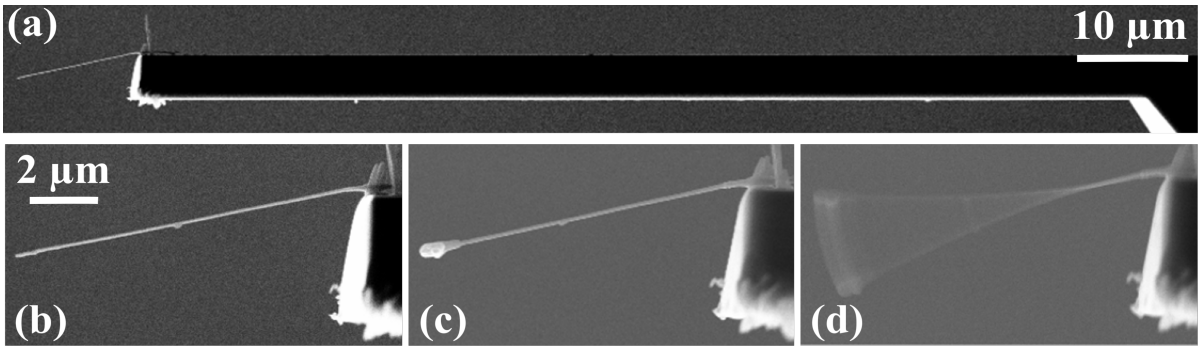

Figure 3: SEM images (a) of the fabricated sensor, (b) and (c) of the free end of the FeCNT before and after carbon deposition and (d) of the co-resonant oscillation of the FeCNT.

plate. The sensor position was fixed throughout the measurement and the sample plate carrying the magnets has been rotated in order to allow measurements with both magnetic field directions as well as at a field-free position. Figure 4 depicts a sketch of the setup with the measurement positions indicated and an image generated by the CCD camera of the instrument.

Furthermore, Figure 5 shows a two-dimensional simulation of the magnetic field obtained with the finite element software FEMM [15]. Close to the surface of the magnet at the height, where the measurements were carried out, the magnetic flux density reaches values of about 460 mT in the direction of the FeCNT's easy axis.

In order to measure at various magnetic field values without moving the sensor to ensure stable measurement conditions, the distance between sensor and magnet was changed by stepwise movement of the sample plate holding the magnet. At each step we measured the amplitude response of the cantilever in the frequency range of interest and determined the two resonance frequencies of the coupled system. Figure 6 shows two amplitude response curves as an example: one being taken at the position closest to the magnet, i.e., at a distance of about 100 µm in a field of approximately 406 mT, and the other one at a field-free position (see Figure 4). As can easily be seen, there is a significant change in the resonance frequencies of the coupled system which we attribute to the magnetic interaction between the iron filling of the FeCNT and the magnetic field of the NdFeB magnet.

Figure 7 depicts the measured resonance frequency shift for each of the two peaks of the coupled system compared to the field free measurement for various magnetic field values. We

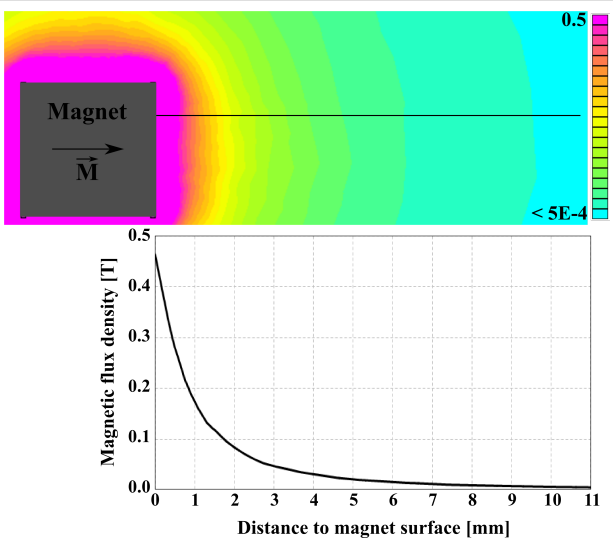

Figure 5: Simulated magnetic field of the permanent magnet. The field dependence on the distance to the surface of the magnet is calculated for the black line, corresponding to the measurement height.

observe a frequency shift of several 100 Hz in high magnetic field compared to the field free measurement for the left peak (a) in Figure 6. The shifts are even higher for the smaller, i.e., the right hand side, peak but it also features a higher measurement uncertainty regarding the determination of the maximum amplitude and hence resonance frequency. Table 2 summarizes the maximum frequency shift for both peaks and orientations of the magnetic field. The differences in the frequency shift values can be attributed to limited position accuracy of the magnets.

Results and Discussion

Compared to previous cantilever magnetometry experiments with similar FeCNTs, the frequency shifts in our experiment of

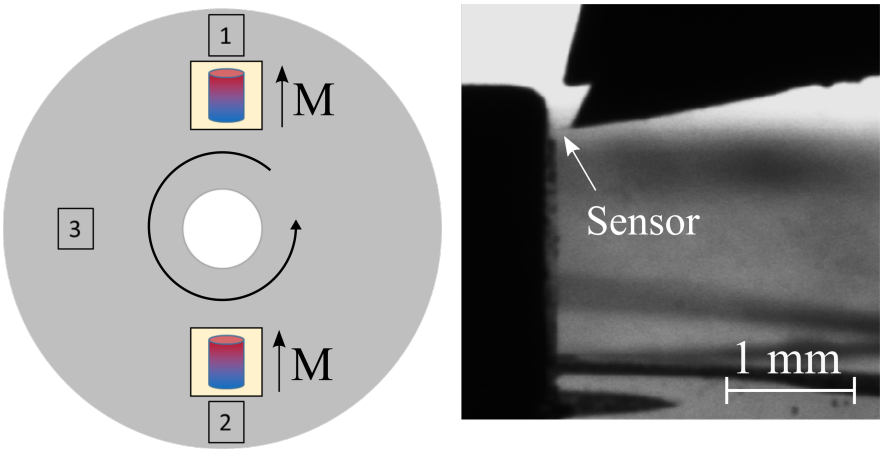

Figure 4: Sketch of measurement positions which are reached by keeping the sensor position fixed and rotating the sample plate. (1) and (2) correspond to the two orientations of the magnetic field and (3) is a field-free position. The CCD camera picture on the right hand side shows the sensor close to one of the magnets.

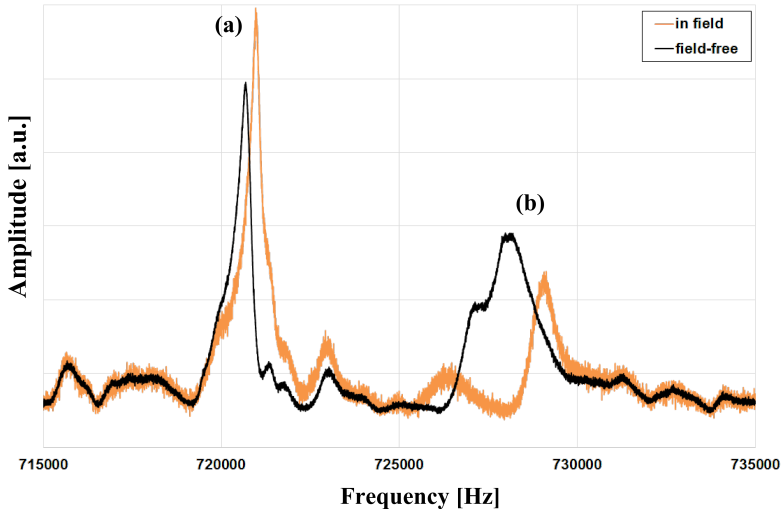

Figure 6: Amplitude response curves of the cantilever measured at the field-free position (3) according to Figure 4 and approximately 100 µm above the surface of the magnet (position (2)). The peaks are marked with (a) and (b) for reference purposes.

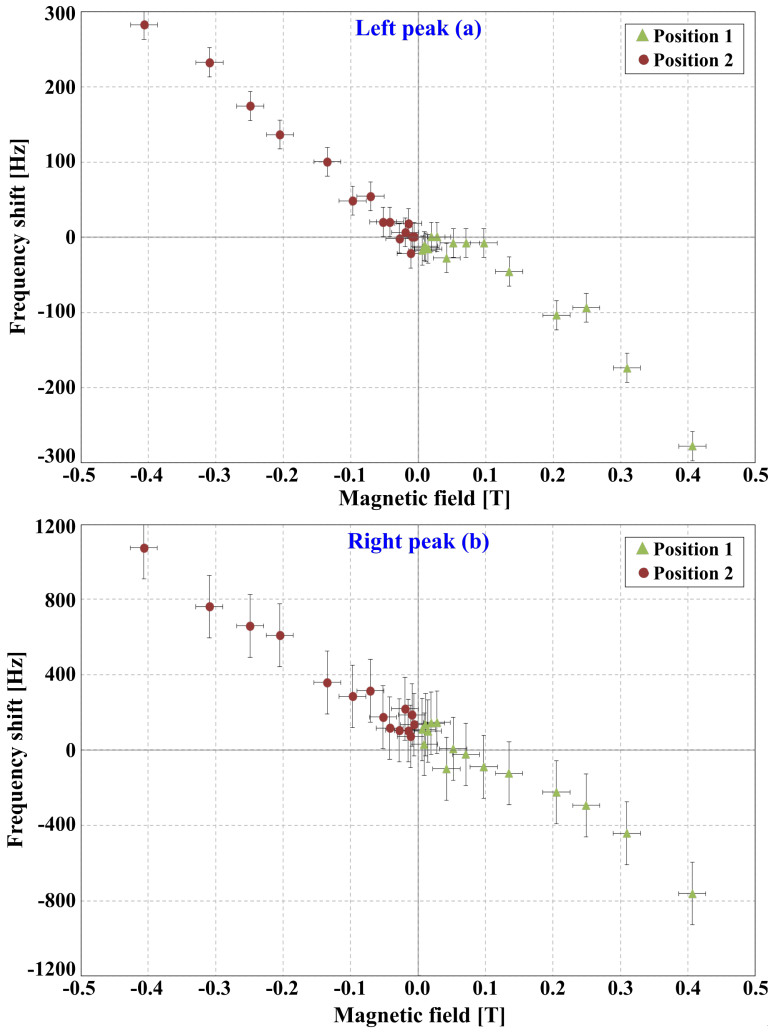

Figure 7: Measured frequency shifts of both peaks (a) and (b) compared to the field free measurement for various magnetic field values.

Table 2: Measured resonance frequencies $f_{a/b}$ of the coupled system for both orientations of the magnet and corresponding frequency shift values Δf compared to a field-free measurement. The values are given for the highest magnetic field.

	Left peak (a)	Right peak (b)
$f_{a/b}$ field-free	(720679.5 ± 10) Hz	(728051.3 ± 83) Hz
Position 1		
$f_{a/b}$ @ 406 mT	(720402 ± 10) Hz	(727290 ± 83) Hz
Δf	(−277.5 ± 20) Hz	(−761.3 ± 166) Hz
Position 2		
$f_{a/b}$ @ −406 mT	(720962 ± 10) Hz	(729124 ± 83) Hz
Δf	(282.5 ± 20) Hz	(1072.7 ± 166) Hz

280 Hz and 1000 Hz, respectively, for the two resonance peaks are increased by several orders of magnitude. For example, Banerjee et al. used similar FeCNTs on sensitive cantilevers with spring constants of about 0.2 N/m at low temperatures and measured frequency shifts in the order of mHz [7]. It has also been shown previously that a FeCNT oscillating in a magnetic field without being placed onto a cantilever can indeed exhibit a large frequency shift compared to the field-free case. However, the detection of the oscillatory state of the small nanotube remained a challenge as stated by Philippi et al. [16]. With our approach of co-resonant coupling we simultaneously allow for a very strong measurement signal and an easy detection of the oscillatory state of the FeCNT.

After the rather qualitative analysis of our obtained data, we now want to show the possibility to extract reliable magnetic information from the measured frequency shifts, making our sensor suitable for quantitative magnetic measurements.

Effective spring constant of the coupled system

In order to derive magnetic information from the measured frequency shift data, we use a relation similar to Equation 2 by introducing effective spring constants $k_{\mathrm{eff}}^{\mathrm{a/b}}$:

$$\frac{\Delta f_{\mathrm{a/b}}}{f_{\mathrm{a/b}}} \approx \frac{k^3}{2k_{\mathrm{eff}}^{\mathrm{a/b}}}, \tag{4}$$

and evaluate it with respect to k_3 which contains the magnetic interaction. Here $f_{\mathrm{a/b}}$ and $\Delta f_{\mathrm{a/b}}$ denote the two resonance frequencies of the coupled system and their respective shifts. The effective spring constants $k_{\mathrm{eff}}^{\mathrm{a/b}}$ determine the sensitivity for each resonance peak of the coupled system and have to be known for a quantitative analysis of the measured data.

In order to obtain them for the given sensor geometry we will be using an approximate formula to calculate the expected resonance angular frequencies of the coupled system $\omega_{\mathrm{a/b}} = 2\pi f_{\mathrm{a/b}}$ for a small interaction spring constant k_3[17]:

$$\omega_{\mathrm{a/b}}^2 = \frac{\omega_{12}^2 + \omega_{23}^2}{2} \pm \sqrt{\left(\frac{\omega_{12}^2 - \omega_{23}^2}{2}\right)^2 + \frac{{k_2}^2}{m_1 m_2}} \tag{5}$$

with $\omega_{12}^2 = (k_1 + k_2)/m_1$ and $\omega_{23}^2 = (k_2 + k_3)/m_2$. Furthermore, $m_{1,2}$ denote the effective masses of the subsystems which can easily be determined from their resonance frequencies (see Table 1) by $m_{1,2} = k_{1,2}/(2\pi f_{1,2})^2$. Equation 5 neglects any damping effects but this is a justified approximation since all our measurements are carried out under high vacuum, limiting damping to intrinsic effects due to the bending of the oscillating structures [9]. This was futhermore confirmed by comparison between the results obtained by Equation 5 and evaluating of the analytical solution of the differential equations describing the system.

With Equation 5 we can calculate the resonance frequencies of the coupled system for the two cases: without interaction, i.e., $k_3 = 0$, and with a small interaction, $k_3 = 1 \cdot 10^{-6}$ N/m, and determine the resulting frequency shifts. By inserting these values in Equation 4 and rearranging it, we are able to obtain the values for the effective spring constants for the two resonance peaks as:

$$k_{\mathrm{eff}}^{\mathrm{a}} = (0.028 \pm 0.007)\,\mathrm{N/m}$$
$$k_{\mathrm{eff}}^{\mathrm{b}} = (0.012 \pm 0.003)\,\mathrm{N/m}.$$

Comparing these values to the spring constants of the single subsystems $k_{\mathrm{cant}} = 133.8$ N/m and $k_{\mathrm{CNT}} = 0.0086$ N/m it is obvious that the effective spring constants of the coupled system are a mixture of the stiffnesses of the individual subsystems and that they are strongly influenced by the low stiffness of the FeCNT. Furthermore, the effective spring constants depend on the grade of frequency matching as can be seen from Equation 5. Closely matched resonance frequencies induce a strong interplay between the two subsystems. Hence, any magnetic interaction between FeCNT and external influences can be sensed with an effective stiffness slightly above the low spring constant of the FeCNT (in our case approximately by a factor of three) but be measured with a rather insensitive cantilever. However, we do not see the full sensitivity of the FeCNT in the measured frequency shift. Instead we observe a reduction leading to the conclusion that the behaviour of the coupled system can be described well by the effective spring constant k_{eff}.

However, it is important to note that k_{eff} is only constant as long as $k_3 << k_1$; k_2 is satisfied. Otherwise it shows a strong dependence on k_3. Calculations for our set of parameters depicted in Figure 8 indicate that k_3 has to be at least two orders of magnitude below the smaller spring constant of the system. This is well fulfilled in our case since the interaction spring constant for the strongest magnetic field of $|B|$ = 406 mT is approximately $2 \cdot 10^{-5}$ N/m (calculated with Equation 4). Please note that the results in Figure 8 are only shown for k_3 ¿ 0 but the behaviour is approximately similar for $k_3 < 0$, only with the deviations from the constant values being in the opposite direction.

Since for closely matched frequencies k_{eff} is mainly dominated by the smaller subsystem, a decrease of its stiffness will lead to an increase in sensitivity. Hence, possible sensor implementations could include the use of single walled carbon nanotubes as smaller oscillator or fabrication of the complete sensor in silicon technology, allowing for production of double cantilever structures with one nanocantilever [13,18].

However, it has to be noted that the low effective spring constant is not the sole reason for the increased signal strength of the proposed sensor setup. Other groups employed low-stiffness cantilevers for magnetometry measurements as well but did not obtain such a strong frequency shift signal. In cantilever magnetometry the signal is related to the length of the sensing cantilever and the spring constant as stated by Equation 3. Therefore, an increased cantilever length would in principle favorably affect the spring constant but nevertheless limits the sensitivity increase. In view of that our geometry is favorable as well since the sensing part, i.e., the nanotube, has a low spring constant while also being relatively short (in the order of 10 µm). Both features contribute to the observed strong increase in signal strength.

Determination of effective magnetic monopole moment from measured data

With the determination of k_{eff} it is possible to extract magnetic information from the measured frequency shift data, i.e., k_3. It has been shown that in case of a FeCNT a suitable magnetic quantity is the effective magnetic monopole moment q of the iron nanowire [19,20]. Due to its single-domain magnetic structure it is acting as an elongated magnetic dipole oscillating in a magnetic field. Since the magnetization of the iron nanowire is considered to be nearly parallel to the axis of the FeCNT, its two magnetic poles are positioned at either end, i.e., at a distance of L_{cnt} = 10 µm. Furthermore, a decrease of the field of the NdFeB magnet along the length of the FeCNT of maximal 5 mT is assumed. The interaction of each of the two poles with the external magnetic field leads to a contribution to the measured frequency shifts $\Delta f_{a/b}$. However, the magnetic pole at the attachement point between nanotube and cantilever gives a much lower contribution for several reasons: its oscillation trajectory radius and sensor stiffness are mainly given by the cantilever. In contrast to that the sensor stiffness at the free end of the FeCNT can be described by the soft effective spring constant of the coupled system. Hence, only the monopole at the free end of the FeCNT contributes to the frequency shift and the influence of the other pole can be neglected. Thus, the effective magnetic monopole moment proves to be a suitable parameter to characterize the magnetostatic behaviour of the iron of the FeCNT filling in the low external field approximation.

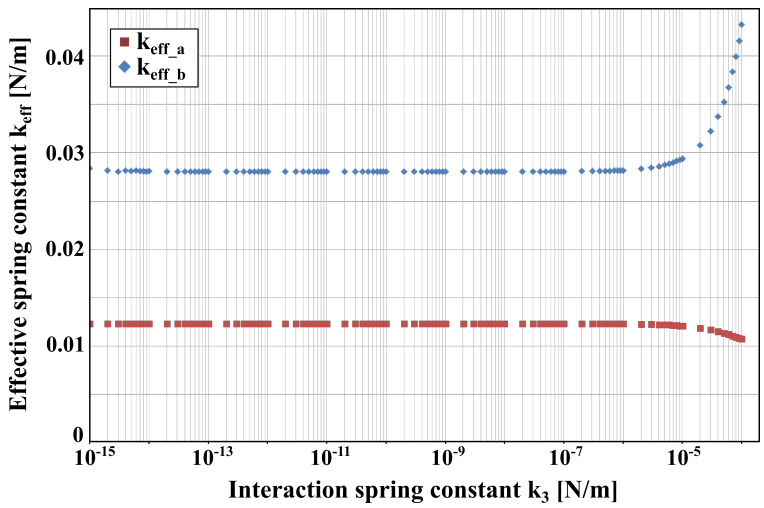

Figure 8: Dependence of the effective spring constant of each peak $k_{eff}^{a/b}$ on the interaction spring constant k_3. The calculations are based on the properties of the system given in Table 1.

Following Philippi et al. [16], the effective magnetic monopole moment q can be related to the interaction spring constant k_3:

$$q = \frac{k_3}{\kappa B}. \tag{6}$$

Here B is the magnetic flux density generated by the NdFeB magnet at the position of the free end of the FeCNT (see Figure 5). The parameter κ is given as the curvature of the oscillating termination point of the FeCNT and has been obtained from SEM pictures. The mechanical behaviour of an oscillating nanowire is discussed in depth elsewhere [16] and for our sensor we determined $\kappa = (0.16 \pm 0.016)\ \mu m^{-1}$.

By inserting Equation 6 in Equation 4 we obtain the relation:

$$\Delta f_{a/b} = \frac{f_{a/b}\kappa B}{2k_{eff}^{a/b}} q \tag{7}$$

which is used for a linear regression analysis of the measured frequency shift data in Figure 7 using the low field range $|B| < 0.25$ T to avoid major deviations from the monopole approach. This evaluation yields two q-values ($q_1 = 3.05 \cdot 10^{-10}$ A·m and $q_2 = 4.37 \cdot 10^{-10}$ A·m) corresponding to the two resonance peaks of the coupled system. Since the effective magnetic monopole moment has to be the same for both peaks we calculate the mean value and finally obtain $q = (3.7 \pm 0.7) \cdot 10^{-10}$ A·m, which corresponds to a magnetic moment of approximately $4 \cdot 10^8 \mu_B$ (CNT length 10 μm).

Geometric effective magnetic monopole moment

For comparison, the q-value of the FeCNT can be determined from geometric information obtained from high-resolution SEM pictures. With a diameter of the iron filling of the FeCNT of $d_{Fe} = (22 \pm 6)$ nm and saturation magnetization of iron $M_{s,Fe} = (1.71 \pm 0.01) \cdot 10^6$ A/m, the corresponding effective monopole moment is:

$$q_{geo} = \pi / 4 d_{Fe}^2 M_{s,Fe} = (6.5 \pm 3.6) \cdot 10^{-10}\ \mathrm{A \cdot m}. \tag{8}$$

Despite the relatively large margin of uncertainty due to the diameter measurement of the iron filling, this result corresponds well to the effective magnetic monopole moment determined from the frequency shift values. Furthermore, we can also compare our results to values obtained in other experiments with iron-filled carbon nanotubes of similar size and find a good agreement [7,16,21]. These results demonstrate that the co-resonant sensor concept applied to cantilever magnetometry allows for a quantitative determination of magnetic sample properties with strongly increased frequency shifts compared to single-cantilever magnetometry experiments [7].

Measurement limits

When proposing a novel sensor concept, inevitably the question regarding the measurement limit arises. The sensitivity limits of cantilever-based magnetometry sensors have already been discussed by various groups [3,22,23], leading to three main considerations which have to be taken into account: the sensitivity of the detection setup and thermal and magnetic noise in the oscillating system. From these, thermal noise is considered to be the most dominant one [24], followed by the detector noise which is statistically independent of the former [25]. For our discussion, we will only focus on thermal noise. Even if only this single noise source is considered it is still an open question how the noise is distributed in the co-resonantly coupled sensor system [26]. We will therefore use the approach of discussing the noise limits for each subsystem, indicating a range of the sensitivity for the coupled system.

In standard cantilever magnetometry the noise limits the detectable frequency shift and, hence, the minimal detectable magnetic moment. The thermal limit for the frequency shift for a cantilever is given by [25]:

$$\delta f_{thermal} = \sqrt{\frac{k_B T B_w f_0}{\pi k_0 Q A^2}}. \tag{9}$$

Hereby k_B denotes the Boltzmann constant, T the temperature, B_w the measurement bandwidth and Q the quality factor. f_0 and k_0 are the resonance frequency and spring constant of the cantilever and A is the amplitude at the free end of the cantilever. By following the reasoning of Gysin et al. [23], the frequency shift Δf induced by a high-aspect ratio, single domain ferromagnetic cylinder placed on a cantilever is given by Equation 3. Combining Equation 3 and Equation 9, the minimal detectable magnetic moment is:

$$\begin{aligned} m_{min} &= \frac{2L_{eff}^2}{\mu_0 H_{ext}} \frac{k_0}{f_0} \cdot \frac{H_{ext} + H_a}{H_a} \cdot \delta f_{thermal} \\ &= \frac{2}{\mu_0 H_{ext}} \frac{L_{eff}^2}{A} \cdot \frac{H_{ext} + H_a}{H_a} \cdot \sqrt{\frac{k_B T B_w}{\pi Q} \frac{k_0}{f_0}}. \end{aligned} \tag{10}$$

From this expression one can conclude that it is favorable to have a small cantilever length, a high oscillation amplitude, a strong magnetic field, small spring constant, high resonance frequency and a large quality factor. Both cantilever length and amplitude have a major influence on the minimal detectable

magnetic moment. Furthermore, m_{min} is maximized if H_{ext} and H_a are high.

The above expression has been derived for a single cantilever and it is still under investigation if and how it can be adapted for the coupled system. It is a reasonable assumption that, in accordance with the considerations of the effective spring constant, the quality factor will as well be an effective one for the coupled system. Similarly, the effective magnetic moment sensitivity of the coupled system is expected to lie in between the sensitivities of the two single systems. Therefore, in Table 3 we calculated the minimal detectable magnetic moment for both of our subsystems at room temperature, an external magnetic field of 1 T and a measurement bandwidth B_w = 1 Hz, in accordance with literature values for such calculations [3,23]. The necessary parameters for both subsystems are taken from Table 1 for the unmatched frequency state and the length of cantilever and nanotube have been taken from SEM pictures: L_{cant} = 85 µm and L_{cnt} = 10 µm. They have been recalculated into effective lengths by $L_{eff} = L/1.377$ for the first bending mode [6]. We are aware of the fact that there are carbon nanotubes, especially single wall CNTs, that can exhibit a much lower stiffness than the FeCNT presented here but we want to stick to our existing experimental system and have taken the mechanical properties of the CNT as measured.

Table 3: Minimal detectable magnetic moment for both subsystems of the coupled system. The calculations have been made for room temperature T = 293 K, a bandwidth of B_w = 1 Hz and magnetic field of B_{ext} = 1 T.

Parameter	Cantilever	FeCNT
spring constant [N/m]	133.8	0.0086
amplitude [nm]	10	1000
δf [mHz]	5	26
length [µm]	85	10
m_{min} [A·m^2]	$6 \cdot 10^{-15}$	$1 \cdot 10^{-20}$
m_{min} / μ_B	$7 \cdot 10^{8}$	$1 \cdot 10^{3}$

From Table 3 we see that the cantilever has a lower minimal detectable frequency shift (due to its better Q-factor and smaller resonance frequency) compared to the nanotube but still the nanotube exhibits a much better magnetic moment resolution of 10^3 μ_B at room temperature. It has to be kept in mind that the magnetization of small particles might not be thermally stable.

Comparing these calculated values to the measured magnetic moment of the section 'Determination of effective magnetic monopole moment from measured data', which was $m_{FeCNT} \approx 4 \cdot 10^8$ μ_B, we see that it is already at the limit of what could be measured with only the silicon cantilever. In our experiment, we observed a frequency shift of several 100 Hertz for the resonance frequencies of the coupled system which already indicates that the magnetic moment sensitivity is significantly increased compared to that of a single cantilever. Extending the considerations of Table 3 to single-wall carbon nanotubes and applying low temperatures, a potential moment sensitivity in the order of single Bohr magnetons could be achieved. However, as for the effective spring constant, it will probably not be possible to obtain the full moment sensitivity of the nanotube due to the strong interplay between the subsystems, but by using softer cantilevers and softer (unfilled) CNTs the coupled sensor concept has a great potential of achieving very low magnetic moment resolution while maintaining an easy detection at the same time.

Conclusion

We applied the universal concept of a co-resonantly coupled sensor to cantilever magnetometry by using a commercially available silicon cantilever and an iron-filled carbon nanotube. The FeCNT acted simultaneously as nanocantilever and magnetic sample and, since the magnetic properties of similar FeCNTs had already been studied, allowed for demonstrating the functionality of the sensor setup. The evaluation of the measurements shows that, once calibrated by determining the effective spring constant, the sensor can be used to derive magnetic properties of nanometer-sized samples and significantly increases the signal strength by several orders of magnitude compared to conventional single-cantilever magnetometry experiments. A further increase is possible by tailoring the components of the coupled system according to the measurement task. The basic principles of the co-resonant sensor concept [9] are of general nature and therefore not limited to cantilever magnetometry but can also be used to fabricate mass and force sensors in general.

Acknowledgements

We thank Siegfried Menzel for supporting the FIB preparation work and Uhland Weissker for preparing the FeCNT sample. This work was funded by the DFG (Grant No. MU 1794/3-2).

References

1. Chappert, C.; Fert, A.; Van Dau, F. N. *Nat. Mater.* **2007,** *6,* 813. doi:10.1038/nmat2024
2. Pankhurst, Q. A.; Connolly, J.; Jones, S. K.; Dobson, J. *J. Phys. D: Appl. Phys.* **2003,** *36,* R167. doi:10.1088/0022-3727/36/13/201
3. Stipe, B. C.; Mamin, H. J.; Stowe, T. D.; Kenny, T. W.; Rugar, D. *Phys. Rev. Lett.* **2001,** *86,* 2874. doi:10.1103/PhysRevLett.86.2874
4. Weber, D. P.; Rüffer, D.; Buchter, A.; Xue, F.; Russo-Averchi, E.; Huber, R.; Berberich, P.; Arbiol, J.; Fontcuberta i Morral, A.; Grundler, D.; Poggio, M. *Nano Lett.* **2012,** *12,* 6139. doi:10.1021/nl302950u

5. Rast, S.; Wattinger, C.; Gysin, U.; Meyer, E. *Rev. Sci. Instrum.* **2000,** *71,* 2772. doi:10.1063/1.1150690
6. Sidles, J. A.; Garbini, J. L.; Bruland, K. J.; Rugar, D.; Züger, O.; Hoen, S.; Yannoni, C. S. *Rev. Mod. Phys.* **1995,** *67,* 249. doi:10.1103/RevModPhys.67.249
7. Banerjee, P.; Wolny, F.; Pelekhov, D. V.; Herman, M. R.; Fong, K. C.; Weissker, U.; Mühl, T.; Obukhov, Y.; Leonhardt, A.; Büchner, B.; Hammel, P. C. *Appl. Phys. Lett.* **2010,** *96,* 252505. doi:10.1063/1.3440951
8. Longenecker, J. G.; Mamin, H. J.; Senko, A. W.; Chen, L.; Rettner, C. T.; Rugar, D.; Marohn, J. A. *ACS Nano* **2012,** *6,* 9637. doi:10.1021/nn3030628
9. Reiche, C. F.; Körner, J.; Büchner, B.; Mühl, T. *Nanotechnology* **2015,** *26,* 335501. doi:10.1088/0957-4484/26/33/335501
10. Leonhardt, A.; Hampel, S.; Müller, C.; Mönch, I.; Koseva, R.; Ritschel, M.; Elefant, D.; Biedermann, K.; Büchner, B. *Chem. Vap. Deposition* **2006,** *12,* 380. doi:10.1002/cvde.200506441
11. Leonhardt, A.; Ritschel, M.; Kozhuharova, R.; Graff, A.; Mühl, T.; Huhle, R.; Mönch, I.; Elefant, D.; Schneider, C. M. *Diamond Relat. Mater.* **2003,** *12,* 790. doi:10.1016/S0925-9635(02)00325-4
12. Wolny, F.; Obukhov, Y.; Mühl, T.; Weissker, U.; Philippi, S.; Leonhardt, A.; Banerjee, P.; Reed, A.; Xiang, G.; Adur, R.; Lee, I.; Hauser, A. J.; Yang, A. J.; Pelekhov, D. V.; Büchner, B.; Hammel, P. C. *Ultramicroscopy* **2011,** *111,* 1360. doi:10.1016/j.ultramic.2011.05.002
13. Li, X.; Ono, T.; Lin, R.; Esashi, M. *Microelectron. Eng.* **2003,** *65,* 1. doi:10.1016/S0167-9317(02)00595-6
14. Datasheet for NdFeB Magnet, grade 48. http://www.mtsmagnete.de/ (accessed Feb 15, 2015).
15. Information on the simulation software Finite Element Method Magnetics. http://www.femm.info/wiki/HomePage (accessed June 12, 2015).
16. Philippi, S.; Weißker, U.; Mühl, T.; Leonhardt, A.; Büchner, B. *J. Appl. Phys.* **2011,** *110,* 084319. doi:10.1063/1.3651392
17. Novotny, L. *Am. J. Phys.* **2010,** *78,* 1199. doi:10.1119/1.3471177
18. Vidal-Álvarez, G.; Agustí, J.; Torres, F.; Abadal, G.; Barniol, N.; Llobert, J.; Sansa, M.; Fernández-Regúlez, M.; Pérez-Murano, F.; San Paulo, A.; Gottlieb, O. *Nanotechnology* **2015,** *26,* 145502. doi:10.1088/0957-4484/26/14/145502
19. Wolny, F.; Mühl, T.; Weissker, U.; Lipert, K.; Schumann, J.; Leonhardt, A.; Büchner, B. *Nanotechnology* **2010,** *21,* 435501. doi:10.1088/0957-4484/21/43/435501
20. Vock, S.; Wolny, F.; Mühl, T.; Kaltofen, R.; Schultz, L.; Büchner, B.; Hassel, C.; Lindner, J.; Neu, V. *Appl. Phys. Lett.* **2010,** *97,* 252505. doi:10.1063/1.3528340
21. Reiche, C. F.; Vock, S.; Neu, V.; Schultz, L.; Büchner, B.; Mühl, T. *New J. Phys.* **2015,** *17,* 013014. doi:10.1088/1367-2630/17/1/013014
22. van Honschoten, J. W.; Koelmans, W. W.; Koning, S. M.; Abelmann, L.; Elwenspoek, M. In *Proceedings of Eurosensors XXII, the European Conference on Solid-State Transducers,* 2008; pp 597 ff.
23. Gysin, U.; Rast, S.; Aste, A.; Speliotis, T.; Werle, C.; Meyer, E. *Nanotechnology* **2011,** *22,* 285715. doi:10.1088/0957-4484/22/28/285715
24. Meyer, E.; Hug, H. J.; Bennewitz, R. *Scanning Probe Microscopy,* 1st ed.; Springer: Heidelberg, Germany, 2004; p 92. doi:10.1007/978-3-662-09801-1
25. Giessibl, F. J. *Rev. Mod. Phys.* **2003,** *75,* 949. doi:10.1103/revmodphys.75.949
26. Majorana, E.; Ogawa, Y. *Phys. Lett. A* **1997,** *233,* 162. doi:10.1016/S0375-9601(97)00458-1

License and Terms